Spectrally Efficient FDM Communication Signals and Transceivers: Design, Mathematical Modelling and System Optimization

by

Safa Isam A Ahmed

A thesis submitted for the degree of Doctor of Philosophy (PhD)

Communications and Information Systems Research Group
Department of Electronic and Electrical Engineering
University College London

October 2011

Statement of Originality

I, Safa Isam A Ahmed confirm that the work presented in this thesis is my own. Where information has been derived from other sources, I confirm that this has been indicated in the thesis.

Signed: _____

Date: _____

Abstract

This thesis addresses theoretical, mathematical modelling and design issues of Spectrally Efficient FDM (SEFDM) systems. SEFDM systems propose bandwidth savings when compared to Orthogonal FDM (OFDM) systems by multiplexing multiple non-orthogonal overlapping carriers. Nevertheless, the deliberate collapse of orthogonality poses significant challenges on the SEFDM system in terms of performance and complexity, both issues are addressed in this work.

This thesis first investigates the mathematical properties of the SEFDM system and reveals the links between the system conditioning and its main parameters through closed form formulas derived for the Intercarrier Interference (ICI) and the system generating matrices. A rigorous and efficient mathematical framework, to represent non-orthogonal signals using Inverse Discrete Fourier Transform (IDFT) blocks, is proposed. This is subsequently used to design simple SEFDM transmitters and to realize a new Matched Filter (MF) based demodulator using the Discrete Fourier Transforms (DFT), thereby substantially simplifying the transmitter and demodulator design and localizing complexity at detection stage with no premium at performance. Operation is confirmed through the derivation and numerical verification of optimal detectors in the form of Maximum Likelihood (ML) and Sphere Decoder (SD). Moreover, two new linear detectors that address the ill conditioning of the system are proposed: the first based on the Truncated Singular Value Decomposition (TSVD) and the second accounts for selected ICI terms and termed Selective Equalization (SelE). Numerical investigations show that both detectors substantially outperform existing linear detection techniques. Furthermore, the use of the Fixed Complexity Sphere Decoder (FSD) is proposed to further improve performance and avoid the variable complexity of the SD. Ultimately, a newly designed combined FSD-TSVD detector is proposed and shown to provide near optimal error performance for bandwidth savings of 20% with reduced and fixed complexity.

The thesis also addresses some practical considerations of the SEFDM systems. In particular, mathematical and numerical investigations have shown that the SEFDM signal is prone to high Peak to Average Power Ratio (PAPR) that can lead to significant performance degradations. Investigations of PAPR control lead to the proposal of a new technique, termed SLiding Window (SLW), utilizing the SEFDM signal structure which shows superior efficacy in PAPR control over conventional techniques with lower complexity. The thesis also addresses the performance of the SEFDM system in multipath fading channels confirming favourable performance and practicability of implementation. In particular, a new Partial Channel Estimator (PCE) that provides better estimation accuracy is proposed. Furthermore, several low complexity linear and iterative joint channel equalizers and symbol detectors are investigated in fading channels conditions with the FSD-TSVD joint equalization and detection with PCE obtained channel estimate facilitating near optimum error performance, close to that of OFDM for bandwidth savings of 25%. Finally, investigations of the precoding of the SEFDM signal demonstrate a potential for complexity reduction and performance improvement.

Overall, this thesis provides the theoretical basis from which practical designs are derived to pave the way to the first practical realization of SEFDM systems.

Acknowledgements

First and foremost I would like to try to express my deepest gratitude to my supervisor Prof. Izzat Darwazeh for the great supervision, guidance, motivation, support and friendship which have been the key to all I accomplished during the past three years. I have greatly benefited from Izzat's knowledge and experience not only to accomplish and improve my PhD project but to leverage and stretch a broad spectrum of my professional and personal skills. I would also like to thank him for supporting me to secure funding for this PhD.

I would like to thank Dr. Ioannis Kanaras for his explanation and work on the SEFDM system that constituted a basis for many aspects of my work. I am specially grateful for the advice, the long and stimulating discussions on the system and above of all for the friendship and moral support.

I would like to thank Ryan Grammenos, Marcus Perrett and Paul Whatmough for the development of the hardware implementations of the receiver and transmitter designs. Special thanks are to Ryan Grammenos for comments on this thesis, Dr. Arsenia Chorti for the discussions about the basics of the system and the comments on the demodulator design and Dr. Manoj Thakur for advice and help with the AWG verifications of the IDFT transmitter. I am also grateful to Goodenough College members and staff for providing a supportive, stimulating and enjoyable living experience during the course of my study.

Last but not least I would like to express my deepest gratitude to my family who supported me through the course of the PhD studies. I am greatly indebted to my wonderful parents Isam and Selma whose love and support now and throughout my life has led me to all that I accomplished. I am also grateful to my wonderful mother in law Fatima and my uncle Salah for the support to me and my family throughout my study time. My deepest thanks are to my husband Abdalla and my two years old son Mazin for accompanying me in this challenging and stimulating experience with all its ups and downs. I would like to thank them for being very supportive, patient, understanding and sacrificing to help me accomplish this work. Special thanks are to Abdalla for help with the drawing of the block diagrams.

During the course of this work I have been funded by the Overseas Research Student (ORS) Award and UCL Graduate School Research Scholarships (GSRS) for three years of study and Gordon Memorial Trust Fund (GMTF) and Izzat's funding for the last three months.

Contents

List of Figures

List of Tables

Glossary and Abbreviations

α	Bandwidth Compression Factor
$\det(.)$	Determinant
$[\cdot]^*$	Hermitian conjugate if the argument is a matrix and a conjugate if the argument is scalar
$[\cdot]^T$	Matrix transpose
$\langle\cdot\rangle$	Inner product
$\lceil\cdot\rceil$	Ceiling function
$\lfloor\cdot\rceil$	Slicing operator
$\lfloor\cdot\rfloor$	Floor function
$\|\cdot\|$	Euclidean norm
$\mathbb{N}$	The group of Natural numbers
$\mathbf{A}$	Uppercase bold character denote a matrix
$\mathbf{A}[i,j]$ or $a_{i,j}$	is the element at the i^{th} row and the j^{th} coulmn of the matrix $\mathbf{A}$
min	Minimize
$\otimes$	The Convolution
chol $\{\}$	Cholesky Decomposition
diag $[\cdot]$	The diagonal elements of the argument matrix

$\mathrm{E}[\cdot]$	Expectation operator
$\mathrm{rank}\{\cdot\}$	Rank of a matrix
$\mathrm{Tr}\{\cdot\}$	Trace of a matrix
A	Uppercase character denote a vector
$A[i]$ or a_i	is the i^{th} element of the vector A
$erfc(\cdot)$	Complementary Error Function
j	$\sqrt{-1}$
ADS	Advanced Design System
ADSL	Asymmetric Digital Subscriber Loop
ASIC	Application Specific Integrated Circuit
AWG	Arbitrary Waveform Generator
AWGN	Additive White Gaussian Noise
BER	Bit Error Rate
BFDM	Biorthogonal Frequency Division Multiplexing
BPSK	Binary Phase Shift Keying
CCDF	Complementary Commulative Distribution Function
CIR	Channel Impulse Response
COFDM	Coded Orthogonal Frequency Division Multiplexing
CR	Clipping Ratio
CSD	Complex Sphere Decoder
CSI	Channel State Information
D/A	Digital to Analoge Converter
DAB	Digital Audio Broadcasting

DCT	Discrete Cosine Transform
DFT	Discrete Fourier Transfrom
DMT	Discrete Mutli-tone
DOFDM	Dense OFDM
DVB-T	Terrestrial Digital Video Broadcasting
FCE	The Full Channel Estimator
FCT	Fast Cosine Transform
FDM	Frequency Division Multiplexing
FFT	Fast Fourier Transform
FOFDM	Fast OFDM
FP	Fichke-Pohst Enumeration
FPGA	Field Programmable Gates Array
FrFT	Fractional Fourier Transform
FSD	Fixed Sphere Decoder
FTN	Faster than Nyquist
GS	Gram Schmidt
HC-MCM	Hign Compaction Multicarrier Communication Modulation
HIPERLAN	High Performance LAN
IC	Iterative Cancellation
ICI	Intercarrier Interference
IDCT	Inverse Discrete Cosine Transform
IDFT	Inverse Discrete Fourier Transform
IEEE	Institute of Electrical and Electronic Engineering

IID	Independent and Identically Distributed
ILS	Integer Least Square
IMD	Inter-Modulation Distortion
IMGS	Iterative Modified Gram Schmidt
IOTA	Isotropic Orthogonal Transform Algorithm
IPM	Interior Point Method
ISI	Intersymbol Interference
LAN	Local Area Network
LHS	Left Hand Side
LM	Löwdin Method
LS	Least Squares
LTE	Long Term Evolution
LUT	Look Up Table
MAP	Maximum a Posteriori
MASK OFDM	M-ary Amplitude Shift Keying OFDM
MC-CDMA	Multicarrier Code Division Multiple Access
MCM	Multicarrier Modulation
MF	Matched Filter
MGS	Modified Gram Schmidt
MIMO	Multiple Inputs Multiple Outputs
ML	Maximum Likliehood
MLSD	Maximum Likelihood Sequence Detection
MMSE	Minimum Mean Square Error

MSE	Mean Square Error
OFDM	Orthogonal Frequency Division Multiplexing
OFDMA	Orthogonal Frequency Division Multiple Access
Ov-FDM	Overlapped Frequency Division Multiplexing
PA	Power Amplifier
PAPR	Peak to Average Power Ratio
PC-OFDM	Parallel Combinatory OFDM
PCE	The Partial Channel Estimater
PDF	Probability Density Function
PDP	Power Delay Profile
PLC	Power Line Communications
PSD	Pruned Sphere Decoder
PTS	Partial Transmit Sequence
QAM	Quadrature Amplitude Modulation
QPSK	Quadrature Phase Shift Keying
RegSD	Regularized Sphere Decoder
RHS	Right Hand Side
RSD	Real Sphere Decoder
S/P	Serial to Parallel Converter
SD	Sphere Decoding
SDP	Semidefinite Programming
SE	Schnorr Euchner Enumeration
SEFDM	Spectrally Efficient FDM

SelE	Selective Equalization
SLM	Selective Mapping
SLW	SLiding Window PAPR Reduction Technique
SNR	Signal to Noise Ratio
SVD	Singular Value Decomposition
TDL	Tapped Delay Line
TSVD	Truncated Singular Value Decomposition
UCL	University College London
WiMAX	World-wide interoperability for Microwave Access
ZF	Zero Forcing

Part I

SEFDM System: Characteristics, Transmitter and Receiver Design

Chapter 1

Introduction

Throughout the 20^{th} century, the rapid development of communications technologies has transformed our economic, social and personal lives. The creation and growth of services and applications facilitated by communications development is expected to continue, and the added value of mobility has taken the change to a new level. Wireless communication services began with simple limited facilities for vital or emergency communications, and moved on to become essential for all aspects of our lives. As such, wireless communications continue to evolve to provide seamless services to accommodate our insatiable demand for bandwidth and speed. However, the wireless channel places a demand for the invention of alternative designs with the objective of saving spectrum and coping with wireless channel impairments. Consequently, modulation, multiplexing and multiple access techniques are evolving to provide higher capacities and to combat wireless channel limitations.

Conventional single carrier modulation systems convey information as a change in the amplitude, frequency or phase of the carrier. The modulated signal is allowed to cover all the available bandwidth. In the case of digital signals, as the bit rate increases the duration of one bit is reduced, therefore the system becomes more susceptible to impairments such as those caused by intersymbol interference (ISI) [1]. Therefore, multicarrier communications are proposed to facilitate increased utilization of the scarce wireless spectrum while combating one of its main impairments namely frequency selective fading [2].

Orthogonal Frequency Division Multiplexing (OFDM) is a well known Multicarrier Modulation (MCM) scheme that is being used at the heart of many applications [3]. The signature feature of OFDM, which is the use of overlapping yet orthogonal subcarriers, has facilitated many advantages that gained the system its wide popularity. In particular, OFDM is advantaged by enabling higher bandwidth utilization when compared to conventional FDM systems employing guard bands and better immunity against channel impairments. Instead of sending one high data rate single carrier signal, OFDM sends multiple overlapped slower subchannels. Such a system provides better immunity against frequency selective fading because the fading is not likely to affect all the bands at the same time, and the slow speed of the subchannels facilitates better immunity against the delay spread of the channel [2]. Historically, the concepts of OFDM appeared as early as the late 1950's [4], developed in the 1960's [5, 6, 7] and was filed for a patent by Chang of Bell Labs in 1966 (granted in 1970) [8]. The OFDM advantages became more attractive with the proposal of using standard Discrete Fourier Transforms (DFT) at both transmitting and receiving ends [9, 10], a feature that became even more handy with the tremendous growth of the digital processing power [11]. Today, OFDM is at the heart of many applications and standards. For example, Coded OFDM (COFDM) is used in Asymmetric Digital Subscriber Loop (ADSL), also known there as Discrete Multi-tone (DMT) [2]. Moreover, OFDM is specified in the standard of the European Digital Audio Broadcasting (DAB) and the Terrestrial Digital Video Broadcasting (DVB-T) systems. In addition, OFDM is specified in wireless LAN standards IEEE 802.11a, g, n and y and in the High Performance LAN (HIPERLAN/2) [3]. OFDM is used in the Fixed Worldwide interoperability for Microwave Access (WiMAX), which is based on IEEE 802.16-2004 standard and the mobile WiMAX, which is based on IEEE 802.16e-2005 standard. Significantly, OFDM with multiple access (OFDMA) became the chosen technique for the 4^{th} generation mobile system known as Long Term Evolution (LTE) [12, 13, 14], where a combination of OFDM and Multiple Input Multiple Output (MIMO) OFDM is utilized for maximizing capacity in multi-service networks. OFDM was also proposed and is currently used for broadband Power Line Communications (PLC) [15, 16], to provide enhanced performance over single carrier and direct sequence spread spectrum techniques. OFDM concepts are not limited only to wireless and copper and have been applied in the optical domain [17, 18].

The OFDM system constrains the subcarriers to exist in fixed positions relative to

each other to maintain orthogonality. Performance of the OFDM system is critically dependent on the orthogonality of the subcarriers. Therefore, frequency shifts and timing errors result in substantial Bit Error Rate (BER) degradation [2]. In terms of spectral efficiency, OFDM is capable of delivering the highest possible efficiency for an orthogonal system. That is to convey $2N$ independent signals on an N subcarrier system. Any attempt to increase efficiency beyond that is impossible with the orthogonality constraint satisfied. This led to the introduction of several non-orthogonal multicarrier Spectrally Efficient FDM (SEFDM) systems promoting higher Spectral Efficiency than the well known OFDM systems.

Generally, SEFDM systems employ non-orthogonal overlapped carriers where the spectral efficiency is increased by reducing the spacing between the subcarriers and/or the per carrier transmission rate, beyond the time-frequency orthogonality rule of OFDM. Many variants of such systems appeared independently under different names. Early examples being the Fast OFDM (FOFDM) [19] and M-ary Amplitude Shift Keying OFDM (MASK) [20] offered to halve spectrum utilization but are constrained only to one dimensional modulations such as BPSK and M-ary ASK. Spectrally Efficient FDM (SEFDM) [21]; High Compaction Multicarrier-Communications (HC-MCM) [22]; Overlapped FDM system (Ov-OFDM) [23]; Multistream Faster than Nyquist Signalling (FTN) [24, 25] and Optical Dense OFDM (DOFDM) [26], all promise variable spectral savings for two dimensional modulations. Furthermore, the concept of non-orthogonal multicarrier systems has been intelligently used in the design of physical layer encryption for OFDM system [27, 28], where, the created intercarrier interference due to the lost orthogonality is utilized to mask the intended message sent over an orthogonal subset of the carriers. Review of the SEFDM system and brief outline of the other systems are provided in chapter 2.

A similar spectral efficiency approach has been tackled in the single carrier case since the 1970's. Salz in [29] discussed Faster than Nyquist (FTN) signalling and suggested that an error penalty is to be expected in most practical cases. FTN signalling attempts to increase transmission rate by reducing transmission time below the Nyquist criteria. However, Mazo in [30] explored the possibility of defining the minimum distance requirement for signals transmitted at a rate faster than Nyquist. Consequently, Mazo established that, provided an optimum detector is deployed, it is possible to increase

the packing of signals in time by 20% and still obtain optimal error performance [31]. Subsequent work in FTN systems considered the problem of identifying the minimum signalling distance and confirmed that no performance degradation should be expected for the reduction of transmission time until the identified limit [32, 33, 34]. Recently, the work in [24] proceeded to extend the Mazo limit to two dimensional signals, exploiting both time and frequency. The established limit shows that it is possible to reduce the combined time-frequency requirement of a system up to a certain level without introducing performance degradation. With the concept being backed by the sum of research work outlined above, it remains to design systems that can achieve the enhancement in spectral efficiency at affordable complexity and the potential for implementation. This is the focus of this thesis.

1.1 Aim and Motivation

The work in this thesis focuses on the SEFDM system of [21]. The SEFDM system enhances bandwidth utilization by reducing the frequency distance between the subcarriers while maintaining the same transmission rate per carrier [21]. Notwithstanding, the deliberate collapse of orthogonality generates significant interference between the subcarriers that turns the detection of the signal to an overly complex problem. Maximum Likelihood (ML) SEFDM detector has demonstrated attractive BER performance. However, ML detection complexity increases exponentially with the increase in the system size. In addition, linear detection techniques such as Zero Forcing (ZF) and Minimum Mean Squared Error (MMSE) perform well only for small sized systems in high Signal to Noise Ratio (SNR) conditions [35]. Finally, Sphere Decoders (SD) is shown to achieve optimum performance at a much reduced but random complexity [36] whose volatility depends on the noise and the system coefficient matrix properties.

Previous work in SEFDM [21, 35, 36] shows that bandwidth savings of 20% can be achieved while maintaining the same error performance as OFDM in AWGN channel. A legitimate question at this point is what is the motivation of this work? A simple answer is that despite the fact that this new frequency-time utilization opens up a new dimension for possible improvement of spectral efficiency, the main limitation remaining is how realistic are the requirements of such a system in terms of transmission and

reception complexity and error performance. The proposed techniques so far require high complexities that can be prohibitive in some cases. The other alternative is to lower performance expectations which may not be able to stand the argument of why not migrate to an OFDM system with high order modulation. This indicates that the appealing offer of bandwidth savings can be seriously demoted due to the impractical realization efforts required. That is, the huge complexity at transmission and reception ends threatening the applicability of the system. Therefore, the work in this thesis aims to bridge the research gap of achieving a feasible SEFDM system while maintaining the performance.

To achieve the above research aim, the work in this thesis commences with developing mathematical models for the transmitted and received signals to asses the fundamental limitations of the system and to identify their links to system parameters. Then, the transmitter design is approached. Generation of the SEFDM signal is developed to be realized with a complexity close to OFDM system, using judiciously arranged standard Inverse Discrete Fourier Transform (IDFT) blocks. Following that, efficient demodulator architectures are proposed based on the DFT. The optimal detector for the proposed demodulator is mathematically derived and numerically evaluated. In addition, new sub-optimal detectors, that require less complexity than the cited work with improved error performance, are proposed and numerically evaluated. After that, investigations of the SEFDM practical limitations are carried out. In particular, the Peak to Average Power Ratio (PAPR) is studied and techniques to control it are proposed and evaluated. Furthermore, investigations of the SEFDM signal equalization in fading channels are presented and a new improved channel estimators are proposed and evaluated. Finally, a new system that employs precoding to improve error performance and reduce receiver complexity is developed.

1.2 Thesis Organization

This thesis is divided into two parts; the first part focuses on identifying key design considerations and fundamental challenges that includes; system modelling; transmitter design; demodulator design and detection in AWGN channel. The second part focuses on practical system considerations, specifically the issue of the PAPR; the performance in

fading channels and the development of precoding techniques to improve signal resilience against impairments and reduce detection complexity.

Chapter 2 introduces the Spectrally Efficient FDM System. The chapter starts with a brief outline of Orthogonal Frequency Division Multiplexing Systems followed by the introduction of the concept of increasing spectral efficiency by employing non-orthogonal multicarrier systems. The SEFDM system is then introduced in terms of system concepts as well as transmitter and receiver arrangements. The chapter discusses the demodulation and detection of the SEFDM signal, describes the systems in the literature that adopt similar approaches to improve spectral efficiency and concludes by identifying the gaps in the SEFDM research area.

Chapter 3 presents the discrete signal model for the transmitted and received SEFDM signal with derivations of the Intercarrier Interference (ICI). In addition, the chapter presents the general linear regression model that describes the demodulated signals when matched filtering or orthonormal bases are used and proceeds to relate the signature attributes of the system to its parameters.

Chapter 4 builds on the discrete SEFDM signal model derived in chapter 3 to develop efficient transmitter architectures based on general purpose IDFT. Furthermore, the examination of the signal realizations with general purpose Field Programmable Gate Array (FPGA) based devices is briefly described together with the implementations on FPGA boards which are currently underway at UCL.

Chapter 5 focuses on the reception of the SEFDM signal. Efficient demodulators based on Matched Filter (MF) theory are proposed and then related to the DFT. The optimal detector that minimizes the error rate for the MF based SEFDM signal is derived and evaluated with numerical simulations. Furthermore, the Sphere Decoder (SD) realization of the derived optimal detector is derived and numerically assessed in terms of error rate performance and complexity. The chapter provides comparisons with the previously developed correlation based demodulator and the ML and SD solution associated with it.

In chapter 6 the reduction of the detection effort is approached. Two enhanced linear detectors are designed on the basis of the discrete model and the ICI characterization

matrix derived in chapter 3, the first based on the Truncated Singular Value Decomposition (TSVD) and the second accounts for selected ICI terms and termed Selective Equalization (SelE). Numerical simulations show that the TSVD and SelE are capable of achieving enhanced error performance. Furthermore, the Fixed Complexity Sphere Decoder (FSD) is proposed to alleviate the variable complexity obstacle faced with the original SD algorithm and to provide enhanced error performance that can be traded off with complexity. Finally, a new FSD algorithm is developed by combining it with the TSVD, with detailed results showing performance improvement at a reduced complexity than the FSD alone.

Chapter 7 addresses the issue of the PAPR of the SEFDM system. The SEFDM is proved to be prone to high PAPR and as such is subjected to the nonlinear distortions if the peaks exceed the dynamic ranges of the system components. However, the SEFDM signal is shown to have lower occurrences of high PAPR when compared to OFDM which decrease further with the increase in bandwidth compression level. PAPR control techniques imported from OFDM are then applied to the SEFDM signal. Clipping, Partial Transmit Sequence (PTS) and Selective Mapping (SLM) are used to reduce the probability of the PAPR exceeding a threshold level. Furthermore, a new PAPR reduction technique is designed for the SEFDM signal based on the signal design proposed in chapters 3 and 4. The technique is termed SLiding Window (SLW) and is described in detail with its numerical results that show an efficacy to reduce the PAPR beyond PTS and similar to SLM with a much reduced complexity.

Chapter 8 addresses the issue of the SEFDM signal in fading channels. First, the MF based demodulation is extended to the case of fading channel and is shown by numerical simulations to achieve the same performance as the system based on orthonormal bases. Following that, a new channel estimator, termed Partial Channel Estimator (PCE), is designed and evaluated by means of numerical simulations that demonstrates improved estimation accuracy when compared to Full Channel Estimation (FCE). Moreover, joint channel equalization and symbol detection using the TSVD, FSD and FSD-TSVD is proposed. The FSD-TSVD equalizer-detector based on PCE obtained channel estimates achieves near-optimal performance with fixed complexity requirements.

Chapter 9 follows a different route to answer the SEFDM problem. In this chapter, precoding of the SEFDM signal prior to transmission is proposed. This arrangement

leads to a two stages reception approach where part of the originally transmitted symbols can be estimated with minimal detection effort, thus the complexity is localized in a fraction of the overall system size.

Finally, chapter 10 summarizes the work in this thesis and discusses the significance of the proposed techniques. In addition, the chapter provides recommendations for future work.

The thesis includes two appendices. Appendix B provides detailed steps for the proof of Lemma 3.1 and Appendix A explains Theorem 3.1 with numerical examples.

1.3 Main Contributions

This thesis documents work in different areas of the SEFDM system, covering system modelling, transmission, reception, optimization and performance investigations. The main contributions of this work, mathematical and engineering wise, are listed below:

- Mathematical system modelling that includes:
  - Development of a mathematical model for the discrete SEFDM system at generation and reception ends and the derivations of closed form formulas for the intercarrier interference for the continuous and discrete time systems.
  - Derivations of mathematical bounds on the conditioning of the SEFDM system based on the number of subcarriers and bandwidth compression level.
  - Development of the mathematical and conceptual framework of the IDFT based representation of the SEFDM signals.
- Design and performance assessment of efficient IDFT based transmitters for SEFDM, verified by simulations and experimentation.
- Proposal and assessment of the MF demodulator and its DFT based implementation which led to the reduction of the complexity of the receiver.
- Design and performance assessment of optimal detectors for the MF based receiver.
- Design and performance assessment of four reduced complexity detectors:

  - Detection based on the Truncated Singular Value Decomposition (TSVD).
  - Design of Selective Equalization (SelE) detection method that utilizes the derivations of the ICI from the mathematical modelling contribution.
  - The proposal and performance assessment of a Fixed Complexity Sphere Decoders (FSD) .
  - The design and performance assessment of a hybrid SEFDM detector combining TSVD and the FSD .

- Investigations of the PAPR in SEFDM system and its reduction mechanisms leading to the design of a new PAPR reduction technique that surpassed conventional techniques in complexity and PAPR reduction efficiency.
- Performance assessment in fading channels that included:
  - Design and performance assessment of PCE channel estimators.
  - Proposals of reduced complexity joint channel equalizers and symbol detectors.
- Introduction of precoding concept of the SEFDM to improve performance and reduce complexity.

1.4 List of Publications

The above contributions have led to 3 journal publications and 12 conference presentations and publications listed in chronological order:

1. S. I. A. Ahmed and I. Darwazeh, IDFT Based Transmitters for Spectrally Efficient FDM System, in London Communication Symposium (LCS'09), Sep 2009.
2. S. Isam and I. Darwazeh, Simple DSP-IDFT Techniques for Generating Spectrally Efficient FDM Signals, in IEEE, IET International Symposium on Communication Systems, Networks and Digital Signal Processing (CSNDSP'10), pp. 20-24, Jul 2010.

3. S. Isam and I. Darwazeh, On the Digital Design of Non-Orthogonal Spectrally Efficient Frequency Division Multiplexed (FDM) signals, in 4th International Symposium on Broadband Communications (ISBC'10), Jul 2010.

4. S. Isam and I. Darwazeh, Investigating the Performance of Spectrally Efficient FDM System in Time Varying Fading Channel, in London Communication Symposium (LCS'10), Sep 2010.

5. S. Isam and I. Darwazeh, Precoded Spectrally Efficient FDM System, in 21th Personal, Indoor and Mobile Radio Communications Symposium (IEEE PIMRC'10), pp. 99-104, Sep 2010.

6. S. Isam and I. Darwazeh, IDFT-DFT Techniques for Generating and Receiving Spectrally Efficient FDM Signals, American Journal for Engineering and Applied Sciences. (Invited, to appear)

7. S. Isam, I. Kanaras, and I. Darwazeh, A Truncated SVD Approach for Fixed Complexity Spectrally Efficient FDM Receivers, in IEEE Wireless Communications & Networking Conference (IEEE WCNC'11), pp. 1584-1589, March 2011.

8. S. Isam and I. Darwazeh, Design and Performance Assessment of Fixed Complexity Spectrally Efficient FDM Receivers, in IEEE 73rd Vehicular Technology Conference (IEEE VTC'11), pp. 1-5, May 2011.

9. S. Isam and I. Darwazeh, Peak to Average Power Ratio Reduction in Spectrally Efficient FDM Systems, in IEEE 18th International Conference on Telecommunications (IEEE ICT'11), pp. 363-368, May 2011.

10. P. N. Whatmough, M. Perrett, S. Isam, and I. Darwazeh, VLSI Architecture for a Reconfigurable Spectrally Efficient FDM Baseband Transmitter, in IEEE International Symposium on Circuits and Systems (IEEE ISCAS'11), pp. 1688-1691, April 2011.

11. R. C Grammenos, S. Isam and I. Darwazeh, FPGA Design of a Truncated SVD Based Receiver for the Detection of SEFDM Signals, in 22nd Personal, Indoor and Mobile Radio Communications Symposium (IEEE PIMRC'11), Sep 2011.

12. S. Isam and I. Darwazeh, Design and Performance Analysis of Enhanced Receivers for Spectrally Efficient FDM System, in London Communication Symposium (LCS'11), Sep 2011.

13. R. G. Clegg, S. Isam, I. Kanaras and I. Darwazeh, A practical system for improved efficiency in frequency division multiplexed wireless networks, IET Communications Journal, 2011. (To appear in 2012)

14. P. N. Whatmough, M. Perrett, S. Isam, and I. Darwazeh, VLSI Architecture for a Reconfigurable Spectrally Efficient FDM Baseband Transmitter, in IEEE Transactions of Circuits and Systems.(Invited, to appear may 2012)

15. S. Isam and I. Darwazeh, Robust Channel Estimators for Spectrally Efficient FDM Receivers, submitted to International Conference on Telecommunications (IEEE ICT'12).

16. S. Isam and I. Darwazeh, Characterizing the Intercarrier Interference of Non-orthogonal Spectrally Efficient FDM System, submitted to International Conference on Telecommunications (IEEE ICT'12).

Chapter 2

The SEFDM System

Introduction

The Spectrally Efficient Frequency Division Multiplexing (SEFDM) system was proposed as a multicarrier modulation (MCM) scheme that promises better utilization of bandwidth than an equivalent Orthogonal Frequency Division Multiplexing (OFDM) system. SEFDM achieves spectral savings by reducing the spacing of the subcarriers and/or transmission time, thus violating the orthogonality rule [21]. However, the reduction in bandwidth requirements comes at the cost of increased complexity at transmitting and receiving ends and much of the research in SEFDM systems focuses on developing high performance systems at low complexity.

This thesis focuses on the SEFDM system of [21], therefore, this chapter aims to provide the necessary background of the system. To put everything into prospective, the chapter starts by briefly reviewing the OFDM system and then the SEFDM system is studied in terms of the principles, generation and detection of the system. Furthermore, an outline of other systems that propose better spectral efficiency than OFDM is presented and the chapter is concluded by the statements of the gaps, limitations, and possible directions of enhancement.

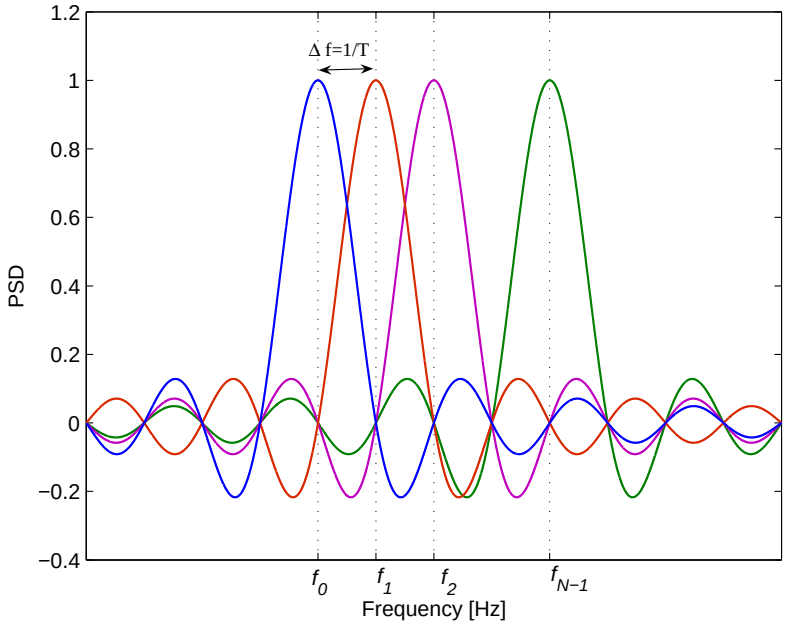

FIGURE 2.1: OFDM spectra: N subcarriers spaced by $1/T$ Hz.

2.1 Orthogonal Frequency Division Multiplexing (OFDM)

In OFDM, a high data rate input symbols stream is divided into slower substreams that are individually modulated onto the orthogonal subcarriers and sent out simultaneously down the channel. In general, for a system transmitting an OFDM symbol every T seconds the OFDM signal $x_O(t)$ can be expressed as

$$x_O(t) = \frac{1}{\sqrt{T}} \sum_{l=-\infty}^{\infty} \sum_{n=0}^{N-1} s_{l,n} g(t - lT) e^{j2\pi n \Delta f t}, \tag{2.1}$$

where $s_{l,n}$ denotes the complex information symbol modulated on the n^{th} subcarrier in the l^{th} OFDM symbol, T is the symbol duration of an OFDM symbol, Δf is frequency separation between the subcarriers, $g(t)$ is a pulseshaping function and $j = \sqrt{-1}$. The subcarriers are spaced out in the frequency spectrum such that their individual spectra overlap but remain orthogonal. If $g(t)$ is taken as a rectangular pulse, Δf has to be equal to the reciprocal of one OFDM symbol duration to satisfy orthogonality, thus resulting in the sinc spectra as in Fig. 2.1. This frequency-time arrangement ensures that the different subcarriers are separable despite the overlapping and the simultaneous transmission.

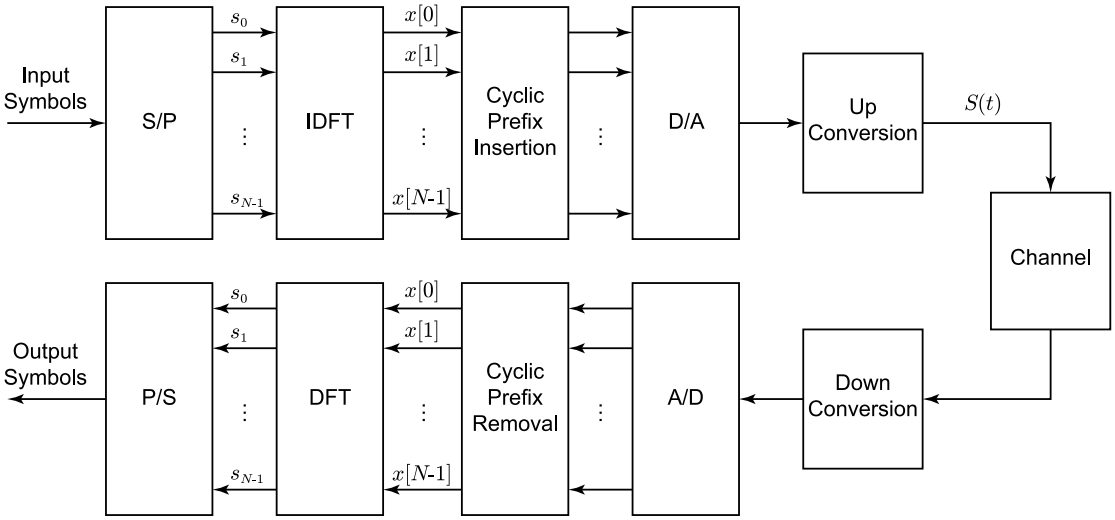

FIGURE 2.2: Block diagram of OFDM modem.

In OFDM, the number of subcarriers is chosen such that the symbol time on each subcarrier much longer than the channel delay spread, hence making the substream bandwidth less than the channel coherence bandwidth [37]. This downgrading of the transmission bandwidth of each substream ensures relatively flat fading on the subcarriers compared to frequency selective fading experienced for the case of single carrier system [38]. In other words, OFDM system spreads out a frequency selective fading over many symbols, so that instead of several adjacent symbols affected by the fading, many symbols are only partially distorted. It is customary in OFDM systems to add a cyclic prefix by adding a copy of a part of the end of the symbol to its start, thus introducing an apparent periodicity within each OFDM symbol which in turn transforms the convolution with the channel response to a circular convolution and simplifies the equalization process [39, 40].

A block diagram of an IDFT/DFT implementation of an N subcarrier OFDM system is depicted in Fig. 2.2. The serial to parallel converter (S/P) groups the serially incoming symbols denoted as s into N long blocks and passes one block at a time to be multiplexed. The IDFT carries the OFDM multiplexing and produces the time samples of the combined signal to be converted to the analogue domain in the digital to analogue converter (D/A) block. The transmitted symbol is up converted to the wanted frequency and passed through the channel. At the receiver the processes in the transmitter are reversed to extract the original input symbols.

The very appealing advantages of OFDM come at a cost. The system mainly relies on the subcarriers remaining orthogonal. Any impairment that can infect the system orthogonality characteristic poses detrimental effects on the widely applauded advantages. Synchronization between transmitter and receiver is crucial. Frequency shifts at transmitting or receiving end can lead to the displacement of OFDM signal in spectrum and/or intercarrier interference (ICI) [38, 41, 42, 43]. Furthermore, the structure of the OFDM signal gives rise to a possibility that all subcarriers power adding up constructively leading to a combined signal with a very high peak power and hence a high Peak to Average Power Ratio (PAPR) [44]. A high PAPR places a constraint on the design of the transmitter as it dictates the dynamic range of its circuitry. In case the circuitry is unable to cater for the high PAPR, the resultant signal become distorted [45].

2.2 Non-orthogonal Multicarrier Communications

OFDM system constrains the subcarriers to reside in fixed relative locations in frequency, therefore, is restricted in terms of spectral efficiency by this upper bound. Multicarrier Modulation (MCM) communications systems with orthogonal pulseshapes [5, 46] provide lower bandwidth utilization but with better localization. The insistence on using orthogonal bases and/or pulseshapes is attributed to the concept that the orthonormal bases are considered optimum in the presence of Additive White Gaussian Noise (AWGN) where the orthogonal bases preserve the whiteness of the noise. In addition, orthogonality guarantees that the bases are linearly independent, hence the system is invertible. Nevertheless, the loss of orthogonality does not necessitate the loss of linear independence which is necessary for inverting the system.

To achieve better efficiency, non-orthogonal multicarrier communications are emerging. These systems come into two main groups. The first did not venture too far from the orthogonality principle by proposing the use of non-orthogonal pulseshapes, however, the overall system remains orthogonal. The second group of systems proposes the use of non-orthogonal bases. Of the first group Non-orthogonal FDM (NOFDM) proposes restoration of orthogonality from the view point of the input symbols by employing orthogonal pulse-shaping [47] and claims that modulation schemes based on incomplete Riesz bases are more robust to frequency selective fading. The pulseshapes are chosen

with sharp decays to improve spectral efficiency and the generation and reception bases form a biorthogonal bases, where biorthogonality is defined as [48, 49]

$$\langle \varphi_i, \tilde{\varphi}_j \rangle = \delta (i - j), \tag{2.2}$$

where $\langle \cdot \rangle$ is the inner product, φ_i or $\tilde{\varphi}_j$ belongs to the non-orthogonal bases sets φ and $\tilde{\varphi}$, respectively and $\delta(1) = 1$ and zero otherwise. The design of the pulseshapes is optimized to improve efficiency and performance such as in [50, 51] proposing to design pulses that generate a targeted Intersymbol Interference (ISI) or ICI pattern and power and bit loading considerations in [52, 53, 54]. In fast time varying channels the Biorthogonal FDM (BFDM) systems are shown to outperform OFDM [55, 56].

SEFDM systems follow a different approach to the non-orthogonal pulseshapes by explicitly defying the orthogonality rules and using non-orthogonal bases. These systems do not assume any special pulse or system designs that restore orthogonality at any point. Sections 2.3 to 2.7 describes the SEFDM system proposed in [21, 57] which is the focus of the work in this thesis and section 2.8 outlines other similar proposals.

2.3 Spectrally Efficient FDM (SEFDM)

The SEFDM signal of [21] consists of a stream of SEFDM symbols each carrying a block of N complex input symbols, denoted by $s = s_{\Re e} + j s_{\Im m}$, transmitted within T seconds. Each of the N complex input symbols modulates one of the non-orthogonal and overlapping subcarriers, hence, giving the SEFDM signal $x(t)$ as

$$x(t) = \frac{1}{\sqrt{T}} \sum_{l=-\infty}^{\infty} \sum_{n=0}^{N-1} s_{l,n} e^{(j2\pi n\alpha(t-lT)/T)}, \tag{2.3}$$

where α denotes the bandwidth compression factor defined as

$$\alpha = \Delta f T, \quad \alpha < 1, \tag{2.4}$$

for Δf denoting the frequency distance between the subcarriers, T is the SEFDM symbol duration, N is number of subcarriers and $s_{l,n}$ denotes the symbol modulated on the n^{th} subcarrier in the l^{th} SEFDM symbol.

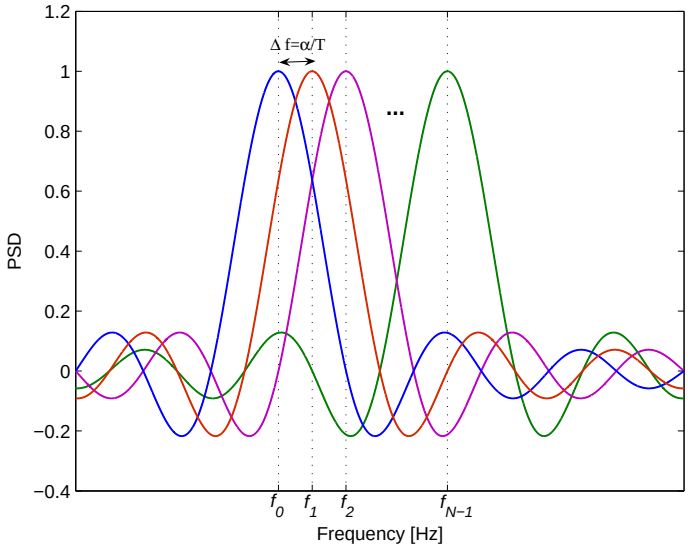

FIGURE 2.3: SEFDM spectra: N subcarriers spaced by α/T Hz.

The fraction α determines the level of the bandwidth compression, thus termed bandwidth compression factor with $\alpha = 1$ corresponding to an OFDM signal. Fig. 2.3 depicts the spectra of an N subcarrier SEFDM system. Due to the relatively closer locations of the subcarriers in frequency, the spectral width of the multiplexed signal is narrower than that of OFDM. However, the orthogonality feature in OFDM is lost and at the peak of any individual subcarrier spectrum, the other subcarriers spectra are no longer zeros. The bandwidth occupied by the system in Fig. 2.3 is approximately equal to

$$BW_{SEFDM} = \frac{\alpha\,(N-1)+2}{T}, \tag{2.5}$$

whereas the N subcarrier OFDM system depicted in Fig. 2.1 has a bandwidth equal to

$$BW_{OFDM} = \frac{N+1}{T}. \tag{2.6}$$

Equations (2.5) and (2.6) show that the occupied bandwidth of the SEFDM system approaches α of the OFDM bandwidth with the increase in N. Fig. 2.4 depicts a block diagram of the transmitter and receiver of the SEFDM system in AWGN channel, sections 2.4 and 2.5 explains the building blocks of the system.

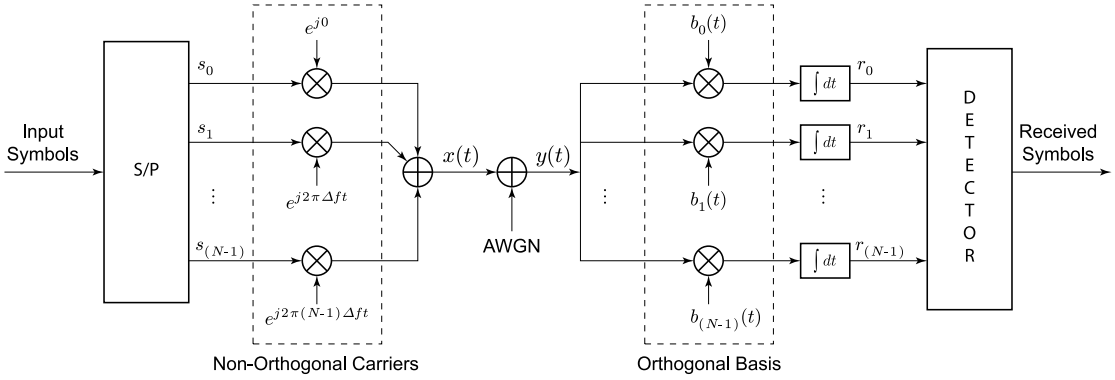

FIGURE 2.4: SEFDM system modem.

2.4 SEFDM Transmitter

The SEFDM signal is composed of a combination of symbols each modulated on one of the subcarriers. Therefore, the conventional SEFDM transmitter consists of a bank of modulators running at the subcarriers frequencies as can be seen in Fig. 2.4. For large system size it becomes exceptionally complex to realize this bank of modulators. In addition, the system will be more susceptible to frequency offsets and timing errors, as the number of oscillators increases to accommodate the increase in the number of subcarriers. However, previous work in SEFDM mainly focused on addressing detection problem, except for [36] where the use of Fractional Fourier Transform (FrFT) for SEFDM signal generations was suggested. The FrFT transform is a transform that relates a vector to a non-orthogonal set of base vectors [58]. The k^{th} output of the FrFT of the N long vector A is expressed as

$$X_\alpha[k] = \frac{1}{\sqrt{N}} \sum_{n=0}^{N-1} A[n] \exp\left(\frac{j2\pi nk\alpha}{N}\right). \tag{2.7}$$

The FrFT can be realized with algorithms based on the Bluestein algorithm for the Fast Fourier Transform (FFT) evaluation [59], requiring a complexity of about $20N \log_2 N$ flops and additional multiplication and addition operations [58]. In contrast, OFDM signal is efficiently generated with a single IDFT [9, 10] or equivalently using IFFT, therefore, suggesting the necessity to invest in the reduction of SEFDM transmitter complexity to stand a chance in surpassing OFDM complexity. In this thesis, a framework for the efficient representation for non-orthogonal signals using IDFTs is presented

in chapter 4, leading to several arrangements of simple to implement transmitter proposed and reported by the authors in [60, 61, 62, 63].

2.5 SEFDM Receiver

The SEFDM receiver, as depicted in Fig. 2.4, is composed of two stages: a demodulator and a detector. The demodulator collects statistics of the incoming signal by projecting it onto orthonormal bases [64] whilst the detector applies detection algorithms to estimate the originally transmitted information symbols based on the collected statistics. The deliberate collapse of orthogonality generates significant interference between the subcarriers that turns the detection of the signal to an overly complex problem. Despite that, it has been shown that acceptable reception in terms of BER is achievable and hence the pursuit of SEFDM system is deemed feasible [57].

Let the received signal be denoted by $y(t)$, where

$$y(t) = x(t) + w(t), \tag{2.8}$$

and $w(t)$ is an AWGN term. The i^{th} collected statistics is obtained as

$$r_i = \int_0^T y(t)\, b_i^*(t)\, dt, \quad i = 0, 1, \cdots, N-1 \tag{2.9}$$

where $b_i(t)$ is the i^{th} orthonormal base obtained by applying an orthonormalization technique on the original SEFDM subcarriers and $[\cdot]^*$ is the Hermitian conjugate of the argument[1]. The bases are orthonormal in order to preserve the white nature of the noise in the system. However, projection onto a set of bases different from the one used for signal generation does not eliminate the ICI. The complete set of received statistics is then described as

$$R = \mathbf{M}S + W, \tag{2.10}$$

[1] $[\cdot]^*$ will denote a conjugate only if the argument is a scalar.

where the correlation between the orthonormal bases and the original subcarriers is denoted by the $N \times N$ matrix $\mathbf{M}$ where

$$M_{ij} = \int_0^T b_j^*(t)\, e^{j2\pi i\alpha t/T} dt, \quad i, j = 0, 1, \cdots, N-1, \tag{2.11}$$

R, S and W are $N \times 1$ statistics of the received signal, transmitted symbols and noise samples vectors, respectively [65]. The properties of matrix $\mathbf{M}$ affects the quality of the obtained statistics and consequently affects the performance and complexity of the detection mechanism [65]. The statistics R are fed to a detector that employs complex detection algorithms to extract the transmitted signal with the aim of minimizing the BER. In the next sections the techniques proposed so far for orthonormalization and detection are discussed.

2.6 Demodulation and Orthonormalization

As mentioned in previous section, the demodulator stage of the SEFDM receiver collects statistics of the incoming signal. In order to collect sufficient statistics from the received signal, the receiver in Fig. 2.4 projects the signal onto a set of orthonormal bases that span the same vector space as the original SEFDM subcarriers at the transmitter. Orthonormal bases are bases that are orthogonal and have a norm of unity. In addition to preserving the white nature of the noise, the bases should be orthogonal to ensure that the collected statistics are independent. In SEFDM, the demodulation bases are obtained by applying orthonormalization techniques on the SEFDM subcarriers. Orthonormalization is the process of generating an orthonormal set of bases from a non-orthonormal one and is a key operation in the demodulator stage in the SEFDM receiver.

Initially, Gram Schmidt (GS) process [64] was suggested for the orthonormalization of the subcarriers in the SEFDM system [21]. GS is a process that generates an orthogonal set of bases from a non-orthogonal linearly independent set of bases. The obtained orthogonal set is then normalized by applying the appropriate weighing. In GS, an orthonormal set of bases that span the same space as the SEFDM subcarriers is obtained by the elimination of the projection of the subcarriers onto the others in sequential order.

For instance, GS starts by accepting one of the subcarriers as the first base and then by the deduction of the projection of the second onto this one another base that is orthogonal to the first is obtained. The process continues until all the bases are orthonormalized. Projection of a vector v onto a vector u is defined by the inner product as

$$proj_u(v) = \frac{\langle u, v\rangle}{\langle u, u\rangle} u. \tag{2.12}$$

The projection can be normalized by dividing by $\|proj_u(v)\|$, where $\|\cdot\|$ is the Euclidean norm. The GS follows these steps to generate the set of orthonormal bases $[e_1 \cdots e_k]$:

$$\begin{aligned}
u_1 &= v_1 & e_1 &= \frac{u_1}{\|u_1\|} \\
u_2 &= v_2 - proj_{u_1}(v_2) & e_2 &= \frac{u_2}{\|u_2\|} \\
u_3 &= v_3 - proj_{u_1}(v_3) - proj_{u_2}(v_3) & e_3 &= \frac{u_3}{\|u_3\|} \\
&\vdots & &\vdots \\
u_k &= v_k - \textstyle\sum_{j=1}^{k-1} v_j proj_{u_j v_k} & e_k &= \frac{u_k}{\|u_k\|}.
\end{aligned} \tag{2.13}$$

GS suffers from accuracy degradation due to its large rounding error [66, 67, 64]. For SEFDM, it was noted that the use of GS leads to performance degradation of SEFDM systems specially with the increase in the number of subcarriers or bandwidth compression level [35]. Therefore, modified versions of GS particularly the Modified Gram Schmidt (MGS) [68] and the Iterative Modified Gram Schmidt (IMGS) methods are proposed in [35] and [36], respectively. MGS is designed to cope with the finite resolution of computation machines by updating the initial base vector after each step. This ensures that the obtained MGS vectors remain mutually orthogonal despite rounding operations. Furthermore, the IMGS technique enhances the performance of the MGS technique by repeating the MGS orthonormalization steps for many iterations [69, 70]. MGS and IMGS achieve better accuracy than GS and in SEFDM systems this is demonstrated in improved BER performance. It is known in the literature that the application of GS on a full column rank matrix[2] resembles the **QR** decomposition, thus generating an orthonormal matrix **Q** and an upper triangular matrix **R**. It is then straightforward that the **M** matrix defined in equation (2.11) is equivalent to the **R** matrix from the **QR** decomposition.

[2] A full column rank matrix is a one whose all columns are linearly independent.

A different orthonormalization technique, termed the Löwdin Method (LM), was proposed for SEFDM systems in [35]. LM was originally proposed for quantum chemistry applications [71, 72]. While GS techniques generate different orthonormal bases for each different sequence of the non-orthonormal vectors, LM bases are sequence independent and are closer to the original non-orthonormal bases in a least squares sense [73]. The LM starts by defining a matrix $\mathbf{Z}$ that generates a set of orthonormal bases $\mathbf{U}$ of $[u_0, u_1, \cdots, u_{N-1}]$ from the SEFDM subcarriers denoted by the matrix Φ where each row of Φ represents the time samples of an SEFDM subcarrier, such that:

$$\mathbf{U} = \mathbf{Z}\mathbf{\Phi}. \tag{2.14}$$

As the columns of $\mathbf{U}$ are orthonormal then

$$\mathbf{U}\mathbf{U}^* = \mathbf{Z}\mathbf{\Phi}\mathbf{\Phi}^*\mathbf{Z}^* = \mathbf{I}. \tag{2.15}$$

A solution for equation (2.15) is

$$\mathbf{Z} = \mathbf{C}^{*-\frac{1}{2}}, \tag{2.16}$$

where $\mathbf{C} = \mathbf{\Phi}^*\mathbf{\Phi}$. The work in [57] showed that LM provides superior performance to GS with all its variances and is attributed to the fact the bases generated with LM are closer to the original subcarriers than GS bases, therefore, will address partially the ICI while preserving the whiteness of the noise.

The orthonormal bases obtained via any of the discussed techniques serve the two set goals: to generate statistics that are independent and preserve the white nature of the noise at the output of the correlators stage. When a GS based technique is adopted, the resultant correlation of the bases with the incoming signal is an upper triangular matrix $\mathbf{M}$ and it is a full matrix when LM is used. It has been numerically identified that the $\mathbf{M}$ matrix has a great impact on the performance of the system, specially that the matrix tends to become ill conditioned[3] with the increase in number of subcarriers and/or level of bandwidth compression in the form of a decrease in the value of α [57]. In this thesis, chapter 3 presents a mathematical investigation of the relationship of

[3]Conditioning may be evaluated by the condition number which is the ratio between the maximum eigenvalue and minimum one. Ill conditioning occurs when the matrices under investigation exhibit large difference between the values of the eigenvalues or in other words when the condition number becomes large.

system conditioning and the system parameters. In addition, chapter 5 investigates the demodulation of the SEFDM signal with easy to obtain non-orthogonal bases and shows that the orthonormalization can be avoided without premium at performance.

2.7 Detection

Due to the loss of orthogonality, detection of SEFDM signals is challenged by the need to extract the original signal from the ICI. The optimum detection of the SEFDM signal requires brute force Maximum Likelihood (ML) which can become extremely complex with the increase in the system size [21]. On the other hand, using linear detection techniques such as Zero Forcing (ZF) and Minimum Mean Square Error (MMSE) constrains the size of the SEFDM system and the level of bandwidth savings [35]. Therefore, Sphere Decoder (SD) was proposed in [36] to provide ML performance at a much reduced complexity. Nevertheless, the SD complexity varies depending on the noise and the conditioning of the system. Attempts to tame the complexity of the SD algorithm appeared in [74] in a quasi-optimal detector combining Semidefinite Programming (SDP) and SD, however, the complexity remains variable. Sections 2.7.1 to 2.7.5 provide an outline of the proposed detection techniques for SEFDM system.

2.7.1 SEFDM Optimal Detector in AWGN Channel

The demodulator feeds the collected statistics to the detector to estimate of the originally transmitted symbols. Due to the loss of orthogonality between the subcarriers, the collected statistics from the received signal will contain ICI leading to increased error rates. With the aim of minimizing the probability of error in estimating the transmitted symbols for an SEFDM signal contaminated with AWGN only, ML was initially proposed as the optimal detector for the SEFDM system [21]. The ML criterion is applied by examining all possible combinations of input symbols for every received SEFDM symbol. Recalling that the orthonormal bases maintain the white nature of the noise in the system, the ML estimate of the transmitted message $\hat{S}_{ML}$ is derived in [57] starting from equation (2.10) to give a Least Squares (LS) problem as

$$\hat{S}_{ML} = \min_{s \in Q^N} \|R - \mathbf{M}S\|^2 , \tag{2.17}$$

where Q^N is the set of all possible SEFDM symbols combinations. Equation (2.17) specifies that the ML estimate for SEFDM system is the one that is closest to the signal statistics in terms of the Euclidean distance. Q^N has M^N entries where M is the constellation cardinality and N is the number of subcarriers. It is clear then that with the increase in number of subcarriers and/or the constellation size of input symbols the complexity of the ML detector grows exponentially which represents a serious impediment to its realization.

2.7.2 Simple SEFDM Detectors

To address the high complexity of ML detection Kanaras et al in [65] investigated using linear detection techniques for the SEFDM signal detection. In particular, ZF and MMSE were suggested as sub-optimal detection techniques.

In principle, a ZF detector reverses forcibly any operation carried at transmission [75]. Starting by constraining the ML detection problem in equation (2.17) to integer values only, the ZF solution $\hat{S}_{ZF}$ of the Integer LS (ILS) problem is obtained as [76, 77, 57]

$$\begin{aligned} \hat{S}_{ZF} &= \left\lfloor \mathbf{M}^{-1} R \right\rceil \\ &= \left\lfloor \mathbf{M}^{-1} (\mathbf{M}S + W) \right\rceil \\ &= \left\lfloor S + \mathbf{M}^{-1} W \right\rceil , \end{aligned} \tag{2.18}$$

where $\lfloor \cdot \rceil$ is a slicing operator that rounds the argument to the closest constellation point. The properties of the $\mathbf{M}$ matrix and its inverse will dictate the quality of the ZF estimation, when the matrices of the system are ill conditioned the ZF detector results in the modulation of the added noise in the system and overall poor BER performance.

Moreover, the work in [57] proposed an iterative technique for detecting the SEFDM signal termed Iterative Cancellation (IC). The proposed detector is based on that the $\mathbf{M}$ matrix is upper triangular when any GS based method is used for orthonormalization and thus proceeds to implement the solution starting from the last line of the SEFDM solution equation in (2.18) and iteratively estimating the input symbols. The IC detector

showed better performance than standard ZF mainly because of the avoidance of direct matrix inversion that leads to noise enhancement.

In order to mitigate the effects of noise enhancement associated with ZF, the MMSE detector is proposed for SEFDM system [65]. MMSE optimizes between noise enhancement and ICI mitigation by including noise whitening term [75]. Estimation based on MMSE is expressed in [65] as

$$\hat{S}_{MMSE} = \left\lfloor \mathbf{M}^* \left(\mathbf{M}\mathbf{M}^* + \frac{1}{\sigma_W^2}\mathbf{I} \right)^{-1} R \right\rceil, \tag{2.19}$$

where σ_W^2 is the noise variance and $\mathbf{I}$ is the identity matrix. The MMSE detector yields better error performance than ZF, however, still considered poor [65].

In summary, simple SEFDM detector, either linear such as ZF and MMSE or iterative IC, require less complexity when compared to ML detection, nevertheless, their performance is severely restricted by the noise and the conditioning of the system and can support small system sizes and/or low bandwidth savings.

2.7.3 Sphere Decoder

Sphere Decoding (SD) is proposed in [35, 36] for detecting SEFDM signals. Basically SD is an algorithm to perform ML detection at a reduced complexity. Whilst ML estimates are obtained by finding the point that gives the minimum distance from the statistics point R from the set of all possible combinations of transmitted symbols, SD achieves the same objective by transforming all possibly transmitted symbols combination into a multi-dimensional hypersphere and then searching for the point that is closest to R within the sphere [78]. The SD achieves complexity reduction by performing the search for candidate solutions within a pre-determined radius g from the received signal statistics point, such that the search sphere is smaller than the whole possible solutions space.

The SD estimate $\hat{S}_{SD}$ is defined as

$$\hat{S}_{SD} = \min_{s \in Q^N,\, \|R - \mathbf{M}S\|^2 \leq g} \|R - \mathbf{M}S\|^2, \tag{2.20}$$

where g is the initial radius of the search hypersphere. In the Real SD (RSD), all the variables in equation (2.20) are expanded using real decomposition [79], thus, doubling the dimension of the problem as

$$\begin{aligned} \tilde{R} &= \begin{bmatrix} \Re\{R\} \\ \Im\mathfrak{m}\{R\} \end{bmatrix}, \quad \tilde{\mathbf{M}} = \begin{bmatrix} \Re\{\mathbf{M}\} & \Im\mathfrak{m}\{\mathbf{M}\} \\ -\Im\mathfrak{m}\{\mathbf{M}\} & \Re\{\mathbf{M}\} \end{bmatrix}, \\ \tilde{S} &= \begin{bmatrix} \Re\{S\} \\ \Im\mathfrak{m}\{S\} \end{bmatrix}, \quad \tilde{W} = \begin{bmatrix} \Re\{W\} \\ \Im\mathfrak{m}\{W\} \end{bmatrix} \end{aligned} \tag{2.21}$$

Using Cholesky decomposition [80], the problem in equation (2.20) can be expressed as

$$\hat{S}_{SD} = \min_{s \in Q^N,\, \|R - \mathbf{M}S\|^2 \leq g} \left\| \mathbf{L}\left(P - \tilde{S}\right) \right\|^2, \tag{2.22}$$

where $\mathbf{L}$ is an upper triangular matrix defined by the Cholesky decomposition as $\tilde{\mathbf{M}}^T\tilde{\mathbf{M}} = \mathbf{L}^T\mathbf{L}$, where $[\cdot]^T$ denotes a matrix transpose and P is the unconstrained ML estimate of S defined as

$$P = \left(\tilde{\mathbf{M}}^T\tilde{\mathbf{M}}\right)^{-1}\tilde{\mathbf{M}}^T\tilde{R}, \tag{2.23}$$

where $\left(\tilde{\mathbf{M}}^T\tilde{\mathbf{M}}\right)^{-1}\tilde{\mathbf{M}}^T$ is the Moore-Penrose pseudoinverse of matrix $\tilde{\mathbf{M}}$ [66]. The SD algorithm then proceeds by examining all the nodes that satisfy the radius constraint starting from the level number $2N$ and moving downwards until reaching level number 1. At each level only the points that satisfy equation (2.22) are kept and the radius is updated accordingly. That is at level number y, all the nodes that satisfy

$$|\hat{p}_y - s|^2 \leq g_y / l_{yy}^2, \tag{2.24}$$

where $|\cdot|$ is the absolute value,

$$\hat{p}_y = p_y - \sum_{j=y+1}^{N} \left(l_{yj}/l_{yy}\right)\left(s_j - p_j\right) \tag{2.25}$$

and

$$g_y = g - \sum_{j=y+1}^{N} l_{jj}\left|\hat{p}_y - s\right|^2, \tag{2.26}$$

are retained where any discarded node will eradicate all its predecessor nodes, and hence

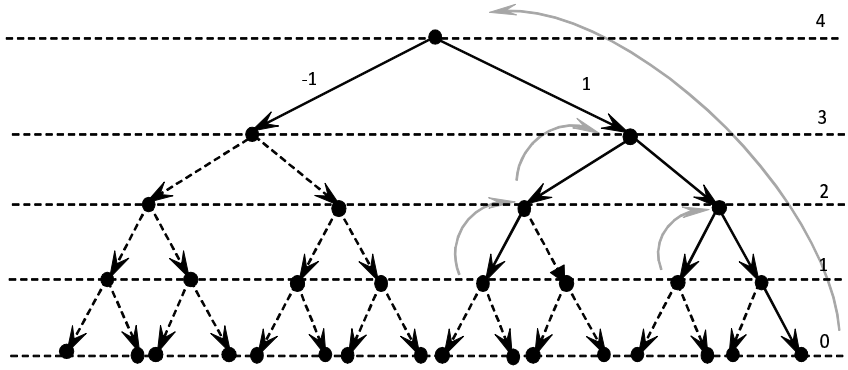

FIGURE 2.5: SD tree search.

reduces the remaining search space compared to the initial one. Fig. 2.6 illustrates a functional diagram of the SD algorithm and shows the decoding steps. Fig. 2.5 depicts the SD tree search. At each search level, the candidate points are examined in a specified order and those that satisfy the radius constraint are accepted.

Two important factors for SD algorithm are the choice of the initial radius and the order of enumeration of candidate points at each decision level; both issues received substantial research effort. The choice of the initial radius g decides the complexity of the algorithm as it decides the initial size of the search hypersphere, however, a trade off between performance and complexity is needed as a small radius will reduce the probability of finding the optimal solution while a large radius will increase the complexity. For SEFDM, the radius is set in the majority of investigated cases to be equal to the distance to an initial estimate of the transmitted symbols obtained using ZF or MMSE. The second factor is the order of the enumeration of candidate points, where two techniques are widely used, namely, Fichke-Pohst (FP) and Schnorr Euchner (SE) [81]. FP orders the point in ascending order from the bound defined in equation (2.24) while SE enumeration orders the candidate points based on their distance from the centre of the search interval as defined in equation (2.25)[82]. In SEFDM, SE enumeration was adopted as SE permits that the initial radius to be set to a large number with no serious effects on the complexity [57].

To avoid doubling the dimension of the problem associated with the RSD, the authors of [36, 57] proposed the Complex SD (CSD) algorithm [83]. CSD represents the SEFDM LS problem in phasor form and follows similar search steps to the RSD to estimate the originally transmitted symbols.

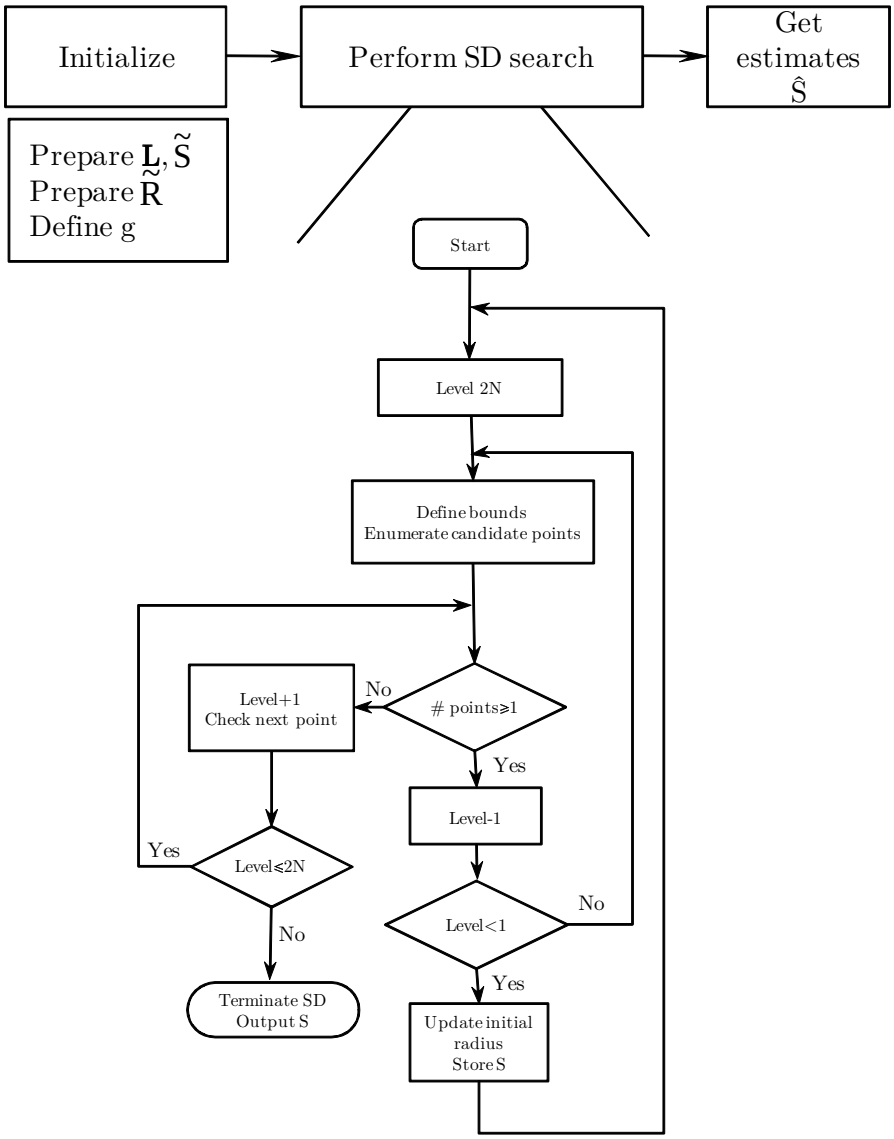

FIGURE 2.6: SD functional diagram.

In terms of the BER the SD algorithm manages to approach the optimum ML performance with lower complexity (in worst cases it is equal to ML complexity). However, there is no guarantee as to the level of complexity needed for a solution to be obtained. The complexity is highly dependent on the noise and in this SEFDM context it is also dependent on the conditioning of the system. The complexity of the SD approaches ML complexity with the increase in the number of subcarriers and/or the decrease of the distance between the subcarriers. Examining the functional diagram for the SD algorithm in Fig. 2.6 demonstrates the iterative and sequential nature of the algorithm, thus, suggesting the unsuitability of the algorithm for hardware implementation. This issue is addressed by the proposal of the Fixed SD in chapter 6.

Finally, the SD concepts were used to develop a joint channel equalizer and symbol detector for SEFDM signals in time dispersive channels [84]. The proposed equalization and detection approach was tested in static fading channels for systems with and without cyclic prefix. Numerical results provided therein confirmed support for systems up to 20% bandwidth saving. The work in [84] serves as a proof of concept in fading channels, however, further analysis in multipath fading will be necessary to asses the performance of the system which is provided in chapter 8.

2.7.4 Semidefinite Programming

Semidefinite Programming (SDP) was proposed for SEFDM detection to provide fixed complexity and improved error performance over linear techniques [85]. An SDP solution is obtained by reformulating the ML detection problem in equation (2.17) based on the relaxation of the constraints of the NP hard detection problem therein. The new SDP solution can be solved in polynomial time [86].

The SDP solution starts from the expanded form of the ML problem obtained via the real decomposition as in (2.21), thus, the problem dimension is doubled to $2N$. Assuming 4QAM information symbols, the expanded ML problem is expressed as [85]

$$\min_{\tilde{s}\in\{\pm 1\}} \quad \tilde{R}^T\tilde{R} - \tilde{R}^T\tilde{\mathbf{M}}\tilde{S} - \tilde{S}^T\tilde{\mathbf{M}}^T\tilde{R} + \tilde{S}^T\tilde{\mathbf{M}}^T\tilde{\mathbf{M}}\tilde{S}, \tag{2.27}$$

where $\tilde{s}$ denotes a single element of $\tilde{S}$, the $2N \times 1$ vector of expanded 4QAM input symbols. Equation (2.27) can be further reduced to

$$\min_{\tilde{s}\in\{\pm 1\}} \quad \tilde{S}^T\tilde{\mathbf{M}}^T\tilde{\mathbf{M}}\tilde{S} - \tilde{R}^T\tilde{\mathbf{M}}\tilde{S} - \tilde{S}^T\tilde{\mathbf{M}}^T\tilde{R}, \tag{2.28}$$

as the term $\tilde{R}^T\tilde{R}$ is a constant. Now define the matrix $\mathbf{\Gamma}$ and the vector Y, such that

$$\tilde{S}^T\tilde{\mathbf{M}}^T\tilde{\mathbf{M}}\tilde{S} - \tilde{R}^T\tilde{\mathbf{M}}\tilde{S} - \tilde{S}^T\tilde{\mathbf{M}}^T\tilde{R} = Y^T\Gamma Y, \tag{2.29}$$

where Γ and Y are block matrices given by

$$\Gamma = \begin{bmatrix} \tilde{\mathbf{M}}^T\tilde{\mathbf{M}} & -\tilde{\mathbf{M}}^T\tilde{R} \\ -\tilde{R}^T\tilde{\mathbf{M}} & 0 \end{bmatrix}, \quad Y = \begin{bmatrix} \tilde{S} \\ 1 \end{bmatrix}. \tag{2.30}$$

Due to the Hermitian nature of Γ, by its definition, and from the definition of matrices inner product the term $Y^T\Gamma Y$ can be reduced to $\mathrm{Tr}\{\Gamma\mathbb{Y}\}$ where $\mathrm{Tr}\{\cdot\}$ is the trace operation[4] and

$$\mathbb{Y} = \begin{Bmatrix} \tilde{S}\tilde{S}^T & \tilde{S} \\ \tilde{S}^T & 1 \end{Bmatrix}. \tag{2.31}$$

The new block matrix $\mathbb{Y}$ properties play a key role in the reformulation of the ML problem. The diagonal elements of $\mathbb{Y}$ will be equal to one and the matrix itself is positive semidefinite[5] and of rank 1 [57]. Therefore, the problem in equation (2.28) can be equivalently expressed as

$$\begin{aligned} \min \quad & \mathrm{Tr}\{\Gamma\mathbb{Y}\} \\ \mathrm{diag}\{\mathbb{Y}\} &= \mathrm{e} \\ \mathbb{Y} &\succeq 0 \\ \mathrm{rank}\{\mathbb{Y}\} &= 1 \end{aligned} \quad , \tag{2.32}$$

where $\mathrm{diag}\{\cdot\}$ refers to the diagonal elements of the argument matrix, e is a $(2N+1)\times 1$ vector of ones, $\succeq$ indicates the matrix is positive semidefinite and $\mathrm{rank}\{\cdot\}$ gives the rank of the argument matrix . The relaxation of the non affine $\mathrm{rank}\{\mathbb{Y}\} = 1$ constraint in equation (2.32) leads to the SDP problem

$$\begin{aligned} \min \quad & \mathrm{Tr}\{\Gamma\mathbb{Y}\} \\ \mathrm{diag}\{\mathbb{Y}\} &= \mathrm{e} \\ \mathbb{Y} &\succeq 0. \end{aligned} \tag{2.33}$$

The SDP solution of the transformed problem searches for $\mathbb{Y}$ that satisfies the conditions of equation (2.33) and can be pursued using well established Interior Point Methods

[4]For an $N \times N$ matrix A, $\mathrm{Tr}\{A\} = \sum_1^N a_{ii}$.

[5]A positive semidefinite matrix is a Hermitian matrix whose all eigenvalues are not negative.

(IPM). Finally, the SDP solution, matrix $\mathbb{Y}$ is used to estimate the vector $\tilde{S}$. The work in [57] discussed the use of three different heuristic methods namely:

1. The rank-1 method where the SDP solution is accepted as the unconstrained estimate of $\tilde{S}$ and thus a slicing function is applied to find the corresponding 4QAM symbols [87].

2. The dominant eigenvector, where the eigenvector, or its negative version, that corresponds to the maximum eigenvalue is used as the argument of a slicing operator depending on whether the sign of the last element of the vector is positive or negative respectively.[88].

3. the randomization techniques, the technique starts by applying the dominant eigenvector method and uses the selected vector to generate a Bernoulli distribution. The technique then proceeds to generate random vectors and choose the one that minimizes the function in equation (2.29) [88, 89, 86].

To assess the performance of the SDP approach for SEFDM detection, [57] presented numerical simulation results. In terms of the BER performance, the SDP solution approximates the ML solution with any deviation from the optimal solution starting to increase with the further deterioration of the conditioning of the SEFDM system. However, SDP solution performance surpassed linear detectors. Simulations using CVX optimization tool led to an SDP solution with a polynomial complexity of $O\left(8\,N^{3.5}\right)$ [88, 57]. The main advantage is the fixed complexity and the insensitivity to noise when compared to the SD algorithm.

2.7.5 Hybrid Detectors

The different detectors for SEFDM system discussed so far provided support for either BER performance or complexity. A trade off between BER performance and affordable complexity leads to the choice of one detector or the other from all proposals. This motivated the search for hybrid detectors that can tackle both factors (i.e. performance and complexity) at the same time. With the goal of reducing the complexity while providing attractive BER performance, a number of detectors were proposed in [90, 85,

91] that start with a simple sub-optimal detector to provide a seed estimate to a more sophisticated detector operated at a reduced complexity.

The first to appear was a detector combining MMSE and ML, proposed in [90], providing better error performance than using only MMSE detection and a reduced complexity when compared with ML detection only. The MMSE-ML detector starts by extracting an estimate of the originally transmitted symbols following MMSE procedure as explained in section 2.7.2. After that an ML search is performed in a restricted neighbourhood around the MMSE estimate. The definition of the neighbourhood is key for the successful detection and complexity reduction. In [90], the neighbourhood D contains the SEFDM symbols that satisfy

$$S_i \in D \; if \; d_H \left(S_i^{'}, \hat{S}^{'} \right) \leq P, \tag{2.34}$$

where $P = 0, ..., N \log_2 M$ and d_H is the Hamming distance between the binary versions of the SEFDM symbols and MMSE estimate denoted by $S_i^{'}$ and $\hat{S}^{'}$, respectively. Thus, the new MMSE-ML estimate becomes

$$\hat{S}_{MMSE-ML} = \min_{s \in D} \left\| R - \mathbf{M}S \right\|. \tag{2.35}$$

In terms of complexity, the MMSE-ML detector requires lower complexity than original ML due to the reduction in the size of the search space. However, the BER performance, though better than MMSE detection, is still sub-optimal.

Another detector that combines SDP and ML was proposed in [85]. The SDP-ML technique starts by generating an SDP estimate of the originally transmitted symbols as explained in 2.7.4. Following that, an ML search is executed within a neighbourhood around the SDP estimate in a similar manner as the MMSE-ML detector. The SDP-ML detector offered BER performance advantage over SDP, however, the complexity is higher now due to the required ML search. Therefore, the work in [74, 91] proposed the use of SD to implement the ML part of the SDP-ML detector and is termed Pruned Sphere Decoder (PSD). The pruning of the SD algorithm is achieved by first setting the initial radius of the SD algorithm so that the SDP estimate lies on the surface of the search sphere. Second, the SD search is modified so that only points that satisfy a specific Hamming distance constraint are examined. In essence, the SD search is constrained to points within a specified neighbourhood around the SDP estimate in a

similar manner as in equation (2.34) for the MMSE-ML case. The PSD achieves the same BER performance of the SDP-ML at a reduced complexity, hence, enabling the increase in the system dimension in terms of the number of subcarriers.

2.7.6 Detection Limitations

In general, all detection techniques reviewed in this chapter showed performance that is dependent on the number of subcarriers and/or bandwidth compression level. Numerical investigations of the underlying matrices, particularly the **M** matrix, [57] have shown that the SEFDM tends to become severely ill conditioned with increase in the number of subcarriers and/or bandwidth compression level. Usually the conditioning of a matrix **A** is reflected in its condition number defined as

$$\kappa\left(\mathbf{A}\right) = \frac{\sigma_{max}}{\sigma_{min}}, \tag{2.36}$$

where σ_{max} and σ_{min} are the maximum and minimum singularvalue of **A** respectively. An ill conditioned matrix is characterized with a large condition number. The main drawbacks of the ill conditioning of a matrix that characterizes a system, is that a solution to the system may not be tractable due to numerical precision limitations and that the implementation of the system will need to support a large dynamic range. The work in [57] has shown by numerical simulations that the condition number of the **M** matrix increases with the increase in number of subcarriers and/or the decrease of α and consequently, classified the SEFDM LS problem as an ill-posed problem[6]. The common practice to solve ill-posed problems is to use some form of regularization to transform the ill-posed problem into an alternative well-posed one. For SEFDM system, Tikhonov regularization was suggested and examined in [36].

Tikhonov regularization is achieved by adding a penalty term, that provides information about the solution, to the problem function as

$$\min_{s \in Q^N} \left\| R - \mathbf{M}S \right\| + \epsilon \left\| \mathbf{L}S \right\|, \tag{2.37}$$

[6] An ill-posed problem is characterized by a coefficients matrix with singularvalues gradually decaying [92] and hence, high sensitivity to small perturbations such as noise.

where ϵ is termed the regulator and $\mathbf{L}$ is termed the regulator matrix. For simplicity, $\mathbf{L}$ is taken as the identity matrix $\mathbf{I}$, hence the solution of the problem in equation (2.37) reduces to

$$\hat{S} = \mathbf{M}^* \left(\mathbf{M}\mathbf{M}^* + \epsilon\mathbf{I}\right)^{-1} R. \tag{2.38}$$

Clearly, equation (2.38) is equivalent to the MMSE solution provided in equation (2.19) if the regulator is set to $\epsilon = 1/\sigma_w^2$. The value of the regulator will dictate the improvement in the conditioning of the initial LS problem. However, regularization adds an error term to the initial problem, therefore, a trade off between the improvement of the conditioning of the system will dictate the choice of the regulator.

Numerical evaluations of the effects of the regularization of the SEFDM problem have confirmed improvement of the performance [57]. Furthermore, a regularized version of sphere decoder (RegSD) of [93] was proposed and investigated in [36] for SEFDM system detection. The performance of the RegSD is shown to be superior to that of the SD in terms of reduction of complexity and its sensitivity to noise. This improvement is due to the improvement of the initial estimate in the SD algorithm obtained from a ZF operation and the improvement of the conditioning of the coefficient matrix which affects the tree search of the SD algorithm. In terms of the BER performance the regulator imposes no penalties due to the equivalence of the two problems before and after regularization.

2.8 Other Spectrally Efficient Systems

The concept of non-orthogonal spectral efficiency improvement has been tackled in other system scenarios. In this section a brief outline of the main proposals is presented.

Early examples of systems proposing higher spectral efficiency is the Fast OFDM (FOFDM) which proposes doubling the bandwidth of OFDM systems [19]. The subcarriers in FOFDM system are placed at half the frequency separation of an equivalent OFDM system, as such the achievable spectral efficiency is doubled. In principle, FOFDM system relies on the fact that when modulating the OFDM subcarriers with real input symbols, the orthogonality rule is valid for half the spacing of the system carrying complex input symbols. Therefore, FOFDM can convey the same information using half the bandwidth of an equivalent OFDM systems if the restriction to one dimensional modulation schemes

such as Binary Phase Shift Keying (BPSK) is satisfied. FOFDM system can be implemented using IDFT/DFT or equivalently IFFT/FFT at transmission and reception sides, respectively. In terms of BER performance, FOFDM delivers similar performance as OFDM for one dimensional modulation schemes [94, 95], yet, for higher dimensional modulations the performance degrades to unacceptable levels [96, 97].

Furthermore, the concepts of FOFDM have been tested in the optical communications field in the so called Optical Fast OFDM [98]. The Optical-FOFDM uses the Inverse Discrete Cosine Transform (IDCT) and Discrete Cosine Transform (DCT) for the multiplexing and de-multiplexing of the signal, respectively. The proposed Optical-FOFDM offers a choice of either reduction in complexity or doubling of the spectral efficiency [98] and is demonstrated in hardware in [99]. Recently, [99] proposed the use of the DFT for the Optical-FOFDM system in a similar manner as in [19].

In terms of spectral efficiency, FOFDM can be equivalent to a 4-QAM OFDM system and the achievable savings in spectral efficiency is restricted due to the restriction to real modulation schemes.

A similar system termed M-ary Amplitude Shift Keying (MASK) OFDM proposing half bandwidth saving of equivalent OFDM bandwidth appeared in [20] for systems supporting M-ary ASK symbols only. The system places the subcarriers at half the distance of orthogonality of conventional OFDM. Similar to FOFDM, the trick used here is that if considering only the real part of the subcarriers, the orthogonality can still be maintained at half the spacing of the complex subcarriers. Therefore, MASK OFDM can only accommodate real modulation schemes. A system based on the DCT and the IDCT is proposed for generation and reception in analogy to the IFFT/FFT based OFDM.

High Compaction Multicarrier Communication Modulation (HC-MCM) is another system that proposed spectral efficiency enhancement [22]. Although, HC-MCM briefly discussed spectral savings exploiting either the frequency or time domain, the work presented in [22] only analyzed the case of time domain compression where the higher spectral efficiency is achieved by transmitting at higher rate than an equivalent OFDM system. A DFT based implementation of the HC-MCM is presented in [22]. Generation of HC-MCM signals is based on standard IDFT as it is generated as ordinary OFDM,

yet only a part of the modulated signal is actually transmitted. Spectral efficiency is achieved by reducing transmission time of HC-MCM symbol compared to an equivalent OFDM system which results in increasing the individual subcarriers bandwidth thus breaking the orthogonality rule. The signal is received by a DFT followed by an ML decoder, however results for systems of 4 subcarrier only were displayed due to the high complexity of the ML detection. To reduce complexity of the ML decoder the use of the M-algorithm is proposed in [100] and is further suggested to be combined with parallel combinatory OFDM (PC-OFDM) to improve its bandwidth efficiency while benefiting from the ability to reduce the PAPR [101].

Similar to SEFDM, Overlapped Frequency Division Multiplexing (Ov-FDM) system proposes spectral efficiency enhancement by locating the subcarriers at spacing less than the required by the orthogonality condition [23]. The initial Ov-FDM proposal followed the same approach as SEFDM in terms of the way the subcarriers are set up and the method adopted for optimum detection, which is the Maximum Likelihood Sequence Detection (MLSD). To enable DFT based implementation, the Ov-FDM system applies a precoding stage before an IDFT stage. In simple terms, the precoding stage manipulates the inputs to the IDFT so that the outputs occupy less bandwidth. As the detection of Ov-FDM is based on MLSD criteria it is expected that the system will be limited in terms of the number of subcarriers or modulation levels. Enhancement of the Ov-FDM system appeared in [102, 103] proposing the use of Gabor transforms for reducing the complexity of detection with the concept of non-orthogonality extended across both time and frequency dimensions [104]. Detection of Ov-FDM signals proposed SD, SDP and lattice reduction techniques [105, 106, 107].

Another system that proposed spectral efficiency improvement is the Multistream Faster than Nyquist System (MFTN). The MFTN system first appeared in 2005 where the Mazo limit defined for faster than Nyquist signalling in [31] was extended to the frequency domain in what is called the two dimensional Mazo limit [24]. The main concept therein, was to repeat the packing achieved in time for FTN system, in the frequency domain. Furthermore, a combined packing effect is approached by packing in time and frequency at the same time. The first proposal for MFTN system used M-algorithms for detection and therefore, was severely constrained in terms of number subcarriers that can be supported. Further development of the MFTN system appeared

in [108, 109, 110, 25] that extended the system to support more subcarriers. As the detection of the MFTN proved to be challenging, various decoding arrangements were proposed in [108, 109, 110, 25, 111] aiming to improve the support of system sizes in terms of number of subcarriers and/or bandwidth savings possibilities. Implementations of MFTN transmitters appeared in [112], whereby a transmitter based on an FTN mapper that maps the appropriate information to the subcarriers of the next stage which is based on the Isotropic Orthogonal Transform Algorithm (IOTA) multicarrier modulation block. The proposed MFTN transmitter has higher complexity than an equivalent OFDM, however, it retained some of the building blocks of OFDM. Furthermore, [113, 114] presented an implementation of an MFTN receiver using Field Programmable Gates Array (FPGA).

Finally, Optical Dense OFDM (DOFDM) system proposed the use of non-orthogonal subchannels [26]. It was shown experimentally that the DOFDM can perform close to OFDM with the signal degradation due to chromatic dispersion possibly mitigated for by optimizing symbols timing and optical polarization of neighbouring subchannels.

2.9 Review Outcome and Conclusions

The main goal of this chapter was to set the scene for the work in this thesis by presenting the advancements achieved in SEFDM system. At the start, OFDM was briefly outlined as being a technique chosen to support high data rates and fading immunity. Brief descriptions of OFDM transmission and reception were provided in addition to brief highlights of main OFDM system characteristics. Then, the concept of using non-orthogonal overlapped signal to achieve higher spectral efficiency was discussed. Appearing under different names, two systems managed to achieve doubling the OFDM spectral efficiency for one dimensional modulation schemes. Effectively, these systems can not be more spectrally efficient than a higher order modulation scheme sent within the same bandwidth. Furthermore, a class of systems proposing the support of higher order modulation schemes in conjunction with non-orthogonal subcarriers was introduced. A review of Spectrally Efficient FDM system (SEFDM) as the first proposal was provided together with an outline of other similar proposals. In principle, all variants of SEFDM systems are equivalent and all findings and remarks can be generalized to other system

with change of notations and consideration of special conditions if any exists. As in their respective proposals, these systems are capable of supporting variable and flexible spectral efficiencies. However, the loss of orthogonality complicated the processes of such systems at both transmission and reception ends. Of the two, the reception end received the majority of the attention as the different variants of the SEFDM systems investigated several detection arrangements. Sub-optimal linear detection techniques required less complexity but offered poor error performance. The performance is found to be highly dependent on the number of subcarriers and/or level of bandwidth compression. Optimum detection techniques in the form of ML or SD facilitated error performance similar or close to that of OFDM system with the SD needing much lower complexity compared to ML detection. In terms of BER performance, it was shown that several detection techniques are able to deliver attractive performance. However, the complexity of the published techniques is still an open area for further enhancements.

Overall, the very appealing concept of improving spectral efficiency has excited much research in the area of non-orthogonal multicarrier systems. However, many issues seem to be unresolved and untouched in some cases. The reduction of complexity is an urgent issue for study, yet, other issues need thorough examination. For instance, the representation of the SEFDM signals as a set of vectors suggest that investigations of the linear dependency can aid to determine if there are fundamental limitations for such an approach and to assess the existence of solutions for the system and the affordability and realizability of such solutions.

It is noted that the performance of the SEFDM system is dependent on the number of subcarriers and the level of bandwidth compression. However, there is no rigorous analysis of how the system becomes dependent on these two parameters and why. This information is necessary for the informed pursuit of interference mitigation techniques. It is expected that representing the system by a detailed mathematical model will facilitate defining the root causes of performance degradation. As there is a need to establish the mathematical basis on which the properties of the system could be extracted, the next chapter in this thesis deals with the issues of modelling and mathematical investigations of the key system parameters.

Moreover, the generation of the SEFDM signal via a bank of modulators is expected to limit the implementation potential of the system, whereas generation with IFrFT has

not received detailed investigations to map clearly the road to hardware implementation. In chapter 4 of this thesis, a framework for the generation of SEFDM signals with IDFT is presented. The framework provides flexible arrangements and specification for IDFT based architectures that led to the successful implementation of the transmitter using FPGA.

Moreover, the demodulator stage has assumed the use of orthonormal bases which in turn requires orthonormalization processes. Furthermore, the correlation with the bases requires a bank of correlators. This arrangement will certainly add to the complexity of the SEFDM receiver. In chapter 5 of this thesis the demodulation of the signal is considered. Other demodulators are investigated, associated with the mathematical derivations and numerical assessment of the respective optimal detectors.

Furthermore, as a multicarrier system, the SEFDM is prone to exhibit high PAPR. The high PAPR will affect the design of the power amplifier and will determine the system dynamic range, hence the dynamic range of all the components in the transmitter. Moreover, uncontrolled PAPR may lead to non-linearity problems. Therefore, chapter 7 of this thesis presents a study of the PAPR of SEFDM system and proposes and evaluates efficient PAPR reduction techniques.

SEFDM system has been thoroughly investigated under AWGN channel. A study of the effects of multipath fading channel is essential before deciding on the feasibility of the system in practical settings. Issues such as channel estimation and equalization are crucial for the proposal of SEFDM systems in practical wireless communications settings, hence, are covered in chapter 8 of this thesis.

As discussed above many issues remain untackled and as such base the work presented in the subsequent chapters. The work in this thesis focuses on and adopts the signal notation of the SEFDM system of [21], where any findings can be generalized to the outlined other SEFDM systems with appropriate change of notation.

Chapter 3

Mathematical Properties of SEFDM Signals

3.1 Introduction

Previous work in SEFDM indicated some performance limitations. It was stated in [35] that the achievable BER deteriorates with the increase in the number of subcarriers and/or the reduction of the frequency spacing between the subcarriers. It is also stated that the complexity of detection strongly depends on the conditioning of the **M** matrix described in section 2.5 [35]. In this chapter, the limitations of the system are investigated by mathematical modelling and analysis. The study is motivated by the need to establish the grounds that govern the performance of the system. The aim of the work presented here is to identify the mathematical characteristics of the SEFDM system and to identify theoretical bounds and drivers of system performance. This is achieved by identifying the mathematical structure of the underlying matrices leading to the derivations of closed form formulas and bounds that explain the observed performance and aid the informed system design. The study includes the determination of important system parameters that can aid in estimating the numerical stability of the system. In particular, closed form representation of the intercarrier interference (ICI) in the system is derived. It is found that the effect from neighbouring subcarriers is higher than relatively distant ones, hence, equalization could be effective for only highly interfering carriers as will be shown in chapter 6. Moreover, it is found that the conditioning

of the system is highly controlled by the number of subcarriers and/or their relative spacing in frequency. The system is proved to be non-singular, though it could become ill conditioned when the amount of bandwidth savings and/or number of subcarriers are increased.

3.2 The Discrete SEFDM Signal

To benefit from signal processing techniques, it is considered useful to address a discrete representation of the SEFDM system instead of the continuous one. In addition, all the work in SEFDM has been numerically evaluated, thus, all published results are approximations to the continuous signal case. In this section, a discrete system model is presented.

The discrete SEFDM signal is prepared by applying periodic sampling. Particularly, without loss of generality, the SEFDM symbol with zero index is considered, corresponding to the symbol at $l = 0$ in equation (2.3)

$$x_0(t) = \frac{1}{\sqrt{T}} \sum_{n=0}^{N-1} s_{0,n} e^{(j2\pi n\alpha t/T)}. \tag{3.1}$$

By sampling the SEFDM symbol in equation (3.1) at (T/Q) intervals where $Q = \rho N$, and ρ is an oversampling factor, the discrete SEFDM signal, with the 0 index omitted, is then expressed as

$$X[k] = \frac{1}{\sqrt{Q}} \sum_{n=0}^{N-1} s_n e^{\frac{j2\pi nk\alpha}{Q}}, \tag{3.2}$$

where $X[k]$ is the k^{th} time sample of the SEFDM symbol in equation (3.1), $k = 0, 1, \cdots, Q-1$ and the factor $1/\sqrt{Q}$ is a normalization constant. The complete discrete model is then expressed in matrix format as

$$X = \mathbf{\Phi} S, \tag{3.3}$$

where $X = [x_0, \cdots, x_{Q-1}]^T$ is a vector of time samples of $x(t)$ in equation (2.3), $S = [s_0, \cdots, s_{N-1}]^T$ is a vector of input symbols, and $\mathbf{\Phi}$ is the sampled carriers matrix. $\mathbf{\Phi}$ is

a $Q \times N$ matrix whose elements are

$$\phi_{k,n} = \frac{1}{\sqrt{Q}} e^{\frac{j2\pi\alpha nk}{Q}}, \tag{3.4}$$

for $0 \leq n < N$, $0 \leq k < Q$. The defined discrete SEFDM signal model forms the basis for the design of efficient transmitting structures that are presented in chapter 4.

3.2.1 The Carriers Matrix

Sampling the subcarriers of the SEFDM system result in a $Q \times N$ matrix $\mathbf{\Phi}$ where

$$\mathbf{\Phi} = \frac{1}{\sqrt{Q}} \begin{bmatrix} 1 & 1 & 1 & \cdots & 1 \\ 1 & e^{\frac{j2\pi\alpha}{Q}} & e^{\frac{j4\pi\alpha}{Q}} & \cdots & e^{\frac{j2\pi(N-1)\alpha}{Q}} \\ \vdots & & & \ddots & \\ 1 & e^{\frac{j2\pi(Q-1)\alpha}{Q}} & e^{\frac{j4\pi(Q-1)\alpha}{Q}} & \cdots & e^{\frac{j\pi(Q-1)(N-1)\alpha}{Q}} \end{bmatrix}. \tag{3.5}$$

An important observation here is that the matrix Φ in equation (3.5) is a Vandermonde matrix. A Vandermonde matrix is a special matrix whose entries are defined by the entries of the generating row (or column) as [80]:

$$V = \begin{bmatrix} 1 & a_1^0 & a_2^0 & \cdots & a_N^0 \\ 1 & a_1^1 & a_2^1 & \cdots & a_N^1 \\ \vdots & & & \ddots & \vdots \\ 1 & a_1^{Q-1} & a_2^{Q-1} & \cdots & a_N^{Q-1} \end{bmatrix}. \tag{3.6}$$

Using Vandermonde matrix notation, the matrix Φ can be expressed as row Vandermonde matrix as

$$\Phi = V\left(1, e^{\frac{j2\pi\alpha}{Q}}, e^{\frac{j4\pi\alpha}{Q}}, \cdots, e^{\frac{j2\pi(N-1)\alpha}{Q}}\right), \tag{3.7}$$

noting that Φ can also be expressed as a column Vandermonde matrix. Furthermore, Φ is constructed from points on the unit circle of the complex z-plane, particularly the elements of the generating row are powers of the Q^{th} root of unity $e^{\frac{j2\pi}{Q}}$[1].

3.3 Characterizing the ICI in the SEFDM System

Expectedly, the SEFDM system will suffer from ICI due to the loss of orthogonality. In order to investigate this interference the cross correlation between the subcarriers is derived to estimate energy leakage amongst all subcarriers. Derivations for the correlation for the continuous time FOFDM system was presented in [95], where the real and imaginary parts of the correlation were explored and hence used to explain how FOFDM facilitates reliable transmission over half the bandwidth of OFDM. In this thesis, the cross correlation is derived for the SEFDM system where the FOFDM system is considered a special case corresponding to $\alpha = 0.5$. Furthermore, the correlation of the discrete time system is derived and analyzed.

Considering two arbitrarily SEFDM subcarriers denoted by $e^{\frac{j2\pi m\alpha t}{T}}$ and $e^{\frac{j2\pi n\alpha t}{T}}$, the cross correlation is given by

$$\begin{aligned} r_c(m,n) &= \frac{1}{T}\int_0^T e^{\frac{j2\pi m\alpha t}{T}} e^{-\frac{j2\pi n\alpha t}{T}} dt \\ &= e^{j\pi\alpha(m-n)}\mathrm{sinc}\left(\alpha\left(m-n\right)\right) \\ &= \mathrm{sinc}\left(2\alpha\left(m-n\right)\right) \\ &\quad + j\sin\left(\pi\alpha\left(m-n\right)\right)\mathrm{sinc}\left(\alpha\left(m-n\right)\right). \end{aligned} \tag{3.8}$$

This correlation may be expressed in terms of amplitude and phase as

$$\left|r_c(m,n)\right| = \left|\mathrm{sinc}\left(\alpha\left(m-n\right)\right)\right|, \tag{3.9}$$

$$\Theta_{r_c(m,n)} = \begin{cases} \pi\alpha\left(m-n\right) & , \ \lceil\alpha\left(m-n\right)\rceil \text{ odd} \\ \pi\alpha\left(m-n\right)+\pi & , \ \lceil\alpha\left(m-n\right)\rceil \text{ even} \end{cases}, \tag{3.10}$$

[1]The Q^{th} root of unity $e^{\frac{j2\pi}{Q}}$ satisfies that $\left(e^{\frac{j2\pi}{Q}}\right)^Q = 1$ and that $\left(e^{\frac{j2\pi}{Q}}\right)^{(kQ+m)} = e^{\frac{j2\pi m}{Q}}$.

where $|\cdot|$ is the absolute value and $\lceil\cdot\rceil$ is the ceiling operation. It is clear from equation (3.8) that the cross correlation is dependent on two parameters of the system, the bandwidth compression factor α and the relative distance between the subcarriers reflected by the indices m and n. The formula for the amplitude shows that the cross correlation is expected to decrease with the increase in the distance between the subcarriers and the one under question. As for the phase, equation (3.10) shows that the phase of the correlation with the subcarriers on the RHS of the subcarrier under examination will be the negative of the phase with the subcarriers on the LHS.

As, the discrete SEFDM system will be the base for more realistic system designs and implementation, the ICI in the case of the sampled system is now evaluated. Considering two discretized SEFDM carriers denoted by $e^{\frac{j2\pi\alpha km}{Q}}$ and $e^{\frac{j2\pi\alpha kn}{Q}}$, $k = 0, ..., (Q-1)$, where Q is an arbitrary number of samples per carrier, the cross correlation of the discrete SEFDM system is derived to be:

$$\begin{aligned} c_{m,n} &= \frac{1}{Q}\sum_{k=0}^{Q-1} e^{\frac{j2\pi\alpha km}{Q}} e^{-\frac{j2\pi\alpha kn}{Q}} \\ &= \frac{1}{Q}\left[\frac{1-e^{j2\pi\alpha(m-n)}}{1-e^{\frac{j2\pi\alpha(m-n)}{Q}}}\right] \\ &= e^{j\pi\alpha(m-n)} e^{\frac{-j\pi\alpha(m-n)}{Q}} \left[\frac{\operatorname{sinc}\left(\alpha\left(m-n\right)\right)}{\operatorname{sinc}\left(\frac{\alpha(m-n)}{Q}\right)}\right], \end{aligned} \tag{3.11}$$

where the derivation is based on the rule of the sum of a geometric series. The amplitude in this case is given as

$$|c_{m,n}| = \left|\frac{\operatorname{sinc}\left(\alpha\left(m-n\right)\right)}{\operatorname{sinc}\left(\frac{\alpha(m-n)}{Q}\right)}\right|, \tag{3.12}$$

Based on equation (3.11), the cross correlation coefficient matrix can be expressed as

$$\mathbf{C} = \frac{1}{Q}\begin{bmatrix} 1 & \frac{1-e^{j2\pi\alpha}}{1-e^{\frac{j2\pi\alpha}{Q}}} & \frac{1-e^{j4\pi\alpha}}{1-e^{\frac{j4\pi\alpha}{Q}}} & \cdots & \frac{1-e^{j2\pi(N-1)\alpha}}{1-e^{\frac{j2\pi(N-1)\alpha}{Q}}} \\ \vdots & & & \ddots & \\ 1 & \frac{1-e^{j2(N-1)\pi\alpha}}{1-e^{\frac{j2(N-1)\pi\alpha}{Q}}} & \frac{1-e^{j4(N-1)\pi\alpha}}{1-e^{\frac{j4(N-1)\pi\alpha}{Q}}} & \cdots & \frac{1-e^{j\pi(N-1)(N-1)\alpha}}{1-e^{\frac{j\pi(N-1)(N-1)\alpha}{Q}}} \end{bmatrix}, \tag{3.13}$$

The matrix $\mathbf{C}$ in (3.13) characterizes the spillage of energy between the subcarriers. $\mathbf{C}$ is a *Toeplitz*[2] and *Hermitian* [3] $N \times N$ matrix where N is the number of subcarriers and it may be expressed in short form as

$$c_{m,n} = \frac{1}{Q} \begin{bmatrix} Q & , m = n \\ \frac{1-e^{j2\pi\alpha(m-n)}}{1-e^{\frac{j2\pi\alpha(m-n)}{Q}}} & , m \neq n \end{bmatrix}. \tag{3.14}$$

Examining equation (3.11) shows that the correlation coefficient matrix is directly related to the carriers matrix $\mathbf{\Phi}$ as

$$\mathbf{C} = \mathbf{\Phi}^* \mathbf{\Phi}. \tag{3.15}$$

Theorem 3.1. *In an SEFDM system with* $\alpha = b/c$ where b , $c \in \mathbb{N}$, $b < c$, *and* $N > c$ *at least two of the subcarriers are mutually orthogonal.*

Proof. From equations (3.9) and (3.12) for the continuous and discrete system, respectively, it is clear that for

$$\alpha\,(m_o - n_o) \in \mathbb{Z}, \tag{3.16}$$

the amplitudes of the correlation coefficients are equal to

$$\begin{aligned} |r_c\,(m_o, n_o)\,| &= 0, \\ |c_{m_o,n_o}| &= 0, \end{aligned}$$

thus indicating orthogonality between the m_o^{th} and n_o^{th} subcarriers, the condition that $N > c$ is to ensure that the available subcarriers indices can satisfy the condition in equation (3.16) for at least two subcarriers. □

[2] An $N \times N$ Toeplitz matrix A has the structure of

$$A = \begin{bmatrix} a_0 & a_1 & a_2 & \cdots & \cdots & a_{N-1} \\ a_{-1} & a_0 & a_1 & a_2 & & \vdots \\ a_{-2} & a_{-1} & \ddots & \ddots & \ddots & \vdots \\ \vdots & \ddots & \ddots & \ddots & a_1 & a_2 \\ \vdots & & \ddots & a_1 & a_0 & a_1 \\ a_{-N-1} & \cdots & \cdots & a_{-2} & a_{-1} & a_0 \end{bmatrix}.$$

[3] A Hermitian matrix A is defined as

$$A = A^*.$$

The significance of Theorem 3.1 is that not all the subcarriers will be interfering with each other and is utilized in chapter (8) to design improved fading channel estimators. This theorem is illustrated by numerical examples in appendix A, where it is also shown that the number of subsets of orthogonal subcarriers and the number of subcarriers within a subset is dependent on α and N.

When Q approaches infinity the discrete case cross correlation becomes equal to the continuous case that is equation (3.11) becomes equivalent to equation (3.8) as

$$\lim_{Q\to\infty} c_{m,n} = e^{j\pi\alpha(m-n)}\text{sinc}\left(\alpha\left(m-n\right)\right) = r_c\left[m,n\right]. \tag{3.17}$$

For any other value of Q, the interference between the m^{th} and n^{th} subcarrier in discrete case will differ from the continuous time case by a factor $\mathbf{f}$ where

$$\mathbf{f} = \frac{e^{\frac{-j\pi\alpha(m-n)}{Q}}}{\text{sinc}\left(\frac{\alpha(m-n)}{Q}\right)}. \tag{3.18}$$

The formulas derived for the correlation coefficients are illustrated with numerical examples for different α and N values in Fig. 3.1 and 3.2. Fig. 3.1 depicts plots for the amplitude of the correlation between SEFDM subcarriers, as in equations (3.9) for different values of α and the distance between the middle subcarrier and the rest of the subcarriers in terms of their integer indices. Fig. 3.1a shows that the amplitude of the correlation is inversely proportional to α which is an expected outcome as the smaller the value of α the more correlated the subcarriers become until all converge to a single carrier case. Moreover, the amplitude of the correlation appears to decrease with the increase in the relative distance between the subcarriers which confirms that the interference from adjacent interfering subcarriers is higher than from relatively distant ones. These observations are confirmed in Fig. 3.1a and 3.1c depicting the amplitudes of the correlation for selected relative distance between the subcarriers or α values, respectively. It is necessary to emphasize that the previous observations exclude the relatively orthogonal subcarriers identified in Theorem 3.1, as these subcarriers will not generate ICI among themselves.

Fig. 3.2 depicts the phase of the correlation with respect to α and the subcarriers relative distance. To keep the figure legible selected distances and α values are displayed.

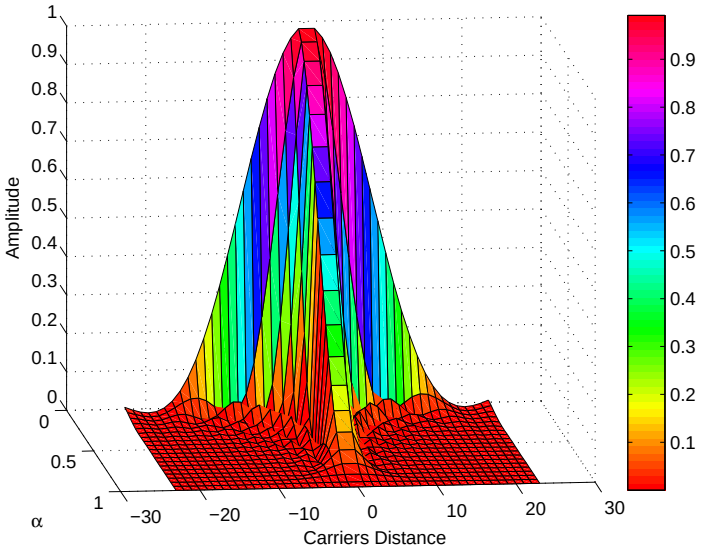

(A) Correlation amplitude vs α and $(m-n)$

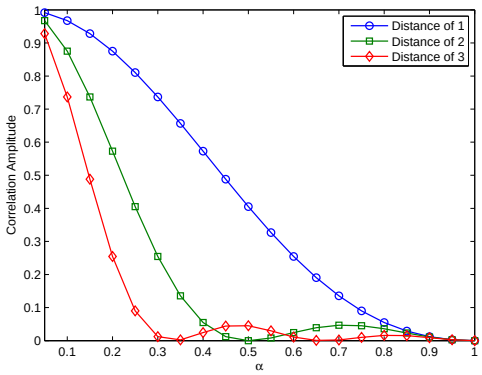

(B) Correlation amplitude vs α.

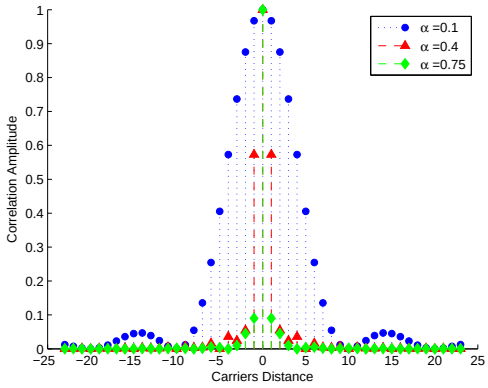

(C) Correlation amplitude vs $(m-n)$

FIGURE 3.1: Correlation amplitude in SEFDM systems.

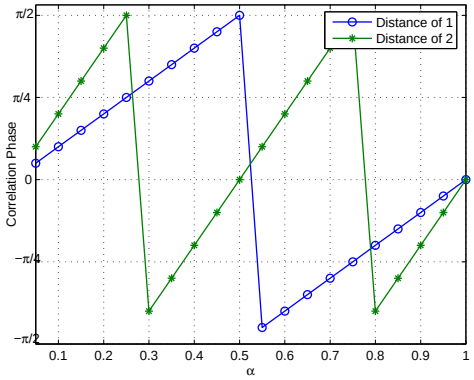

(A) Correlation phase vs α

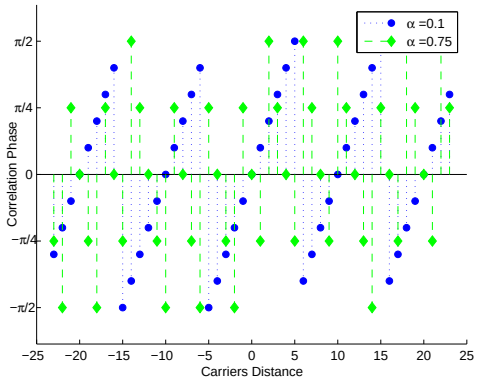

(B) Correlation phase vs $(m-n)$

FIGURE 3.2: Correlation phase in SEFDM systems

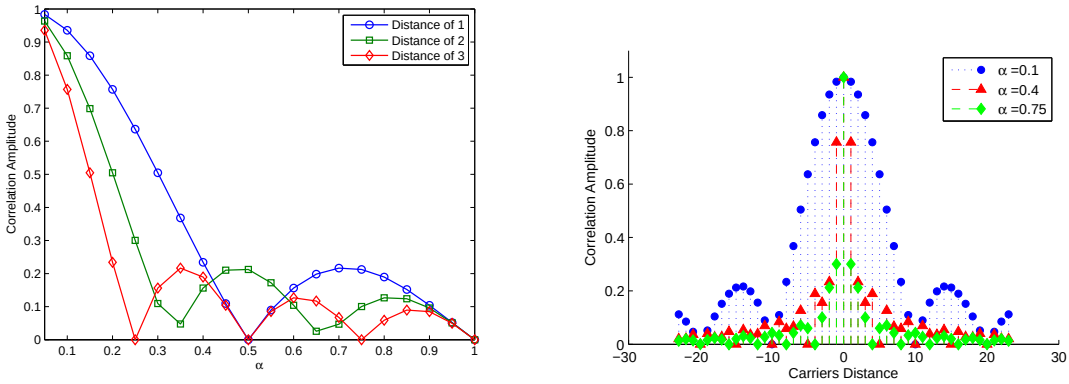

(A) Correlation amplitude vs α. (B) Correlation amplitude vs $(m-n)$

FIGURE 3.3: Discrete correlation amplitude in SEFDM systems

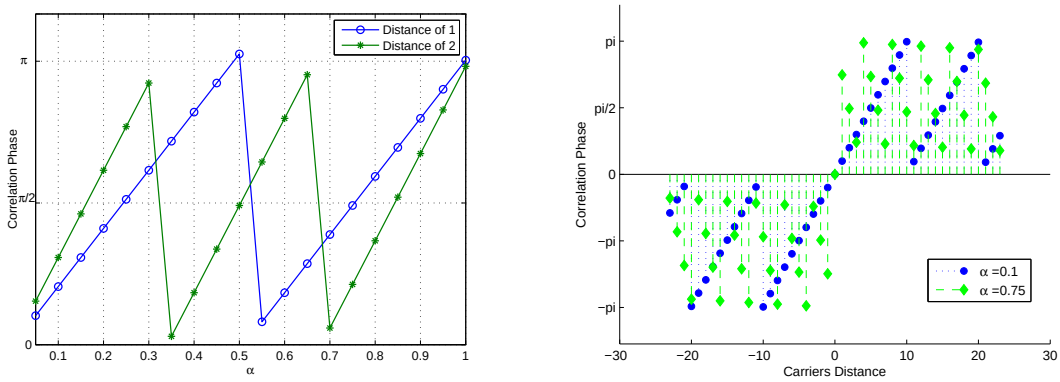

(A) Correlation phase vs α (B) Correlation phase vs $(m-n)$

FIGURE 3.4: Discrete correlation phase in SEFDM systems

Fig. 3.2a shows that the phase of the correlation changes periodically with α for the same distance between subcarriers. Fig. 3.2b confirms that the correlation exhibits a conjugate symmetry around the subcarrier in question (middle subcarrier in this case), which explains that the correlation matrix being Hermitian. Fig. 3.3 and 3.4 display the amplitude and phase of the cross correlation for the discrete SEFDM system. The figure shows that the amplitude of the correlation is higher than that of the continuous system case, specially the ICI contributions from distant subcarriers to the one under consideration. This is due to the fact that the discrete signal is represented by a fraction of the samples of the continuous system case ($\longrightarrow \infty$), thus the subcarriers appear closer in the subspace of the signal. In addition, the phase of the discrete system correlation experiences changes as depicted in Fig. 3.4 which shows the conjugate symmetry reflected in the correlation matrix being Hermitian. The effect of the sampling process

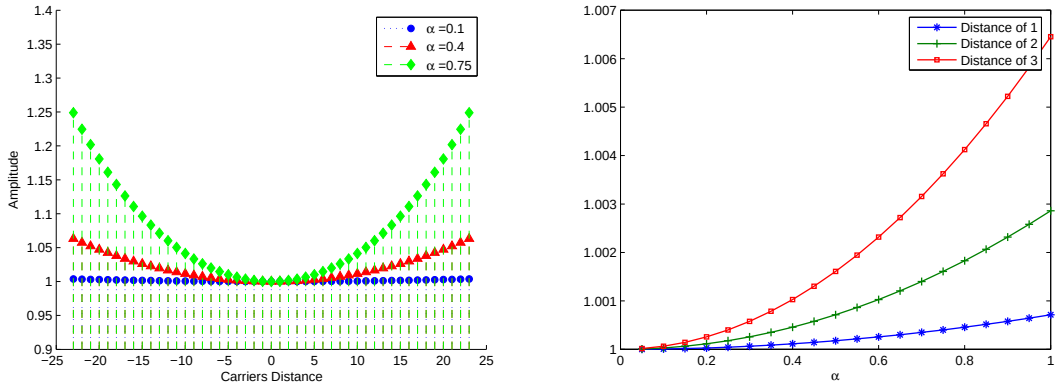

(A) Amplitude vs $(m-n)$ (B) Amplitude vs α

FIGURE 3.5: Amplitude of the factor $\mathbf{f}$ for $Q = 2N$.

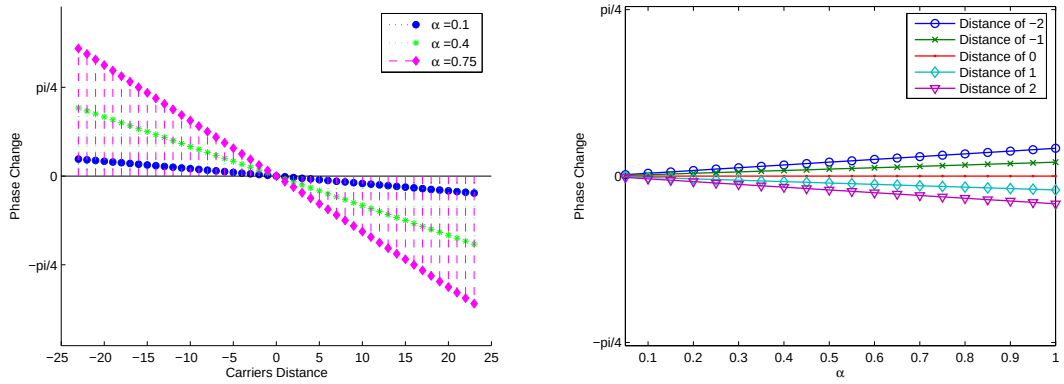

(A) Phase vs $(m-n)$ (B) Phase vs α

FIGURE 3.6: Phase of the factor $\mathbf{f}$ for $Q = 2N$.

on the ICI is further investigated by plotting the amplitude and phase of the factor $\mathbf{f}$, derived in equation (3.18), with respect to the subcarriers distance and α as shown in Fig. 3.5 and 3.6. From the plots it can be seen that the amplitude and phase of the correlation increase with the increase in α and the distance between the subcarrier in question and the other subcarriers. Moreover, the figures further confirm that the effects of discretizing the system are more serious on the ICI contribution from the subcarriers that are relatively remote. In the case of orthogonal systems, there is no effect of the process of discretization as the system is free from ICI in the first place.

The study of the ICI in the SEFDM system is essential for the understanding of the behaviour of the system. Clearly, the loss of orthogonality results in ICI that is in proportion to the level of bandwidth compression and the number of interfering subcarriers.

However, this ICI is deterministic with values that can be pre-calculated. Therefore, the design of the SEFDM system can accommodate the knowledge of the ICI for the reception process as will be shown in chapters 5 and 6.

3.4 The Discrete SEFDM Receiver

On the reception side the fundamental question in communication system arises, that is how to estimate efficiently the originally transmitted signal based on observations of the received signal $y(t)$. One widely used technique is to collect statistics of the received signal and use it to estimate the transmitted message. The SEFDM receiver follows this two stage process. The first stage is a demodulator that extracts statistics of the incoming signal whereas the second stage generates estimates of the originally transmitted symbols based on the collected statistics. In this section, the model of the SEFDM signal after demodulation is identified and used in subsequent sections to derive the relationships between system parameters and performance.

Considering SEFDM symbol with index $l = 0$ as defined in equation (3.1), the received signal corresponding to this symbol will arrive contaminated with AWGN and is thus described as

$$y_0(t) = x_0(t) + w(t), \tag{3.19}$$

where $w(t)$ denotes the noise. Equivalently, the discrete received signal can be described as

$$Y[k] = \frac{1}{\sqrt{Q}} \sum_{n=0}^{Q-1} s_n e^{\frac{j2\pi nk\alpha}{Q}} + W[k], \tag{3.20}$$

for $k = 0, 1, \cdots, N-1$ where W is a $Q \times 1$ vector of AWGN noise samples.

The demodulator stage works on the samples of the incoming signal to produce a vector R that contains the statistics of the signal $r_0(t)$:

$$R = f(Y). \tag{3.21}$$

The vector R must provide sufficient information for subsequent stages to successfully decode the signal. In the literature, there are two widely used reception techniques namely correlation reception and matched filter [64]. A correlation receiver generates

signal statistics by projecting the signal onto an orthonormal set of bases spanning the same signal space as the transmitted signal. Matched filtering aims to maximize the signal to noise ratio at the receiver output, therefore, matches the processes followed to generate the signal.

All SEFDM detectors proposed before this thesis used the correlation receiver technique as described in section 2.5, thus a brief summary of the process in this receiver is provided in section 3.4.2. The next section is devoted for the derivation of the matched filter for the SEFDM system. The obvious advantage of using a matched filter in the SEFDM system is the elimination of the orthonormalization process. However, it is crucial to verify that a similar error performance to that of the correlation receiver is achievable, which is the focus of chapter 5.

3.4.1 The Matched Filter (MF)

The MF[4] for the discrete SEFDM system is equivalent to the carriers matrix $\mathbf{\Phi}$. MF reception is expressed as

$$\begin{aligned} R &= \mathbf{\Phi}^*\mathbf{\Phi}S + \mathbf{\Phi}^*W \\ &= \mathbf{C}S + W_{\mathbf{\Phi}^*}, \end{aligned} \tag{3.22}$$

where $W_{\mathbf{\Phi}^*}$ is the expanded noise term on $\mathbf{\Phi}$. The properties of the noise can be identified based on the knowledge of the matrix $\mathbf{\Phi}$ and $\mathbf{C}$. The noise term associated with the i^{th} observation from R is given as

$$W_{\mathbf{\Phi}^*,i} = \mathbf{\Phi}_i^* W, \tag{3.23}$$

where $\mathbf{\Phi}_i^*$ refers to the i^{th} row of $\mathbf{\Phi}^*$. Therefore, each noise term is basically a linear transformation of the AWGN noise samples vector W. The mean of the noise term $W_{\mathbf{\Phi}^*,i}$ is given by

$$\begin{aligned} \mathrm{E}\{W_{\mathbf{\Phi}^*,i}\} &= \mathrm{E}\{\mathbf{\Phi}_i^* W\}, \\ &= \mathbf{\Phi}_i^* \mathrm{E}\{W\} \\ &= 0, \end{aligned} \tag{3.24}$$

[4]In this context the general definition of the matched filter is adopted in that the filter response is chosen to maximize the signal to noise ratio [115].

where $\mathrm{E}[\cdot]$ is the expectation operator. The final line of equation (3.24) is obtained due to the assumption that the noise in the system has a zero mean.

In addition, the covariance matrix of the transformed noise vector needs to be evaluated as the subcarriers are not orthogonal, thus the noise samples will be correlated. The covariance matrix denoted as Ψ of the transformed noise signal is derived as follows

$$\Psi_{i,k} = \mathrm{E}\left\{\left(W_i - \mathrm{E}\left\{W_i\right\}\right)\left(W_k^* - \mathrm{E}\left\{W_k\right\}\right)\right\}. \tag{3.25}$$

Substituting for $\mathrm{E}\{W_i\}$ and $\mathrm{E}\{W_k\}$ from equation (3.24) leads to

$$\begin{aligned} \Psi_{i,k} &= \mathrm{E}\left\{W_i W_k^*\right\}, \\ &= \mathrm{E}\left\{\mathbf{\Phi}_i^* W_i W_k^* \mathbf{\Phi}_k\right\}, \\ &= \mathbf{\Phi}_i^* \mathrm{E}\left\{W_i W_k^*\right\} \mathbf{\Phi}_k, \end{aligned} \tag{3.26}$$

where $\mathbf{\Phi}_k$ is the k^{th} row of $\mathbf{\Phi}$ and the expectation operator is moved inwards due to the deterministic nature of the carriers matrix. Recalling that $\mathrm{E}\{WW^*\}$ is equal to $\sigma^2\mathbf{I}$, where σ^2 is the noise variance because by definition the original noise samples are uncorrelated, equation (3.26) is further reduced to

$$\begin{aligned} \Psi_{i,k} &= \sigma^2 \mathbf{\Phi}_i^* \mathbf{\Phi}_k, \\ &= \sigma^2 c_{i,k}. \end{aligned} \tag{3.27}$$

Equation (3.27) confirms that the transformed noise is correlated and has a covariance matrix that is equal to $\sigma^2\mathbf{C}$.

3.4.2 The Correlation Receiver

The original SEFDM proposal uses the correlation receiver technique to extract the sufficient statistics of the transmitted signal [21]. The receiver relies on using orthonormal bases onto which the incoming signal is projected. The discrete correlation receiver for the SEFDM system follows the same principles as the continuous one. The incoming

signal samples as in equation (3.20) are projected onto orthonormal vectors corresponding to the orthonormal bases described in section 2.5, which can be obtained from the subcarriers matrix following the orthonormalization techniques discussed in section 2.6. Thus, the statistics vector R in this case is expressed as

$$\begin{aligned} R &= \mathbf{B}^*\mathbf{\Phi}S + \mathbf{B}^*W, && (3.28)\\ &= \mathbf{M}S + W_{\mathbf{B}^*}, && (3.29) \end{aligned}$$

where $\mathbf{B}$ is an an $N \times N$ matrix whose columns are orthonormal vectors obtained from the columns of the carriers matrix $\mathbf{\Phi}$, $\mathbf{M}$ is an $N \times N$ matrix whose elements represent the correlation between the subcarriers and the orthonormal bases and $W_{\mathbf{B}^*}$ is the expanded noise on $\mathbf{B}^*$. It is straight forward to show that the mean of the elements of $W_{\mathbf{B}^*}$ is an $N \times 1$ vector of zeros. Furthermore, the orthogonal nature of the bases ensures that the elements of $W_{\mathbf{B}^*}$ remain uncorrelated. The covariance matrix denoted again as Ψ of the transformed noise signal can be derived as follows

$$\Psi_{i,k} = \mathrm{E}\left\{\left(W_i - \mathrm{E}\left\{W_i\right\}\right)\left(N_k^* - \mathrm{E}\left\{W_k\right\}\right)\right\}. \tag{3.30}$$

Substituting for $\mathrm{E}\left\{W_i\right\}$ and $\mathrm{E}\left\{W_k\right\}$ from equation (3.24) leads to

$$\begin{aligned} \Psi_{i,k} &= \mathrm{E}\left\{W_i W_k^*\right\}, \\ &= \mathrm{E}\left\{\mathbf{B}_i^* W W^* \mathbf{B}_k\right\}, \\ &= \mathbf{B}_i^* \mathrm{E}\left\{W W^*\right\} \mathbf{B}_k, \\ &= \mathbf{B}_i^* \mathbf{B}_k, && (3.31) \end{aligned}$$

where $\mathbf{B}_k$ is the k^{th} column of $\mathbf{B}$. However, by definition of the orthonormal bases

$$\mathbf{B}^*\mathbf{B} = \mathbf{B} \times \mathbf{B}^* = \mathbf{I}, \tag{3.32}$$

thus leading to

$$\Psi_{i,k} = \begin{bmatrix} 1 & , i = k \\ 0 & , i \neq k \end{bmatrix}. \tag{3.33}$$

Equation (3.31) confirms that the expanded noise terms are uncorrelated unlike the case with the matched filter.

Furthermore, equation (3.29) shows that the information symbols are related to the statistics vector via the matrix $\mathbf{M}$. The $\mathbf{M}$ matrix as described in section 2.5 is basically the correlation of the original subcarriers with the orthonormal bases, and is simply expressed as

$$\mathbf{M} = \mathbf{B}^* \times \mathbf{\Phi}. \tag{3.34}$$

Examining the Gram matrix of the $\mathbf{M}$ matrix given by $\mathbf{M}^*\mathbf{M}$:

$$\begin{aligned} \mathbf{M}^*\mathbf{M} &= \mathbf{\Phi}^* \times \mathbf{B} \times \mathbf{B}^*\mathbf{\Phi} \\ &= \mathbf{\Phi}^*\mathbf{\Phi} = \mathbf{C}. \end{aligned} \tag{3.35}$$

Now define $\mathbf{\Sigma_M}$ a matrix containing the singularvalues of $\mathbf{M}$, and $\mathbf{U}$ and $\mathbf{D}$ as unitary matrices[5] that contain the left singularvectors and right singularvectors of $\mathbf{M}$, respectively. $\mathbf{M}$ is related to $\mathbf{\Sigma_M}$ by the Singular Value Decomposition (SVD) as in equation (3.36).

$$\mathbf{M} = \mathbf{U}\mathbf{\Sigma_M}\mathbf{D}^*. \tag{3.36}$$

Substituting equation (3.36) in equation 3.35 yields:

$$\begin{aligned} \mathbf{U}\mathbf{\Sigma_M}\mathbf{D}^*\mathbf{D}\mathbf{\Sigma_M^*}\mathbf{U}^* &= \mathbf{C} \\ \mathbf{U}\mathbf{\Sigma_M}\mathbf{\Sigma_M^*}\mathbf{U}^* &= \mathbf{C} \\ \mathbf{\Sigma_M}\mathbf{\Sigma_M^*} &= \mathbf{U}^*\mathbf{C}\mathbf{U} \end{aligned} \tag{3.37}$$

The RHS of equation (3.37) describes the Eigenvalue Decomposition of the $\mathbf{C}$ matrix, where $\mathbf{U}^*\mathbf{C}\mathbf{U} = \mathbf{\Lambda}$ for $\mathbf{\Lambda}$ is an $N \times N$ diagonal matrix containing the eigenvalues[6] of $\mathbf{C}$. The LHS contains the squares of the singularvalues of the $\mathbf{M}$ matrix. From equation (3.37) it is clear that the squares of the singularvalues of $\mathbf{M}$ are equal to the eigenvalues

[5] A unitary matrix is a square matrix that satisfy the condition $\mathbf{U}\mathbf{U}^* = \mathbf{U}^*\mathbf{U} = \mathbf{I}$, where $\mathbf{I}$ is the identity matrix

[6] In principle, the eigenvalues of the $N \times N$ matrix $\mathbf{C}$ are the roots of its characteristic equation $\det(\lambda\mathbf{I} - \mathbf{C}) = 0$, which is a polynomial of degree N.

of **C**. Hence it can be deducted that regardless of the type of demodulation, the matrix **C** can provide the required information about the system. Therefore, the work in this chapter focuses on the matrix **C** to explain the complexity and performance of the detection schemes described in [65, 90, 35, 36].

3.5 SEFDM Solution Determinants

Based on equations (3.22) and (3.29), the demodulated SEFDM signal can be expressed as

$$R = \mathfrak{C}S + W, \tag{3.38}$$

where $\mathfrak{C}$ denotes the **C** or **M** matrix for MF or correlation receiver respectively and W is used here to refer to the expanded noise term onto the conjugate subcarriers or orthonormal bases according to which type of receiver is adopted. Equation (3.38) shows that the SEFDM system is represented by a linear combination of the vector of N transmitted information symbols plus a noise term. Thus, the SEFDM model is classified as multiple linear regression model, where R is the dependent variable, $\mathfrak{C}$ is the design matrix and W is the noise. There are many estimation methods for systems described with linear regression models, yet it is essential for all methods that the design matrix has full column rank[7] and error free elements. The rank of a matrix can be efficiently evaluated by the SVD, however, the decision on the rank will depend on the numerical precision of the evaluating machine and the targeted application of the system. Therefore, it is deemed useful to examine the properties of the design matrix $\mathfrak{C}$ not in terms of rank but on conditioning as a matrix may have full rank with poor conditioning which in turn affects the dynamic range of the required hardware and the BER performance.

In addition, equation (3.35) shows whether MF or correlation receiver is used the underlying matrices that describe the system remain closely related. Having derived closed formulas for the matrices **Φ** and **C** in sections 3.2 and 3.3 and established the links to the **M** matrix in section 3.4.2, the rest of the work in this chapter focuses on the study of the properties of these matrices to extract the properties of the system, particularly, to define how and why it becomes ill conditioned. Recalling that section 3.4.2 related the **M** matrix to the **C** matrix, in this work the focus will be on identifying the properties

[7]Column rank of matrix corresponds to the maximum number of linearly independent column vectors and the same for row rank matrix. A full column rank matrix has all its column linearly independent.

TABLE 3.1: Summary of relationships between key matrices in SEFDM system.

	$\mathbf{\Phi}$	$\mathbf{B}$	$\mathbf{M}$	$\mathbf{C}$
$\mathbf{\Phi}$	=	GS or LM	$= \mathbf{BM}$	$= [\mathbf{\Phi}^*]^{-1}\mathbf{C}$
$\mathbf{B}$	GS or LM	=	$= [\mathbf{\Phi}^*]^{-1}\mathbf{M}^*$	through $\mathbf{\Phi}$
$\mathbf{M}$	$= \mathbf{B}^*\mathbf{\Phi}$	$= \mathbf{B}^*\mathbf{\Phi}$	=	$= \mathbf{B}^*[\mathbf{\Phi}^*]^{-1}\mathbf{C}$
$\mathbf{C}$	$= \mathbf{\Phi}^*\mathbf{\Phi}$	through $\mathbf{\Phi}$	$= \mathbf{M}^*\mathbf{M}$	=

of the $\mathbf{C}$ and $\mathbf{\Phi}$ matrices as the key indicators of the system properties and all results on the $\mathbf{C}$ matrix can be extended to the $\mathbf{M}$ matrix. Table. 3.1 summarizes the relationships between these matrices.

3.5.1 Singularity Investigation

Kanaras et al. have indicated that the system suffers from performance degradations with the increase in the number of subcarriers and/or bandwidth compression level, and related this degradation to the ill conditioning of the system [35]. Based on numerical examinations, it was noted that the $\mathbf{M}$ matrix can become numerically singular[8] [57]. This section presents a mathematical examination of the singularity of the SEFDM system by examining the carriers matrix $\mathbf{\Phi}$ and that the findings can be extended to $\mathbf{C}$, and $\mathbf{M}$ through Table. 3.1.

A starting point is the finding in section 3.2.1 that the carriers matrix $\mathbf{\Phi}$ is Vandermonde. Vandermonde matrices have a reputation of being ill conditioned [116, 117, 118]. This is specially the case of matrices constructed from real entries. When the entries of the matrix are complex, the matrices are sometimes well conditioned as is the case of a DFT matrix which is a perfectly conditioned Vandermonde matrix. By rule a Vandermonde matrix is non-singular *if and only if* the entries of the generating row or column are distinct [80]. The rule defining singularity of a Vandermonde matrix $\mathbf{V}$ follows from its determinant formula as

$$\det(\mathbf{V}) = \prod_{1 \le i < k \le n} (a_k - a_i), \tag{3.39}$$

[8]Singular matrices are characterized by a zero determinant, consequently, the singular matrix has no inverse.

where a_i and a_k are the elements of the generating row or column. The determinant of a matrix can provide an indicator of the conditioning of a matrix. The smaller the value of the determinant the more ill conditioned the matrix becomes and a zero determinant matrix is certainly singular. Therefore, a close investigation of the determinant of Φ can provide information about the system overall. For the case of the Vandermonde matrix, if any two elements a_i and a_k are equal the determinant in equation (3.39) will be equal to zero and thus, the matrix is singular and has no matrix inverse. The elements of the generating row of the $\mathbf{\Phi}$ matrix are powers of the main element $e^{\frac{j2\pi k\alpha}{Q}}$ for $k = 0, 1, 2, \cdots, (N-1)$ therefore, the elements a_i and a_k will be equal to $e^{\frac{j2\pi i\alpha}{Q}}$ and $e^{\frac{j2\pi k\alpha}{Q}}$, respectively for i and $k = 0, 1, 2 \cdots, (N-1)$. It is necessary to find if these two elements will be equal and the respective values of i and k in this case as

$$\begin{aligned} e^{\frac{j2\pi i\alpha}{Q}} &= e^{\frac{j2\pi k\alpha}{Q}}, \\ \frac{2\pi i\alpha}{Q} &= \frac{2\pi k\alpha}{Q} \pm 2\pi m, \ m = 1, 2, \cdots \\ \frac{\alpha}{Q} &= \frac{\pm m}{(i-k)}, \end{aligned} \tag{3.40}$$

where $i - k$ is the distance between the two elements under investigation. The last line shows that the equality of the i^{th} and k^{th} terms of the generating row can only hold for $i - k > Q$, but by definition $Q \geq N$ and $(i, k) < N$. This proves that the elements $\{a_n\}_0^{N-1}$ will always be distinct and confirms that the $\mathbf{\Phi}$ matrix is not singular.

Although, it is proved that the matrix Φ is not singular, numerical analysis showed that for a given machine precision $\mathbf{\Phi}$ can appear to be singular. The implication of a singular carriers matrix is that the system becomes non-invertible, hence, non-solvable by simple linear detection methods. This observation necessitates further investigation of the determinant of Φ matrix to obtain knowledge of its behaviour.

Lemma 3.1. The determinant of Φ could be expressed as

$$\det(\Phi) = (-j)^{N\left(\frac{N-1}{2}\right)} e^{\frac{j\pi\alpha\left(N^2-1\right)}{6}} \prod_{\delta \geq 0}^{N-1} 2\sin\left(\frac{\pi\delta\alpha}{N}\right)^{N-\delta}. \tag{3.41}$$

Proof. Following equation (3.39) for the determinant of Vandermonde matrices, and taking $Q = N$ to obtain a square matrix, the determinant of the carriers matrix $\mathbf{\Phi}$ is given by

$$\det(\Phi) = \prod_{0 \le i < k \le N-1} \left(e^{\frac{j2\pi k\alpha}{N}} - e^{\frac{j2\pi i\alpha}{N}} \right). \tag{3.42}$$

Equation (3.42) can be manipulated as follows:

$$\begin{aligned} \det(\Phi) &= \prod_{0 \le i < k \le N-1} e^{\frac{j2\pi k\alpha}{N}} \left(1 - e^{\frac{j2\pi(i-k)\alpha}{N}} \right), \\ &= \prod_{0 \le i < k \le N-1} e^{\frac{j\pi\alpha(k+i)}{N}} \left(e^{\frac{-j\pi(i-k)\alpha}{N}} - e^{\frac{j\pi(i-k)\alpha}{N}} \right), \\ &= \prod_{0 \le i < k \le N-1} 2j\, e^{\frac{j\pi\alpha(k+i)}{N}} \sin\left(\frac{\pi(i-k)\alpha}{N} \right). \end{aligned} \tag{3.43}$$

Recalling that $\sin(-x) = -\sin(x)$, equation (3.43) can be expressed as the product of a magnitude term and angular term as

$$\det(\Phi) = \prod_{0 \le i < k \le N-1} -j\, e^{\frac{j\pi\alpha(k+i)}{N}} \prod_{0 \le i < k \le N-1} 2\sin\left(\frac{\pi(k-i)\alpha}{N} \right). \tag{3.44}$$

Next each term of the RHS of equation (3.44) will be evaluated separately. Starting with the magnitude term of the determinant of $\mathbf{\Phi}$

$$|\det(\mathbf{\Phi})| = \prod_{0 \le i < k \le N-1} 2\sin\left(\frac{\pi(k-i)\alpha}{N} \right), \tag{3.45}$$

where $|\cdot|$ denotes the magnitude of a complex number. Equation (3.45) can be equivalently expressed as

$$|\det(\Phi)| = \prod_{k>1}^{N-1} \prod_{i \ge 0}^{k-1} 2\sin\left(\frac{\pi(k-i)\alpha}{N} \right),$$

which can be further simplified to

$$|\det(\Phi)| = \prod_{\delta \ge 0}^{N-1} 2\sin\left(\frac{\pi\delta\alpha}{N} \right)^{N-\delta}, \tag{3.46}$$

where $\delta = k - i$ and corresponds to the distance between the elements of the generating row of the matrix. The angular term is expressed as

$$\angle\{\det(\Phi)\} = \prod_{0\leq i<k\leq N-1} -j\, e^{\frac{j\pi\alpha(k+i)}{N}} \tag{3.47}$$

which is simplified to

$$\angle\{\det(\Phi)\} = (-j)^{N\left(\frac{N-1}{2}\right)} e^{\frac{j\pi\alpha\left(N^2-1\right)}{6}}. \tag{3.48}$$

The intermediate steps between equation (3.47) and (3.48) are shown in appendix B. □

The formula for the determinant of the carriers matrix shows direct relationship to α and N. With the increase in bandwidth compression which is reflected in a decrease in the value of α, the sin argument will decrease which in turn decreases the determinant value. The same effect occurs for the increase in the number of subcarriers. Moreover, the combined effect of the term $\frac{\alpha}{N}$ will affect the system performance in a similar manner as decreasing α or increasing N separately.

Lemma 3.2. *An upper bound for the determinant of* $\mathbf{\Phi}$ *is*

$$|\det(\Phi)| < 1. \tag{3.49}$$

Proof. Recalling that $\mathbf{C} = \mathbf{\Phi}^*\mathbf{\Phi}$, hence

$$\det(\mathbf{C}) = |\det(\Phi)|. \tag{3.50}$$

Now applying the identity

$$\det(\mathbf{A}) \leq \prod_i a_{ii}, \tag{3.51}$$

where a_{ii} represents the i^{th} element of the main diagonal for the matrix $\mathbf{A}$ [119], with the equality valid only for diagonal matrices. Equation (3.14) shows that $c_{ii} = 1$ and recalling that for $\alpha < 1$, which is the SEFDM case, the $\mathbf{C}$ matrix is not diagonal, it is thus concluded that its determinant will be less than one which consequently proves the same holds for the magnitude of the determinant of $\mathbf{\Phi}$. □

Worth noting, that for the case of OFDM the correlation matrix is diagonal, thus has a unity determinant.

Corollary 3.1. *For $\alpha < 1$, then*

$$|\sigma_{min}| \;\leq\; 1 \;\leq\; |\sigma_{max}|\,, \tag{3.52}$$

where σ_{min} and σ_{max} are the minimum and maximum singularvalues of $\mathbf{\Phi}$.

Proof. Recalling that

$$|\det(\Phi)| = \prod_{i=1}^{N} |\sigma_i|\,, \tag{3.53}$$

where σ_i is i^{th} singularvalue of $\mathbf{\Phi}$, the following bound is straightforward

$$\left|\sigma_{min}^{N}\right| \;\leq\; |\det(\Phi)| \;\leq\; \left|\sigma_{max}^{N}\right|. \tag{3.54}$$

Finally substituting the bound for $|\det(\Phi)|$ from Lemma 3.2 proves the Corollary. □

Equation (3.54) indicates that the minimum singularvalue will decrease with the increase in N or the decrease of α as suggested by the det formula, whilst Corollary 3.1 bounds the maximum singularvalue to be always greater than one for $\alpha < 1$.

Fig. 3.7 displays plots of the magnitude of the determinant of Φ as in equation (3.41) as well as the determinant of the numerically generated SEFDM subcarriers. The figure shows that the formula yields the same values as the generated carriers and that the determinant is less than 1 for $\alpha < 1$ as proved by Lemma 3.2. The plot confirms that the determinant decreases significantly with the increase in the number of subcarriers and the decrease in the value of α. The numerical values observed in the figure indicate that the system can appear singular to machine precision even for a moderate number of subcarriers and bandwidth compression levels.

3.5.2 Conditioning of the SEFDM System

The results of the study of the determinant of the carriers matrix indicate that the conditioning of the SEFDM system deteriorates with the increase in the number of

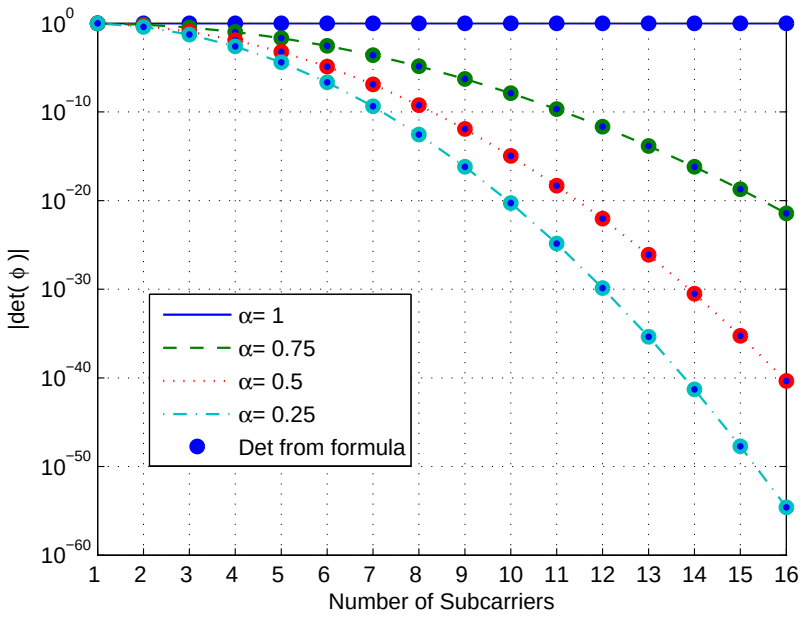

FIGURE 3.7: Determinant of carriers matrix Φ. The circles denote the determinant obtained using the formula in equation (3.41) while the lines are the determinant obtained by numerical simulations.

subcarriers and/or bandwidth compression levels. The implications of ill conditioning are two folds: first the system will be sensitive to small perturbations and second, the system will require higher resolution to represent the extreme values, both affecting the applicability of SEFDM in practical systems. In this section, the conditioning of the SEFDM system is further analyzed by investigating the condition number of the $\mathbf{C}$ matrix defined by

$$\kappa\left(\mathbf{C}\right) = \frac{\lambda_{max}}{\lambda_{min}}, \tag{3.55}$$

where λ_{max} and λ_{min} are the maximum and minimum eigenvalues of $\mathbf{C}$.

Lemma 3.3. For α being a rational number in the form $\alpha = \frac{b}{c}$ where b , $c \in \mathbb{N}$, $b < c$ and $b \neq 1$, the upper bound on the maximum eigenvalue of the $\mathbf{C}$ matrix is

$$\lambda_{max} \leq \left(\frac{N-1+l}{Q} + \frac{\beta^2 Q}{3l\,\sin^2\left(\beta\right) b^2}\right) c, \tag{3.56}$$

and the lower bound on minimum eigenvalues is

$$\lambda_{min} \geq \left(\frac{N+1-l}{Q} - \frac{\beta^2 Q}{3l \sin^2(\beta) b^2} \right) c, \tag{3.57}$$

where l is $\frac{\beta Q}{\sqrt{3}\ b\ sin(\beta)}$, β is chosen to satisfy $0 \leq \beta \leq \pi$.

Proof. The key to the proof is the rational form of α , where for this case the $N \times N$ matrix $\mathbf{C}$ can be written as

$$c_{i,j} = \frac{1}{Q} \sum_{k=0}^{Q-1} e^{\frac{j2\pi bk(j-i)}{\mathfrak{M}}},$$

where $\mathfrak{M} = cQ$, Q represents an arbitrary number of samples per carrier. Define an $\mathfrak{M} \times \mathfrak{M}$ matrix $\breve{\mathbf{C}}$ as

$$\breve{c}_{i,j} = \frac{1}{\mathfrak{M}} \sum_{k=0}^{Q-1} e^{\frac{j2\pi k(j-i)}{\mathfrak{M}}}. \tag{3.58}$$

By definition the $\mathbf{C}$ matrix is given as

$$c_{i,j} = \breve{c}_{p,q} \text{ for } p, q \bmod b = \{1, 2, ..., Q-1\}. \tag{3.59}$$

For this case of α (a rational number), the SEFDM correlation matrix is equivalent to a class of matrices found in superresolution and missing samples restoration field [117]. Thus, it is possible to apply the bounds identified in [117] since the condition set there is met by ensuring that the minimum distance between any adjacent elements is never equal to 1, in this case it is equal to b. The bounds are then adjusted according to new systems parameters with respect to $\alpha = b/c$. □

Lemma 3.4. For the same parameters as in Lemma 3.3 another upper bound on the maximum eigenvalue is obtained as

$$\lambda_{max} \leq \frac{1}{\alpha}, \tag{3.60}$$

and for minimum eigenvalue as

$$\lambda_{min} \geq 0. \tag{3.61}$$

Proof. Assuming $\alpha = b/c$ and applying the same analysis to maintain the equivalence of the cross correlation matrix and the matrices in superresolution and samples restoration as in Lemma 3.3. The bounds for the adjusted matrix can be derived from the bounds in [120]:

$$\frac{\lfloor KB \rfloor}{K} \leq \lambda_{min} \leq \lambda_{max} \leq \frac{\lceil KB \rceil}{K}, \tag{3.62}$$

where $\lceil \cdot \rceil$ and $\lfloor \cdot \rfloor$ denote the ceiling and floor functions, respectively. In this case $K = b$ and $B = (N - 1 - 0 + 1)/M = 1/c$, substituting values of K and B in equation (3.62) yields:

$$\begin{aligned} \frac{\lfloor b/c \rfloor}{b} c \leq \lambda_{min} \leq \lambda_{max} \leq \frac{\lceil b/c \rceil}{b} c \\ \frac{\lfloor \alpha \rfloor}{\alpha} \leq \lambda_{min} \leq \lambda_{max} \leq \frac{\lceil \alpha \rceil}{\alpha} \\ 0 \leq \lambda_{min} \leq \lambda_{max} \leq \frac{1}{\alpha}, \end{aligned} \tag{3.63}$$

because $\lfloor \alpha \rfloor = 0$ and $\lceil \alpha \rceil = 1$. □

The upper bound for the maximum eigenvalue depends only on the bandwidth compression factor α. The lower bound for the minimum eigenvalue confirms that all eigenvalues are non-negative. Combining Corollary 3.1 and Lemma 3.4 shows that for the $\mathbf{C}$ matrix

$$0 \leq \lambda_{min} \leq 1 \leq \lambda_{max} \leq \frac{1}{\alpha}. \tag{3.64}$$

Corollary 3.2. *The eigenvalues of the* $\mathbf{C}$ *matrix are real and non-negative.*

Proof. The $\mathbf{C}$ matrix is shown to be Hermitian in equation (3.13), consequently all its eigenvalues will be real. Lemma 3.4 has shown that the minimum eigenvalue is never negative. A matrix with non-negative eigenvalues is termed positive semidefinite, where the minimum eigenvalue is greater than zero then the matrix is positive definite. □

The derived bounds for the maximum and minimum eigenvalues of the correlation matrix $\mathbf{C}$ show that these values are expected to grow, or shrink, respectively, with the changes

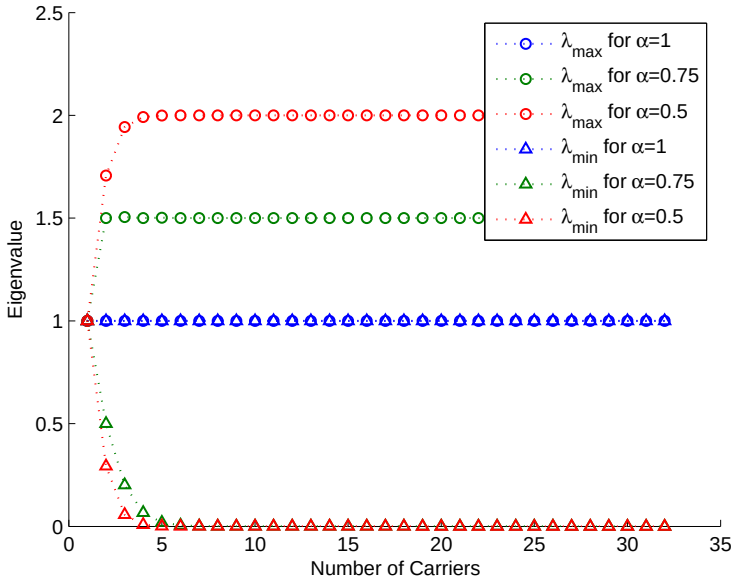

FIGURE 3.8: Extreme eigenvalues of the $\mathbf{C}$ matrix for $\alpha = 0.5, 0.75$ and 1 and $N = 1 - 32$.

in the system parameters. Numerical examples of extreme eigenvalues for different sets of N and α are provided here to highlight these changes. Fig. 3.8 depicts the maximum and minimum eigenvalues obtained by simulations. From Fig. 3.8 it is noted that the maximum eigenvalue increases with the decrease in the subcarriers spacing and/or their number until a quick saturation point after which it becomes dependent on α only. For $\alpha = 1$, the case of OFDM system, the system is perfectly conditioned as all eigenvalues are equal to unity. Furthermore, Fig.3.9 focuses on the decay of the minimum eigenvalue. From the figure it can be seen that the minimum eigenvalue shrinks with the increase in the number of subcarriers until a saturation point beyond which the value exhibits very slight changes. The actual value at the the saturation point may be dependent on the precision of the computation machine. Nevertheless, the figure shows that the saturation point occurs at different α and N pairs as listed in Table 3.3. The table shows that the ratio α/N for which the minimum eigenvalue reaches a saturation point is always the same, hence, suggesting that the minimum eigenvalue is affected by both α and N at the same time.

Furthermore, Fig. 3.10 displays all the eigenvalues for the $\mathbf{C}$ matrix for different values of α. It is noted from the figure that for a system of N carriers, αN of the eigenvalues will have values very close to one while the remaining eigenvalues can take very small

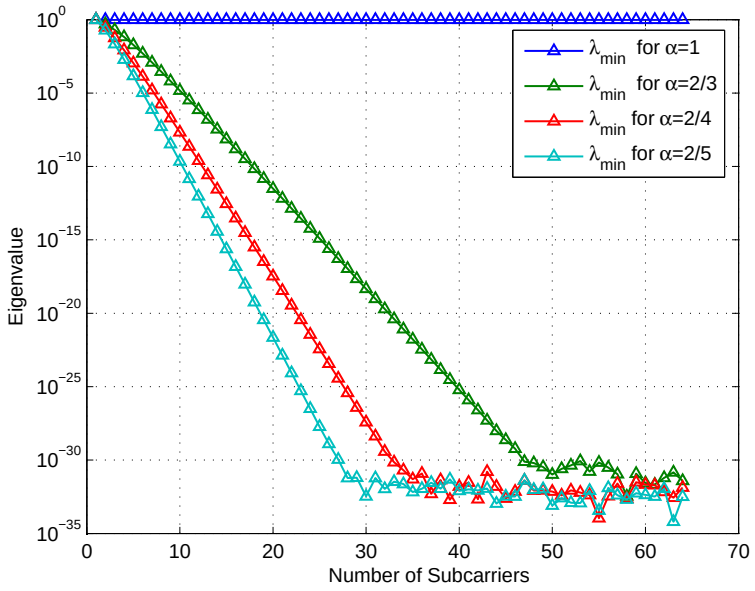

FIGURE 3.9: Minimum eigenvalues of the $\mathbf{C}$ matrix for $\alpha = 2/3, 2/4, 2/5$ and 1 and $N = 1 - 64$.

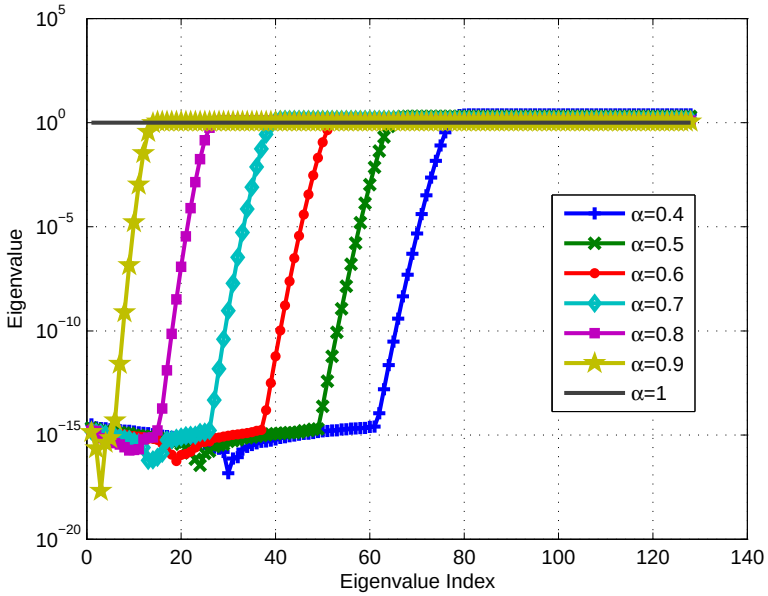

FIGURE 3.10: All the eigenvalues of the $\mathbf{C}$ matrix. The plots show the number of the eigenvalues that are less than 1 is approximately equal to αN .

TABLE 3.3: Parameters of saturation points of the minimum eigenvalue of matrix **C**.

$\lambda_{min_{sat}}$	α	N	α/N
6×10^{-32}	2/5	28	0.01428
5×10^{-32}	2/4	35	0.01428
8×10^{-31}	2/3	47	0.01418

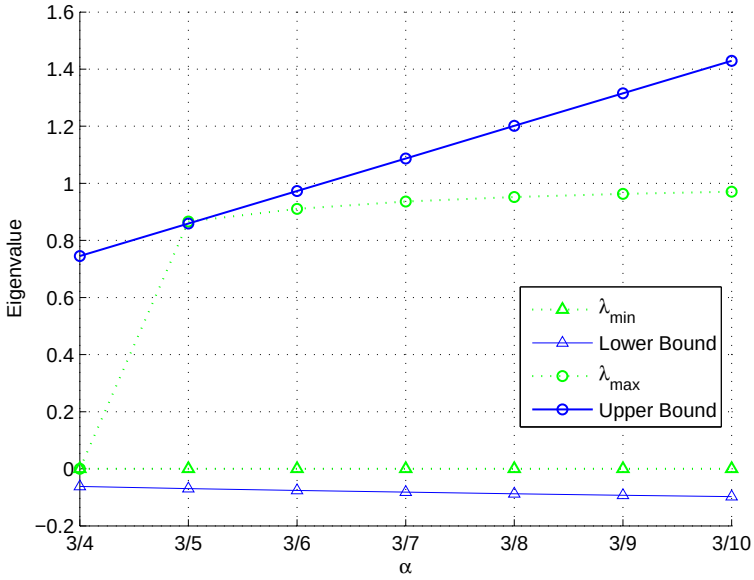

FIGURE 3.11: Upper and lower bounds of maximum and minimum eigenvalues of the **C** matrix for 16 subcarrier SEFDM system based on Lemma 3.3.

values depending on the value of α. Simulation investigations of the condition number of the **M** matrix, provided in [57], has shown that the singularvalues of **M** exhibit the same performance as the **C** matrix, which is an expected outcome as the two matrices are linked as explained in section 3.4.2.

Numerical results for the bounds derived in Lemmas 3.3 and 3.4 are obtained by simulations for different values of α and N . The choice of β decides the quality of the bounds. For the bounds in Lemma 3.3, simulations for $\beta = \alpha/cQ$ are conducted. For this specific value of β Fig. 3.11 shows plots of the bounds driven in equations (3.56) and (3.57) with respect to α for a 16 subcarrier SEFDM system. The upper bound on the maximum eigenvalue is loose, yet it shows the general trend. The lower bound on the minimum eigenvalue is loose and negative.

The derived bounds and subsequent numerical analysis have shown that the minimum

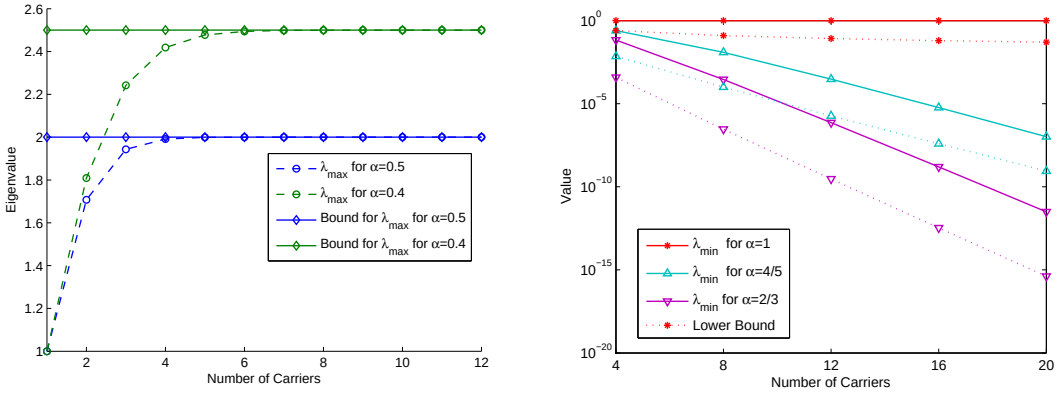

(A) Bound on the maximum eigenvalue of the **C** matrix based on equation (3.63).

(B) Bound on the minimum eigenvalue of the **C** matrix based on equation (3.65).

FIGURE 3.12: Bounds on maximum and minimum eigenvalue of **C** matrix

eigenvalue is non-negative but changes with the change in N and α. Based on this analysis and by further numerical examination of the minimum eigenvalue, an an empirical lower bound on it is defined as

$$\lambda_{min} \geq \frac{1}{N}\alpha^{4N}. \tag{3.65}$$

Fig. 3.12 displays the upper bound on the maximum eigenvalue in equation (3.60) and the lower bound on the minimum eigenvalue from equation (3.65). The bounds in Fig. 3.12 provide closer approximations to the behaviour of the extreme eigenvalues.

From equation (3.60) and equation 3.65 an upper bound on the condition number of **C** is derived as

$$cond\,(C) \leq \frac{1}{N}\alpha^{-4N+1}. \tag{3.66}$$

This bound is plotted in Fig. 3.13 with respect to α and number of subcarriers. The figure confirms the dramatic growth in the condition number which leads to the SEFDM system becoming singular to machine precision. The derived bounds and numerical investigations of the maximum and minimum eigenvalues and condition number indicate that the minimum eigenvalue significantly affects the conditioning of the system.

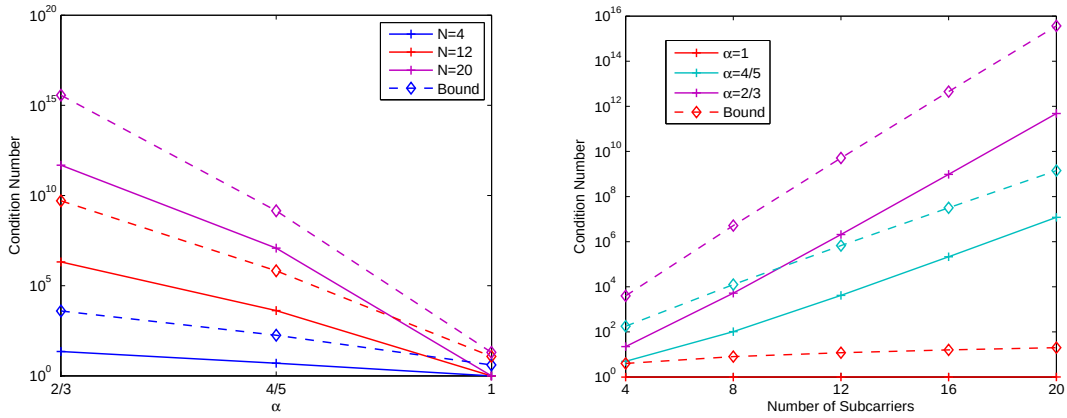

(A) Vs α. (B) Vs N.

FIGURE 3.13: Maximum bound on condition number of the $\mathbf{C}$ matrix.

3.6 Discussion and Conclusions

In this chapter the properties of the SEFDM system were investigated. The work started by establishing the discrete model for the system as the base for determining the properties of the system. Characteristics of the system were obtained from the structure of the subcarriers and linked to the bandwidth compression factor and the number of subcarriers.

The issue of the derivations of the intercarrier interference (ICI) was addressed. Closed form representations of the ICI in the system in the case of continuous and discrete system were derived. The ICI was shown to be dependent on the number of subcarriers and the bandwidth compression level. Furthermore, it has been identified that some of the subcarriers will be relatively orthogonal and that the ICI contributions from closer carriers in frequency is expected to be higher. These two findings form the base for the Selective Equalization (SelE) detector detailed in chapter 6 and the Partial Channel Estimator in chapter 8.

Moreover, the discrete model for the matched filter demodulated signal was derived and the system is expressed neatly in matrix format, where the characteristic matrices were linked to the correlation receiver in the original SEFDM proposal. Consequently, a unified linear regression model for matched filtering or correlation demodulation was built.

This representation of the system accomplished the objective of identifying the mathematical entities that describe the SEFDM system which then constituted the subject of the mathematical analysis of the conditioning of the system.

The existence and practicality of a solution of the SEFDM system was assessed by examining its numerical stability in the form of investigating the singularity and conditioning of the system. Investigations have shown that the SEFDM system can be non-singular, thus has a solution. Nevertheless, it can become severely ill conditioned that it appears singular to machine precision which hinders the possibility to retrieve that solution.

Derivations of bounds on the condition number and it constituents confirmed that the conditioning of the system deteriorates with the decrease of the subcarriers spacing or with the increase in the number of subcarriers in the system. The deterioration in the conditioning of the system leads to the degradation of the system performance due to the fact that ill conditioning can blur the uniqueness of a solution as some values become close to being linearly dependent and thus cannot be separated unless other conditions are imposed on the solution. In addition, the conditioning of the system affects its implementation due to the usually limited numerical range of system components. Therefore, the bounds derived on the condition number can be used to determine suitable pairs of α and N. In addition, the information about the condition number may be utilized for complexity analysis as it is directly related to the performance of the detection algorithms. Armed with the knowledge of the signals mathematical properties, the following three chapters are concerned with the derivation of new transmitter architectures chapter 4 and new receiver and detector architectures chapters 5 and 6, respectively. Such architectures satisfy the criteria described in this chapter and allow for easy to implement solutions of SEFDM systems.

Chapter 4

SEFDM Transmitter Design

4.1 Introduction

The non-orthogonal subcarriers in the SEFDM system mean that conventional OFDM transmission techniques cannot automatically be applied for SEFDM. Analogue generation of the SEFDM signal is realized by modulating the incoming input stream through a bank of modulators running at the different subcarriers frequencies. With the increase in the number of subcarriers it becomes exceptionally complex to realize this bank of modulators. In addition, the system will be susceptible to higher frequency offsets and timing errors, as the number of oscillators increases. Thus, motivating the search for systems employing efficient digital generation techniques such as the Fourier Transform.

The use of Fourier Transform communications dates back to 1969 when Salz and Weinstein published their paper on "Fourier Transform Communications" [9] proposing a communication system transmitting the IDFT of a sequence. At the receiver, the original sequence is retrieved using the DFT. The system described in [9] promised robustness against channel linear impairments. Soon later the frequency division multiplexed signal was linked to the DFT in [10], where they showed that the FDM systems are implementable using the IDFT-DFT pairs provided that the subcarriers are orthogonal, a system that is now widely known as OFDM.

Non-orthogonal multicarrier systems violate the obvious translation of the subcarriers to the frequencies provided by the IDFT. Nevertheless, systems that are based on time

compression of OFDM signals have maintained the use of the IDFT. In particular, Fast OFDM (FOFDM) systems is based on the symmetry property of the IDFT for real signals. The FOFDM signal is initially generated as an OFDM signal where only half the samples are transmitted to provide 50% bandwidth savings, whereas the discarded half is equal to the conjugate of the transmitted one [19]. Therefore, an FOFDM transmitter is basically a conventional OFDM transmitter except that the transmitted time domain samples are reduced by half, thus the FOFDM symbols are sent at rate twice of that of an equivalent OFDM system.

In addition, the High Compaction Multi Carrier Modulation (HC-MCM) signal [22], introduced in section 2.8, follows the same principle as FOFDM. The difference here is that the length of the HC-MCM symbols in time is an arbitrary fraction of an equivalent OFDM system (not necessarily 50%). Reducing the symbol transmission time is effectively equivalent to increasing the transmission rate per individual subcarrier. Therefore, the HC-MCM system employs a conventional OFDM transmitter, with the spectral efficiency increased by reducing the transmission time.

Moreover, the Overlapped Frequency Division Multiplexing (Ov-FDM) system examined the issue of signal design using IDFTs. The approach in [23] is to apply frequency domain coding prior to using the IDFT for modulation. However, it was not assessed whether the effort exerted in the coding process will justify the use of the IDFT. The author of this thesis believes the coding complexity of [23] is close to that of generating a signal with complex multipliers as the coding operation requires the same number of multiplications and additions needed to construct the signal by direct multiplications with the carriers matrix $\mathbf{\Phi}$.

In [36] the use of Fractional Fourier Transform (FrFT) for SEFDM signal generation was proposed. The m point FrFT is based on fractional roots of unity $e^{j2\pi\alpha/m}$, unlike the IDFT which is based on the integral roots of unity $e^{j2\pi/m}$ for an m point DFT [58]. The FrFT can be evaluated with algorithms using IDFTs by first expressing the FrFT as a convolution in the same manner proposed in the Bluestein algorithm for the FFT evaluation [59]. This led to the proposal of an algorithm for the evaluation of the FrFT using three IDFTs operations and some pre-processing in [58]. Such an algorithm may be used in the FrFT implementation of the SEFDM signal. It is necessary to emphasize that the described transform in [58] is widely known in the literature as the

chirp z-transform [64], and that the term Fractional Fourier Transform is originally used to describe a generalized Fourier transform using orthogonal fractionally spaced bases [121].

The M-ary Amplitude Shift Keying (MASK) OFDM proposed the use of the Discrete Cosine Transform (DCT) for generating its signals[1] [20]. Basically, the DCT uses cosine functions with different frequencies to express a series of data points [122] and can be evaluated with the Fast Cosine Transform (FCT) algorithms [123].

As discussed, there have been several attempts to generate non-orthogonal multicarrier signals with similar ease as OFDM. However, these attempts lack the foundation and are mainly based on observations, thus are restricted to their respective systems. Therefore, in this chapter a framework to generate SEFDM signals based on the IDFT is drawn. The framework facilitates the IDFT design of any FDM signal with arbitrary subcarriers spacing. The proposed framework eliminates the need for a bank of analogue modulators to generate the SEFDM signal, therefore allowing for the digital implementation of the SEFDM transmitter. The framework is interpreted into three different SEFDM transmitter architectures, each providing different implementation complexity. The proposed designs employ similar building blocks as OFDM based systems, hence, would facilitate an easy migration and/or coexistence with OFDM on the transmitter side. Only minor changes are required in the input symbols stream to facilitate the IDFT design of any signal with an arbitrary subcarriers spacing such as SEFDM and MASK OFDM system proposed in [20].

4.2 The IDFT Design of SEFDM Signals

Conventionally the SEFDM signal is generated with a bank of modulators running at the subcarrier frequencies as shown in Fig. 4.1. The input symbols modulate the non-orthogonal subcarriers generated by the bank of independent modulators. This method of generation can severely hinder the applicability of the system with the focus of current designs on reducing size and complexity of equipment. Furthermore, the system will be more susceptible to frequency errors specially when the number of subcarriers increases.

[1] Although the authors in [20] stated wrongly that it is impossible to implement the system using the IDFT, the transmitters designed here are automatically applicable to the MASK OFDM system.

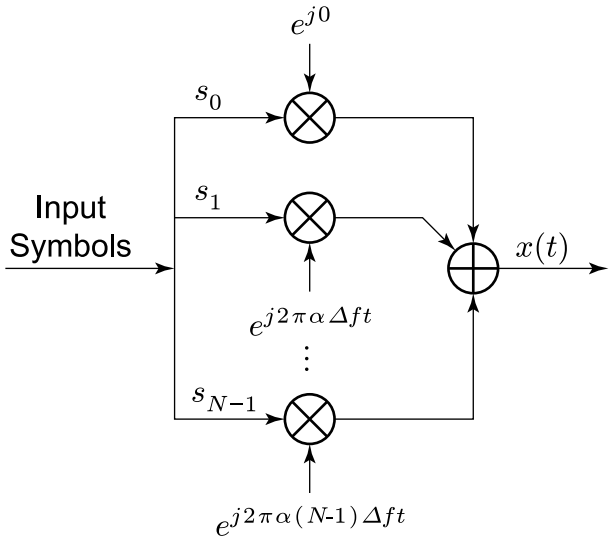

FIGURE 4.1: A conventional SEFDM transmitter.

In contrast, OFDM signals are usually generated using the IDFT. For an N subcarrier OFDM system, the input symbols are fed into an N point IDFT and the outputs are fed to a Digital to Analogue Converter (D/A) to generate the time domain signal [10, 124]. Basically, the orthogonal structure of OFDM facilitates the use of the IDFT for its generation. In contrast, SEFDM lacks orthogonality, therefore is not readily implementable with the standard IDFT operation. This section explores the possible relationship between the SEFDM and the IDFT to lay the foundation for the IDFT implementation of the SEFDM system.

The discrete SEFDM signal model presented in section 3.2 shows how the signal can be generated from frequency and time samples of the subcarriers and the input symbols. Equation (3.2), derived previously in section 3.2 and reproduced below, presented the representation of the discrete SEFDM as

$$X[k] = \frac{1}{\sqrt{Q}} \sum_{n=0}^{N-1} s_n e^{\frac{j2\pi nk\alpha}{Q}}. \tag{3.2}$$

where $X[k]$ is the k^{th} time sample of the SEFDM symbol in equation (3.1), $k = 0, 1, \cdots, Q-1$, $Q = \rho N$, ρ is an oversampling factor and the factor $1/\sqrt{Q}$ is a normalization constant. The aim of this section is to show how the IDFT can be used to generate non-orthogonal signals such as the SEFDM signal, where the IDFT of a

sequence $Y = [y_0, y_1, \cdots, y_{N-1}]^T$, denoted with the vector $\underline{Y}$, is given by [125]

$$\underline{Y}[k] = \frac{1}{\sqrt{N}} \sum_{n=0}^{N-1} y_n e^{\frac{j2\pi nk}{N}}. \tag{4.1}$$

Theorem 4.1. *Any multicarrier signal as in equation* (3.2) *can be expressed as* $X = \left[x_i^{'}\right]_0^{Q-1}$ *where:*

$$X^{'} = \zeta \mathbf{\Omega} S, \tag{4.2}$$

$\mathbf{\Omega}$ *is an* $L \times L$ *IDFT matrix with the entries* $\omega_{n,k} = \frac{1}{\sqrt{L}} e^{\frac{j2\pi nk}{L}}$ *for* $0 \leq n, k < L$, $L > Q$, ζ *a normalization correction constant, and the* $N \times 1$ *vector* $S^{'}$,L *and* ζ *defined as:*

case 1:

$$S^{'} = \begin{cases} S_i & 0 \leq i < N \\ 0 & N \leq i < L \end{cases}, \tag{4.3}$$

when $\zeta = \sqrt{1/\alpha}$,$L = Q/\alpha$ *for* $Q/\alpha \in \mathbb{N}$, *and*

case 2:

$$S_i^{'} = \begin{cases} S_{i/b} & i \bmod b = 0 \\ 0 & otherwise, \end{cases} \tag{4.4}$$

when $L = cQ$,$\zeta = \sqrt{c}$ *for* $\alpha = b/c$, $b, c \in \mathbb{N}$ *and* $b < c$.

Proof. The IDFT matrix $\mathbf{\Omega}$ is expressed as

$$\Omega = \frac{1}{\sqrt{L}} \begin{bmatrix} 1 & 1 & \cdots & 1 \\ 1 & \omega & \cdots & \omega^{L-1} \\ \vdots & & \ddots & \\ 1 & \omega^{L-1} & & \omega^{(L-1)^2} \end{bmatrix}. \tag{4.5}$$

$\mathbf{\Omega}$ is a Vandermonde matrix constructed from points on the unit circle, thus can be equivalently expressed as

$$\Omega = \frac{1}{\sqrt{L}} V \left(1, e^{\frac{j2\pi}{L}}, e^{\frac{j4\pi}{L}}, \cdots, e^{\frac{j2\pi(L-1)}{L}}\right). \tag{4.6}$$

Now define the $L \times L$ matrix $\Phi^{'}$ such that $\phi^{'}_{ij} = \phi_{ij}$ for $0 \leq i < Q, 0 \leq j < N$, that is

$$\phi'_{n,k} = \frac{1}{\sqrt{Q}} e^{(j2\pi\alpha nk/Q)} \tag{4.7}$$

for $0 \leq n, k < L$. Clearly, $\Phi^{'}$ is a Vandermonde matrix, hence, can be expressed as

$$\Phi^{'} = \frac{1}{\sqrt{Q}} V \left(1, e^{\frac{j2\pi\alpha}{Q}}, e^{\frac{j4\pi\alpha}{Q}}, \cdots, e^{\frac{j2\pi(L-1)\alpha}{Q}}\right). \tag{4.8}$$

The proof now focuses on deriving the conditions such that $\left[\phi'_{1j}\right]_{j=0}^{L-1} = [\omega_{1j}]_{j=0}^{L-1}$, and thus guarantee that $\Phi' = \mathbf{\Omega}$, due to the Vandermonde nature. Noting that $[\omega_{1j}]_{j=0}^{L-1}$ are uniformly spread around the unit circle. As the dimensions of $\Phi^{'}$ and $\mathbf{\Omega}$ are the same and by definition the first elements are equal then to guarantee the equality of $\Phi^{'}$ to Ω it remains to find the value of L with regards to α and Q so that $\left[\phi'_{ij}\right]_{i,j=0}^{L-1}$ are uniformly spread around the unit circle.

The work in [118], proved that the elements of the generating row of a Vandermonde matrix constructed from points on the unit circle and expressed as$\left\{e^{\frac{j2\pi\alpha n}{L}}\right\}_{n=0}^{L-1}$ are spread uniformly around the unit circle *if and only if* $\{\alpha n\}_0^{L-1}$ mod L is a complete residue system[2]. Hence, this rule will be applied for the parameters defined here to prove the theorem, that is to find L that makes $\{\alpha n\}_0^{L-1}$ mod Q a complete residue system.

For case 1: define that $Q/\alpha = \beta$, where $\beta \in \mathbb{N}$, hence$\{\alpha n\}_0^{L-1}$ mod Q can be rewritten as $\{\alpha n\}_0^{L-1}$ mod $\alpha\beta$, which is equivalent to $\{n\}_0^{L-1}$ mod β. The system $\{\alpha n\}_0^{L-1}$ mod Q in this case will be a complete residue system *if and only if* $L{=}\beta$, hence $L = Q/\alpha$. Substituting for L and N in equation (4.7) yields

$$\phi'_{n,k} = \frac{1}{\sqrt{Q}} e^{j2\pi nk/L} = \zeta\omega_{n,k}, \tag{4.9}$$

for $0 \leq n, k < L$ where $\zeta = \frac{1}{\sqrt{\alpha}}$. Equation (4.9) shows that for $L = N/\alpha$ and $\zeta = \sqrt{1/\alpha}$, $\Phi^{'} = \xi\Omega$. Now define the $L \times 1$ vector S' such that

$$S' = \begin{bmatrix} S \\ \check{S} \end{bmatrix}. \tag{4.10}$$

[2]A set of numbers $(a_0, a_1, \cdots, a_{q-1})$ mod q is a complete residue system if $a_i = i \,(\mathrm{mod}\, q)$, for $i = 1, 2, \cdots, m-1$ [126].

Hence

$$X' = \Phi^{'} S' \tag{4.11}$$

$$= \xi \Omega S' \tag{4.12}$$

Setting $\check{S} = 0$ leads to

$$X' = \xi \Omega S' = \begin{bmatrix} \Phi \\ \Phi'' \end{bmatrix} S, \tag{4.13}$$

where $\phi_{ij}^{''} = \phi_{ij}^{'}$ for $Q \leq i < L, 0 \leq j < N$. It is then straight forward that

$$\Phi S = \left[x_i'\right]_0^{Q-1}. \tag{4.14}$$

For case 2, $\alpha = b/c$: $X'[k]$ from equation (4.2) can be expressed as

$$\begin{aligned} X'[k] &= \frac{\zeta}{\sqrt{L}} \sum_{0}^{L-1} S_l' e^{2\pi jlk/L}, \\ &= \frac{\zeta}{\sqrt{L}} \sum_{l \bmod b=0} S_l' e^{2\pi jlk/L} + \frac{\zeta}{\sqrt{L}} \sum_{l \bmod b \neq 0} S_l' e^{2\pi jlk/L}. \end{aligned} \tag{4.15}$$

The second term equals zero by the definition of $S^{'}$ in equation (4.4). The Substitution by $l = bl^{'}$, $L = cQ$ and $\zeta = \sqrt{c}$ yields

$$\begin{aligned} X'[k] &= \frac{1}{\sqrt{Q}} \sum_{l'=0}^{Q-1} S_{bl'}^{'} e^{\frac{2\pi jbl^{'}k}{cQ}} \\ &= \frac{1}{\sqrt{Q}} \sum_{l'=0}^{Q-1} S_{l'} e^{\frac{2\pi jbl^{'}k}{cQ}} \\ &= X[k] \end{aligned} \tag{4.16}$$

the last line is obtained as by definition $S_{bl'}^{'} = S_{l'}$. □

Theorem 4.1 shows that there are ways to express the SEFDM signal with an IDFT operation with simple manipulations of the input symbol vectors. These manipulations are merely in the form of zero insertions at the end of the vector, in a manner similar to zero padding and/or between the symbols. The time samples of the SEFDM signal in equation (3.2) are equivalent to Q consecutive outputs of an IDFT operation on an

elongated input symbol vector composed of the original input symbols and zeros. The change in length ensures the alignment of the IDFT frequency samples and the SEFDM subcarriers while the zero inputs suppress the unwanted frequencies.

4.3 SEFDM IDFT Based Transmitters

Theorem 4.1 shows that it is possible to express the SEFDM signal using IDFT operations. This section details the design of a set of transmitter arrangements based on the derived IDFT representations of the SEFDM signals.

4.3.1 Proportional Inputs IDFT Transmitter

Theorem 4.1 shows that the SEFDM signal can be expressed with the first Q outputs of the IDFT of a modified input symbols vector. Case 1 of the theorem specifies that the term Q/α is integer and proceeds to insert zeros at the tail of the input symbols vector. Fig. 4.2 illustrates this concept by plotting the frequency samples of the SEFDM system and those of a corresponding IDFT. The unit circle plots emphasize that the SEFDM frequency samples span a fraction of the IDFT frequency samples which covers the whole circle. Thus, the reduction in bandwidth offered by the SEFDM system can be achieved by suppressing the unwanted frequency tones in an equivalent IDFT based OFDM system. This can be simply achieved by setting the corresponding inputs to zero. The silenced tones are those with frequencies outside the SEFDM bandwidth. That is, for an N subcarrier SEFDM system with bandwidth compression factor α, it is possible to modify a Q/α long IDFT operation by appending zeros to the last $\left((1-\alpha)/\alpha\right)Q$ inputs to the IDFT, where $Q = \rho N$. Then, Q consecutive outputs corresponding to Q time samples are selected to represent the SEFDM signal. The number of time samples taken is crucial to maintain the required spectral efficiency. A condition for this arrangement is that Q has to be divisible by b for $\alpha = b/c$ to have the exact bandwidth compression, although it is possible to round the Q/α to the nearest integer and accept a modified version of α in the system.

Fig. 4.3 depicts a transmitter for the case of Q/α an integer. The change in the size of the input symbols vector ensures that the frequency samples of the SEFDM system

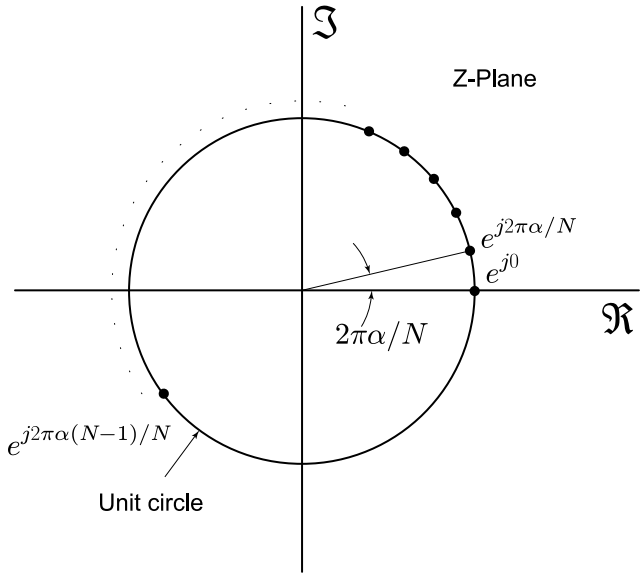

(A) Frequency samples of an N subcarrier SEFDM system on the unit circle.

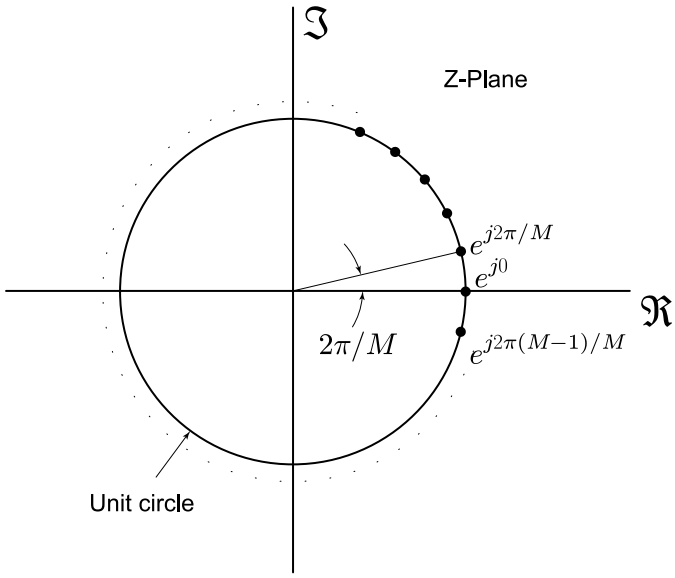

(B) Frequency samples of an M point IDFT on the unit circle.

FIGURE 4.2: Frequency samples of an N subcarrier SEFDM system and an M point IDFT on the unit circle.

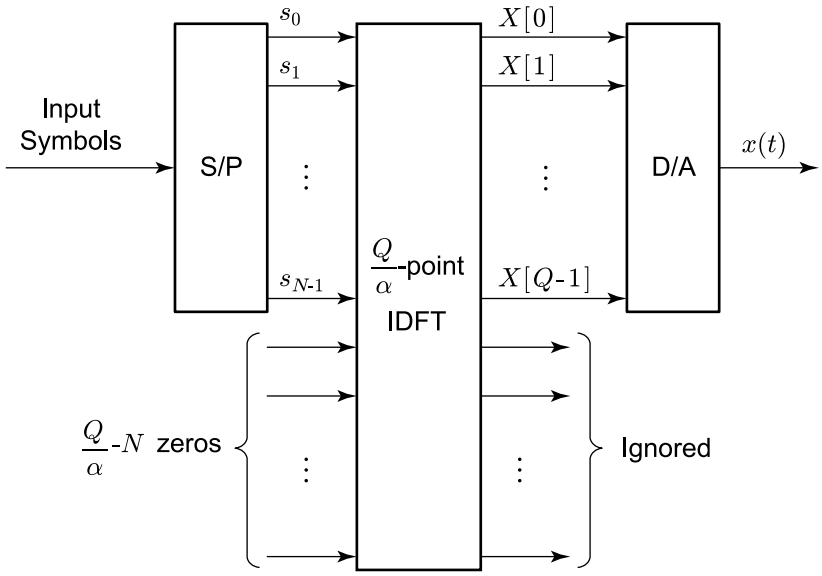

FIGURE 4.3: The IDFT implementation for SEFDM proportional inputs transmitter. Zeros are inserted after the input symbols to suppress unwanted frequency tones.

coincides only with the frequency samples of the IDFT that are within the bandwidth of the SEFDM signal. The figure shows how the desired bandwidth savings is maintained by suppressing the unwanted frequency tones by setting the corresponding inputs to zero. Then, Q consecutive IDFT outputs are fed to the D/A to generate the analogue signal. If more than Q outputs are considered the effective spectral efficiency will be reduced as the Q outputs correspond to a symbol duration of T and any increases in the number of samples beyond that is effectively an increase in the symbol duration and hence a larger α.

The transmitter in Fig. 4.3 appears similar to the zero padding in IDFT evaluation when a higher frequency resolution is needed. The distinguishing feature is that only part of the outputs of the IDFT is considered in order to maintain the characteristic relationship for SEFDM signals; $\Delta f = \alpha/T$. An advantage of this design is that the zeros could be positioned before, after or around the input symbols so as to determine the location of the SEFDM signal in the spectrum.

4.3.2 The IDFT Transmitter for Rational α

The fraction α is a key parameter in the design of SEFDM systems as it defines the amount of bandwidth compression offered by the system. Without loss of practicality

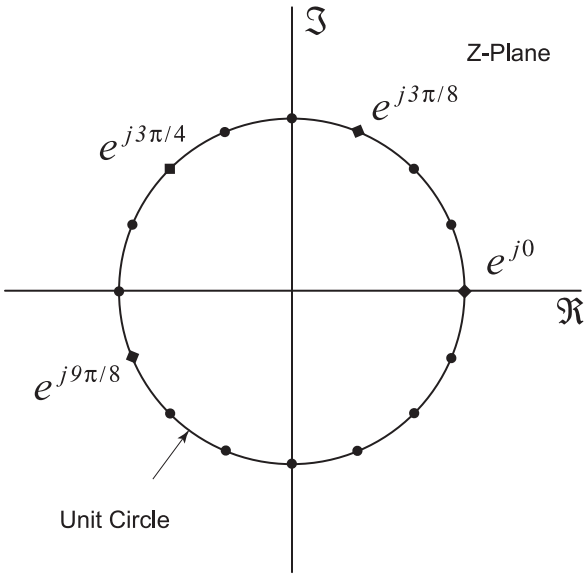

FIGURE 4.4: Frequency samples of a 16 point IDFT (diamonds and circles) and a 4 carrier SEFDM system for $\alpha = 3/4$ (diamonds only) on the unit circle.

it may be assumed that α is a rational number, recalling that there are series that can generate best rational approximations. For the case α being a rational number, it is shown in case 2 in Theorem 4.1 that the SEFDM signal can be expressed using an IDFT operation on the input symbols. Fig. 4.4 illustrates an example SEFDM system with 4 subcarriers and $\alpha = \frac{3}{4}$ and a 16 point IDFT plotted on the unit circle. The figure shows the overlapping of the frequency samples of the SEFDM system with the samples of the IDFT. Again, setting the inputs corresponding to the unwanted IDFT frequency samples to zero will ensure obtaining the SEFDM spectrum.

Fig. 4.5 depicts the block diagram of an SEFDM transmitter based on the described criteria. The equivalence of the IDFT of a sequence of data points to the sampled SEFDM signal is achieved by ensuring that all frequency tones that are outside the SEFDM bandwidth and in between the SEFDM subcarriers are removed from the output of the IDFT by setting the corresponding input symbols to zero. At the output of the IDFT Q samples are carried forward and the rest are discarded.

4.3.3 SEFDM as a Sum of Multiple IDFT

Manipulation of the SEFDM signal representation in equation (3.2) can lead to another new design that uses multiple shorter IDFT operations. Case 2 in theorem 4.1 shows

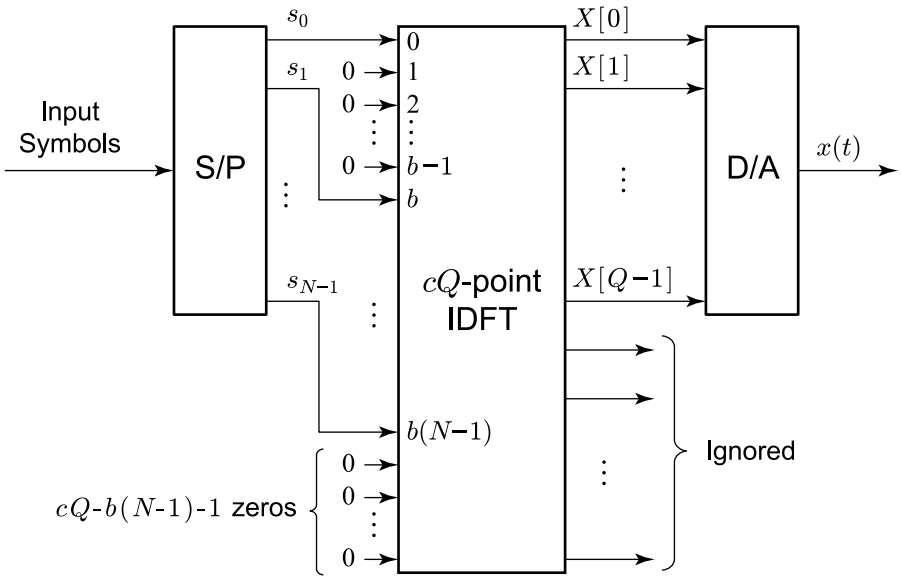

FIGURE 4.5: The IDFT implementation of SEFDM transmitter for α rational number. Zeros are inserted between input symbols to suppress unwanted frequency tones.

that the SEFDM signal for α a rational number and $S^{'}$ defined as in equation (4.4), can be represented as

$$X\left[k\right]=\frac{1}{\sqrt{Q}}\sum_{m=0}^{Q-1}S_{m}^{'}e^{2\pi jmk/Q}. \tag{4.17}$$

For such system settings, $X\left[k\right]$ in equation (4.17) can be rearranged to:

$$X\left[k\right]=\frac{1}{\sqrt{Q}}\sum_{l=0}^{Q-1}\sum_{i=0}^{c-1}s_{i+lc}e^{\frac{j2\pi(i+lc)k}{cQ}}, \tag{4.18}$$

by setting $m=i+lc$, and can be further simplified to:

$$X\left[k\right]=\frac{1}{\sqrt{Q}}\sum_{i=0}^{c-1}e^{\frac{j2\pi ik}{cN}}\sum_{l=0}^{Q-1}s_{i+lc}e^{\frac{j2\pi lk}{Q}}. \tag{4.19}$$

The last term in equation (4.19) is the Q long IDFT of the sequence $s_{(i+lc)}$. This could be implemented by arranging the input as a $c\times Q$ matrix in column major order, performing a Q point IDFT on each row and multiplying the result by complex exponentials. In matrix format equation (4.19) can be represented as

$$X=\mathrm{diag}\left[\mathbf{\Omega S}\nabla\right] \tag{4.20}$$

where diag $[\cdot]$ denotes the diagonal elements of the argument matrix, $\mathbf{\Omega}$ now represents the Q point IDFT matrix given as

$$\Omega = \frac{1}{\sqrt{Q}} \begin{bmatrix} 1 & 1 & \cdots & 1 \\ 1 & \omega & \cdots & \omega^{Q-1} \\ \vdots & & \ddots & \\ 1 & \omega^{Q-1} & & \omega^{(Q-1)^2} \end{bmatrix} \tag{4.21}$$

$\mathbf{S}$ and ∇ are given as

$$\mathbf{S} = \begin{bmatrix} s_0^{'} & s_1^{'} & \cdots & s_{c-1}^{'} \\ s_c^{'} & s_{c+1}^{'} & & s_{2c-1}^{'} \\ \vdots & & \ddots & \vdots \\ s_{cQ-1-c}^{'} & \cdots & & s_{cQ-1}^{'} \end{bmatrix} \tag{4.22}$$

and

$$\nabla = \begin{bmatrix} 1 & 1 & \cdots & 1 \\ 1 & \omega^{\frac{1}{c}} & \cdots & \omega^{\frac{Q-1}{c}} \\ \vdots & & \ddots & \\ 1 & \omega^{\frac{Q-1}{c}} & & \omega^{\frac{(Q-1)^2}{c}} \end{bmatrix}. \tag{4.23}$$

Fig. 4.6 shows a transmitter structure using multiple shorter IDFTs when compared to the designs using one larger IDFT as in Fig. 4.3 and 4.5. In the post processing block the k^{th} outputs of the c IDFT stages are multiplied each by the corresponding complex exponential of the k^{th} column of the matrix ∇ to produce $X[k]$. The main advantage of this design is the use of shorter IDFT operations. In addition, the complexity can be reduced by generating the complex exponentials $\exp\left(\frac{j2\pi ik}{cQ}\right)$ for $i = 0, \cdots, c-1$ and $k = 0, \cdots, Q$ beforehand by applying an IDFT (or more efficiently an IFFT) operation of length cQ points initialized with $\{1, 0, 0, \cdots, 0\}$ for c circular shifts. This scheme could be especially useful for systems with large numbers of subcarriers as it becomes less feasible to increase the length of the IDFT to generate the signal as in the single module designs in sections 4.3.1 and 4.3.2. Equation (4.18) shows that SEFDM could be effectively seen as a combination of multiple OFDM systems translated in frequency so as to reduce the spacing of the subcarriers.

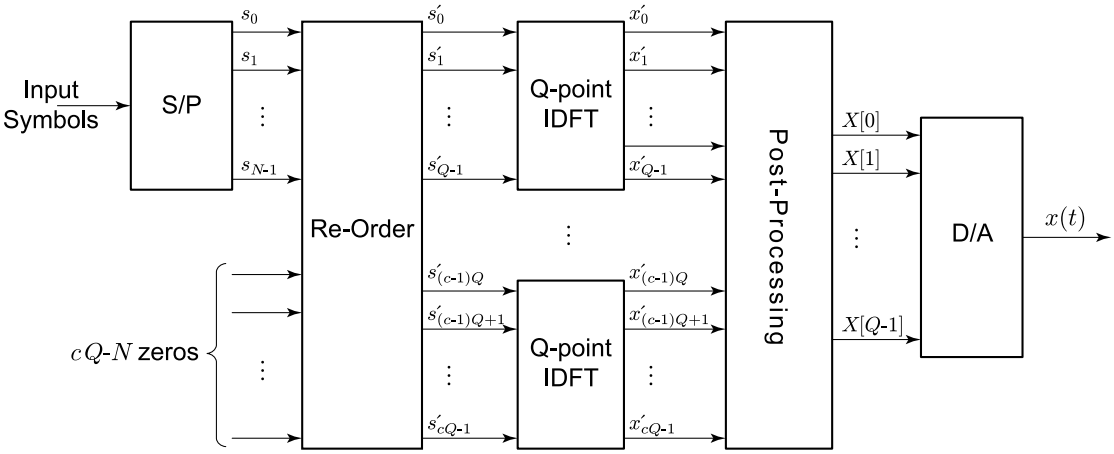

FIGURE 4.6: Multiple IDFTs implementation of SEFDM transmitter.

4.4 Performance Analysis

Sections 4.3.1, 4.3.2 and 4.3.3 presented different SEFDM transmitters based on the IDFT. This section evaluates the performance of the systems in terms of the generated signal and complexity, noting that the IDFT can be efficiently generated with the IFFT algorithm.

To verify numerically the designs, SEFDM transmitters were modelled using MATLAB. The IDFT based designs are benchmarked against the signal generated by direct multiplications of the subcarriers samples and the input symbols vector. Fig. 4.7 shows the time samples of a randomly chosen SEFDM symbol generated by the proportional inputs design and generated using simulated analogue system. The figure shows that the time samples of both systems are equal. In addition, Fig. 4.8 shows the time samples of an SEFDM symbol generated with each of the three transmitters. The figure shows that the real and imaginary parts of the signal obtained from the three transmitters are equal.

The spectrum of the generated signal with the proportional inputs design is displayed in Fig. 4.9. The figure shows that the transmitter generated the required bandwidth reduction and the result includes the other two transmitter designs as all the proposed systems generate the same time signals. When $\alpha = 1$, the proposed transmitter generated an OFDM spectrum. There are no restrictions in terms of the sampling rate which can be achieved by the scaling of the IDFT length and number of outputs according to the desired oversampling factor. In addition, Fig. 4.10 illustrates how the positioning

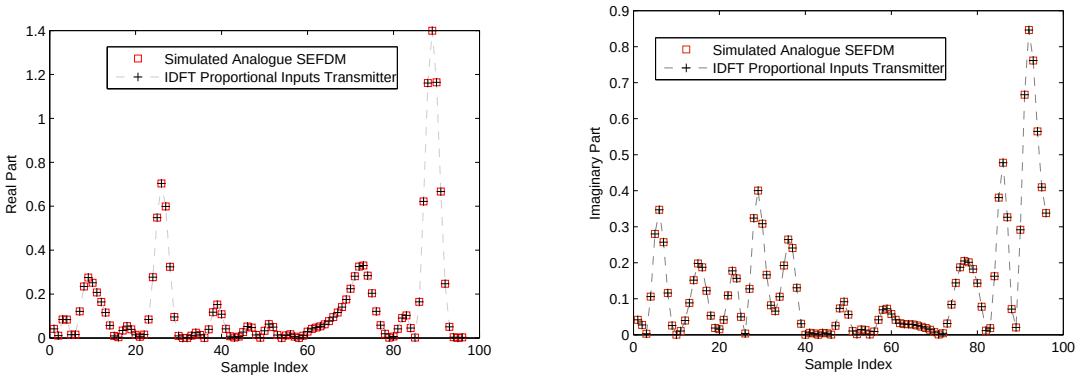

(A) Real part of time samples. (B) Imaginary part of time samples.

FIGURE 4.7: Real and imaginary parts of the time samples of one symbol of a 16 subcarrier SEFDM for $\alpha = 0.8$, generated using IDFTs as in section 4.3.1 and simulated analogue system.

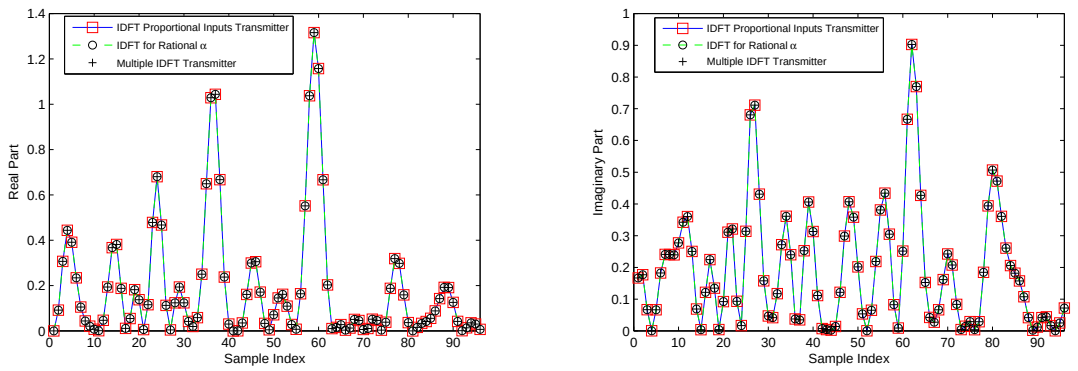

(A) Real part of time samples. (B) Imaginary part of time samples.

FIGURE 4.8: Real and imaginary parts of the time samples of one symbol of a 16 subcarrier SEFDM for $\alpha = 0.8$, generated using the three IDFT based transmitters.

of the inserted zeros in the proportional inputs transmitter can be used to translate the signal spectrum in frequency.

Reception of the signals generated with any of the three transmitters could follow any method used to receive the original signal described in [35]. Nevertheless, an end to end SEFDM system was simulated in AWGN channel as in [21]. Detection is realized by projecting the signal onto the conjugate carriers realized with the DFT blocks as described in section 5.3 of the next chapter followed by an ML detector. Fig. 4.11 shows numerical results for the BER of the digitally generated SEFDM signal. The digital signal exhibited the same BER as the analogue one. From BER results it is confirmed that the new way of generating the SEFDM signal exhibited the same BER performance as

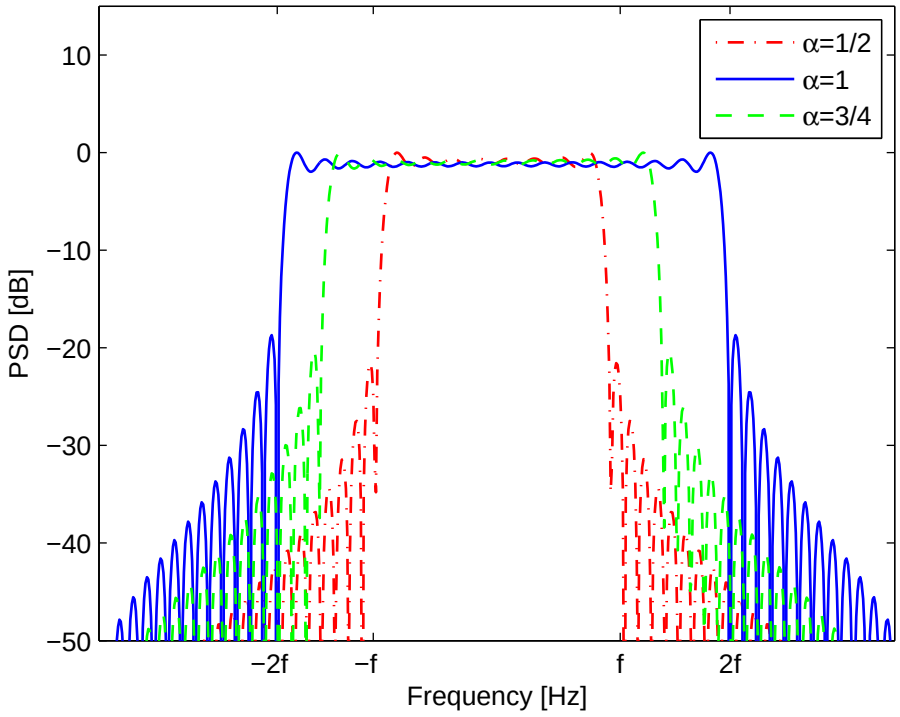

FIGURE 4.9: IDFT SEFDM spectrum for 32 subcarrier SEFDM for $\alpha = 1/2$, $3/4$ and 1.

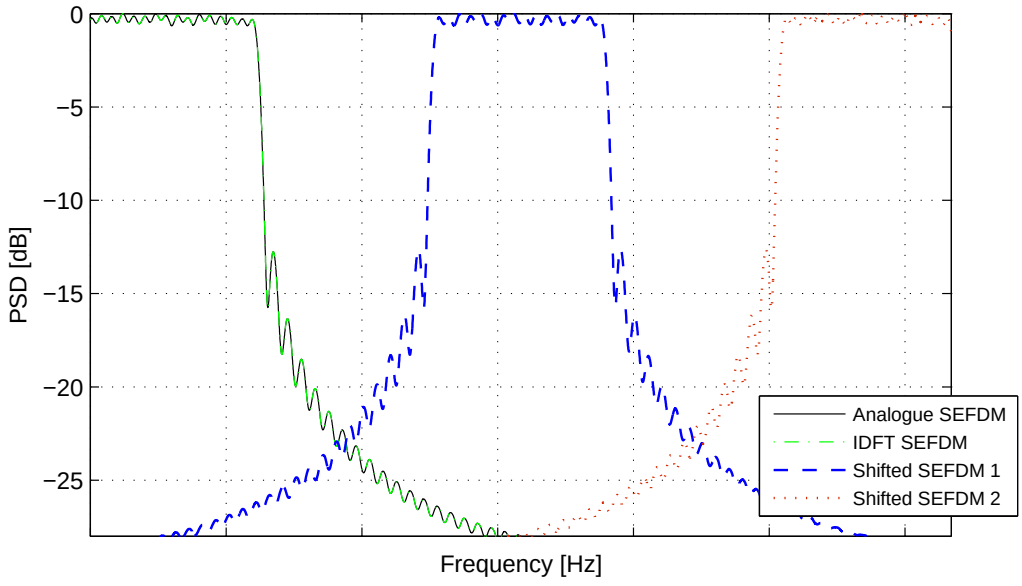

FIGURE 4.10: Shifting the IDFT based SEFDM spectrum for 16 subcarrier system for $\alpha = 0.8$.

the analogue method, thereby verifying the correctness of the new approaches described in this chapter.

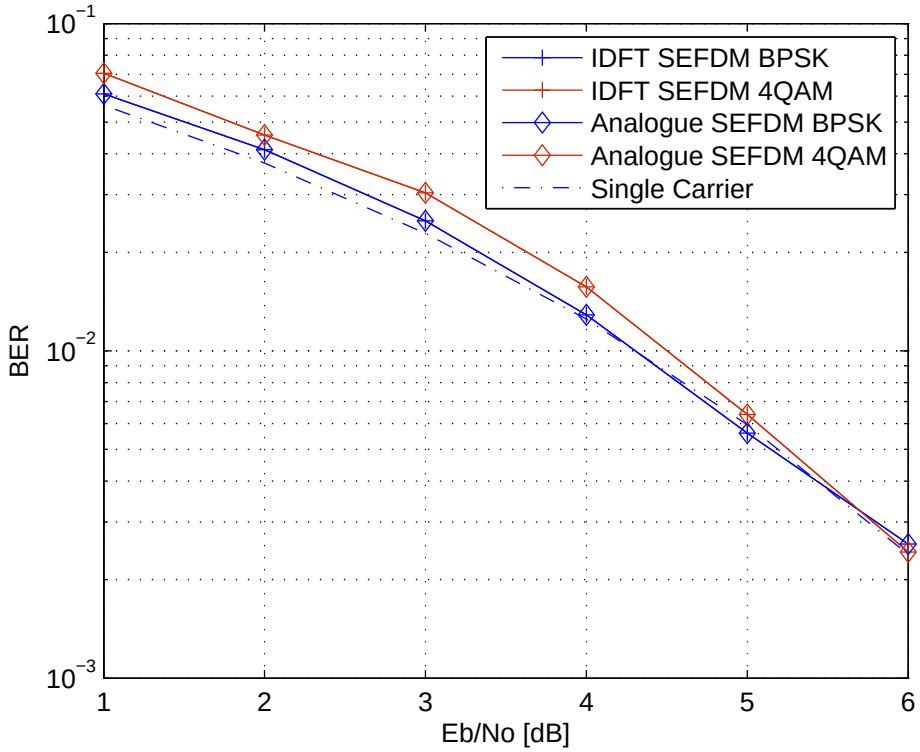

FIGURE 4.11: BER performance of an IDFT based SEFDM system with 8 subcarriers, $\alpha = 0.8$ and BPSK and 4QAM input symbols detected with ML.

4.4.1 Design Comparisons

The transmitters described in sections 4.3.1, 4.3.2 and 4.3.3 provide the means to generate an SEFDM signal. The main differences between the proposed designs are in the size and number of IDFT modules in the transmitter. The design in section 4.3.1 uses a single IDFT module of size Q/α, hence, requires that Q/α is an integer number. The design proposed in section 4.3.2 uses a single IDFT module that is $c \times Q$ long and it places a constraint on α to be a rational number. The transmitter designed in section 4.3.2 interleaves zeros with the message symbols in order to maintain the frequency profile of the SEFDM signal. Hence, for large Q and c (in the denominator of α) the transmitter will require an IDFT stage of length cQ. Both designs require one IDFT module but with different lengths. There are some reasons to favour one over the other such as the shorter length of the IDFT module of the proportional inputs transmitter is an obvious advantage over the one with rational α. However, for some system practical restrictions (such as an IFFT length being a power of 2) it may not be possible to satisfy the requirement of Q/α being an integer number. A special case is when $\alpha = 1/c$ for

$c \in \mathbb{N}$, where the two described transmitter arrangements converge and produce the same transmitter structure. An advantage of both designs is the support of spectrum positioning based on the locations of the zero inputs which may be added to the head, tail or around the input symbols.

The design in section 4.3.3 uses multiple IDFT modules which are shorter in length when compared to the single IDFT based designs. For systems with a large number of subcarriers it can be less convenient or economic to use larger IDFTs as in the proportional inputs and the rational α transmitters. This design requires the IDFT to be of the same length as the subcarriers. The multiple IDFTs design poses no restriction on the value of α or Q/α, thus can support a wider range of α values. Overall, for any combination of N and α there can be a compatible option from the proposed transmitters.

4.4.2 Complexity Analysis

Differences in the number and size of the IDFTs in the proposed design will offer different computational complexity. The computational complexity of the directly generated SEFDM signal as in equation 4.1 is $Q \times N$ complex multiplications and $Q\,(N-1)$ complex additions. The complexity of the proposed transmitters in sections 4.3.1, 4.3.2 and 4.3.3 depends on the complexity of the evaluation of the IDFT. When the IFFT algorithm is used for evaluating the IDFT, the complexity is reduced to $O\,(Q \log Q)$ complex multiplications and additions.

Assuming that the complexity of the IFFT algorithm is $\gamma Q \log_2 Q$ complex multiplications and additions, where γ is a constant; The complexity of the proportional transmitter, as described in section 4.3.1, will be

$$\gamma(Q/\alpha \log_2 Q/\alpha) = \gamma(Q/\alpha \log_2 Q - Q/\alpha \log_2 \alpha). \tag{4.24}$$

The complexity of the design in section 4.3.2 will be

$$\gamma(cQ \log_2 cQ) = \gamma(cQ \log_2 Q + cQ \log_2 c). \tag{4.25}$$

Nevertheless, in both designs zeros are inserted at some input indices and a subset of the outputs is actually needed, suggesting complexity reduction using pruning of the inputs

[127] and the outputs [128]. Pruning of the inputs of the proportional inputs transmitter transmitters is suggested in [129] leading to complexity of

$$\gamma(Q/\alpha \log_2 N). \tag{4.26}$$

The same concept can be applied on the transmitter design for α a rational number, hence the complexity of the pruned system will be

$$\gamma(cQ \log_2 bN). \tag{4.27}$$

The reduction in complexity for both transmitters is achieved by first considering the zeros inserted to realize the SEFDM frequency samples and then the zero padding to achieve the number of samples of Q where $Q \geq N$ by definition in equation (3.2).

Section 4.3.3 described a multiple IDFT based design. The computational complexity of this design is a combination of the complexity of the c Q long IDFTs, cQ complex multiplications and $(c-1)\,Q$ complex additions.

Fig. 4.12 shows the complexity of the proposed transmitters in sections 4.3.1, 4.3.2 and 4.3.3 by plotting the number of multiplications with respect to the number of subcarriers and three values of α as an example of the expected computational savings for the proposed systems. It is clear that the proposed systems provide substantial computational savings specially for large system sizes when compared with the direct generation of the signal. The plots show that the complexity of the transmitter for rational α and the multiple IDFTs increases with the increase in the value of α. The plots did not consider the pruning of the IFFTs which will result in further complexity reduction. Nevertheless, the main advantage of the use of the IDFT is that it is a standard operation supported in many hardware platforms. Therefore, the implementation of the IDFT based transmitter relieves the implementation task from custom designing complex multipliers for specific system parameters (i.e. number and sample of the subcarriers).

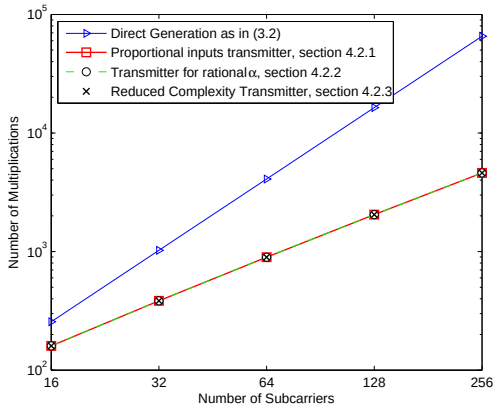

(A) $\alpha = 1/2$

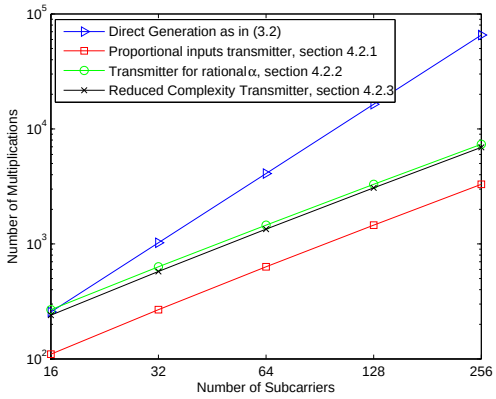

(B) $\alpha = 2/3$

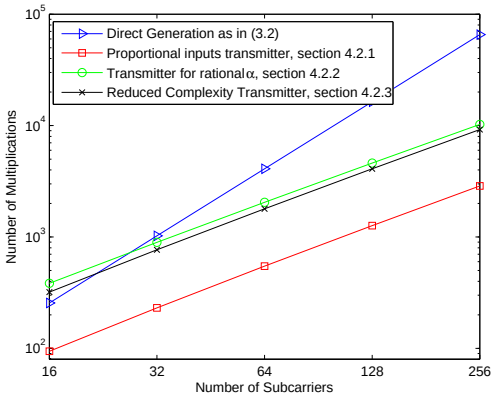

(C) $\alpha = 3/4$

FIGURE 4.12: Number of multiplications as an indicator of the computational complexity for the proposed transmitters for $\alpha = 1/2$, $2/3$ and $3/4$.

4.5 Hardware Signal Generation

The efficient representation of the SEFDM signal with IDFT operations sets the scene for hardware implementations. Based on the IDFT generation for SEFDM signals, a realization of the signal was obtained using Aeroflex PXI Arbitrary Waveform Generator (AWG) equipment [130]. The I and Q values of the time samples obtained from MATLAB simulations of the proposed transmitters are fed to the device which generated the corresponding analogue signal. The generated signal was captured with a spectrum analyzer and is depicted in Fig. 4.13 .

Moreover, implementations of the proposed designs are currently underway at UCL[3].

[3]The implementations are part of the EngDs of Marcus Perrett and Paul Whatmough currently underway at UCL.

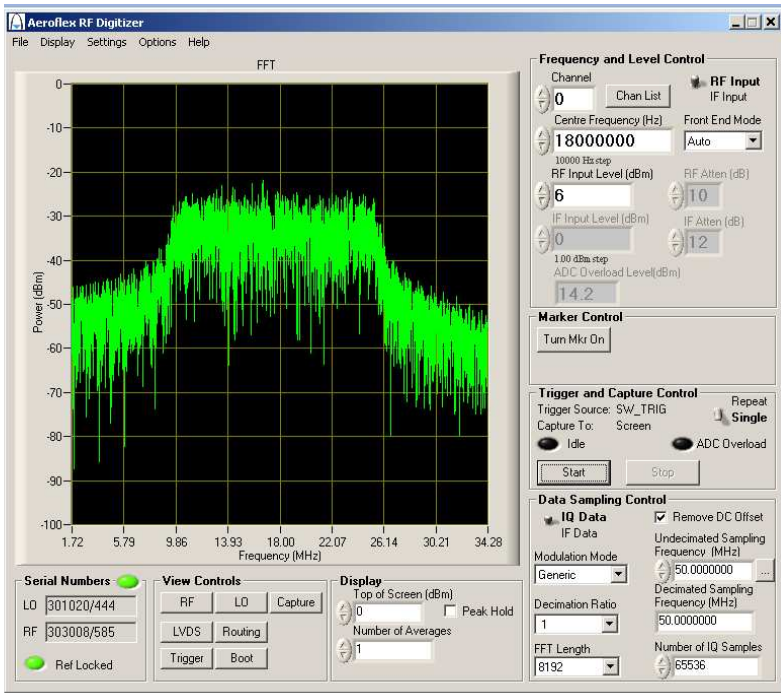

FIGURE 4.13: Spectrum of AWG generated SEFDM signal for 16 subcarrier system and $\alpha = 0.5$.

An implementation of the multiple IDFT transmitter in VLSI architecture is reported [131]. The transmitter is treated as three functional blocks reflecting the matrix representation in equation (4.20). The hardware presented in [131] supports three working modes: OFDM, SEFDM with $\alpha = 2/3$ and $1/2$, the last being equivalent to FOFDM. Nevertheless, it is expected that other values of α can be supported in a similar manner. Furthermore, Perrett et al. presented a reconfigurable architecture for SEFDM systems implemented on an FPGA [132]. The new system support several values of α and allows real-time reconfigurability by developing a modified Ethernet stack [133]. The system employs an additional IDFT module to calculate the values of the rotations in place of the Look Up Table (LUT) and the design itself is set to accommodate up to the highest requirement of the supported α values. The system aims to provide a testbed for research purposes therefore is optimized in terms of the functionality rather than resource utilization. Nevertheless, the new system employs a direct indexing strategy for the re-ordering block, thus reduces substantially the complexity when compared to the implementation in [131] due to the elimination of the divider stage needed to create the column major order of the symbols as in equation (4.22).

4.6 Discussion and Conclusions

In this chapter a new framework to generate SEFDM signals is proposed. The framework is based on using standard IDFTs to generate fractionally spaced signals in frequency. The framework established can be applied for the IDFT design of any multicarrier communication system with any frequency spacing. The framework poses no restrictions on the input symbols type and requires minor alterations to the order of the input symbols stream to realize systems with any frequency spacing, therefore, support universal transmitter design for different MCM systems. The mathematically proven IDFT representation of non-orthogonal multicarrier signals is particularly important for the implementation of such systems and the manipulation and study of their signals. The proposed framework eliminates the need for a bank of analogue modulators and uses standard IDFT operations for modulating the signals. Three IDFT transmitters were designed with different requirements of number and length of the needed IDFT operation. Numerical verification confirmed that the transmitters produce the required bandwidth compression with identical BER performance to that of an ideal oscillator based design. In addition to the reduction of complexity, the IDFT based transmitters have a range of advantages over analogue ones and over direct generation with complex multipliers and adders. The structure of the proposed transmitters employ similar building blocks as OFDM systems, hence, will facilitate a smooth changeover between existing systems based on OFDM to systems employing SEFDM. Moreover, systems that allow for multirate communications could benefit from these methods where the operation could be switched between OFDM and SEFDM. Such a feature could be especially useful for applications where the available spectrum changes. Such a mode of operation can be more suited for the uplink as the base station is more capable to accommodate the complex SEFDM receiver. The main limitation of these simple transmitters is that they require a larger IDFT when compared to OFDM with the same number of subcarriers. Finally, it will be shown in the next chapter that the proposed framework can be extended to the reception side leading to the proposal of the DFT based SEFDM demodulator.

Chapter 5

The SEFDM Receiver

5.1 Introduction

Previous chapters have demonstrated how the SEFDM signal can be neatly modelled and efficiently generated using standard IDFT modules. However, reception of the SEFDM signal still remains a challenge due to the ICI created by the non-orthogonal subcarriers. The SEFDM receiver comprises two main stages: the demodulator and the detector. The demodulation of the incoming signal leads to the collection of a set of sufficient statistics on which detection algorithms are applied to retrieve the originally transmitted symbols. In the original proposal for SEFDM systems, the sufficient statistics are generated by correlating the incoming signal with orthonormal bases, where the orthonormal bases are obtained through the orthonormalization of the non-orthogonal subcarriers using Gram Schmidt (GS) and its modifications or Löwdin Method (LM) [57]. After that Maximum Likelihood (ML) criterion is applied to the sufficient statistics to estimate the originally transmitted symbols for optimal detection [21] and/or sub-optimal techniques as outlined in section 2.7.

For the demodulation of the SEFDM signal, correlation with orthonormal bases was initially suggested in [21] and adopted in all subsequent work [134, 57], whilst several detection algorithms have been investigated for the SEFDM signal. The use of orthonormal bases is motivated by the desire to maintain the whiteness of the noise. However, as the bases are different from the subcarriers that create the signal, the ICI is not accounted for. In addition to the residual ICI, the orthonormal bases require generation

from the initial subcarriers following orthonormalization techniques such as GS and its modifications and LM, hence adding to the complexity of the receiver. The demodulation process itself requires a bank of correlators customized to the used bases. Furthermore, the bases will need to be fundamentally changed if the number of subcarriers and/or bandwidth savings level changes, thus a system relying on orthonormal bases will not be readily supported in reconfigurable architectures.

Therefore, new choices for the demodulator are presented in this chapter. In particular, demodulation following the Matched Filter (MF) principle is proposed. The MF in SEFDM is designed from the subcarriers and is shown to be efficiently realizable using DFT. The main advantage of the MF demodulator is the reduction of complexity due to the total elimination of the orthonormalization stage and the standardized DFT based implementation. In addition, reception with the DFT bases is proposed which is considered as an alternative form of correlation with orthonormal bases.

Furthermore, optimal detection requirements for the different demodulators are mathematically derived and tested with numerical simulations. The main aim is to decide if there is a fundamental performance difference between the different demodulators. In all cases of demodulation, the optimal detector is found to require an exhaustive search of all possibly transmitted combinations of symbols satisfying a cost function relevant to the demodulator technique in use. The complexity of the optimal detector can become prohibitive with the increase in the system dimensions. Therefore, the realization of the optimal detector with the Sphere Decoding (SD) algorithm is proposed and derived for the MF demodulator. Numerical investigations are provided for different system settings.

5.2 The SEFDM Demodulator

In this section, it is proposed that the SEFDM signal to be alternatively correlated with the conjugates of the original subcarriers instead of the orthonormal bases. This arrangement is effectively a matched filter for the system. The main advantage of this proposal is the elimination of the orthonormalization process which adds to the complexity of the system. Section 3.4.1 showed the derivations for the MF demodulation,

where the obtained statistics are described as

$$R = \mathbf{C}S + W_{\mathbf{\Phi}^*}, \tag{5.1}$$

where $\mathbf{C}$ represents the correlation coefficient matrix as derived in equation (3.15), whereas the MF is given as the conjugate subcarriers matrix $\mathbf{\Phi}^*$, thus $\mathbf{C} = \mathbf{\Phi}^*\mathbf{\Phi}$ and the noise term $W_{\mathbf{\Phi}^*}$ has a zero mean and a covariance matrix $\mathbf{\Psi} = \sigma^2\mathbf{C}$ as derived in equations (3.26) and (3.27).

Another option is to use orthonormal bases that span the same space as the SEFDM signal. Recalling that the Q point DFT represents a set of Q orthogonal bases, another demodulator based on standard DFT is proposed. The collected statistics in this case can be expressed as

$$R = \mathbf{\Omega}^*S + W_{\mathbf{\Omega}^*}, \tag{5.2}$$

where $\mathbf{\Omega}^*$ represents the Q point DFT matrix.

In general, it is shown in chapter 3 that the SEFDM system can be expressed by the linear regression model with the equation reproduced below

$$R = \mathfrak{C}S + W, \tag{3.38}$$

where $\mathfrak{C}$ represent the design matrix of the system and is composed from the correlation of the carriers matrix $\mathbf{\Phi}$ and the vectors of the chosen demodulator (i.e Gram Schmidt bases, MF bases, DFT). Therefore, the detection of the SEFDM system focuses on solving the linear regression model in equation (3.38) whereas the differences between the different demodulators is incorporated in the different design matrices as well as the noise properties associated with them.

5.3 The DFT Based MF Demodulator

The realization of the demodulator is a key design consideration in the SEFDM receiver. The orthonormal bases require orthonormalization if GS or LM is used. On the other hand, if DFT bases are used, as proposed in equation (5.2), then the implementation

is straightforward with standard DFT/FFT modules. Of concern in this section, is the efficient realization of the MF demodulator.

The MF demodulator is constructed from the conjugates of the subcarriers. Applying the same concepts as in chapter 4, it will be shown that the MF can be realized with the DFT operation with some modifications on the input vector. The DFT of a sequence $Y = [y_0, y_1, \cdots, y_{N-1}]^{'}$ denoted with the vector $\mathcal{F}\{Y\}$ is given by [125]:

$$\mathcal{F}_k\{Y\} = \frac{1}{\sqrt{N}} \sum_{n=0}^{N-1} y_n \exp\left(\frac{-j2\pi nk}{N}\right). \tag{5.3}$$

Hence, following a similar route to prove Theorem 4.1, equation (5.1) can be realized as

$$R = \left[R^{'}\right]_0^{N-1}, \tag{5.4}$$

where

$$R^{'} = \zeta \mathbf{\Omega}^* Y^{'}, \tag{5.5}$$

where $\mathbf{\Omega}^*$ represents the L point DFT matrix for

$$Y^{'} = \begin{cases} Y_i & 0 \leq i < N \\ 0 & N \leq i < L \end{cases}. \tag{5.6}$$

when $\zeta = \frac{1}{\sqrt{\alpha}}$, $L = Q/\alpha$ for $Q/\alpha \in \mathbb{N}$, or equivalently

$$Y^{'}[i] = \begin{cases} Y_{i/b} & i \; mod \, b = 0 \\ 0 & otherwise, \end{cases} \tag{5.7}$$

when $L = cQ$,$\zeta = \sqrt{c}$ for $\alpha = b/c$, $b, c \in \mathbb{N}$ and $b < c$.

Furthermore, the MF can be expressed as the sum of multiple DFTs, similar to the transmitter design detailed in section 4.3.3, as

$$R[k] = \frac{1}{\sqrt{N}} \sum_{i=0}^{c-1} \exp\left(\frac{j2\pi ik}{cN}\right) \sum_{l=0}^{N-1} Y^{''}(i + lc) \exp\left(\frac{j2\pi lk}{N}\right), \tag{5.8}$$

where

$$Y^{''}[i] = Y^{'}[i]. \tag{5.9}$$

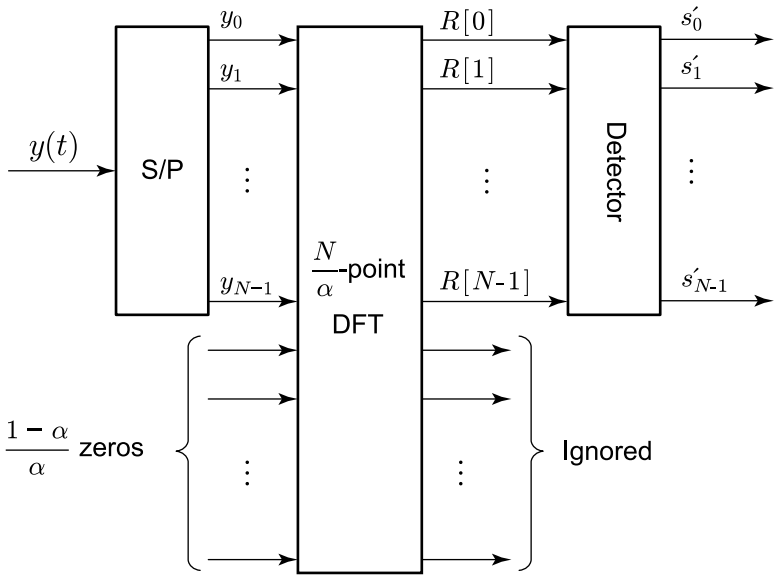

FIGURE 5.1: Proportional inputs DFT based MF demodulator design.

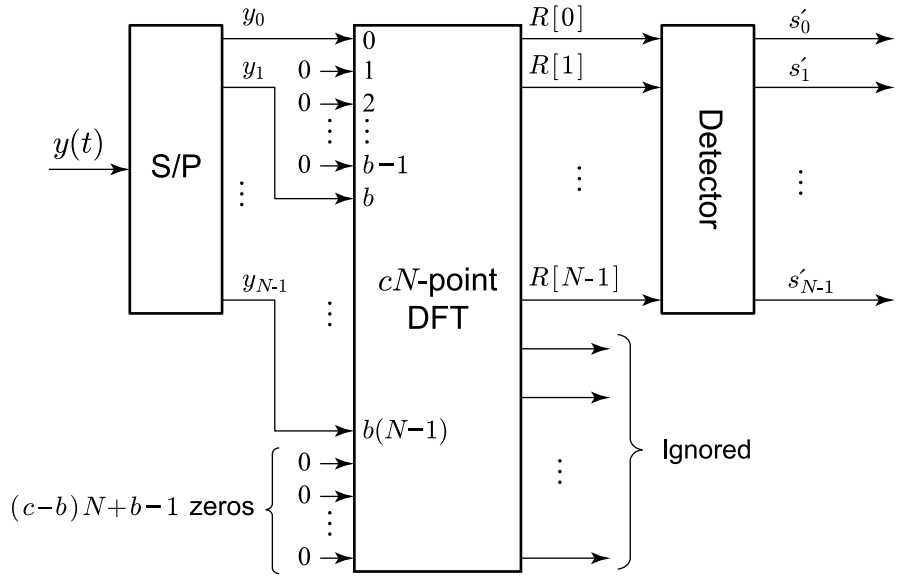

FIGURE 5.2: DFT based MF demodulator design for α rational number.

Fig. 5.1, 5.2 and 5.3 depict three receiver structures based on equations (5.4) and (5.8). The designs show how the correlation with the conjugate carriers is realized with standard DFT blocks. The generated statistics are fed to the detector that employs algorithms to estimate the originally transmitted symbols.

The DFT based demodulator reduces the complexity of the SEFDM receiver. First, the demodulator uses general purpose components that can in turn be efficiently realized with the FFT. The receiver is relieved from the orthonormalization process and the bank of modulators are replaced by the standard DFT blocks, hence, the complexity of the

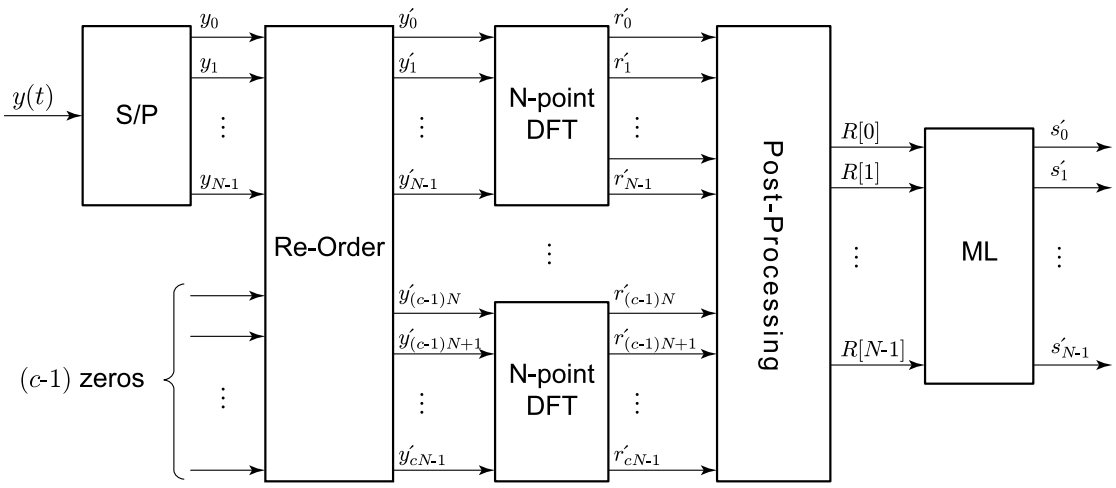

FIGURE 5.3: Multiple DFTs design for the MF demodulator.

receiver is mainly concentrated in the detection stage. Furthermore, the DFT based demodulator is similar to OFDM receiver, hence can facilitate coexistence between the systems and smooth migration.

5.4 The Optimal Detection for the SEFDM Signal

The second stage of the SEFDM receiver is a detector that estimates the originally transmitted symbols based on the collected statistics in the demodulation stage. In this section, the optimal detector for the SEFDM signal is discussed. In particular, the optimal detector for the statistics obtained via the DFT bases and MF are derived. The detector is optimal in the sense that it minimizes the probability of error.

5.4.1 Orthonormal Bases

For the original SEFDM system proposal, the receiver starts by correlation with orthonormal bases obtained via GS or LM orthonormalization [21, 57]. The optimal detector is derived for the demodulated signal in that case as

$$\hat{S}_{ML} = \min_{s \in Q^N} \|R - \mathbf{M}S\|, \tag{5.10}$$

where $\mathbf{M}$ is the matrix describing the correlation of the subcarriers and the orthonormal bases [21].

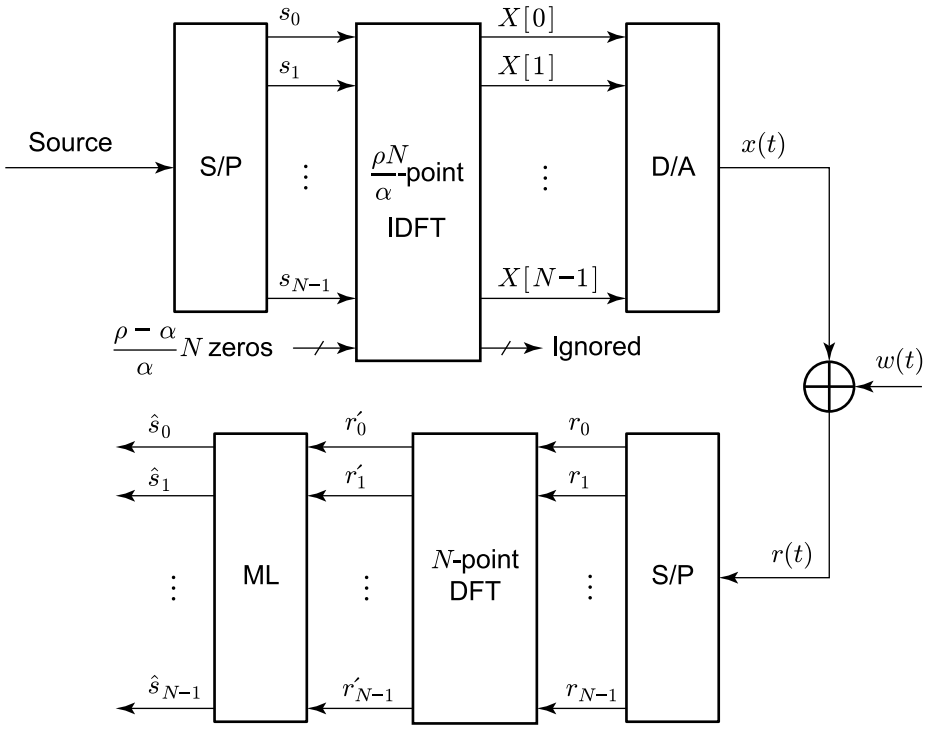

FIGURE 5.4: The block diagram of an SEFDM system employing DFT bases for the demodulation, $r'_i = R[i]$.

If DFT bases are used, the derivation of the optimal solution will follow the same steps as the case of orthonormal bases in the original system proposal. The noise properties are key for this similarity, as the DFT bases constitutes an orthogonal set of bases, hence, the noise at the output of the DFT will remain white with zero mean and covariance matrix of $\sigma_N^2\mathbf{I}$. Therefore, the optimal detector for the use of the DFT bases remains in the same format as the detector described by equation (5.10), the only difference is in the values taken by the $\mathbf{M}$ matrix in this case. Fig. (5.4) depicts a block diagram of an SEFDM system employing DFT bases in place of the GS/LM bases.

5.4.2 MF Demodulation

The MF demodulator generates a statistics vector with different properties when compared to the use of orthonormal bases. In particular, the noise characteristics after the demodulation are affected by the non-orthogonal structure of the demodulator. Section 3.4.1 examined the properties of the expanded noise term onto the vectors of the MF. Therefore, the optimal detector for this case has to accommodate for the altered noise. The optimal detector estimates the originally transmitted data symbols by applying

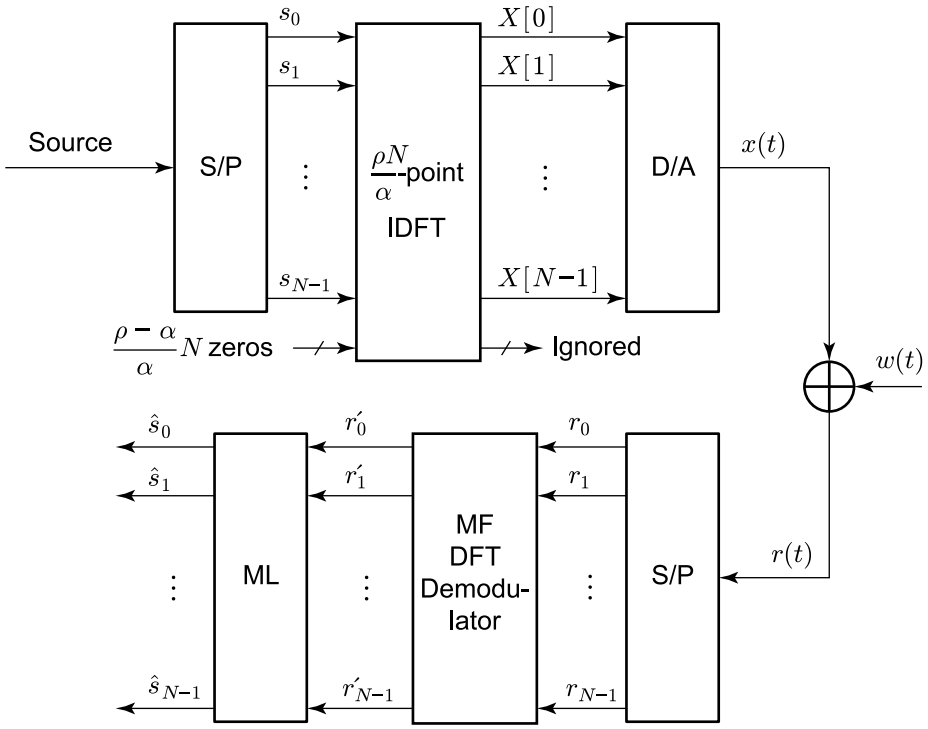

FIGURE 5.5: The block diagram using IDFT based MF demodulator, $r'_i = R[i]$.

Maximum a Posteriori (MAP) detection. For received statistics denoted by the vector R as described in equation (5.1) and a sent message denoted by the vector S_m, the a 'posteriori' probability is expressed as [135]

$$p(S_m|R) = \frac{p(R|S_m)\,p(S_m)}{p(R)}. \tag{5.11}$$

The MAP detector aims to maximize the probability in equation (5.11). The a 'priori' $p(S_m)$ is set equal to $1/M^N$ to satisfy the assumption that all transmitted symbols are Independent and Identically Distributed (IID) and belong to the same constellation, therefore, revealing that the probability $p(S_m|R)$ on the LHS of equation (5.11) depends mainly on the likelihood function $p(R|S_m)$, hence maximizing the likelihood function will guarantee the maximization of equation (5.11).

Noting that for a transmitted message S_m, R has a multivariate normal distribution with mean vector $U_m = \mathbf{C}S_m$ and covariance matrix $\mathbf{\Psi}$ where $\mathbf{\Psi} = \sigma^2\mathbf{C}$, thus, the $p(R|S_m)$ is given by

$$p(R|S_m) = \frac{1}{(2\pi)^{N/2}\left|\det(\mathbf{\Sigma_N})\right|^{1/2}} e^{-\frac{1}{2}(R-\mathbf{C}S_m)^*\mathbf{\Psi}^{-1}(R-\mathbf{C}S_m)}. \tag{5.12}$$

Therefore, minimizing the exponent term in equation (5.12) will result in maximizing the likelihood function $p(R|S_m)$:

$$\begin{aligned}(R-\mathbf{C}S_m)^*\,\mathbf{\Psi}^{-1}\,(R-\mathbf{C}S_m) &= \frac{1}{\sigma^2}\,(R-\mathbf{C}S_m)^*\,\mathbf{\Phi}^{-1}\mathbf{\Phi}^{*^{-1}}\,(R-\mathbf{C}S_m)\\ &= \frac{1}{\sigma^2}\left\|\mathbf{\Phi}^{*^{-1}}\,(R-\mathbf{C}S_m)\right\|^2 \end{aligned} \tag{5.13}$$

The detector reduces to find

$$\hat{S}_{ML} = \min_{s\in Q^N}\ \left\|\mathbf{\Phi}^{*^{-1}}\,(R-\mathbf{C}S_m)\right\|^2. \tag{5.14}$$

Equation (5.14) shows that the optimal solution for the MF obtained statistics is the one that maximizes the likelihood function (ML) and can be achieved by minimizing the Euclidean norm of the cost function. Clearly, the solution differs from the optimal solution for the GS based system, shown in equation 2.17, as the function contains terms related to the noise and the design matrix itself is different (i.e. $\mathbf{C}$ in MF case and $\mathbf{M}$ in orthonormal bases case).

Applying the Cauchy–Schwarz inequality [48], reveals an upper bound for the term in equation (5.13) as

$$\begin{aligned}\left\|\mathbf{\Phi}^{*^{-1}}\,(R-\mathbf{C}S_m)\right\|^2 &\leq \left\|\mathbf{\Phi}^{*^{-1}}\right\|^2\|R-\mathbf{C}S_m\|^2\\ &\leq \sigma_{max}\,\|R-\mathbf{C}S_m\|^2, \end{aligned} \tag{5.15}$$

where σ_{max} is the maximum singular value of the matrix $\mathbf{\Phi}^{*^{-1}}$, and is independent of the transmitted or received message. Therefore, the inequality in equation (5.15), leads to an upper bound for the minimization of the MF optimal detector in equation (5.14) as

$$\min_{s\in Q^N}\ \|R-\mathbf{C}S_m\|^2. \tag{5.16}$$

This bound shows that minimization of the term $(R-\mathbf{C}S_m)$ yields an upper bound for the minima of the term $\left(\mathbf{\Phi}^{*^{-1}}\,(R-\mathbf{C}S_m)\right)$. The upper bound neglects the colouring of the noise and thus, shows a similar structure to the cost function of the system with orthonormal bases (whether GS or DFT bases) in equation (5.10), with the exception of the different design matrix. In other words, the upper bound focuses on the collected

statistics relationship to the possibly transmitted symbols and ignores the noise colouring. Recalling that the conditioning of the system affects the level of noise colouring as the system swings from being perfectly conditioned (i.e. no colouring effect) to close to singular with the increase in the bandwidth compression level and the number of subcarriers as discussed in chapter 3, therefore it is expected that the tightness of the upper bound will consequently depend on the bandwidth compression level and number of subcarriers.

Fig. 5.5 depicts a block diagram of an SEFDM system. The demodulator is a matched filter and is thus, realized with the DFT block. The detector uses the ML criteria derived in equation (5.14). The ML detector examines all the possibly transmitted symbol sets and chooses the one that minimizes the norm in equation (5.14).

5.4.3 Numerical results

Section 5.4 discussed several demodulator choices for the SEFDM system and the relevant optimal detectors that aim to minimize the error rate. The optimal solution for the MF, derived in equation (5.14) indicates the need to account for the correlated noise term. The performance of the proposed detectors is investigated through numerical simulations. The simulations assume perfect knowledge of the subcarriers' frequencies on the reception side and that the received signal is impaired by AWGN. The simulations provide the error performance for SEFDM demodulation with orthonormal bases obtained with the IMGS algorithm described in section 2.6 or as DFT bases and the MF demodulation as described in section 5.2. For all types of demodulation, an optimal detector is implemented. The optimal detection is achieved by an exhaustive search of all possibly transmitted combinations of input symbols to satisfy the ML criterion relevant for each demodulator choice as provided in section 5.4. Due to the complexity, the systems simulated have only four subcarriers.

Fig. 5.6 depicts the BER performance for MF detection and the upper bound for systems carrying BPSK and 4QAM input symbols for different values of α and E_b/N_0. The figure shows that the upper bound tightness is in an inverse proportion to the bandwidth compression level. This is directly linked to the conditioning of the SEFDM system as with the increase in bandwidth compression levels the system starts to deviate from

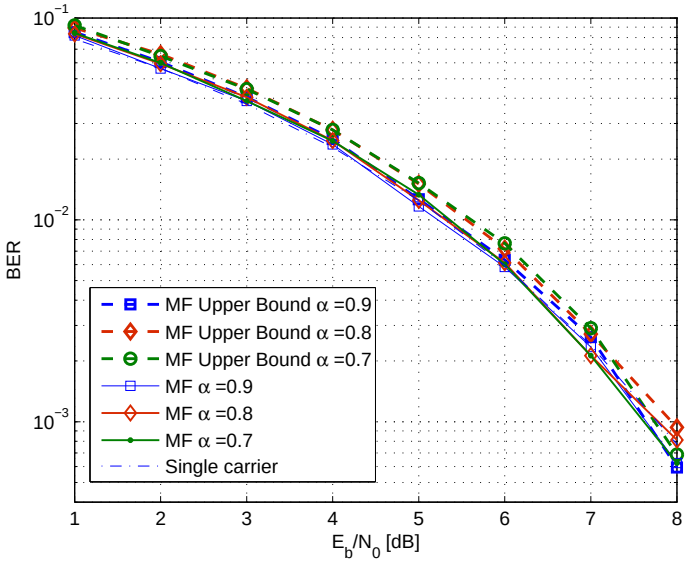

(A) BPSK.

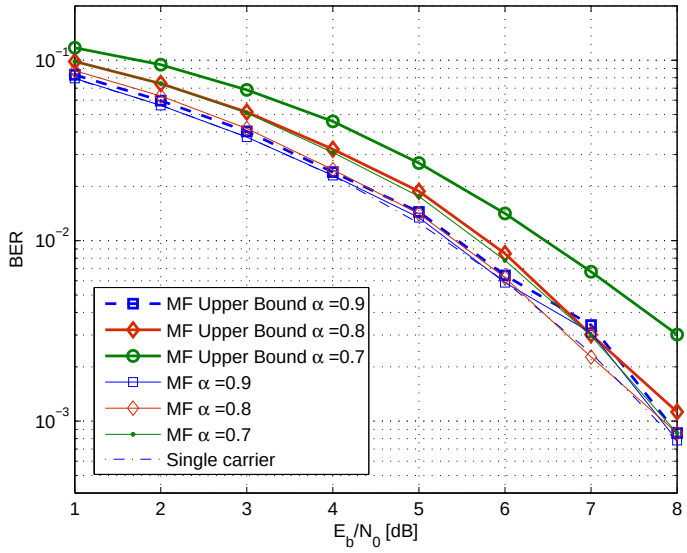

(B) 4QAM.

FIGURE 5.6: BER of MF demodulator optimal detection and its upper bound derived in equation (5.16) for $\alpha = 0.7 - 0.9$, 4 subcarrier system with BPSK and 4QAM input symbols.

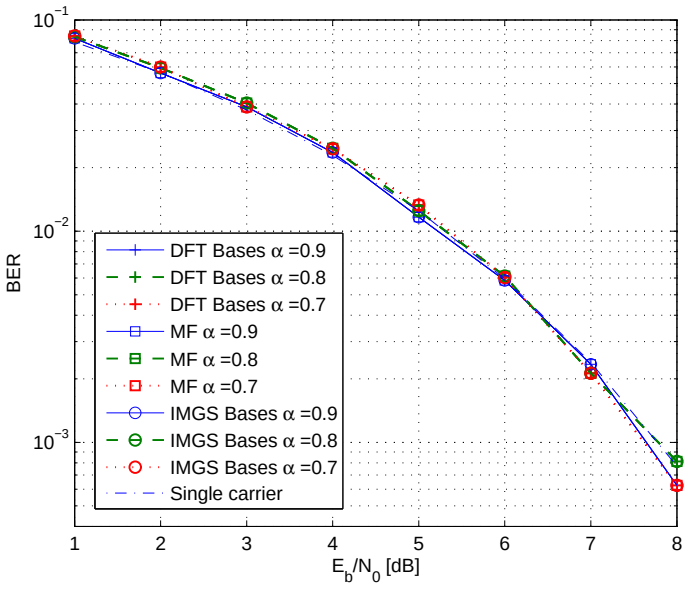

(A) BPSK.

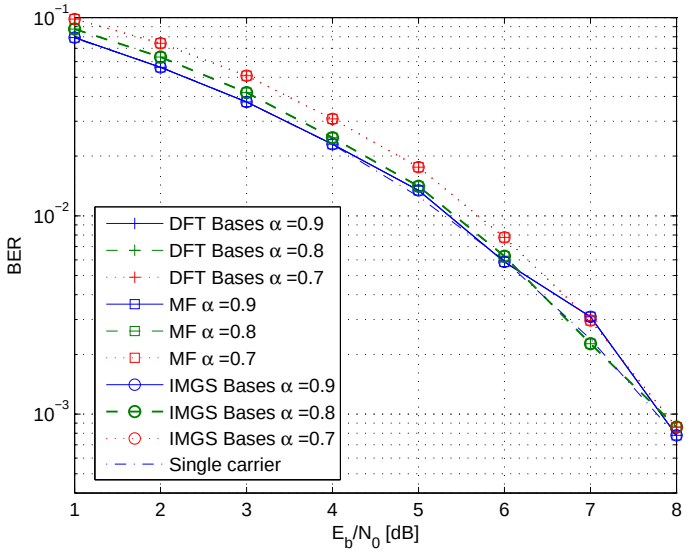

(B) 4QAM.

FIGURE 5.7: BER of different demodulators and optimal detection for $\alpha = 0.7 - 0.9$, 4 subcarrier system with BPSK and 4QAM input symbols.

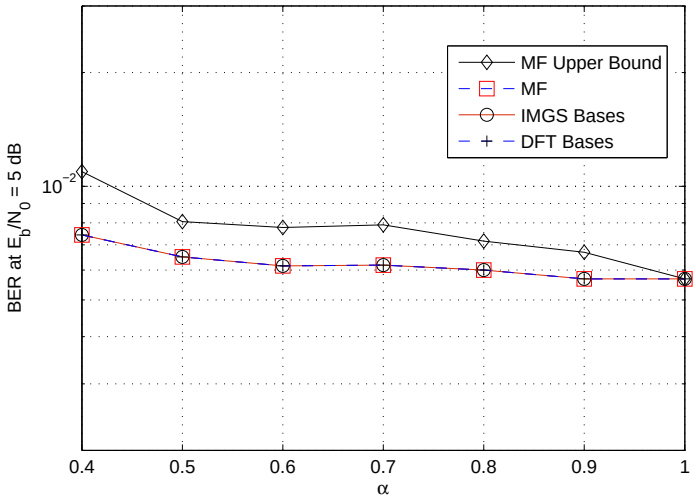

(A) BPSK.

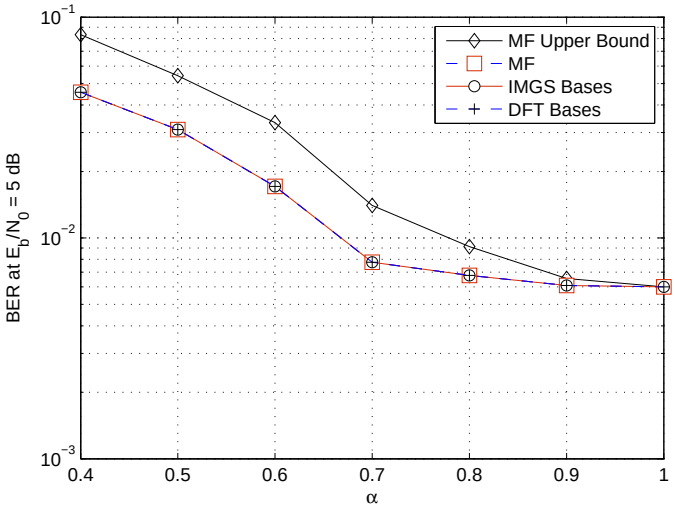

(B) 4QAM.

FIGURE 5.8: BER of different demodulators and optimal detection at $E_b/N_0 = 5$ dB for $\alpha = 0.4 - 1$, 4 subcarrier system and BPSK and 4QAM input symbols.

the end close to orthogonality to the one close to singularity, thus the MF effect on the noise is emphasized with the deterioration in the conditioning. Consequently the upper bound, which does not account for the noise colouring, looses its tightness. In addition, the figures show that the performance for 4QAM input symbols is more vulnerable to bandwidth compression than BPSK.

Furthermore, optimal solutions for the three different demodulators are simulated. Fig. 5.7 and 5.8 show the BER performance for optimal detection for DFT bases, MF and

IMGS demodulators. In all cases, the optimal detector is applied which required an exhaustive search of all possibly transmitted combinations of input symbols to satisfy the corresponding cost function. The figures show that the three detectors achieve the same performance for different values of α and BPSK and 4QAM input symbols. The plots confirm that no performance degradation is expected for the MF demodulation. Based on this it is concluded that the choice of one demodulator over the other will be influenced by other factors such as complexity of realization and compatibility with other system components and other systems (i.e. OFDM). However, it is necessary to evaluate the different performances with other detectors which will be covered in the next section and chapter where new detectors are proposed.

5.5 Sphere Decoder (SD) for the MF Based System

The MF shows a remarkable advantage of reducing complexity as it can be efficiently realized with standard components. However, the optimal solution as derived in section 5.4 requires exhaustive search over all the possibly transmitted combination of symbols. In practice, such a task can become overly demanding specially with the increase in the number of subcarriers and/or modulation level of the input symbols. This motivated the exploration of low complexity implementation of the exhaustive search as provided by the SD algorithm. The use of the SD algorithm was proposed for the detection of the IMGS based system to overcome the complexity burden of the brute force ML [36]. The SD algorithm achieves the ML search with lower complexity by transforming the search space to a multi-dimensional sphere and then searches only candidate solutions that exist within a specific radius from the statistics point.

Section 2.7.3 explains the use of the SD algorithm for the SEFDM system based on orthonormal bases. Having a different cost function for the matched filter, the original SD derivations for the orthonormal bases can not be used immediately. Thus, this section presents a step by step derivation of the SD algorithm for the MF demodulator case.

In the case of the MF, the optimal detection is obtained as the one that satisfies equation (5.14). The SD algorithm places an additional constraint on the optimal solution, which is to exist within a predefined radius g. Thus the SD solution will be

$$\hat{S}_{SD} = \min_{s \in Q^N,\, \|R-\mathbf{C}S\|^2 \leq g} \left\| \mathbf{\Phi}^{*^{-1}} (R - \mathbf{C}S) \right\|^2, \tag{5.17}$$

The variables in equation (5.17) are expanded using real decomposition [79] as

$$\begin{aligned} \tilde{R} &= \begin{bmatrix} \Re\{R\} \\ \Im\mathfrak{m}\{R\} \end{bmatrix}, \quad \tilde{\mathbf{C}} = \begin{bmatrix} \Re\{\mathbf{C}\} & \Im\mathfrak{m}\{\mathbf{C}\} \\ -\Im\mathfrak{m}\{\mathbf{C}\} & \Re\{\mathbf{C}\} \end{bmatrix}, \\ \tilde{\mathbf{\Phi}} &= \begin{bmatrix} \Re\{\mathbf{\Phi}\} & \Im\mathfrak{m}\{\mathbf{\Phi}\} \\ -\Im\mathfrak{m}\{\mathbf{\Phi}\} & \Re\{\mathbf{\Phi}\} \end{bmatrix}, \qquad (5.18) \\ \tilde{S} &= \begin{bmatrix} \Re\{S\} \\ \Im\mathfrak{m}\{S\} \end{bmatrix}. \qquad (5.19) \end{aligned}$$

While the dimension of the problem is doubled, real candidate symbols are useful for the simplification of the solution. Substituting with the real decomposed variables and expanding the norm term of equation (5.17) leads to

$$\begin{aligned} \left(P - \tilde{S}\right)^T \tilde{\mathbf{C}}^T \tilde{\mathbf{\Phi}}^{-1} \left(\tilde{\mathbf{\Phi}}^{-1}\right)^T \tilde{\mathbf{C}} \left(P - \tilde{S}\right) = \\ \left(P - \tilde{S}\right)^T \tilde{\mathbf{C}}^T \left(P - \tilde{S}\right) \leq g, \end{aligned} \tag{5.20}$$

where P is the unconstrained ML estimate defined as

$$P = \left(\tilde{\mathbf{C}}^T \tilde{\mathbf{C}}\right)^{-1} \tilde{\mathbf{C}}^T \tilde{R}. \tag{5.21}$$

The work in chapter 3 proved that the matrix $\mathbf{C}$ and consequently $\tilde{\mathbf{C}}$ have real diagonal entries and that $\mathbf{C}$ is positive definite for α and N values that result in the minimum eigenvalue that is not equal to zero for the computation machine precision. For such combinations of α and N, the Cholesky decomposition can be applied to $\tilde{\mathbf{C}}$ as

$$\text{chol}\left\{\tilde{\mathbf{C}}^T\right\} = \mathbf{L}^T \mathbf{L}. \tag{5.22}$$

This step shows the main difference between the SD solution for the MF and IMGS

systems, which is reflected in the different argument for the Cholesky decomposition. Then, equation (5.17) can be equivalently expressed as

$$\hat{S}_{SD} = \min_{s \in Q^N,\, \left\|\mathbf{L}\left(P-\tilde{S}\right)\right\|^2 \leq g} \left\|\mathbf{L}\left(P-\tilde{S}\right)\right\|^2, \tag{5.23}$$

Due to the triangular structure of $\mathbf{L}$, the search for the solution is pursued in $2N$ consecutive steps. Starting from level $2N$, the algorithm examines candidate input symbol points (i.e. from the used alphabet) that satisfy

$$\lceil p_{2N} - \sqrt{g_{2N}}/l_{2N,2N} \rceil \leq s_{2N} \leq \lfloor p_{2N} + \sqrt{g_{2N}}/l_{2N,2N} \rfloor, \tag{5.24}$$

where $\lceil \cdot \rceil$ and $\lfloor \cdot \rfloor$ refer to rounding to the nearest integer greater or smaller than the argument, respectively. The candidate points are then enumerated following Schnorr Euchner (SE) or Fichke-Pohst (FP). The former orders the points according to their distance from the centre of the search interval and the latter orders the points based on their distance from the lower bound of the search interval; information on both techniques was provided in section 2.7.3. Definition of the radius is important as previously discussed in section 2.7.3. A widely used choice is to set the radius equal to an initial estimate of the transmitted symbols. The initial estimate can be obtained by applying Zero Forcing (ZF) or Minimum Mean Square Error (MMSE) detection. For MF based systems the ZF and MMSE are defined as

$$\begin{aligned} \hat{S}_{ZF} &= \left\lfloor \mathbf{C}^{-1} R \right\rceil \\ &= \left\lfloor \mathbf{C}^{-1} \left(\mathbf{C}S + N\right) \right\rceil \\ &= \left\lfloor S + \mathbf{C}^{-1} N \right\rceil, \end{aligned} \tag{5.25}$$

and

$$\hat{S}_{MMSE} = \left\lfloor \mathbf{C}^{*} \left(\mathbf{C}\mathbf{C}^{*} + \frac{1}{\sigma_W^2}\mathbf{I} \right)^{-1} R \right\rceil, \tag{5.26}$$

respectively. Clearly the only difference between the ZF and MMSE detectors for MF or IMGS system is in the different matrices $\mathbf{M}$ and $\mathbf{C}$.

5.5.1 Note on SD Application to DFT Bases Demodulation

In the case of DFT demodulation as proposed in section 5.2, the SD algorithm cannot be applied as the diagonal entries are non-real. The correlation between the DFT bases and the subcarriers is given by

$$\begin{aligned} \breve{c}_{m,n} &= \frac{1}{Q}\sum_{k=0}^{Q-1} e^{\frac{j2\pi\alpha km}{Q}} e^{-\frac{j2\pi kn}{Q}} \\ &= \frac{1}{Q}\left[\frac{1-e^{j2\pi(\alpha m-n)}}{1-e^{\frac{j2\pi(\alpha m-n)}{Q}}}\right]. \end{aligned} \tag{5.27}$$

Equation 5.27 shows that not all the diagonal elements will be real which is the condition for the Cholesky decomposition needed for the work of the SD algorithm. This shows that the use of the MF demodulation is superior to DFT bases as it combines ease of realization with support of SD detection.

5.5.2 Numerical Results

Numerical results of simulations using SD detection in conjunction with MF are presented in this section. Results are provided for 4QAM input symbols for systems with different number of subcarriers and α values. For comparison purposes the results show performance of the SD detector for an IMGS based SEFDM system. The SD algorithm adopts SE enumeration and the initial radius is set to a value arbitrarily greater than the distance from the ZF estimate of the transmitted symbols. In addition, some figures included BER curves for ZF and MMSE detectors for the IMGS and MF based systems to highlight the SD performance advantage.

Fig. 5.9 and 5.10 depicts the error performance for the SD detector for different values of E_b/N_0, α values and number of subcarriers. Noting that the SD algorithm is capable of achieving the ML performance for larger system dimensions than is achievable for the exhaustive ML search. The plots confirm that the SD algorithm achieves the same error performance for MF and IMGS based SEFDM demodulators. In addition, Fig. 5.9 highlights the effects of the reduction of the bandwidth compression level expressed by the α value in terms of deterioration in the BER.

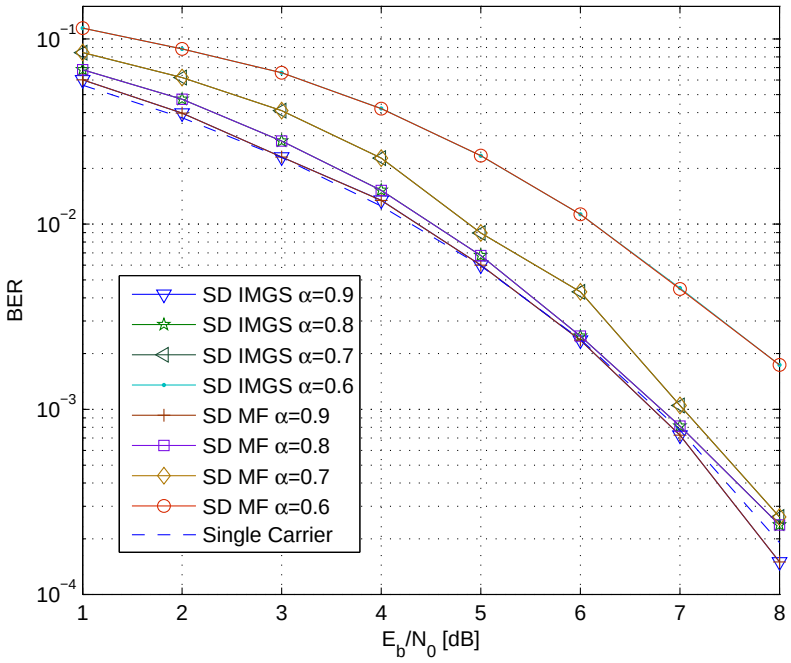

FIGURE 5.9: BER of SD detection with MF and IMGS demodulation vs E_b/N_0 for a 16 subcarrier system with $\alpha = 0.6 - 0.9$ and 4QAM input symbols.

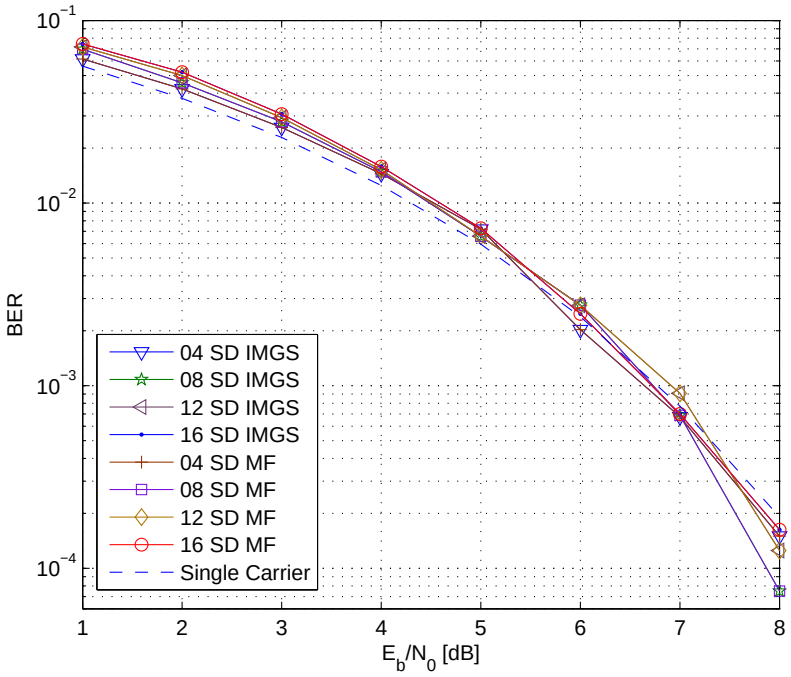

FIGURE 5.10: BER of SD detection with MF and IMGS demodulation vs E_b/N_0 for $\alpha = 0.8$ for $4, 8, 12$ and 16 subcarriers and 4QAM input symbols.

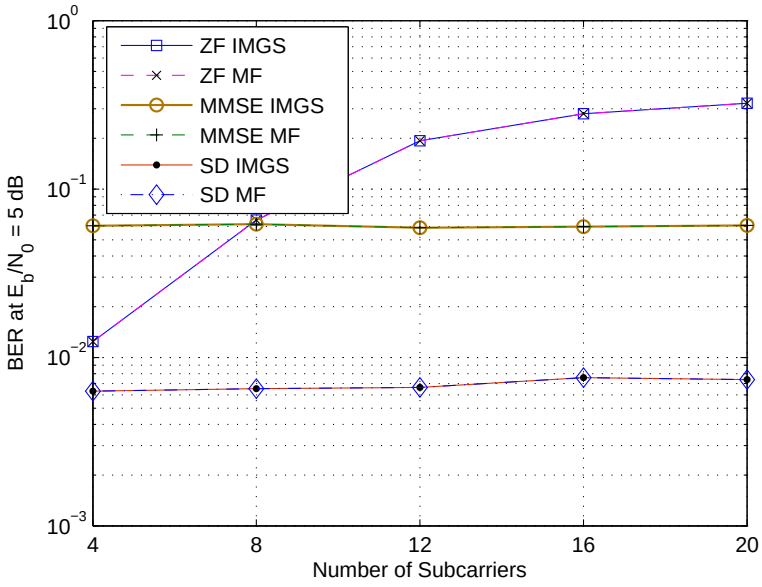

FIGURE 5.11: BER of SD detection with MF and IMGS demodulation vs the number of subcarriers for $E_b/N_0 = 5$ dB.

Fig. 5.11 depicts the BER of SD detection with respect to the number of subcarriers at a fixed $E_b/N_0 = 5$ dB. Performance of ZF and MMSE detectors is presented for comparison purposes. The figure clearly shows the error performance advantage offered by the SD detection which showed slight deterioration with the increase in the number of subcarriers. Fig. 5.12 focuses on the error performance for different values of α at $E_b/N_0 = 5$ dB. The figure confirms the equivalence of the MF and IMGS demodulators and further shows the degradation of the error performance with the decrease in the value of α.

In addition, the simulations addressed the complexity of detection for the MF and IMGS based SEFDM systems in terms of the average number of node visits taken to decode a single SEFDM symbol from the simulation of 1000 SEFDM symbols (i.e. 16000 4QAM input symbols), as depicted in Fig. 5.13 and 5.14. Both figures confirm that the SD algorithm requires the same number of node visits whether MF or IMGS is used to generate the statistics of the received signal. Fig. 5.13 highlights the dramatic increase in the average number of nodes visits with the increase in the number of subcarriers. Fig. 5.13 shows the increase in detection complexity with the reduction in the value of α. However, the results indicate that complexity showed less sensitivity to the reduction in the value of α when compared to the number of subcarriers. Even for a given value of

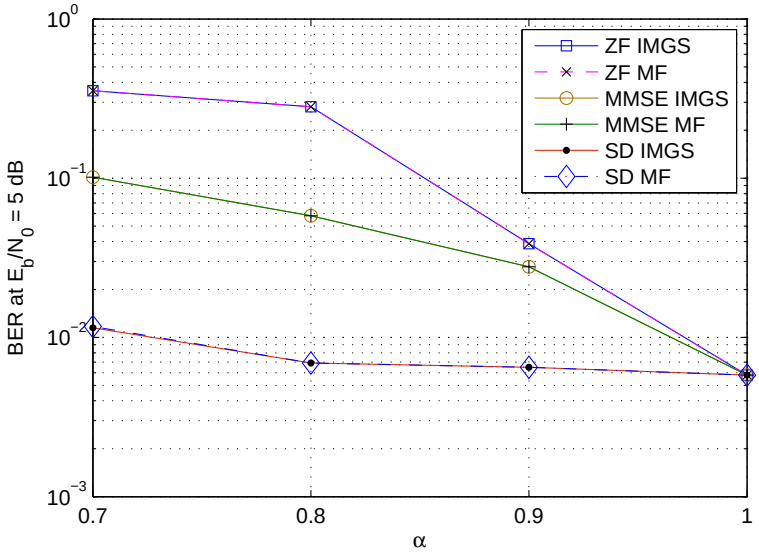

FIGURE 5.12: BER of SD detection with MF and IMGS demodulation for $\alpha = 0.7 - 1$ for $E_b/N_0 = 5$ dB, 16 subcarriers and 4QAM input symbols.

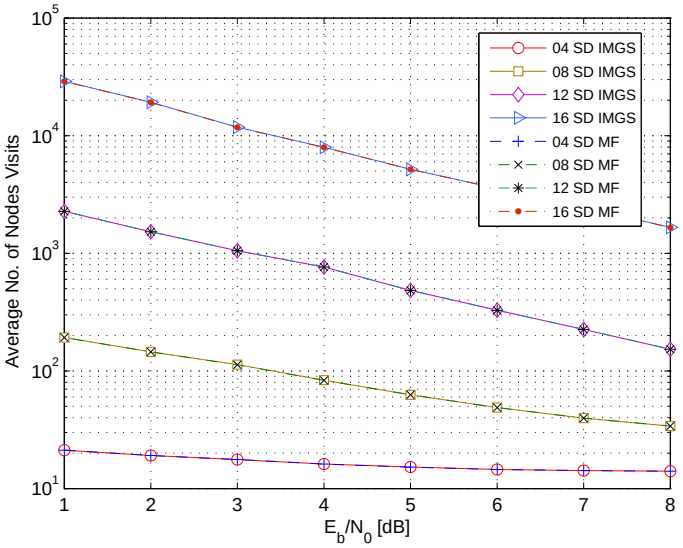

FIGURE 5.13: Average node visits required to decode one SEFDM symbol for $4, 8, 12$ and 16 subcarriers and $\alpha = 0.8$.

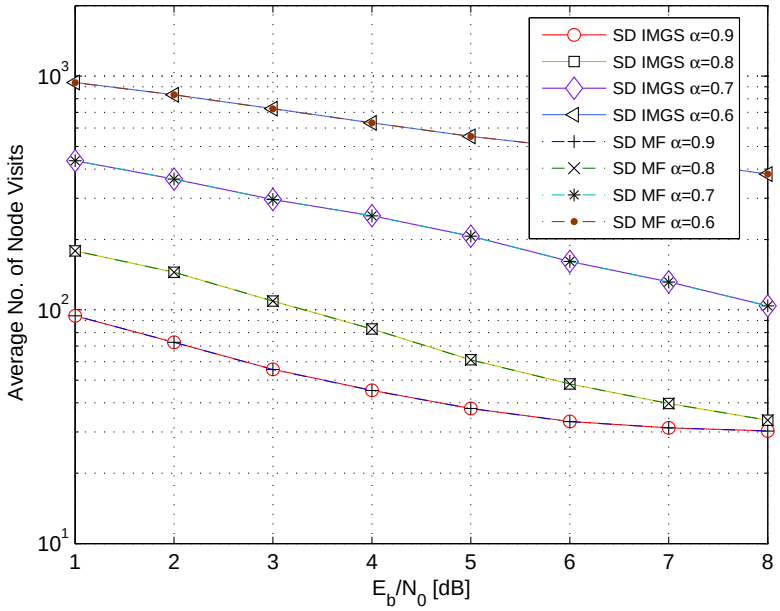

FIGURE 5.14: Average node visits required to decode one SEFDM symbol for $\alpha = 0.6 - 0.9$ and 16 subcarriers.

α and/or number of subcarriers, both figures show that the complexity varies with the signal to noise ratio.

5.6 Hardware Implementation of the MF Demodulator

The DFT design of the MF based demodulator, presented in section 5.3, prepares the front end of the SEFDM receiver for hardware implementation where the DFT is efficiently implemented using the FFT algorithm. The work in [136] presented for the first time the hardware design of the demodulator on FPGA[1]. The implementation uses the MF demodulator depicted in Fig. 5.1. The design requires one DFT/FFT module and zero insertion at the extra inputs of the DFT/FFT.

The implementation of the detection part remains challenged with the high ML complexity and the variable complexity of the SD. ML detectors have exponential complexity that grows with the increase in the number of subcarriers and modulation level. On the other hand, the SD search continues until a solution is reached, as such the resources required can range from minimal requirements to ML requirements. Furthermore, the

[1]Implementations on an FPGA are carried out as part of the Engineering Doctorate program by Ryan Grammenos at UCL in 2011.

typical SD algorithm is sensitive to the noise in the system and in the SEFDM context the algorithm is dependent on system parameters as seen from complexity plots in Fig. 5.13 and 5.14 where the average number of node visits showed changes with changes in α and N. Nevertheless, implementations of ML and SD detectors for Multiple Inputs Multiple Outputs (MIMO) systems have been previously reported [137]. Section 6.7 discusses in more details the considerations for hardware implementation of SEFDM detectors.

5.7 Discussion and Conclusions

In this chapter, the SEFDM demodulator stage in the receiver was investigated. Previously, only demodulation based on the use of orthonormal bases obtained via GS based technique or LM was adopted. In this chapter a new demodulator for the SEFDM system was proposed and investigated. The demodulator is matched to the SEFDM subcarriers and aims to tackle the intercarrier interference in the system in contrast to the IMGS system that focuses on maintaining the whiteness of the AWGN noise. The main advantage of the MF demodulator is the elimination of the need for orthonormalization on reception side, thus can support reconfigurable architectures and in principle reduces the complexity of the system. Furthermore, an efficient algorithm for the implementation of the demodulator based on the DFT was developed. Three topologies using single or multiple DFT modules were proposed to support flexibility. In addition, the DFT based demodulator facilitated compatibility with OFDM on the reception side and is symmetric to the transmitter, therefore, can facilitate dual operation.

Moreover, the optimal detector that minimizes the error probability for the MF based demodulator was derived and was found to follow ML criteria. The non-orthogonal structure of the MF leads to the colouring of the noise. Therefore, the derived ML detector was shown to account for the colouring of the noise, where a derived upper bound showed that ignoring this effect leads to error performance deterioration. Numerical simulations have confirmed that the same performance as the IMGS based demodulator is achievable. Hence, the new demodulator is considered superior to the IMGS due to the simple implementation potential.

The ML detector of the MF based system requires an exhaustive search over all possibly transmitted combinations of the input symbols. With the increase in the number of subcarriers and/or the modulation level of the input symbols, the ML becomes overly complex. This issue was faced in the IMGS based SEFDM system and motivated the search for lower complexity alternatives. Following the same footsteps, and in order to reduce the complexity of the optimal detector for the MF, the SD algorithm was applied for the MF based SEFDM system. The SD algorithm performs the search for the ML solution for the MF based system with reduced complexity. Numerical simulations have shown that the MF system can achieve the optimal solution and also the same error performance as the IMGS based system. Results for the complexity of detection have confirmed that the SD algorithm required the same complexity regardless of using IMGS or MF for the demodulation of the signal.

The work in this chapter shows that for the demodulation of the SEFDM signal a reduced complexity MF demodulator can be used. The MF demodulator reduces the complexity of the system by eliminating the orthonormalization stage. Furthermore, an efficient implementation structures based on the general purpose DFT or equivalently FFT are proposed, thus facilitating more complexity reduction and supporting reconfigurable structures and compatibility with existing system in a matching manners to the transmitter design. Investigations of the error performance of the optimal solution and its low complexity realization via SD algorithms confirm that no error penalty is expected with the use of the MF for demodulation. In addition, no additional complexity for the detector is expected as confirmed by numerical results for SD nodes visits. Moreover, demodulation based on DFT bases as an alternative set of orthonormal bases is considered in this chapter. The optimal ML detector for this case is derived and evaluated numerically. The DFT bases demodulator achieves the same error performance as MF and IMGS. Nevertheless, the DFT based demodulator does not support detection with the SD algorithm, hence, poses restriction on the size of the system as opposed to MF or IMGS.

In conclusion, the MF demodulator is proposed as a new simpler alternative to IMGS demodulation with no penalties in terms of error performance nor complexity increases in the detection stage. The MF based demodulator poses no restrictions on the detector whether being ML or SD. Demodulation using DFT bases is recommended for small sized

systems and ML detection. These recommendations result in localizing the complexity of the SEFDM receiver at the detection stage. The next chapter is dedicated to the design and testing of low complexity detectors that can provide attractive error performance.

Chapter 6

Low Complexity Detectors for SEFDM System

6.1 Introduction

Analysis of the SEFDM signal has shown that the signal suffers from intercarrier interference (ICI) resulting from the non-orthogonal structure of the subcarriers. Consequently, the detection of the SEFDM signal requires efficient handling of such ICI. Regardless of which method is followed for the demodulation of the SEFDM signal, chapter 5 showed that the ML detector can produce optimal BER performance but is prohibitively complex. SEFDM literature has shown that simple linear detectors fail to provide competitive BER performance for moderate bandwidth savings and/or number of subcarriers. On the other hand iterative detection techniques are impaired by high realization complexity and hence constitute a challenge for the hardware implementation of SEFDM systems. Thus, the pursuit for low complexity detectors remains a challenge and is the focus of this chapter.

This chapter presents the details of the design of several low complexity detectors that can achieve competitive error performance. Two new linear detectors are proposed for the SEFDM system and are shown to demonstrate superior BER performance than previously proposed designs using Zero Forcing (ZF) and Minimum Mean Square Error (MMSE), with almost the same complexity. Firstly, a detector based on the Truncated

Singular Value Decomposition (TSVD) is proposed. The TSVD based detector tackles the ill conditioning attribute of the SEFDM system that impairs the ZF and MMSE performance. In principle, the TSVD technique provides an approximate well conditioned system to the one in question, thus can exhibit more resilience to noise effects. Investigations of the error performance of the TSVD detector show superior performance to ZF and MMSE. In addition, the TSVD based detector support systems with large number of subcarriers while maintaining an error performance close to that of the systems with a small number of subcarriers. Moreover, another linear detector that invests in the knowledge of the intercarrier interference (ICI) pattern in the SEFDM system is proposed. The detector is termed Selective Equalization (SelE) as it only equalizes for the interference of selected subcarriers. The choice of the selected subcarriers is based on their ICI contributions. The SelE detector has shown superior performance to the ZF and MMSE and a similar performance to the TSVD.

Furthermore, new modified iterative detector that overcomes the variable complexity constraint of SD is proposed and evaluated. The Fixed Sphere Decoder (FSD) is first applied to offer a fixed complexity detection algorithm. The error performance is sub-optimal but can be enhanced by increasing the complexity. The work then proceeds to propose a hybrid FSD-TSVD detector that combines the BER performance enhancement facilitated by the TSVD and the fixed complexity of the FSD to produce a new SEFDM detector that answers both questions of performance and complexity. Overall, the proposed FSD-TSVD detector enhances the error performance of the standard FSD without introducing any premium in computational cost.

6.2 The Truncated Singular Value Decomposition (TSVD)

Analysis of the SEFDM system presented in chapter 3 has confirmed that the system is ill conditioned and thus the SEFDM problem is classified as a discrete ill posed problem. As the conditioning of the system worsens, the system becomes sensitive to any perturbations (i.e. noise). In the mathematical literature, this class of problems has been addressed, where the regularization, as introduced in section 2.7.6, is an example of manipulating ill posed problems to produce a more stable solution. In this section, the use of the Truncated Singular Value Decomposition (TSVD) [138, 139] is proposed

for the detection of the SEFDM signals. TSVD is a method widely used to produce a better quality pseudoinverse of ill conditioned matrices. Thus, TSVD is proposed to manage the effect of the ill conditioning of the SEFDM system, and hence provide better BER performance when compared to ZF and MMSE detectors.

In essence, TSVD is a method to generate an approximated inverse of an ill conditioned matrix to yield a modified least squares problem that is less sensitive to perturbations. The approximated inverse is derived by finding the Singular Value Decomposition (SVD) of the argument matrix and then truncating its small singularvalues that overly multiply the noise. The TSVD detector solves the MF based SEFDM system described by equation (5.1) by first finding the SVD of the $\mathbf{C}$ matrix given as

$$\mathbf{C} = \mathbf{U}\mathbf{\Sigma}\mathbf{V}^{*}, \tag{6.1}$$

where $\mathbf{U}$ and $\mathbf{V}$ are unitary matrices whose columns are the eigenvectors of $\mathbf{C}\mathbf{C}^{*}$ and $\mathbf{C}^{*}\mathbf{C}$, respectively and $\mathbf{\Sigma}$ =diag $(\sigma_1, \sigma_2, \cdots, \sigma_N)$, for σ_i the i^{th} singular value of $\mathbf{C}$. The TSVD based pseudoinverse of $\mathbf{C}$, denoted by $\mathbf{C}_\xi$, is defined as

$$\mathbf{C}_\xi = \mathbf{V}\mathbf{\Sigma}_\xi^{-\mathbf{1}}\mathbf{U}^{*}, \tag{6.2}$$

where $\mathbf{\Sigma}_\xi^{-\mathbf{1}} = \text{diag}\,(1/\sigma_1, 1/\sigma_2, \cdots, 1/\sigma_\xi, 0, \cdots, 0)$, ξ is the truncation index. The truncation index, ξ, defines the number of singularvalues that are accepted, and therefore determines the quality of the generated matrix and consequently the obtained solution. In other words, to calculate the pseudoinverse, TSVD filters out the elements in $\mathbf{\Sigma}^{-1}$ that correspond to small singular values in $\mathbf{\Sigma}$ starting at index $\xi + 1$. The TSVD based detector is then defined as

$$\hat{S}_{TSVD} = \lfloor \mathbf{C}_\xi R \rceil\,. \tag{6.3}$$

The same approach can be applied to the IMGS based system to arrive at a solution

$$\hat{S}_{TSVD} = \lfloor \mathbf{M}_\xi R \rceil\,, \tag{6.4}$$

where $\mathbf{M}_\xi$ is the TSVD based pseudoinverse of the matrix $\mathbf{M}$ defined in equation (2.11) following the same steps to derive $\mathbf{C}$.

The complexity of the TSVD detector is of similar order as ZF as it only requires the inversion of the matrix which is usually carried out with the aid of the SVD.

6.2.1 The TSVD Truncation Index

The TSVD technique generates an approximated inverse of an ill conditioned matrix. As illustrated in section 6.2, the technique is based on filtering out the effects of the small singular values. Therefore, it is noted that the closeness of the obtained inverse to the original one will depend on the number of filtered out singularvalues. It is crucial to strike a balance between generating a matrix that does not carry any components of the small singularvalues and obtaining an inverse that is still representative of the original matrix. Thus, the choice of the truncation index becomes a dominant factor of the quality of the obtained solution and has been the focus of research in the subject of solving discrete ill posed problems [140, 141]. In [140] the optimum truncation index is stated to satisfy the picard condition. That is for a system expressed using the generalized singularvalue decomposition, the Fourier coefficients on the right hand side decay faster than the generalized singularvalues. In SEFDM particularly, it has been observed by simulation that αN of the eigenvalues of $\mathbf{C}$ are larger than or equal to 1 while $(1-\alpha)N$ of the eigenvalues quickly decay to values close to 0, as depicted in Fig. 3.10. Therefore, the search for the best detector matrix $\mathbf{C}_\xi$ is performed based on truncation indices around this benchmark.

Particular to the SEFDM system, the quality of the detector matrix $\mathbf{C}_\xi$, which in turn is dependent on the truncation index will be translated to the transmitted symbols estimates and will certainly affect the error performance of the system. Fig. 6.1 and 6.2 illustrate how the BER performance is dependent on the truncation index ξ for the case of BPSK and 4QAM input symbols, respectively. The figures show performance for MF and IMGS based systems and indicate the same behaviour for both systems. Both figures show that the TSVD detector is capable for outperforming the MMSE detection for many truncation index values. Furthermore, the figures show that for different α values there is an optimum value for the truncation index ξ that achieves the lowest BER. It is observed that this optimum value is approximately αN for BPSK input symbols and $\alpha N+1$ for 4QAM input symbols which is consistent with the value anticipated from the conditioning of the $\mathbf{C}$ matrix. The truncation index decides whether the system is

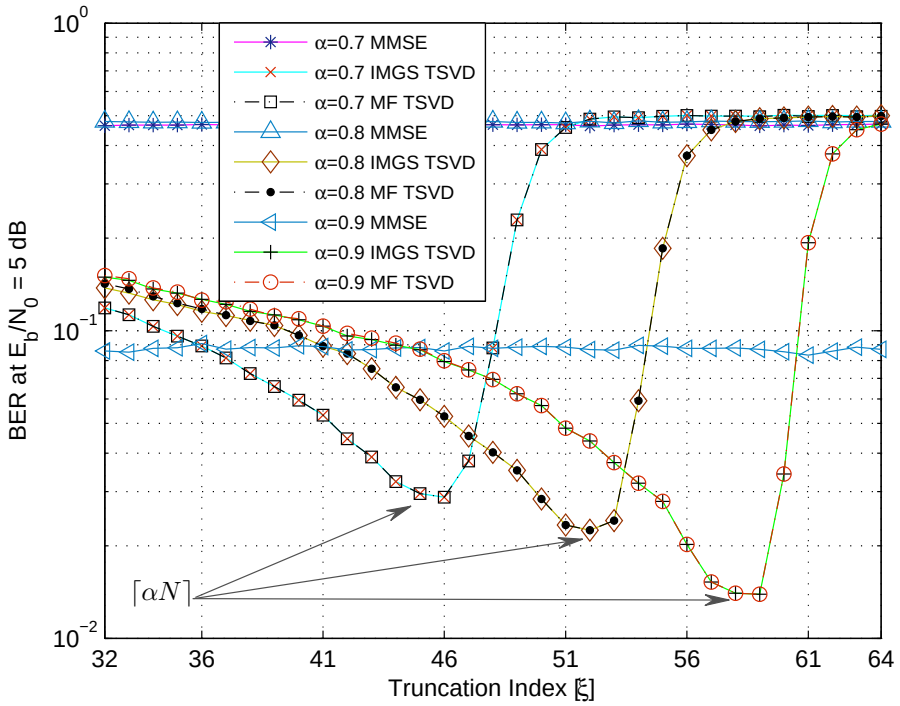

FIGURE 6.1: BER performance of TSVD detector vs the truncation index ξ for a 64 subcarrier system carrying BPSK symbols.

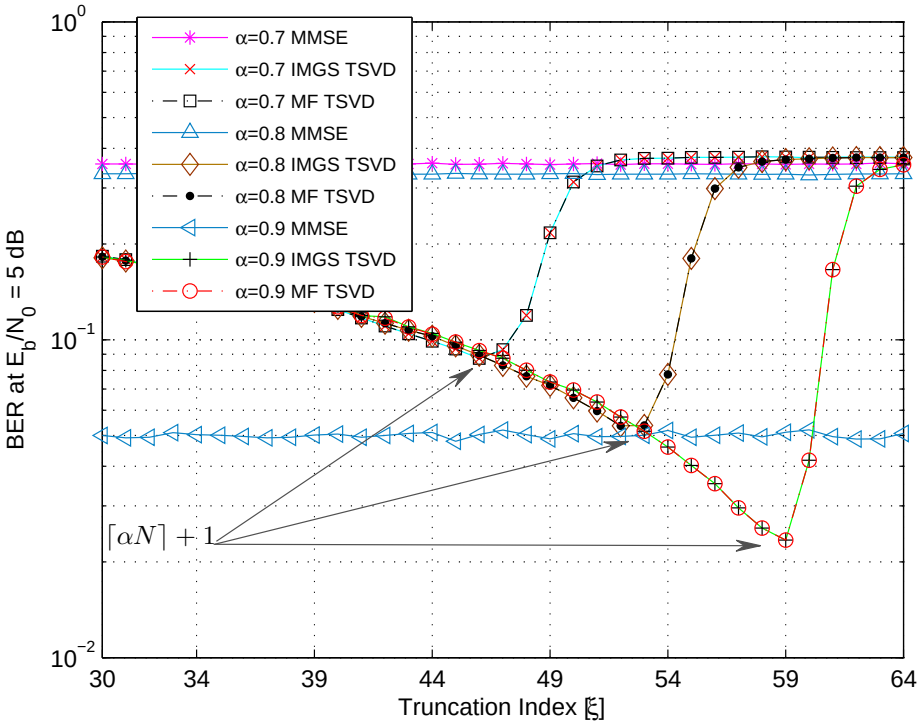

FIGURE 6.2: BER performance of TSVD detector vs the truncation index ξ for a 64 carriers system carrying 4QAM symbols.

optimized for noise or interference, as it decides the closeness of the approximated inverse to the actual one. The optimum point is the one that tackles the ICI while maintaining limited colouring of the noise. For the sake of brevity, detailed performance analysis of the TSVD detector is presented in section 6.4 after the introduction of another improved linear detector in the next section.

6.3 The Selective Equalization (SelE)

Studies of the conditioning of the SEFDM system have shown that the system tends to become ill conditioned with the increase in the number of subcarriers and/or bandwidth compression levels. Thus, linear detection techniques such as ZF and MMSE fail to cope with error rate requirements due to the noise enhancement associated with the ill conditioning. The previous section introduced the use of TSVD for SEFDM signal detection to overcome the ill conditioning effects on the system performance. In this section, a newly developed technique that approaches the ill conditioning of the system from a different angle is presented. The technique exploits the a priori knowledge of the behaviour of the correlation coefficient matrix in order to produce a better estimate of the transmitted message.

Equation (5.25) showed the ZF detector for the MF based system, where all the ICI terms are eliminated by the multiplication with the inverse of the matrix $\mathbf{C}$. Theorem 3.1 has shown that some subcarriers within the SEFDM system will be orthogonal. Furthermore, the formula for the ICI terms derived in equation (3.14) and plotted in Fig. 3.1, shows that in general interference from closer subcarriers is higher than distant ones. Motivated by this finding, a new detector for SEFDM is presented in this section. The detector basically equalizes for the subcarriers that contribute significantly to the total ICI on a given subcarrier. Therefore, a selected subset of the subcarriers is considered by the detector, thus this procedure is termed Selective Equalization (SelE).

In essence, SelE is based on constructing an approximate version of the correlation matrix by discarding the small ICI contributions. A trade off between the closeness to the original system and the simplicity of the detector matrix is to be considered. The SelE can swing between a full equalization of the ICI terms which is merely a ZF

detector to the complete discard of all ICI terms which is equivalent to receiving an SEFDM signal using a demodulator and a slicer.

The SelE detector can be represented by the matrix $\mathbf{C}_\kappa$, defined as

$$\mathbf{C}_\kappa = [\mathbf{C} : c_{m,n} > \kappa], \tag{6.5}$$

where κ is termed the selection parameter and it denotes the minimum accountable interference level measured from the subcarrier in question and will be expressed in dB. Therefore, any ICI term in $\mathbf{C}$ with a difference in power from the subcarrier in question exceeding κ dB will be considered in the equalization process. Recalling that the derived formula for the elements of $\mathbf{C}$ for a normalized system in equation (3.14) shows that the diagonal elements of $\mathbf{C}$ are equal to one, the elements of $\mathbf{C}_\kappa$ can be expressed as

$$\mathbf{C}_\kappa [m,n] = \begin{cases} c_{m,n} & \text{if } [c_{m,n}]_{dB} > \kappa \\ 0 & \text{otherwise} \end{cases}. \tag{6.6}$$

The SelE detector is then defined as

$$\hat{S}_{SelE} = \left\lfloor \mathbf{C}_\kappa^{-1} R \right\rceil. \tag{6.7}$$

The decision of the value of the selection parameter κ will dictate the closeness of the SelE detector to the ZF one. A small value of κ will result in more interference contributions to be considered. Fig. 6.3 and 6.4 depicts the error performance with respect to the value of κ. The performance is compared to that of the TSVD detector with the best truncation index. Both figures show that the performance is dependent on the selection parameter. BER remains at a relatively low level until a specific value of κ is reached for each α after which the performance deteriorates till levelling at ZF performance. Furthermore, the figure shows that the SelE concept for the IMGS based system is not capable of generating tangible performance improvement.

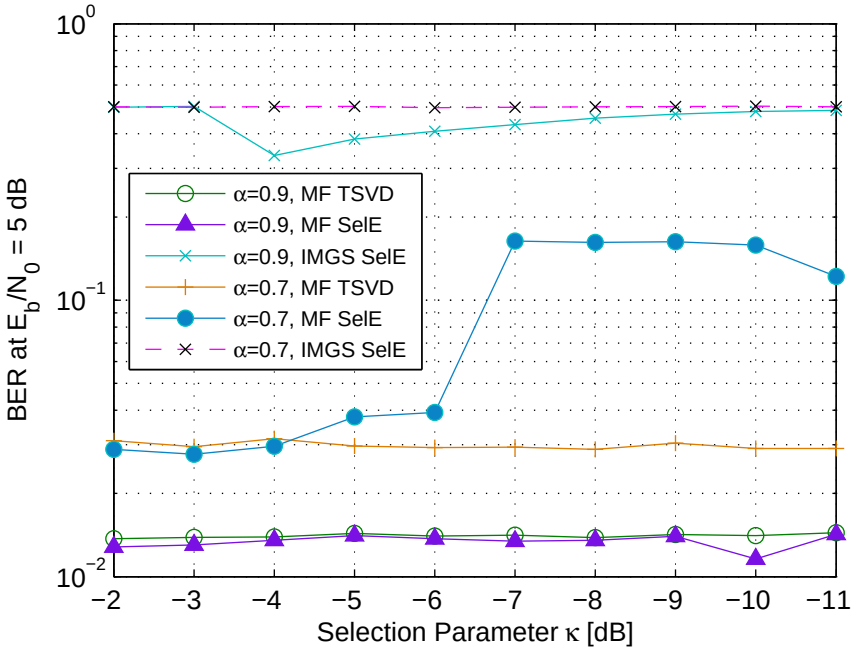

FIGURE 6.3: BER performance of SelE detector vs the selection parameter κ for a 64 subcarrier system carrying BPSK symbols.

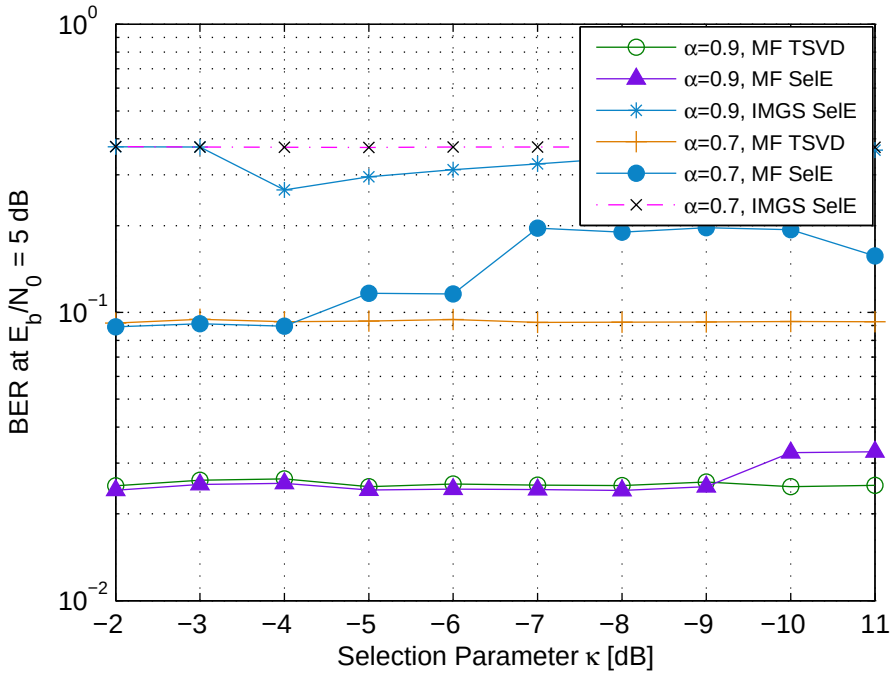

FIGURE 6.4: BER performance of SelE detector vs the selection parameter κ for a 64 subcarrier system carrying 4QAM symbols.

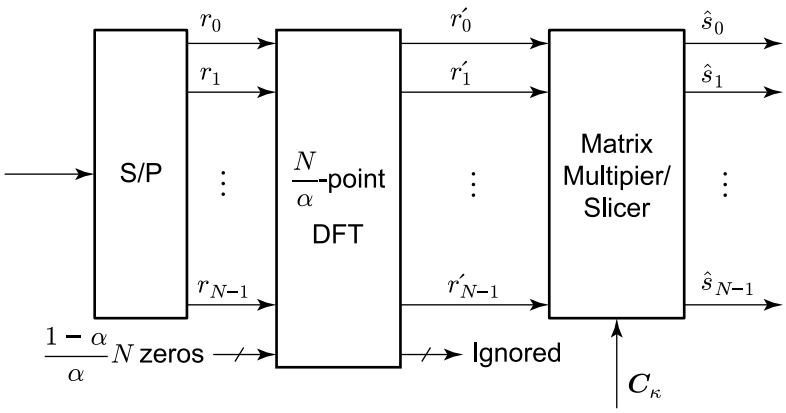

FIGURE 6.5: SelE detector block diagram, $r'_i = R[i]$.

6.4 TSVD and SelE Detectors Performance Assessment

Fig. 6.5 depicts a block diagram for an SEFDM system employing SelE. The detector part requires a multiplier followed by a slicer. The TSVD detector will differ from the one in Fig. 6.5by the input matrix $\mathbf{C}_\xi$ in place of $\mathbf{C}_\kappa$. The performance of TSVD and SelE detectors in terms of BER is assessed by means of numerical simulations of systems with a variable number of subcarriers and bandwidth compression levels. The systems assume perfect knowledge of the subcarriers frequencies on the reception side and that the received signal is impaired by AWGN. The results displayed in this section show the performance for the MF based system only because for the TSVD detector the MF and IMGS based systems achieves the same performance as shown in Fig. 6.1 and 6.2 and that for the SelE system the IMGS based failed to achieve error performance improvement.

Fig. 6.6 depicts the BER performance of the TSVD and SelE detectors for different α values for a 64 subcarrier system at $E_b/N_0 = 5$ dB, along with MMSE and ZF. Both TSVD and SelE provided remarkable error performance improvement for BPSK and 4QAM input symbols specially BPSK case. Moreover, for $\alpha > 0.5$, the figure shows that for BPSK input symbols, the SelE provided performance slightly better than that of the TSVD while for QPSK the performance is the same. In addition, for the case of BPSK input symbols, the figure shows that for $\alpha = 0.5$, both the TSVD and SelE systems achieve the same performance as the FOFDM system.

Fig. 6.7 and 6.8 depict the BER for the TSVD and SelE detectors for BPSK and 4QAM input symbols for different numbers of subcarriers at $E_b/N_0 = 5$ dB, optimum

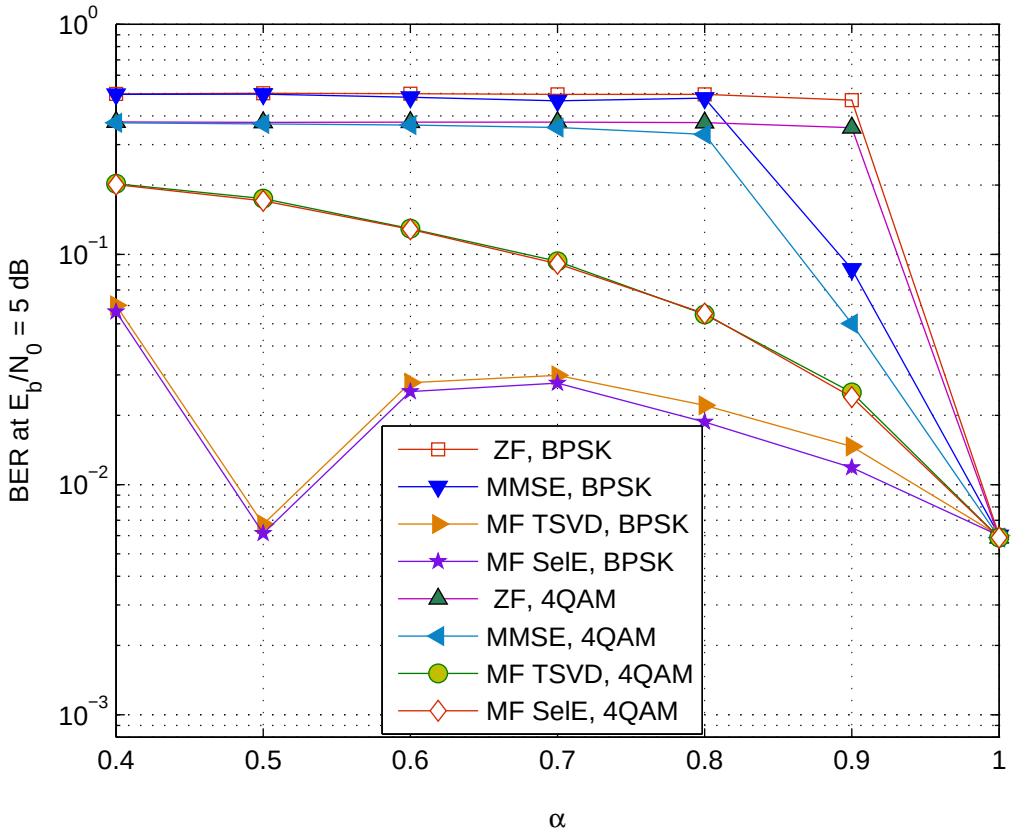

FIGURE 6.6: BER performance of TSVD and SelE detectors for $\alpha = 0.4 - 1$, 64 subcarrier system, $\xi = \alpha N + 1$ and $\kappa = -10$ dB.

truncation indices and selection parameters. Both figures indicate that the advantage of both detectors becomes more prominent with the increase in the number of subcarriers. For a small number of subcarriers (4-16) there is a small BER degradation observed with the increase in the number of subcarriers, however, for relatively larger numbers of subcarriers the performance saturates and ceases to deteriorate.

Fig. 6.9 and 6.10 show the BER performance with respect to E_b/N_0 for BPSK and 4QAM input symbols, respectively. Both figures demonstrate substantial BER improvement when compared to MMSE for both detectors. Furthermore, Fig. 6.9 demonstrates BER advantage for the SelE detector over the TSVD detector for systems with BPSK input symbols, whereas for 4QAM input symbols both detectors achieved the same error performance as seen in Fig. 6.10.

Overall, both techniques provided substantial BER improvement over ZF and MMSE. Furthermore, the techniques enabled the use of large numbers of subcarriers where ZF

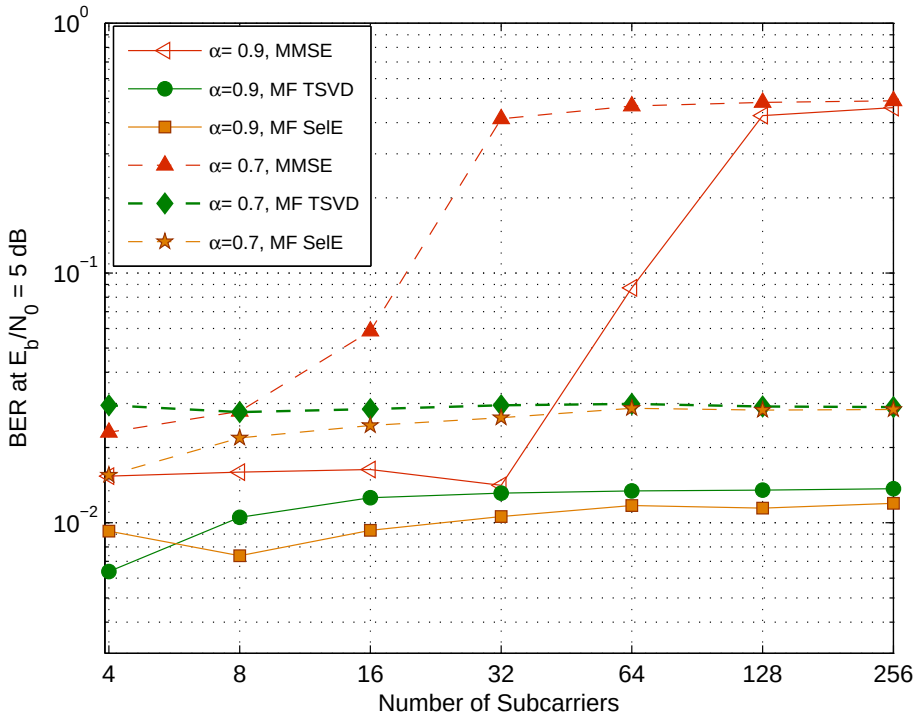

FIGURE 6.7: BER performance of TSVD and SelE detectors for $\alpha = 0.7, 0.9$, 64 subcarrier system, $\kappa = -4, -10$ dB, respectively and $\xi = \alpha N$.

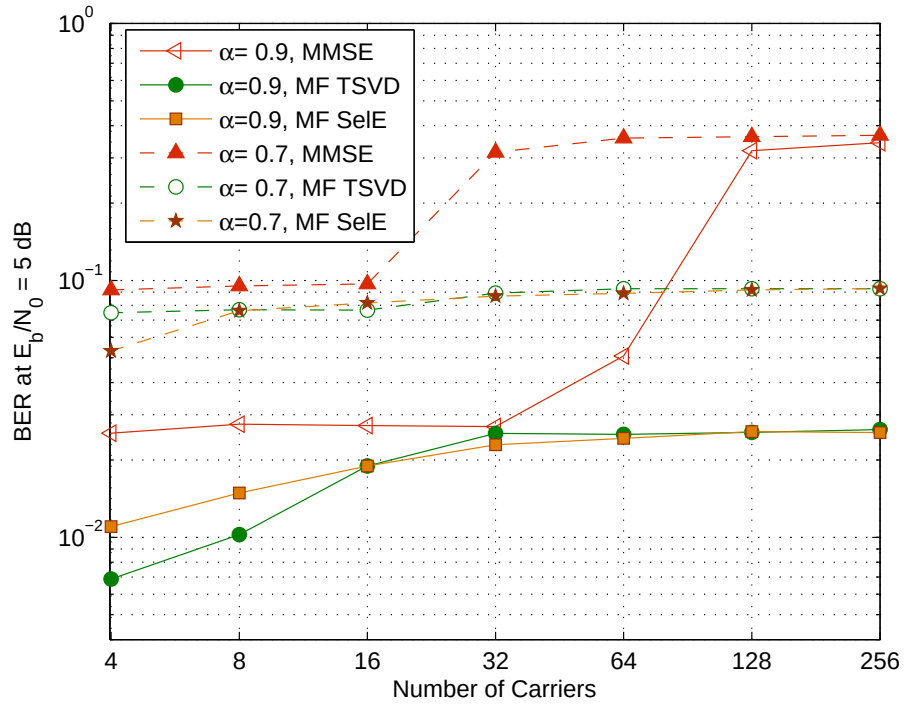

FIGURE 6.8: BER performance of TSVD and SelE detectors for $\alpha = 0.7, 0.9$, 64 subcarrier system, $\kappa = -4, -9$ dB, respectively and $\xi = \alpha N + 1$.

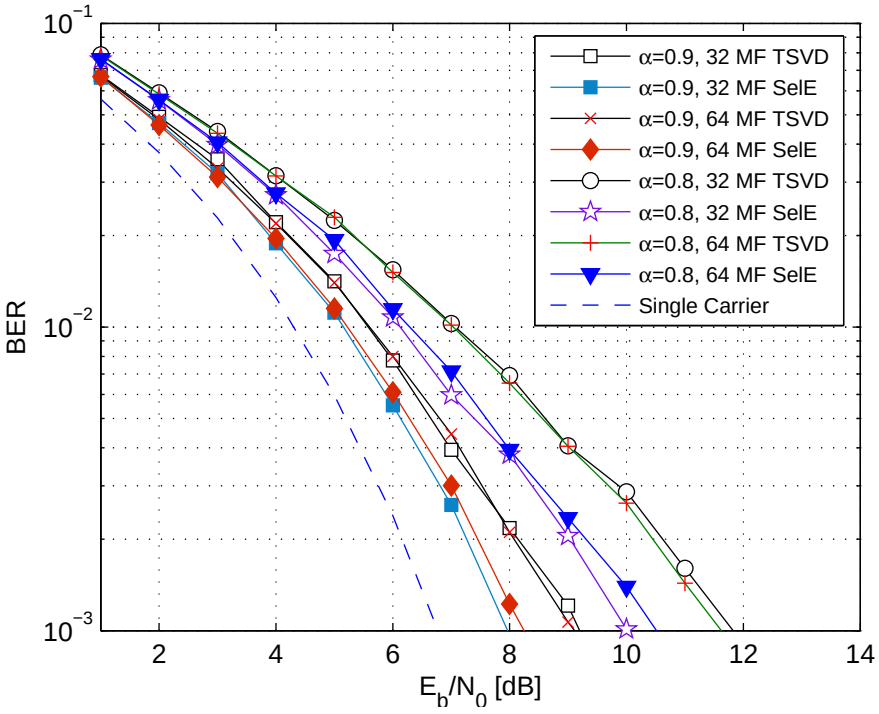

FIGURE 6.9: BER for TSVD and SelE detection for systems with $\alpha = 0.8, 0.9$; 32 and 64 subcarriers and BPSK input symbols.

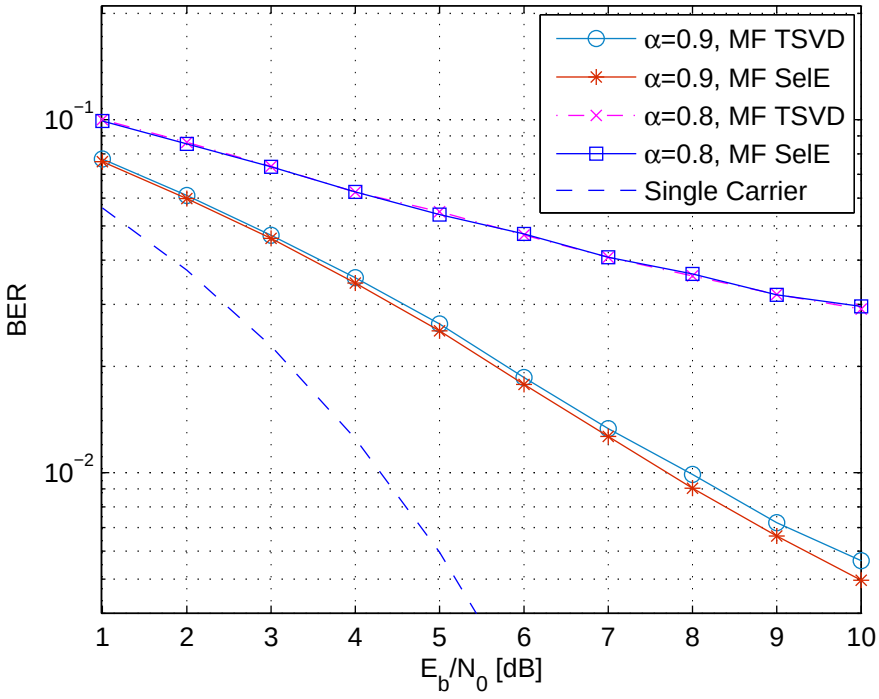

FIGURE 6.10: BER for TSVD and SelE detection for systems with $\alpha = 0.8, 0.9$; 32 subcarriers and 4QAM input symbols.

and MMSE totally fail. TSVD achieves the same performance for both IMGS and MF based systems whereas SelE suits the MF based system only. Nevertheless, the design of the SelE detector is simpler than the TSVD as it eliminates the need to perform SVD. Despite the substantial BER reduction, the BER performance is still not comparable to OFDM. These results are provided here to demonstrate the BER performance enhancement offered by the techniques which is the base for further performance enhancement when combined with sophisticated detectors to be introduced in the following sections.

6.5 The Fixed Sphere Decoder (FSD)

The detection of SEFDM with TSVD or SelE results in remarkable BER improvements over the use of ZF and MMSE. In addition, both TSVD and SelE have demonstrated the support of systems with a large number of subcarriers. The error rate performance is shown to be stable with the change in the number of subcarriers for a given α value. However, the performance is still sub-optimal specially for higher cardinality modulations, thus, in this section, detection of SEFDM with iterative detectors is revisited with a special focus on fixing the complexity while maintaining attractive BER performance.

Detection of the SEFDM system with Sphere Decoders (SD) as proposed in [36] for IMGS based systems has shown the ability to achieve optimal error performance. The SD solution in conjunction with the MF based demodulator as presented in chapter 5 has demonstrated the same performance as the IMGS based system. The SD algorithm obtains the ML solution by allowing the search to continue until the ML estimate is reached, therefore the complexity of the algorithm is variable and depends on the noise and the properties of the system. This behaviour is illustrated in Fig. 6.11 showing the number of node visits taken to decode each symbol from 1000 SEFDM symbols for each E_b/N_0. The figure shows that the number of node visits decrease with the increase in E_b/N_0, however, for the same E_b/N_0 value the node visits required for decoding a single SEFDM symbol varies. Attempts to tame the complexity of the SD algorithm appeared in [74] in a quasi-optimal detector combining semidefinite programming (SDP) and SD, however, the complexity still remains variable.

The variable complexity and the sequential nature of the SD algorithm can impede the implementation of communication system.Therefore, the Fixed complexity Sphere

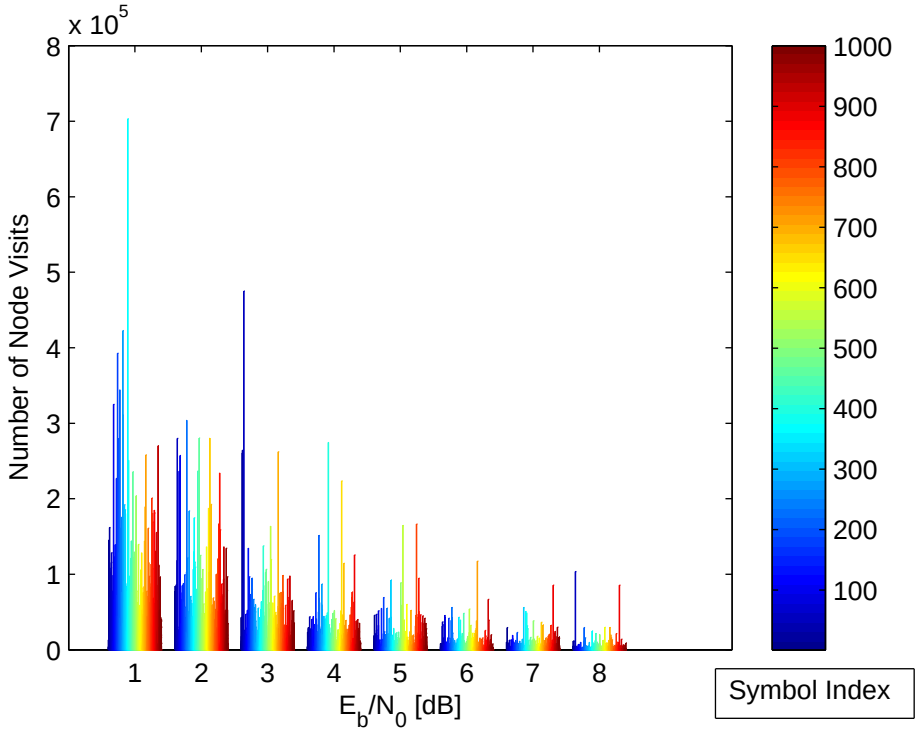

FIGURE 6.11: Number of node visits to decode each of 1000 SEFDM symbols using SD algorithm for each value of E_b/N_0, for a 16 subcarrier system with $\alpha = 0.8$ and 4QAM input symbols.

Decoder (FSD) was introduced for Multiple Input Multiple Output (MIMO) systems detection [142, 143, 144]. The FSD fixes the complexity of the SD by restricting the search space to a fixed size subspace. The fixed complexity lends the technique more suitable to hardware implementation [145]. However, the FSD does not guarantee an optimal solution like the standard SD since it enumerates a fraction of the points within the sphere search space. In this section, the FSD algorithm is applied to the SEFDM problem.

6.5.1 FSD Application to SEFDM System

The FSD algorithm fixes the complexity of the SD algorithm by restricting the search within a limited subspace of the problem. As the conventional SD, FSD converts the SEFDM problem to an equivalent depth-first problem. At every level, a fixed number of nodes, termed here as the tree width, are examined. The FSD estimate is given by

$$\hat{S}_{FSD} = \min_{\tilde{S} \subset \mathcal{H},\, \tilde{s} \in M} \left\| \mathbf{L} \left(P - \tilde{S} \right) \right\|^2 \leq \breve{g}, \tag{6.8}$$

where $\mathbf{L}$ defined from the Cholesky Decomposition in equation (5.22) $\mathcal{H}$ is the search subspace of the FSD algorithm of which $\tilde{S}$ is a candidate vector, P is the unconstrained ML estimate defined in equation (5.21) and $\breve{g}$ is the radius of the search sphere. $\breve{g}$ corresponds to the distance from the ZF estimate $\hat{S}_{ZF}$ and is given by $\breve{g} = \left\| R - \mathbf{C}\hat{S}_{ZF} \right\|^2$, where $\hat{S}_{ZF}$ is obtained from $\hat{S}_{ZF} = \left\lfloor \mathbf{C}^{-1} R \right\rceil$.

The FSD relies on the assumption that as the search continues downwards the levels, the probability of finding a node within the sphere decreases, that is

$$\mathrm{E}\left[d_N\right] \geq \mathrm{E}\left[d_{N-1}\right] \cdots \geq \mathrm{E}\left[d_1\right], \tag{6.9}$$

where d_i is number of candidate nodes for level i and $\mathrm{E}\left[\cdot\right]$ is the expected value. This constraint was proved for MIMO systems in [142] and [143] and here it is proved that it holds for the SEFDM system. Starting by emphasizing that any retained node at search level y, should satisfy

$$\left|p_y - s\right|^2 \leq \breve{g}_y / l_{yy}^2, \tag{6.10}$$

the proof proceeds to show that the RHS of (2.24) decreases as the search moves downwards the spheres and this indicates the probability of having constellation points satisfying the condition should decrease. It is by definition that the radius $\breve{g}_y$ satisfy

$$\breve{g} \geq \breve{g}_{N-1} \geq \cdots \geq \breve{g}_1. \tag{6.11}$$

By the definition of the Cholesky Decomposition, the elements of $\mathbf{L}$ are given by

$$l_{yy} = \sqrt{c_{yy} - \sum_{k=1}^{y} l_{k,y} l_{k,y}^*}\ , \tag{6.12}$$

and

$$l_{yi} = (1/l_{yy}) \left(c_{yi} - \sum_{k=1}^{y} l_{k,i} l_{k,y}^* \right). \tag{6.13}$$

However, for the SEFDM system c_{yy} is deterministic and can be calculated based on equation (3.14) as

$$c_{yy} = 1. \tag{6.14}$$

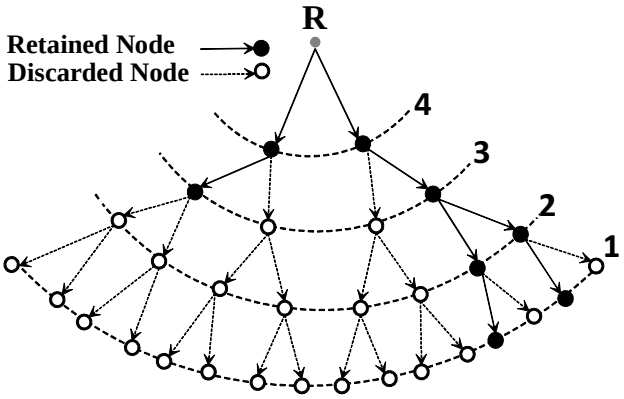

FIGURE 6.12: The FSD tree search algorithm with tree width equal to 2.

Equation (6.14) shows c_{yy} and recalling that $\mathbf{C}$ is Toeplitz, it is straight forward that

$$l_{NN} \leq l_{N-1N-1} \leq \cdots \leq l_{11}. \tag{6.15}$$

Equations (6.11) and (6.15) lead to

$$\frac{\breve{g}}{l_{NN}} \geq \frac{\breve{g}_{N-1}}{l_{N-1N-1}} \geq \cdots \geq \frac{\breve{g}_1}{l_{11}} \tag{6.16}$$

which in turn indicates that the probability of nodes satisfying equation (6.10) decreases as the search moves from level y to level $y-1$ due to the shrinking of the parameter $\breve{g}_i/l_{ii}$. This relationship justifies how the FSD can reach a solution even within the limited search space.

Fig. 6.12 illustrates the FSD tree search for a 4 subcarrier system with BPSK symbols. In this particular example, the FSD tree width is fixed to 2. At each level, a fixed number of nodes (=2) is retained, whereas the discarded nodes at that level result in discarding all their children nodes. Fig. 6.13 is a functional diagram for the FSD algorithm as implemented in the SEFDM system. The algorithm has a fixed number of iterations. Some steps for the initialization of the algorithm are independent of the decoded symbols, thus can be calculated once and stored for the duration of the transmission as long as the number of subcarriers and bandwidth compression level remain the same.

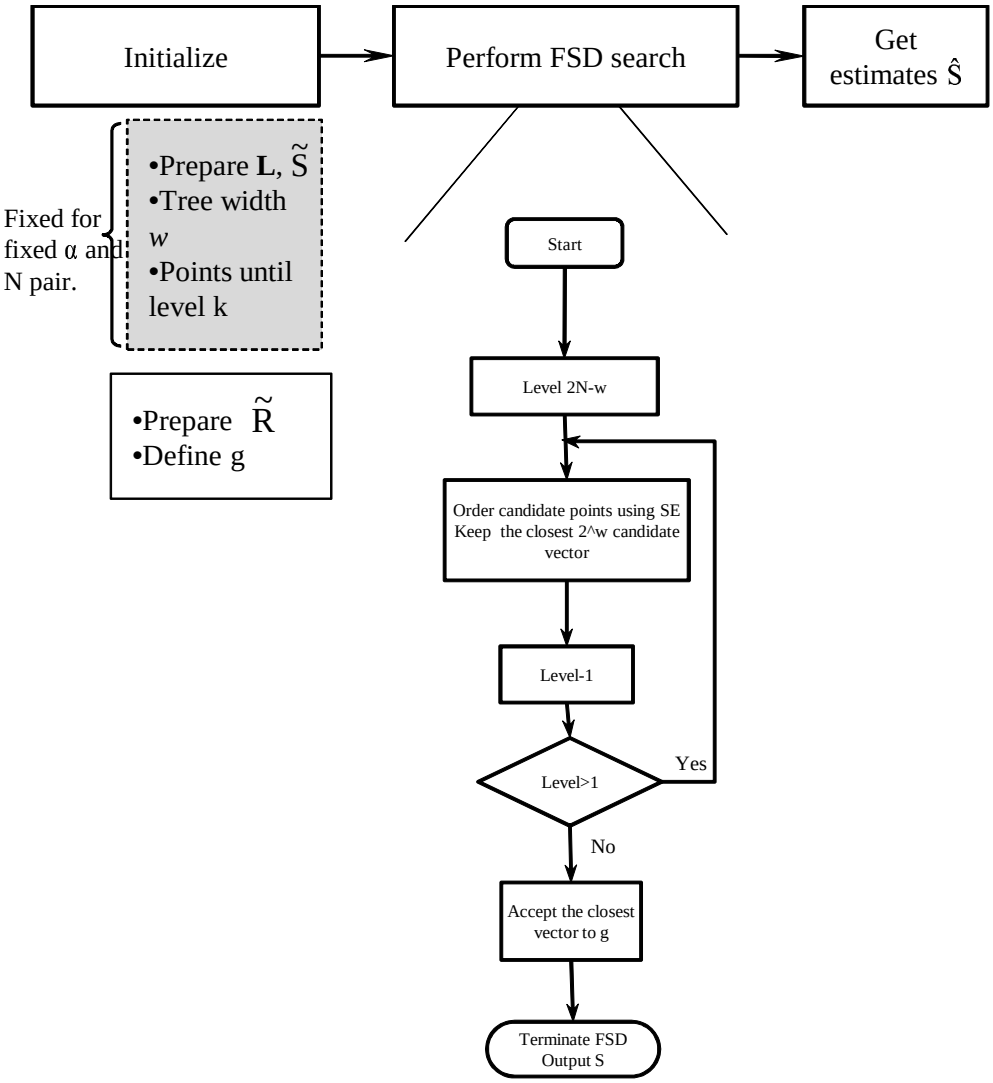

FIGURE 6.13: The FSD functional diagram.

6.5.1.1 Complexity Analysis

The FSD enumerates a number of w nodes corresponding to the tree width. This means that from level k where $k = \log_2 w$, a number of $w \log_2 M$ where M is the constellation cardinality will be examined. From the first search level which corresponds to the level number $2N$, where N is the number of subcarriers, until the level number $2N - k$ all the nodes will be retained, hence can be added to the initialization of the decoder stage. The algorithm will have $2N - k$ iterations, where in each iteration number of $w \log_2 M$ points will be examined. Furthermore, the decision on the distance of all the nodes in the FSD subset is independent from each other and can be performed simultaneously.

The overall number of effective nodes visits will be equal to the $2N - k$ for a system employing $w \log_2 M$ parallel processing capabilities.

6.5.2 FSD Design Concepts

Due to the limitation of the SD search in a subset of the points within the initial hypersphere, the choice of the subset $\mathcal{H}$ and its size are crucial determinants of the performance of the FSD algorithm as they directly affect the probability of reaching the optimum solution. The quality of the initial estimate plays a significant role in the determination of the search subset as it defines the initial radius, hence defines which candidate points are included in the FSD search space. The size of the search subset is a design parameter that may be set according to the targeted BER performance and/or detection complexity. One main difference between SEFDM and MIMO systems is that SEFDM aims to accommodate a large number of subcarriers whereas the typical maximum order of a MIMO system is 4×4, therefore, it is expected that the tree width for SEFDM will include a higher number of nodes than MIMO although the ratio of the searched nodes to the overall problem space may be smaller.

In this work, at each tree level a fixed number of nodes corresponding to the tree width are considered. The decision on the next level nodes is based on Schnorr-Euchner (SE) enumeration [82] of the constellation candidates. SE orders the children nodes based on their respective distances from the received signal statistics vector or equivalently from the centre point decided by P in equation (5.21). At the end of the search, the retained points will be distinguished by their distance from the statistics point and the closest point is accepted.

Fig. 6.14 depicts an FSD based SEFDM detector. The design of the FSD block is simpler than SD and allows the trade-off between complexity and error performance which can be implemented as a reconfigurable architecture. Furthermore, the FSD is suitable for parallel processing as it allows for the independent checking of candidate nodes within a tree level.

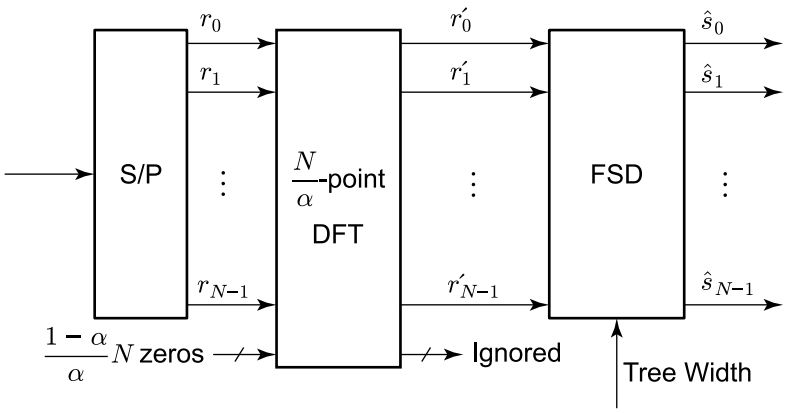

FIGURE 6.14: FSD detection block diagram, $r'_i = R[i]$.

6.5.3 Performance Investigations

Performance of the FSD algorithm for SEFDM detection was evaluated in an AWGN channel by numerical simulations. BER performance is recorded for FSD and SD for different tree widths and different system settings. Tests of the FSD in AWGN are carried out to verify that the proposed techniques are fundamentally valid, where the extension to fading channels is covered in chapter 8. The simulations considered 4QAM modulated input symbols as BPSK symbols can be efficiently detected with linear detectors with a attractive quality.

Fig. 6.15 shows the performance of the FSD detector for different values of E_b/N_0 for a 16 subcarrier system with $\alpha = 0.8$ carrying 4QAM input symbols. The figure shows that the FSD detector provides BER performance that approaches SD with the increase in the tree width which is effectively the increase of the size of the search subset. Noting that the ML search space of the system is given by $M^N = 4^{16} (= 4.3 \times 10^9)$, and the simulations checked for tree widths of 2^4 $(= 16)$, 2^6 $(= 64)$ and 2^8 $(= 256)$, it is clear that the FSD requires reduced complexity at the cost of BER degradation.

Fig. 6.16 shows the FSD performance for different levels of bandwidth compression at $E_b/N_0 = 5$ dB. The figure shows that the FSD performance approaches SD with the increase in α. In addition, the figure confirms that the deviation from the SD performance is inversely proportional to the complexity, which is an expected result of increasing the search subset size.

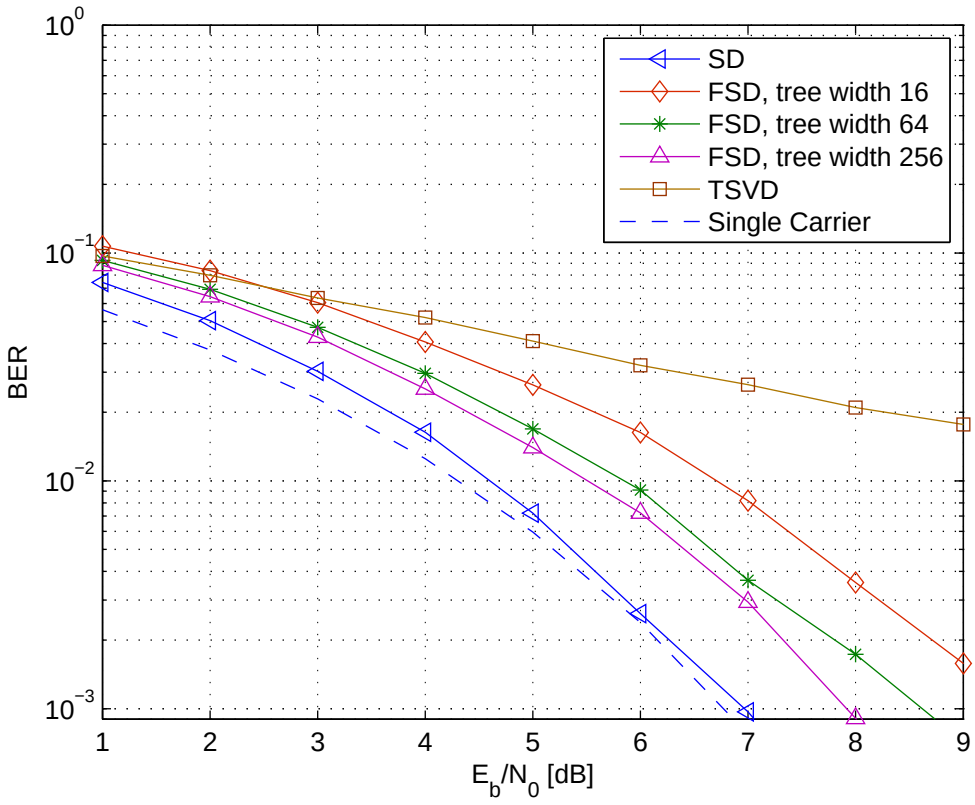

FIGURE 6.15: BER performance of the FSD detector for $\alpha = 0.8$ and 16 subcarrier system carrying 4QAM symbols for maximum tree width of 16, 64 and 256.

Fig. 6.17 shows the BER improvement with the increase in the tree width for $\alpha = 0.7, 0.8$ and 0.9 at $E_b/N_0 = 5$ dB. The figure confirms the improvement with the increase in the search subspace, however, the figure indicates that this advantage is not in linear proportion to the increase in tree width and effectively the complexity. Furthermore, the figure indicates that the effect of the size of the search subspace increases with the reduction in α (i.e. tree width of 1024 is needed in the case of $\alpha = 0.7$ in contrast to 64 for $\alpha = 0.8$ to achieve the same BER).

Fig. 6.18 depicts the performance for different values of α for the same tree width of 256. The figure shows the expected deterioration in the error performance with the reduction in the value of α. The main cause is expected to be attributed to the worsening conditioning of the system with the reduction in α value that in turn is reflected in the likelihood of finding the solution within the limited search subspace.

Fig. 6.19 depicts the BER performance for systems with different number of subcarriers for the same decoder tree width of 256. The figure indicates degradation in the error

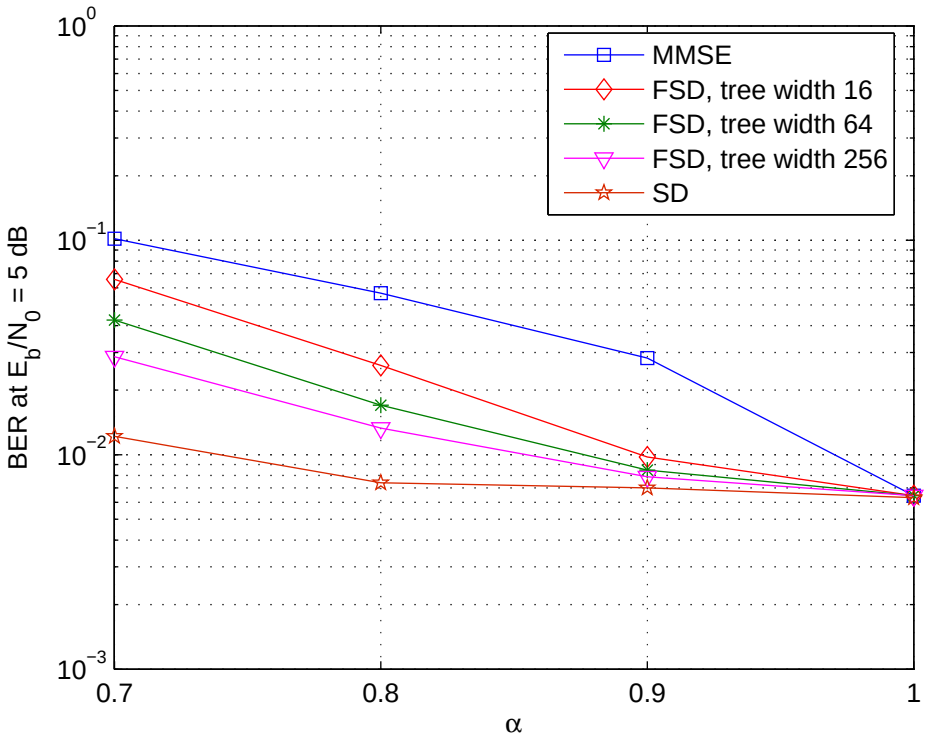

FIGURE 6.16: BER performance of FSD detector for a 16 subcarrier system carrying 4QAM symbols for $\alpha = 0.7 - 1$, $\alpha = 1$ corresponds to OFDM for a maximum tree width of $16, 64$ and 256.

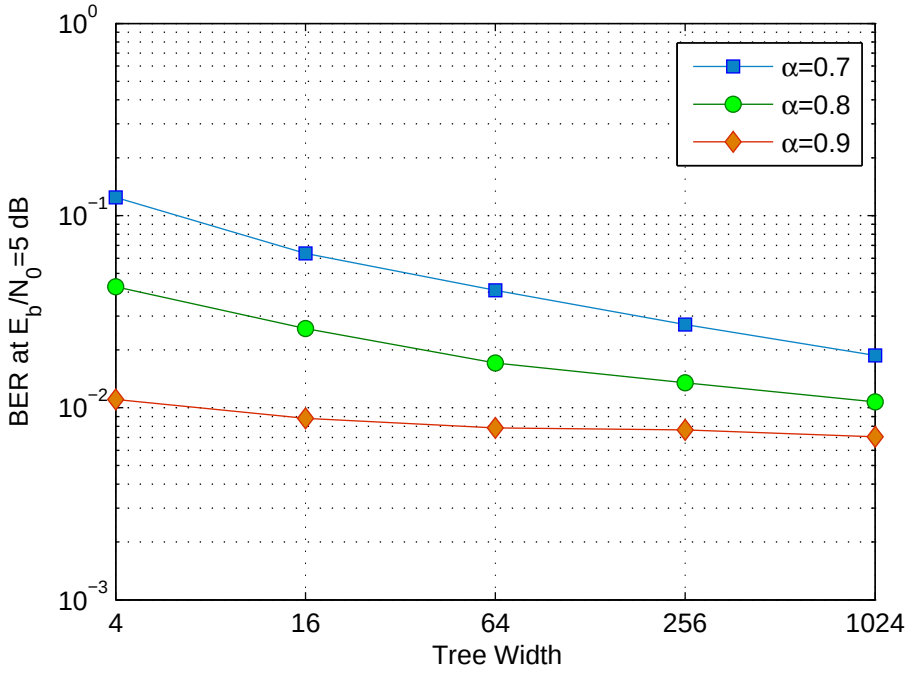

FIGURE 6.17: BER performance of the FSD for different tree width for 16 carriers SEFDM system carrying 4QAM symbols with $\alpha = 0.7, 0.8$ and 0.9.

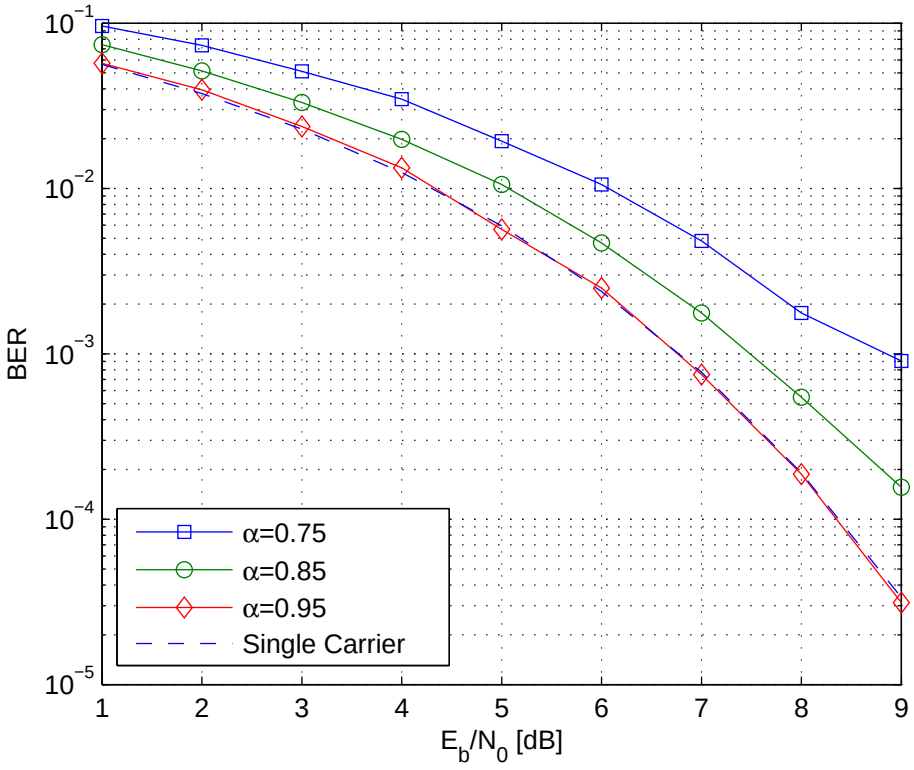

FIGURE 6.18: BER performance of the FSD detector for a 16 subcarrier SEFDM system carrying 4QAM symbols for $\alpha = 0.75 - 0.95$.

performance with the increase in the number of subcarriers. The main reason can be attributed to the fixed tree width as the subspace covered by the decoder for the system with more subcarriers is relatively smaller than the one with fewer subcarriers.

Fig. 6.20 illustrates the complexity of detection by plotting the average number of node visits for the original SD and FSD systems with three different tree widths. The figure shows how the SD complexity varies with E_b/N_0 while the FSD complexity remains constant. In addition, the dynamic range of the average number of node visits for SD is large, thus implementing the algorithm will require the allocation of resources that can accommodate the highest possible number of node visits. The figure reflects the two extreme cases from a completely sequential search to completely parallel search.

Overall, the numerical results confirms that the FSD provides good BER performance at a much reduced complexity, with the highest complexity used in most figures being a very small fraction of the ML search space $\left(\sim 2^8/2^{32}\right)$. Finally, the proposed detector allows the trade off performance and complexity which is governed by the choice of the tree width.

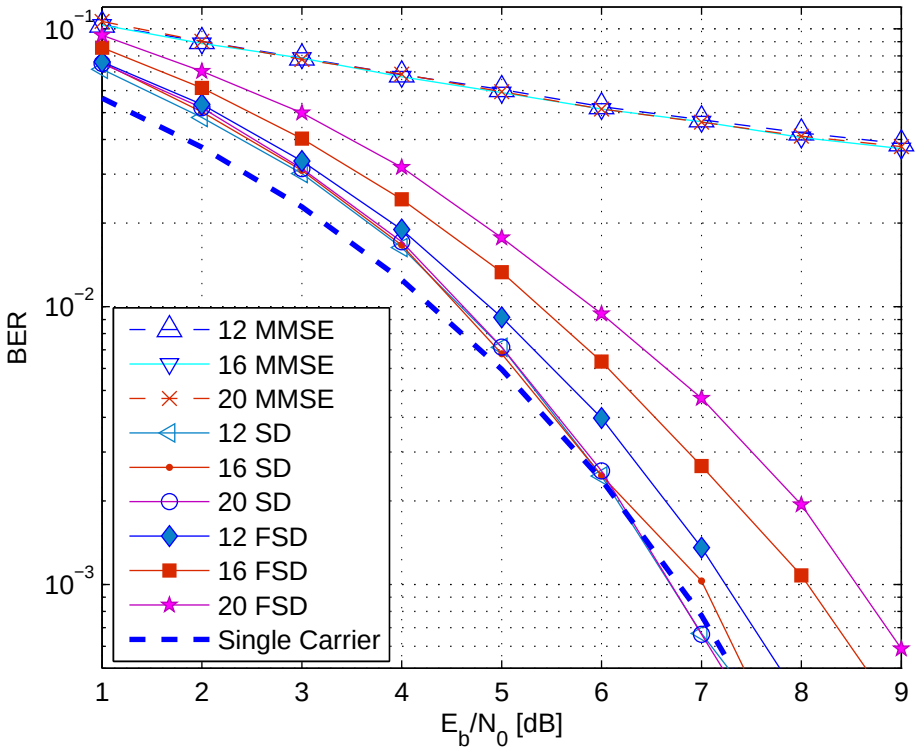

FIGURE 6.19: BER performance of the FSD detector for 12, 16 and 20 subcarrier system for $\alpha = 0.8$ and maximum tree width of 256.

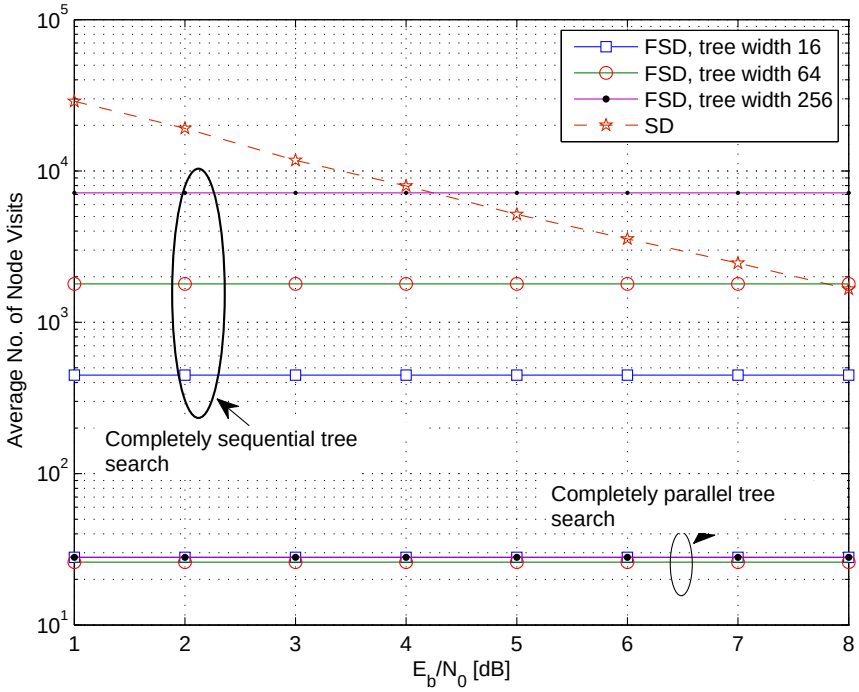

FIGURE 6.20: Average nodes visits for original SD and FSD for maximum tree width of 16, 64 and 256 for a 16 carriers SEFDM system carrying 4QAM symbols for $\alpha = 0.8$.

6.6 Hybrid SEFDM Detectors

Examining the proposed SEFDM detectors show that there is a need to trade off performance for complexity. On one hand, simple detectors can provide low complexity, yet poor error performance or restricted system size and bandwidth compression levels. On the other hand, iterative detectors are capable of delivering attractive error performance at the cost of complexity. In this section, a detector that tackles both issues is presented. This is achieved by employing a simple detector at receiver front end followed by a complex one. The first detector provides an improved seed estimate to the second one. The improved quality of the first estimate facilitates the reduction of the complexity of the second one. The idea of having hybrid detection is not new [90, 85, 91], however, the proposed technique provides enhanced error performance and reduced complexity than previously proposed systems. Furthermore, the new detector facilitates fixing the complexity by employing the FSD algorithm at receiver back end.

6.6.1 The FSD-TSVD Detector

The FSD constrains the subspace of the search covered by the original SD algorithm, thus fixes the complexity but no longer guarantees optimal solution. Noting that the FSD relies on the unconstrained ML estimate P obtained by matrix division, the accuracy of the evaluation of the estimate P can affect the FSD solution. Particular to the SEFDM system, this estimate will suffer from the ill conditioning of the system. Therefore, in this section it is proposed to combine the concepts of the TSVD detector with the FSD to cope better with the ill conditioning of the system and consequently enhance the BER performance and/or reduce complexity.

The combined FSD-TSVD detector, applies TSVD detection concepts to obtain the unconstrained ML estimate P and an initial estimate of the transmitted symbols $\hat{S}_{TSVD}$. The initial estimate $\hat{S}_{TSVD}$ provides a benchmark for the tested points in the FSD algorithm. The FSD solution, therefore, has to be closer to the statistics points than the estimate $\hat{S}_{TSVD}$. Recalling that the estimate $\hat{S}_{TSVD}$ is of better quality than the ZF or MMSE estimates as discussed in section 6.4, the accuracy of the FSD part of the detector will improve consequently. Furthermore, applying TSVD concepts to obtain

the unconstrained estimate P results in improving the accuracy of the FSD, as for ill conditioned systems the TSVD gives a better solution when compared to exact inverses.

In terms of complexity, the TSVD can be computed using a QR factorization of the matrix $\mathbf{C}$ [146], which can be exchanged with the Cholesky decomposition in the FSD algorithm. Fig. 6.21 depicts the combined FSD-TSVD detector. The detector starts by finding the TSVD estimate of the transmitted symbols as in (6.3). This estimate is then used to calculate the radius that positions the TSVD estimate at the surface of the sphere as

$$\hat{g} = \left\| \mathbf{\Phi}^{*^{-1}} \left(R - \mathbf{C}\hat{S}_{TSVD} \right) \right\|^2 . \tag{6.17}$$

The FSD-TSVD algorithm, then enumerates a fixed number of points at each level. The FSD-TSVD estimate is given by

$$\hat{S}_{FSD-TSVD} = \arg \min_{\tilde{s} \in M} \left\| \mathbf{L} \left(\hat{P} - \tilde{S} \right) \right\|^2 \leq \hat{g} \tag{6.18}$$

where $\hat{P}$ is the unconstrained TSVD estimate defined as $\hat{P} = \mathbf{C}_{\xi} R$ and $\tilde{S} \subset \mathcal{H}$ for $\mathcal{H}$ the subspace of the FSD algorithm. If no node is discovered within the sphere then

$$\hat{S}_{FSD-TSVD} = \hat{S}_{TSVD}. \tag{6.19}$$

The proposed FSD-TSVD detector has two main differences from the original SD detector. The first is that the complexity of the FSD-TSVD is fixed to a number of nodes equal to the FSD tree width. The second, is that the FSD-TSVD measures the distance of the nodes with the FSD subspace from the unconstrained TSVD estimate $\hat{P}$. This last difference distinguishes the proposed FSD-TSVD algorithm from the conventional FSD algorithm presented in section 6.5. The FSD initialization block in Fig. 6.21 ensures that the FSD uses the reference point $\hat{P}$ and calculates $\hat{g}$.

6.6.2 Performance Investigations

Performance of the FSD-TSVD detector is examined for different number of subcarriers and levels of bandwidth compression. For comparison purposes results for the TSVD, FSD, and SD detectors are plotted where applicable. Fig. 6.22 depicts the BER of FSD-TSVD detector for tree widths of 16 and 256 for a 16 subcarrier system with $\alpha = 0.8$.

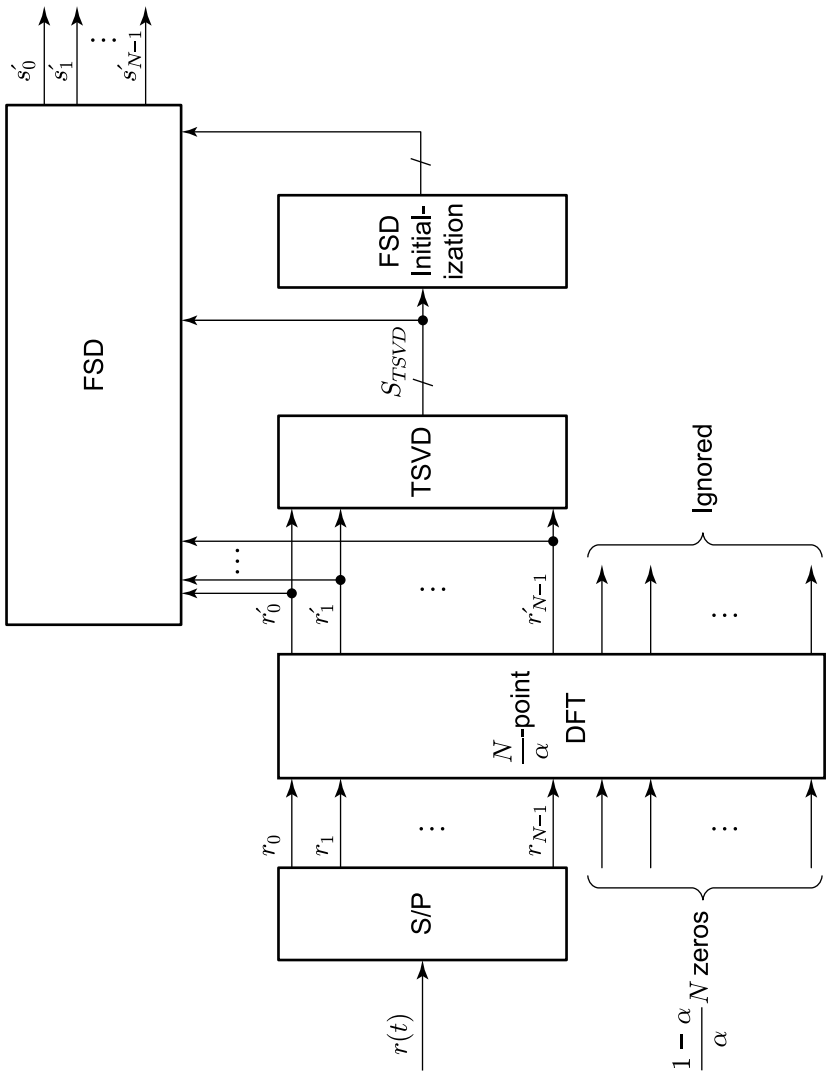

FIGURE 6.21: The FSD-TSVD detector block diagram.

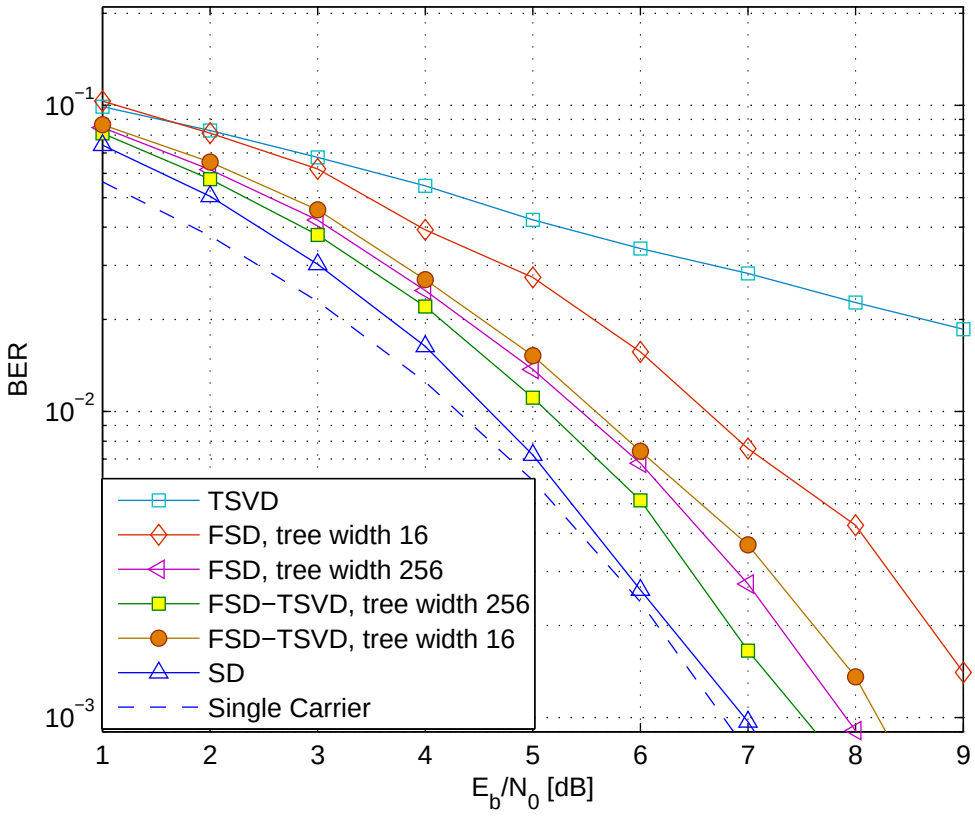

FIGURE 6.22: BER performance for the FSD-TSVD detector for a 16 subcarrier SEFDM system for $\alpha = 0.8$ carrying 4QAM symbols.

The figure shows that the FSD-TSVD detector is capable of delivering performance with a penalty of about 0.5 dB from the single carrier case or OFDM. In addition, the FSD-TSVD detector shows the capability of substantially reducing the complexity of detection when compared to regular FSD as the FSD-TSVD detector with tree width of 16 achieved close error performance to the FSD with tree width of 256. This effect is further demonstrated in Fig. 6.23 where the BER for α values of $0.7 - 1$ is plotted at $E_b/N_0 = 5$ dB. Again the figure confirms that the FSD-TSVD detector improves the BER performance when compared to the regular FSD for the same complexity requirement. For the different values of α, the figure shows that the FSD-TSVD detector is capable of delivering performance near SD's at a fraction of the complexity of either the SD or the regular FSD.

Fig. 6.24 depicts the BER performance of the FSD-TSVD detector for different values of α for a fixed complexity. The figure indicates that for fixed complexity there will be some performance degradation. This is due to the conditioning of the system that

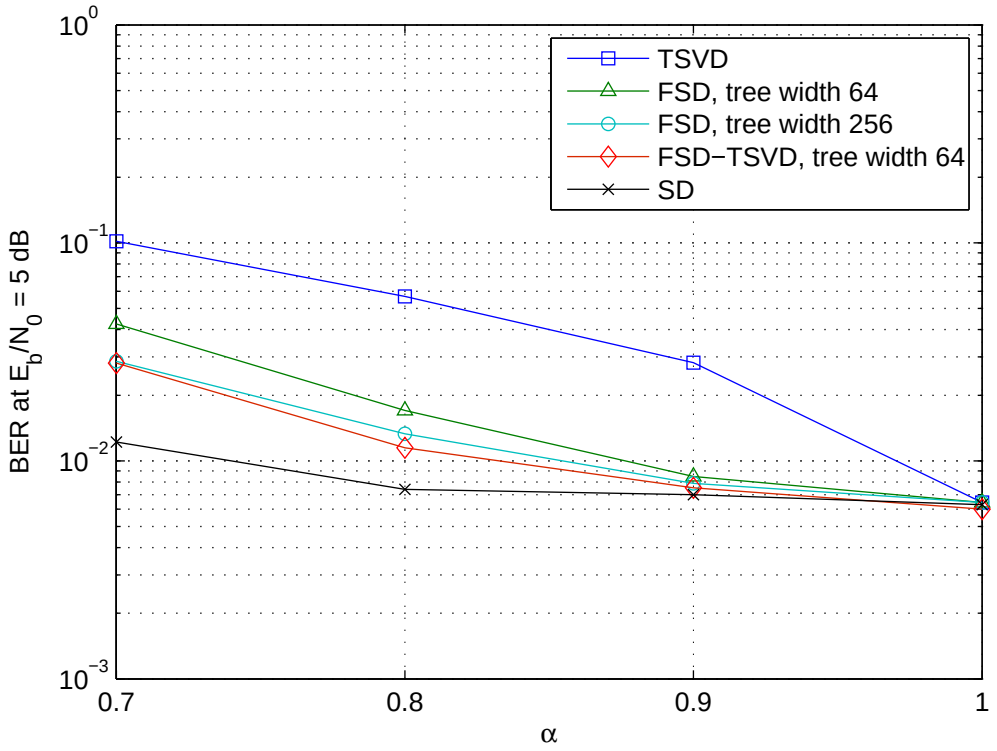

FIGURE 6.23: BER performance of the FSD-TSVD and FSD detectors for a 16 sub-carrier system carrying 4QAM symbols, $\alpha = 0.7 - 1$ and maximum tree width 64 for FSD-TSVD and 256 for FSD.

worsens with the decrease in α values and that results in degrading the performance of the SD detector as illustrated in Fig. 5.9. However, for the FSD-TSVD detector the sub-optimal performance can be improved by increasing the tree width (i.e. complexity) as illustrated in Fig. 6.25. The figure illustrates this BER performance enhancement by increasing the complexity for $\alpha = 0.7, 0.8$ and 0.9 for E_b/N_0 =5dB. The figure shows more impact of the increase in tree width for systems with smaller α values. This suggests that detection effort increases with the increase in bandwidth compression. Furthermore, Fig. 6.26 depicts the BER performance of the FSD-TSVD detector with different complexities for $E_b/N_0 = 1 - 8$ dB. It is clear from Fig. 6.25 and Fig. 6.26 that the BER performance improves with the increase in complexity, however, the improvement is not linearly proportional to the complexity increases and the trade off between complexity and performance can benefit from the fact that after some point limited BER improvement is attainable until a very high complexity is reached.

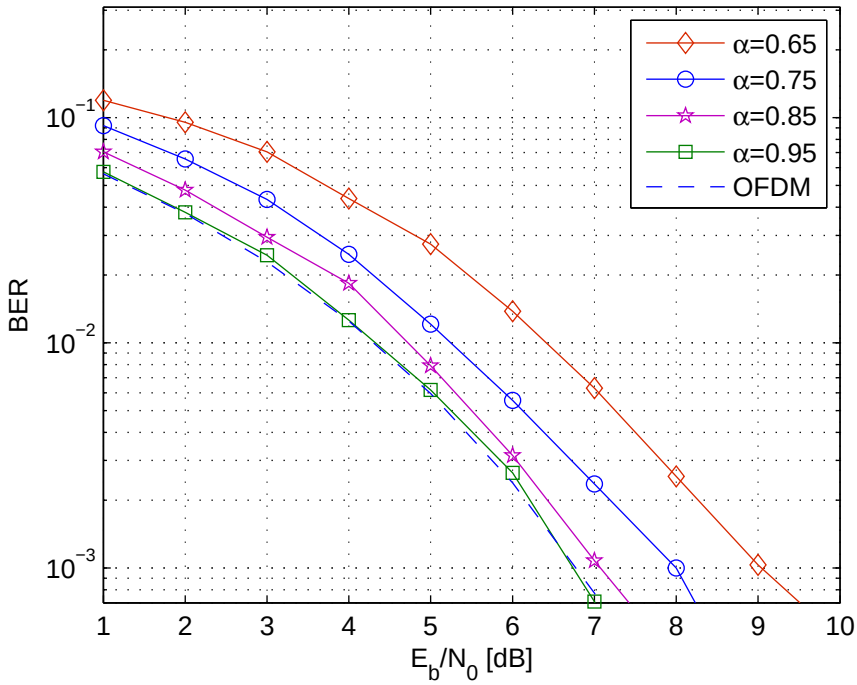

FIGURE 6.24: BER performance of the FSD-TSVD detector for a 16 subcarrier SEFDM system carrying 4QAM symbols for $\alpha = 0.65 - 0.95$ maximum tree width 512.

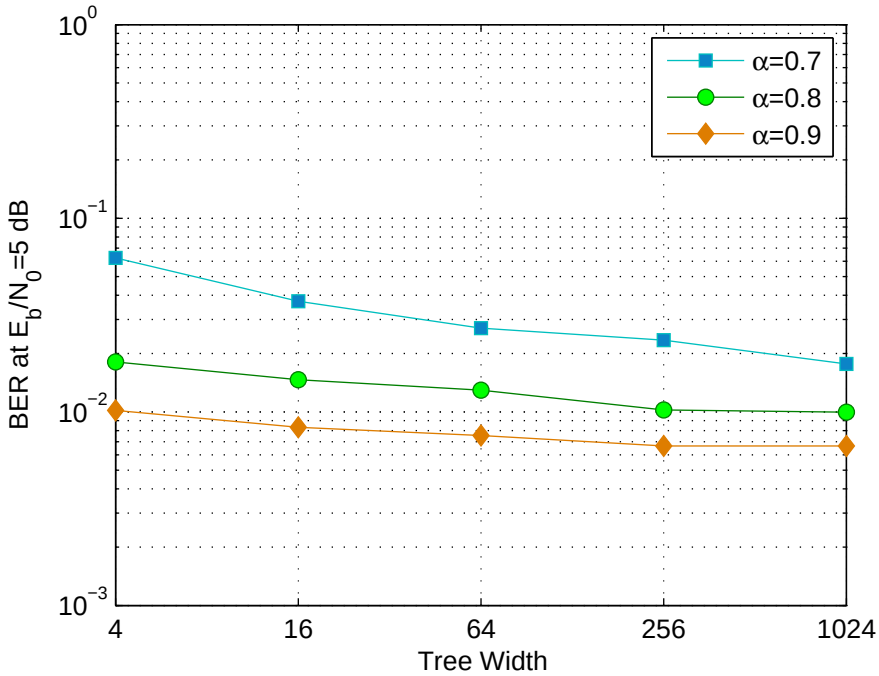

FIGURE 6.25: BER performance of the FSD-TSVD detector for different tree widths for a 16 carriers SEFDM system carrying 4QAM symbols with $\alpha = 0.7 - 0.9$.

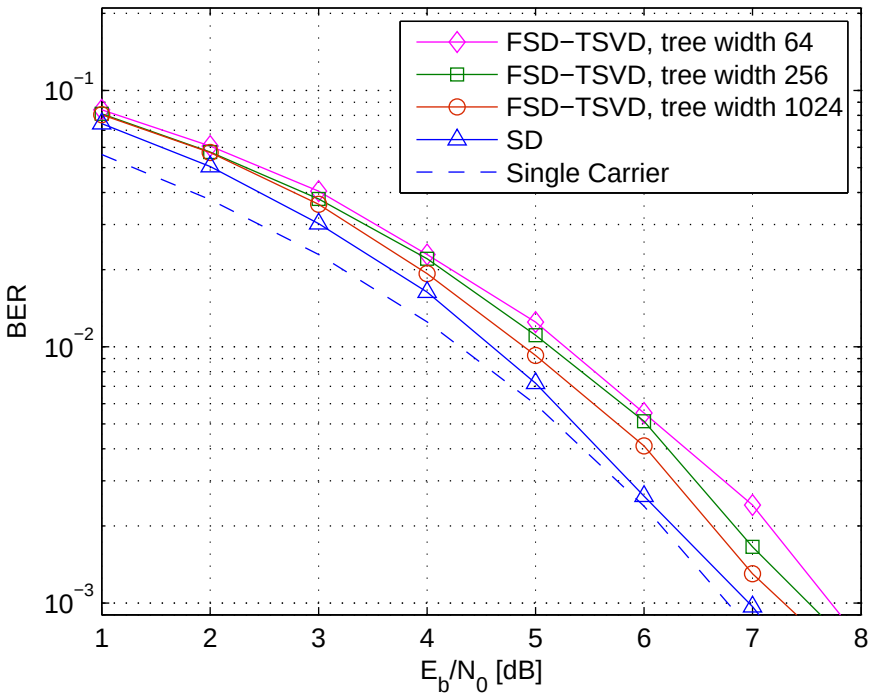

FIGURE 6.26: BER performance of the FSD-TSVD detector for different tree width for a 16 subcarrier SEFDM system carrying 4QAM symbols for $\alpha = 0.8$.

6.7 Hardware Implementation of SEFDM Receivers

Chapters 4 and 5 presented transmitter and demodulator options that can be readily implemented using IDFT/DFT or IFFT/FFT blocks. However, the detection of the signal is presented with two main challenges. First, the ill conditioning of the SEFDM system is translated to large dynamic range of the system numbers and thus will impact the needed resolution and the dynamic range of the building blocks of the detector. Second, the complexity of the detector itself can be substantial in order to handle the ICI.

Both challenges are addressed in the case of the TSVD and SelE detectors. Both detectors use well conditioned detection matrices, thus requiring a smaller dynamic range. As for the complexity, the detection process requires matrix multiplication and a slicer. All SEFDM detectors require the generation of the $\mathbf{C}$ matrix. Based on the principles of the IDFT transmitter and the DFT demodulator, the $\mathbf{C}$ matrix for a system of N subcarriers and $\alpha = b/c$, can be generated by applying an IDFT operation of length cN points initialized with $\{1, 0, 0, \cdots, 0\}$ for c circular shifts, extract the first N outputs of

each IDFT output and apply it to the inputs of a cN long DFT operation and use the first N outputs as the first row of the $\mathbf{C}$ matrix, and the process is repeated until all the rows of $\mathbf{C}$ are obtained.

Furthermore, for a system with fixed parameters the required detection matrices can be generated once and stored for the duration of the transmission. After this point, the SelE detection matrix can be built by discarding the ICI terms less than the defined threshold. The crucial point remains to achieve matrix inversion. SVD can be used to achieve this and the literature shows FPGA based hardware implementation of the decomposition [147]. This operation is also needed to construct the TSVD detector matrix. When SVD is used for the inversion process, the complexity of the TSVD and SelE becomes the same. Nevertheless, the ultimate case of SelE is to perform MF based demodulation and apply a slicer at the output of the DFT block, thus requiring no computational detection. Based on the proposed TSVD detector herein, an FPGA design of the receiver is proposed in [136]. The detector uses stored values for the TSVD detection matrix for selected values of α and N. Furthermore, the stored matrices can be designed to realize the ZF and SelE detectors and if there is information on the signal to noise ratio, the detector can implement MMSE.

Implementations of the FSD are reported in [148] for MIMO system detection. The algorithm as illustrated in Fig. 6.13 has some steps that need to be evaluated only once for the detection duration. Therefore, for an SEFDM system with fixed parameters, these steps can be evaluated once and stored for future detection where a fully reconfigurable system which can change tree width, number of subcarriers and α will need to have the needed circuitry to perform all these steps on the fly. Obviously, a fixed system on the other end can be much simpler with all the complicated steps performed once and stored for detection work.

6.8 Discussion and Conclusions

In this chapter several detectors for the SEFDM signal were presented with the common denominator being the reduced and fixed complexity of detection. In the beginning, the use of the Truncated Singular Value Decomposition (TSVD) for the detection of Spectrally Efficient FDM (SEFDM) signals was proposed. In principle, the TSVD detector

modifies the ill posed problem for SEFDM detection to an approximate well posed one, thus improves the stability of the system in the presence of noise. Numerical simulations showed that the TSVD based detector achieved a sub-optimal solution of the SEFDM least squares problem that was more immune to small perturbations than Zero Forcing (ZF) and Minimum Mean Squared Error (MMSE), hence yielding a better BER performance. Furthermore, the complexity of the TSVD detector is of the same order as the ZF one as the SVD operation which is necessary for the TSVD detector represents a simple method to find the inverse for the case of the ZF detector. Moreover, the results show that the TSVD detector exhibited the same error performance with respect to the increase in the number of subcarriers.

Then, another linear detector based on utilizing the intercarrier interference (ICI) pattern derived in chapter 3 was proposed. The detector was termed Selective Equalization (SelE) due to the fact that the solution acknowledges only ICI terms exceeding a predefined threshold. Numerical results confirmed that the SelE detector outperforms the ZF and MMSE in terms of the error performance with the same complexity. For BPSK input symbols, the SelE detector outperformed the TSVD in terms of the error performance and matched it for 4QAM input symbols. In addition, the SelE achieved the same error performance with the increase in the number of subcarriers. Moreover, the concepts of SelE provide a basis to assess the potential problems in the case of approximated detection systems that due to the finite resolution of devices will need to use shortened representations of the detection matrices.

The TSVD and SelE detectors both offered improved error performance when compared to standard linear detectors such as ZF and MMSE. In addition, both detectors managed to provide consistent error performance for systems with large numbers of subcarriers. For small bandwidth savings, both detectors offered attractive error performance with 1-2 dB power penalty at BER of 10^{-3} . However, for higher levels of bandwidth compression, the performance was sub-optimal and with a substantial error margin when compared to the optimal detection using ML and SD. Therefore, the work turned back to iterative decoding techniques and the use of the Fixed complexity Sphere Decoding (FSD) algorithm for SEFDM signals detection was proposed.

The FSD provides sphere-wise detection, therefore, is capable of ameliorating the effects of the inherent ICI in the SEFDM signal. Furthermore, FSD offers fixed complexity

and is therefore more suitable for hardware implementation when compared to the original SD. Performance investigations of the proposed FSD detector have demonstrated attractive BER performance. Results have shown that the FSD error performance is sub-optimal, however, the degradation in the performance is compensated for by the attractive low and fixed complexity and the potential for parallel processing, noting that the BER performance can be improved by increasing the complexity.

Furthermore, a novel detector for SEFDM signal that combines the TSVD and the FSD was proposed. The FSD-TSVD detector improves the design of the original FSD algorithm by firstly generating a TSVD estimate of the transmitted symbols and then applying TSVD principles for respective parts of the FSD algorithm. The new algorithm is better suited to systems suffering from ill conditioning effects. Numerical results have shown that the proposed FSD-TSVD detector achieves superior BER performance to that of the FSD and performs close to the standard SD. Therefore, it constitutes an enhancement of the standard FSD since it improves FSD error performance while maintaining its merits of low and fixed complexity. The FSD-TSVD detector offers the best detection possibility for a practical SEFDM system as it addresses both performance and complexity issues, and may be applied in other systems that suffer from ill conditioning such as MIMO systems [149].

Part II

Practical Limitations and System Enhancements

Chapter 7

SEFDM Peak to Average Power Ratio (PAPR): Studies and Routes to Mitigation

7.1 Introduction

Most of the previous work on SEFDM systems focused on developing efficient transmission [60, 61] and detection techniques [21, 35, 90, 36, 74, 91, 150, 151]. In practice, implementations of communication systems require optimization to satisfy size, power consumption and ultimately cost constraints. An important parameter in design optimization is the dynamic range of the signals in the system which in turn dictates the dynamic range of the components of the system. The Peak to Average Ratio (PAPR) provides a measure of the variation in the power of the signal and hence the required dynamic range of the components. In particular, multicarrier signals are prone to high PAPR as the multiple subcarriers may add up and generate high peak signals resulting in a high PAPR. The implication of this high PAPR is that the components of the system must have linear response for the complete range of the signal power. The PAPR of the digital signal dictates the dynamic range of the digital circuitry while the continuous PAPR dictates the dynamic range of the analogue components. In particular, the Power Amplifier (PA) in the transmitter must provide gain without compression for the complete range of the signal. In other words the PA should include a predefined back

off[1] in order to ensure that the amplifier continues to work in its linear region for the highest possible peak, otherwise the amplified signal can be distorted. Nevertheless, the efficiency of the PA will be greatly affected if a high back off is needed. Hence the power consumption of the whole transmitter will be affected. Power efficiency is a critical issue in wireless communication specially when dealing with end users where the focus is on power savings. The increase in power consumption has other consequences such as the increase in heat dissipation which adds up to other system design challenges. In addition, a high PAPR and hence a large dynamic range of the signal requires a large dynamic range for the digital to analogue converters (D/A) at the transmitter, thus increasing further the complexity and power consumption. On the other hand, when the dynamic range of the signal is greater than the equipments the system will be operating in non linear regions, hence, will undergo nonlinear distortion. For a PA working in the nonlinear region Inter-Modulation Distortion (IMD) occurs resulting in spectral widening and increase the out of band interference. Furthermore, the non linear response will generate in band distortion that contributes to the inter-carrier interference and consequently leads to higher BER.

The SEFDM signal as a multicarrier system is expected to exhibit high PAPR and due to the discussed complications associated with the high PAPR. This chapter is dedicated to first study the PAPR of SEFDM signal and then to pursue mitigation techniques and evaluate their performance. The study covers the currently used methods for PAPR reduction in OFDM and evaluates the performance of such methods in SEFDM system. In particular, PAPR reduction using clipping, Partial Transmit Sequences (PTS) and Selective Mapping (SLM) are evaluated for the PAPR reduction of SEFDM signals. Furthermore, a novel PAPR reduction algorithm is proposed and based on sliding a time window across an extended SEFDM symbol period, therefore termed the SLiding Window (SLW) PAPR reduction technique. Numerical simulations confirm the SLW efficacy in PAPR reduction and show no side effects. In addition, a complete transmitter that employs SLW is proposed based on the SEFDM IDFT transmitter. SLW shows remarkable PAPR reduction with no spectral spreading or BER compromises at a much reduced complexity when compared to standard PTS and SLM PAPR reduction techniques.

[1]Back off refers to the ratio of the maximum possible output of the power amplifier and the mean transmit power.

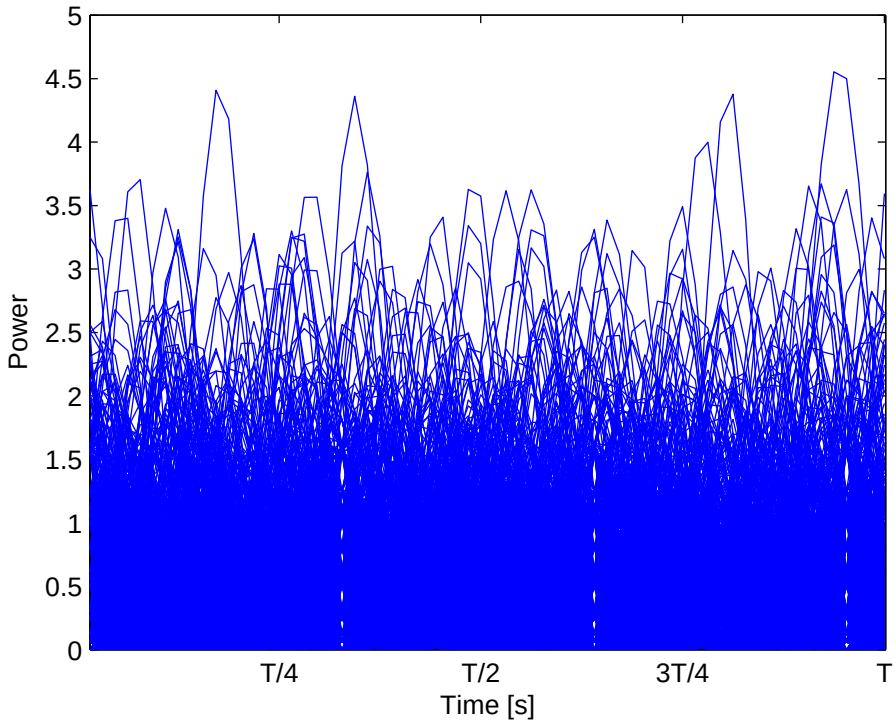

FIGURE 7.1: Instantaneous power for 1000 SEFDM symbols overlaid on one symbol duration for $\alpha = 0.8$ and 16 subcarriers.

7.2 Evaluation of the PAPR of SEFDM Signals

Before delving into design of PAPR reduction techniques, this section examines the power of the SEFDM signal. Fig. 7.1 depicts the instantaneous power of 1000 SEFDM symbols overlaid on a symbol duration. It can be seen from the figure that the instantaneous power varies randomly within the period of the symbols. In addition, the figure depicts the occurrences of high peaks. To evaluate the PAPR of SEFDM signals consider the l^{th} SEFDM symbol:

$$x\left(t\right) = \frac{1}{\sqrt{T}} \sum_{n=0}^{N-1} s_{l,n} e^{j2\pi n\alpha t/T}, \tag{7.1}$$

where $s_{l,n}$ is the n^{th} complex input symbol. The PAPR of $x\left(t\right)$ is generally defined by

$$PAPR = \frac{\max\ \left|x\left(t\right)\right|^2}{\mathrm{E}[\left|x\left(t\right)\right|^2]}, \tag{7.2}$$

where max $|x(t)|^2$ denotes the peak power of the signal $x(t)$ and $\mathrm{E}[|x(t)|^2]$ is the average power. The instantaneous power P_i of the time domain signal in Fig. 7.1 and equation (7.1) is a random variable. P_i can be expressed as follows:

$$\begin{aligned} P_i &= |x(t)|^2 \\ &= \frac{1}{T}\sum_{n=0}^{N-1}\sum_{m=0}^{N-1} s_{l,n}s_{l,m}^{*}e^{j2\pi\alpha t(n-m)/T}. \end{aligned} \tag{7.3}$$

The last line in equation (7.3) is obtained by introducing the intermediate variable m in order to move the sum operators outwards. P_i can be further modified as

$$\begin{aligned} P_i &= \frac{1}{T}\sum_{n=0}^{N-1}|s_{l,n}|^2 \\ &+ \frac{1}{T}\sum_{n=0}^{N-1}\sum_{\substack{m=0\\m\neq n}}^{N-1} s_{l,n}s_{l,m}^{*}e^{\frac{j2\pi\alpha t(n-m)}{T}}. \end{aligned} \tag{7.4}$$

According to equations (7.3) and (7.4) the instantaneous power is dependent on α. For instance, Fig. 7.2 depicts the instantaneous power for a 16 subcarrier SEFDM symbol with $\alpha = 0.5$ and a 16 subcarrier OFDM symbol modulated with the same information symbols. From the figure it can be seen that the SEFDM instantaneous power is a stretched version of half of the OFDM signal power, that is the length of the stretched part is αT in time units from the OFDM symbol.

The peak power P_{peak} will be

$$P_{peak} = \max(P_i). \tag{7.5}$$

Using the expectation operator $\mathrm{E}[\cdot]$, the average power $\overline{P}$ may be estimated from

$$\overline{P} = \mathrm{E}\left[\sum_{n=0}^{N-1}\sum_{m=0}^{N-1} s_{l,n}s_{l,m}^{*}e^{\frac{j2\pi\alpha t(n-m)}{T}}dt\right]. \tag{7.6}$$

The independence of the symbols and subcarriers allows the simplification of $\overline{P}$ by applying the expectation operator independently onto the symbols part and the subcarriers part of equation (7.6) as:

$$\overline{P} = \sum_{n=0}^{N-1}\mathrm{E}\left[|s_{l,n}|^2\right] + \sum_{n=0}^{N-1}\sum_{\substack{m=0\\m\neq n}}^{N-1}\mathrm{E}\left[s_{l,n}s_{l,m}^{*}\right]\mathrm{sinc}(\pi\alpha(n-m))e^{\left(\frac{j\pi\alpha t(n-m)}{T}\right)}. \tag{7.7}$$

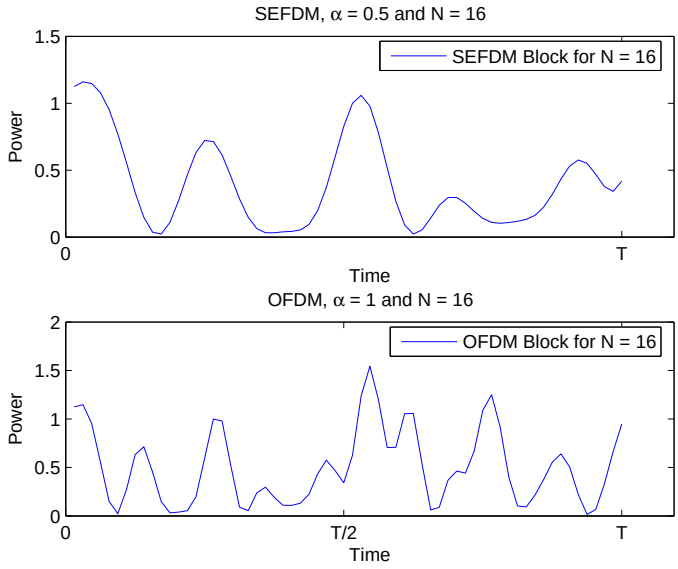

FIGURE 7.2: Instantaneous power of one SEFDM symbol (upper) for $\alpha = 0.5$ and one OFDM symbol (lower) both systems have 16 subcarriers.

Equation (7.7) shows that the average power is composed from two components: the first is the power of the individual subcarriers reflected in the norm of the individual symbols given by the term

$$\left(\sum_{n=0}^{N-1} \mathrm{E}\left[|s_{l,n}|^2 \right] \right) \tag{7.8}$$

and the second is composed from the power spillage between the subcarriers given by the term

$$\left(\sum_{n=0}^{N-1} \sum_{\substack{m=0 \\ m \neq n}}^{N-1} \mathrm{E}\left[s_{l,n} s_{l,m}^{*} \right] \mathrm{sinc}(\pi\alpha\,(n-m)) e^{\left(\frac{j\pi\alpha t(n-m)}{T} \right)} \right). \tag{7.9}$$

Furthermore, the second term, shown in equation (7.9), shows that the power spillage between the subcarriers given by $\mathrm{E}\left[s_{l,n} s_{l,m}^{*} \right]$ is multiplied by the factor

$$\mathbf{g} = \mathrm{sinc}(\pi\alpha\,(n-m)) e^{\left(\frac{j\pi\alpha t(n-m)}{T} \right)}. \tag{7.10}$$

When $\alpha = 1$, the factor $\mathbf{g} = 0$, therefore, the average power will constitute of the first term only as shown in equation (7.8). While for $\alpha < 1$ the average power will be affected by the value of $\mathbf{g}$ which is in turn dependent on α. Fig. 7.3 depicts the values of the factor $\mathbf{g}$ for a 16 subcarrier system for α ranging from 0.1 to 1. It can be seen from the figure that the effect of the factor $\mathbf{g}$ is a reduction in the power leakage among the subcarriers as the term is upper bounded by 1. Fig. 7.4 and 7.5 depict the average

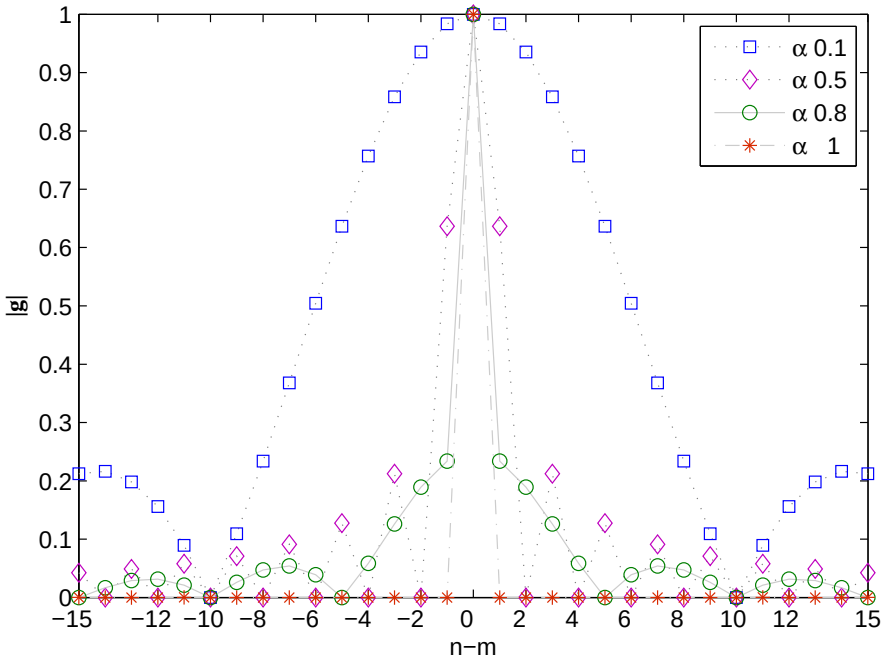

FIGURE 7.3: The absolute value of the factor $\mathbf{g}$ in equation (7.10). The dotted lines to distinguish the values of $|\mathbf{g}|$ associated with the different α values.

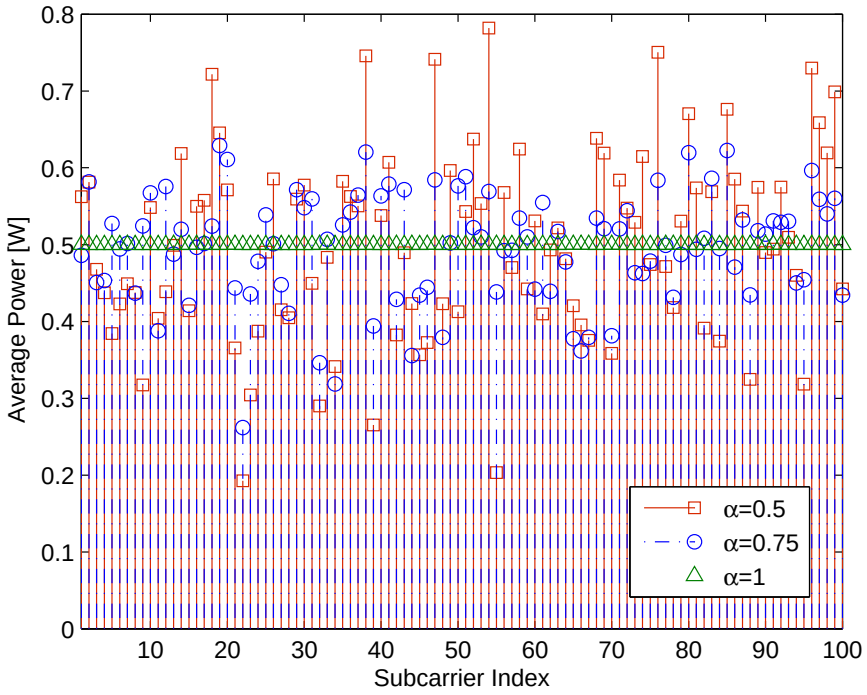

FIGURE 7.4: Average power of 100 SEFDM symbols for a system with 16 subcarriers and 4QAM input symbols for $\alpha = 0.5$, 0.75 and 1.

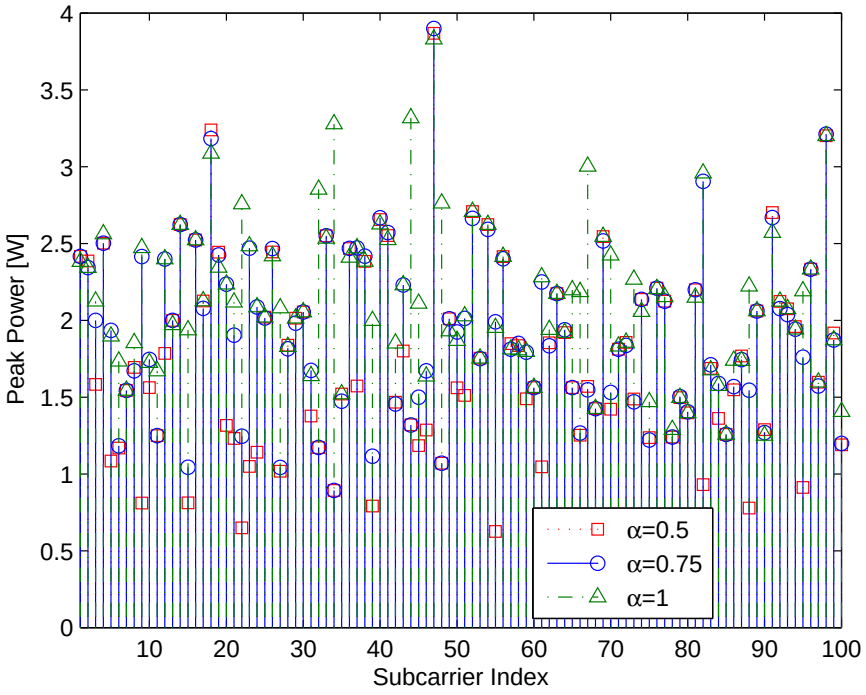

FIGURE 7.5: Peak power of 100 SEFDM symbols for a system with 16 subcarriers and 4QAM input symbols for $\alpha = 0.5$, 0.75 and 1.

power and peak power for three values of α. Fig. 7.4 shows that the average power varies from symbol to symbol for $\alpha < 1$ whereas for OFDM system where $\alpha = 1$ the average power is fixed for all symbols as anticipated from equation (7.7). Fig. 7.5 shows the peak power for the same symbols whose average power is plotted in Fig. 7.4. The figure shows that the peak power varies from symbol to symbol for all α values.

The previous analysis shows that the peak and average power of the SEFDM signal are random variables as shown from equations (7.4), (7.5) and (7.7) and is further indicated by the plots in Fig. 7.4 and 7.5, consequently, the PAPR is a random variable. In addition, in theory the PAPR in multicarrier systems is a function of the number of carriers [39], however, in practice the likelihood of all carriers reaching their maximum can reduced by using scrambled data and large constellation size [152] in [45]. Due to the random nature of the PAPR the Complementary Cumulative Distribution Function[2] (CCDF) is used to characterize the probability of the PAPR of the signal exceeding a threshold denoted by γ that is $P_r\{PAPR > \gamma\}$. Fig.7.6 depicts the CCDF of the PAPR

[2]The Complementary Cumulative Distribution Function(CCDF) describes the probability of a random variable being larger than a certain value.

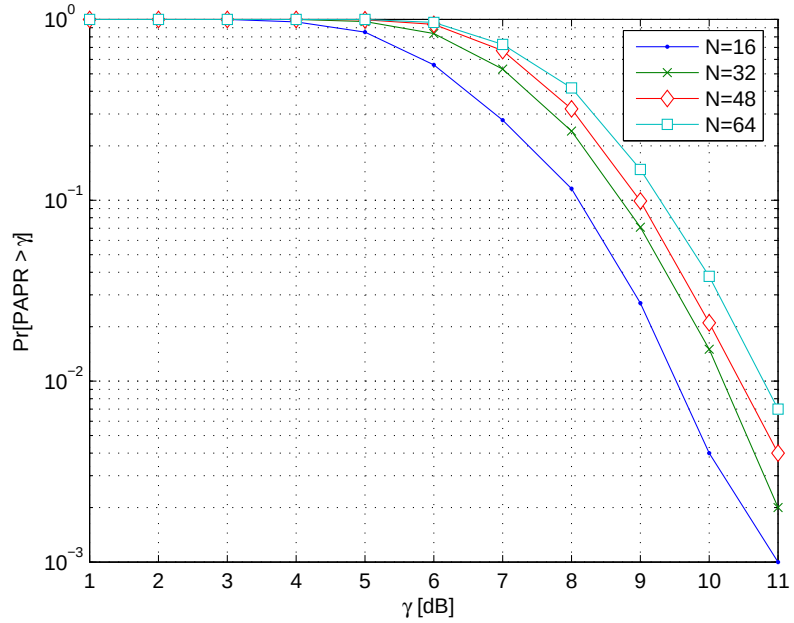

FIGURE 7.6: CCDF of the PAPR for SEFDM system modulated with 4QAM symbols for $\alpha = 0.5$ and different number of sub-carriers

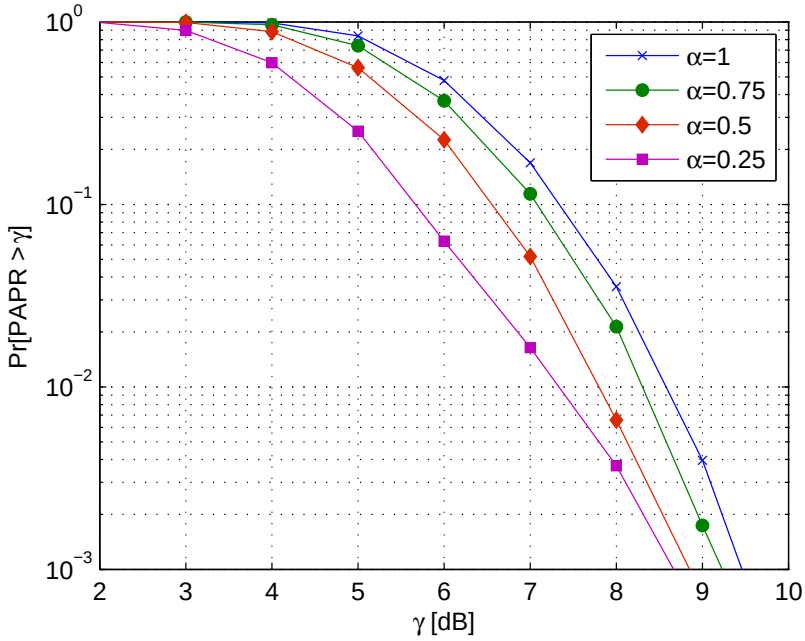

FIGURE 7.7: CCDF of a 16 subcarrier SEFDM system modulated with 4QAM symbols with respect to α.

of the SEFDM signal exceeding a threshold of γ for different number of subcarriers obtained by numerical simulations. Fig. 7.6 shows that the probability of PAPR exceeding the threshold γ increases expectedly with the increase in the number of sub-carriers. In addition, Fig 7.7 depicts the CCDF of the PAPR of SEFDM systems with different values of α. The figure shows that the probability of the SEFDM PAPR exceeding the threshold γ decreases with the reduction in α.

7.3 Overview of Conventional PAPR Reduction Techniques

PAPR reduction is a topic extensively researched in OFDM system, leading to the proposal of many reduction techniques [153]. In general, PAPR reduction techniques may be classified as distortionless or distorting. The distortionless techniques reduce the PAPR without introducing non linear distortion. Such techniques involve performing reduction operations at the transmitter and inform the receiver of the needed information to reverse the effects of the applied operations. The information necessary for decoding the signal is made available to the receiver by sending side information along the data. Hence, the reduction in PAPR is achieved at the cost of reduced throughput as the introduced side information is deducted from the overall throughput. Prominent examples of distortionless techniques are Selective Mapping (SLM) [154], Partial Transmit Sequence (PTS) [155] and Precoding. The distorting techniques introduce non linear distortion as a side effect of the PAPR reduction. There is no need for side information, nevertheless, these techniques lead to performance degradation usually in the form of spectral spreading and/or BER degradation. Distorting techniques include clipping and additive and multiplicative correction functions [156].

A simple method for PAPR reduction is by clipping the high peaks of the signal. Clipping can happen unintentionally in the system due to the limit in the highest power tolerated by the system circuitry. In OFDM systems usually clipping is followed by a filtering stage to reduce out of band emission. However, filtering results in peak re-growth, hence clipping is repeated many times until the wanted PAPR probability is obtained which in turn will result in non linear changes in the signal and may corrupt the orthogonality between the carriers. Other amplitude limiting techniques are proposed such as adding a correcting function to the time domain signal [156]. In addition multiplicative

manipulations of the time domain signal is proposed in [43]. Tone reservation limits the amplitude of the signal by dedicating certain frequency tones for transmitting PAPR reduction signals [157, 153]. Such reserved tones must be known to the receiver.

PAPR reduction in OFDM signals can be realized by multiplying the data vector by a set of different phase vectors and then choosing the set that gives the lowest peak factor as in SLM and PTS. The phase vectors are known to both the transmitter and the receiver [43]. The concept of SLM is based on that the probability of the power of an OFDM symbol exceeding a certain level is lower if that symbol is expressed in different format and thus the symbol with the lowest PAPR is chosen for transmission [154]. The transmitter sends side information to aid the receiver to extract the original signal. The main issue in SLM is how to generate different representation of the same symbol. Many proposals for generation of equivalent frames are found in the literature. Of these the simplest is to generate a set of random vectors; multiply these vectors with the original frame and compare the resultant PAPR then select the frame with the lowest PAPR. The efficiency of SLM in PAPR reduction increases with the increase in the number of vectors, however, the computational complexity will increase consequently. There is a need to send side information along the transmitted symbols resulting in decreased throughput. Many variance of SLM have been proposed in the literature [158, 159, 160] to improve the efficiency of SLM and reduce the overhead of the side information.

PTS is based on partitioning the OFDM signal into sub-blocks and apply different phase shifts on each block. The phase shifts are chosen such that the combined output of the blocks is optimized in terms of PAPR [155]. There are many procedures for combining the sub-blocks in the literature that trade the reduction in the PAPR with the complexity of searching for the optimum phase shifts [161, 162, 163]. Again there is a need to inform the receiver of the operation performed at the transmitter to enable the decoding of the received signal by sending side information. The side information constitutes a reduction in the overall throughput.

Other PAPR reduction techniques rely on using codes that ensures that only low peak power OFDM symbols are chosen as in [156] and [164], resulting in a reduced system throughput. In addition, precoding is suggested as a solution for PAPR reduction problem where each data block is multiplied by a precoding matrix prior to OFDM modulation and transmission [165].

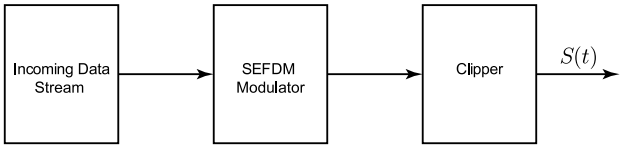

FIGURE 7.8: Block diagram of an SEFDM transmitter employing clipping for PAPR control.

7.4 PAPR Reduction in SEFDM System

Studies of the PAPR of the SEFDM signal in section 7.2 have shown that the system is susceptible to high PAPR. Noting the similarity between the SEFDM system and the OFDM system, this section presents three PAPR reduction techniques that are imported from OFDM system and are implemented in SEFDM system namely: clipping, SLM and PTS. Particularly, clipping is studied to evaluate the possible effects of the uncontrolled PAPR on the SEFDM system performance as it is expected to be created by the limited dynamic range of the circuitry of the transmitter. The performance of the three techniques is evaluated in terms of efficiency in PAPR reduction by numerical simulations. In addition, simulations looked at possible side effects in terms of spectral spreading and/or error performance degradation. To ensure accurate simulations, oversampling by a factor of 4 of the discrete signals is applied in accordance with the recommendation in [162] for multicarrier signals.

7.4.1 Clipping

Clipping is basically limiting the amplitude of the signal to a certain level. When no PAPR controlling scheme is applied, clipping occurs naturally by the circuitry of the system which naturally have a limited dynamic range. As a method for PAPR reduction, clipping is the easiest to implement, however, clipping usually increases the errors in the system and causes spectral spreading as it adds nonlinear distortion to the signal. In this section clipping is examined within the context of SEFDM signal as a method for PAPR reduction but the study serves the objective of evaluating the effects of the uncontrolled PAPR in SEFDM system on the spectrum of the signal and the BER performance. Fig. 7.8 illustrates an SEFDM system employing clipping. The clipping block can take many forms in a similar manner as OFDM. Some forms of clipping associated with OFDM are classical clipping, deep clipping and smooth clipping [166]. Classical clipping

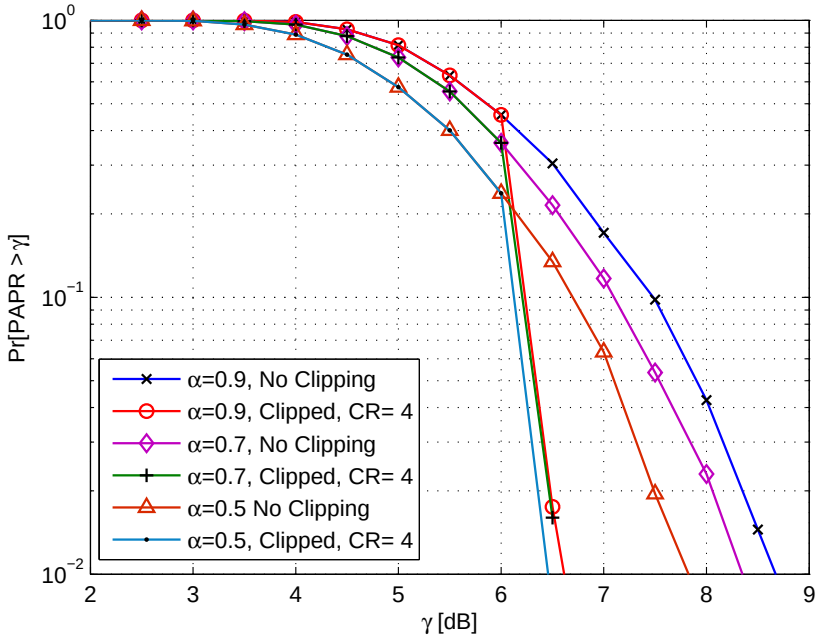

FIGURE 7.9: CCDF of the PAPR of 16 subcarrier SEFDM system employing clipping for $\alpha = 0.9, 0.7$ and 0.5 with 4QAM symbols.

clips any amplitude in the signal exceeding a certain level to a predefined level. Deep clipping perform large clips for the high amplitude peaks to overcome the peaks re-growth problem. Smooth clipping uses functions to map amplitude peaks to reduced ones.

The performance of clipping in SEFDM system is investigated by numerical simulations focusing on the CCDF to provide information about the efficiency of clipping in PAPR reduction, the spectrum and the BER performance after clipping. Clipping is performed by limiting the amplitude of the SEFDM signal to generate a pre-defined Clipping Ratio (CR) so that the PAPR denoted by γ is limited to

$$\gamma \leq \text{CR}. \tag{7.11}$$

Fig. 7.9 shows the CCDF of an SEFDM system employing clipping for different values of α for a CR of 4 corresponding to limiting the system to highest PAPR of 6 dB. Fig. 7.10 depicts the CCDF for 16 and 64 carriers systems. In both figures it can be seen that, for all cases, clipping achieved the PAPR reduction goal.

The spectrum of the clipped signal for different values of CR is plotted in Fig. 7.11. The

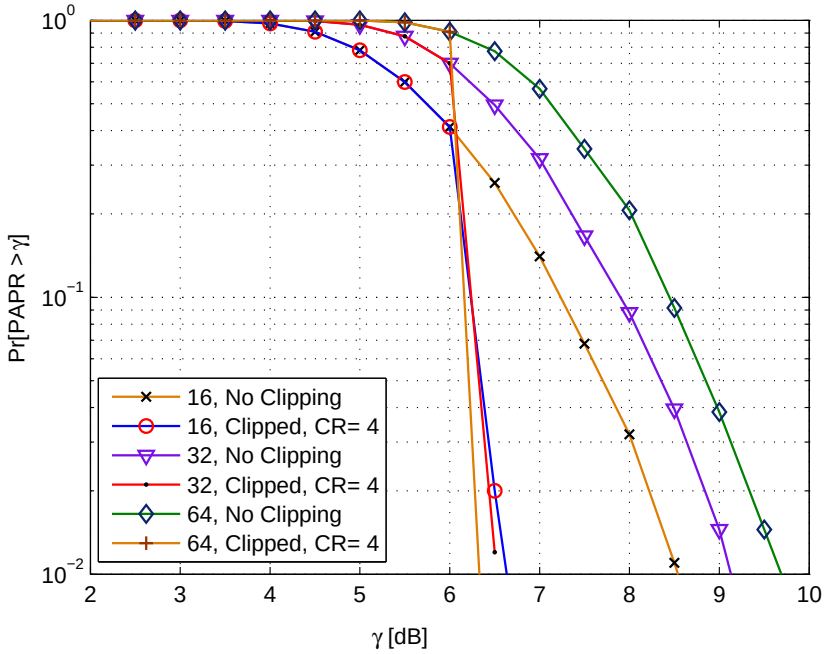

FIGURE 7.10: CCDF of PAPR of SEFDM system employing clipping for $N = 16, 32$ and 64 , 4QAM input symbols and $\alpha = 0.8$.

spectrum of the clipped signal showed an increase in the out of band emission compared to the non-clipped signal. In addition, the out of band emission increases with the increase in the clipping ratio. In OFDM systems clipping is usually followed by filtering to reduce the out of band emission [162, 167, 166], however, the filtering may create in band distortion.

As clipping adds non-linear distortion to the signal it is expected that the BER performance of the clipped system will be affected. The level of BER deterioration depends on the CR as this ratio will determine the frequency of clipping. Fig. 7.12 depicts the BER of clipped SEFDM system modulated with BPSK and 4QAM input symbols for clipping ratio of 4 for system with 4 subcarrier detected with ML and 12 subcarrier detected with SD algorithm. Although ML detection is employed for a small size system with 4 subcarriers, it is found that there is performance penalty in the form of degraded BER performance. Furthermore, the SD detected system shows more deterioration in the BER performance. These results indicate that the detection of the SEFDM signal will suffer from the uncontrolled PAPR if it leads to peaks clipping due to the finite dynamic range of the transmitter circuitry. In addition, the results show that if clipping is used as a PAPR control method then performance deterioration is to be expected as

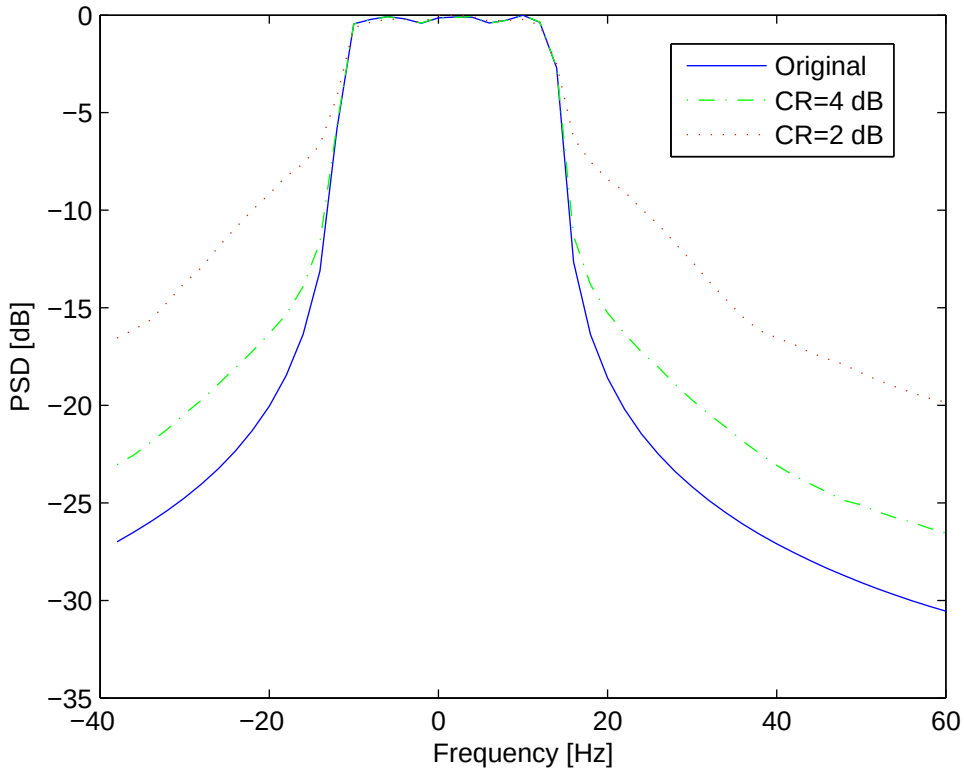

FIGURE 7.11: Spectrum of clipped 16 subcarrier SEFDM system modulated with 4QAM symbols for $\alpha = 0.8$.

well as the increase of the out of band emission.

7.4.2 Selective Mapping (SLM)

SLM is a technique used for the control of the PAPR of OFDM system. SLM mainly relies on generating equivalent representations of each OFDM symbol and then transmitting symbols with the lowest PAPR [154]. As the structure of the SEFDM symbol is similar to that of OFDM, SLM is suggested here for the control of the PAPR of SEFDM signals.

Of the many proposals for the generation of equivalent representations of OFDM [158, 159, 160], the simplest is to generate a set of random vectors (generating randomized phases); multiply these vectors with replicas of the original input symbols block, compare the resultant PAPR and select the SEFDM symbol with the lowest PAPR for transmission. The efficiency of SLM in PAPR reduction increases with the increase in

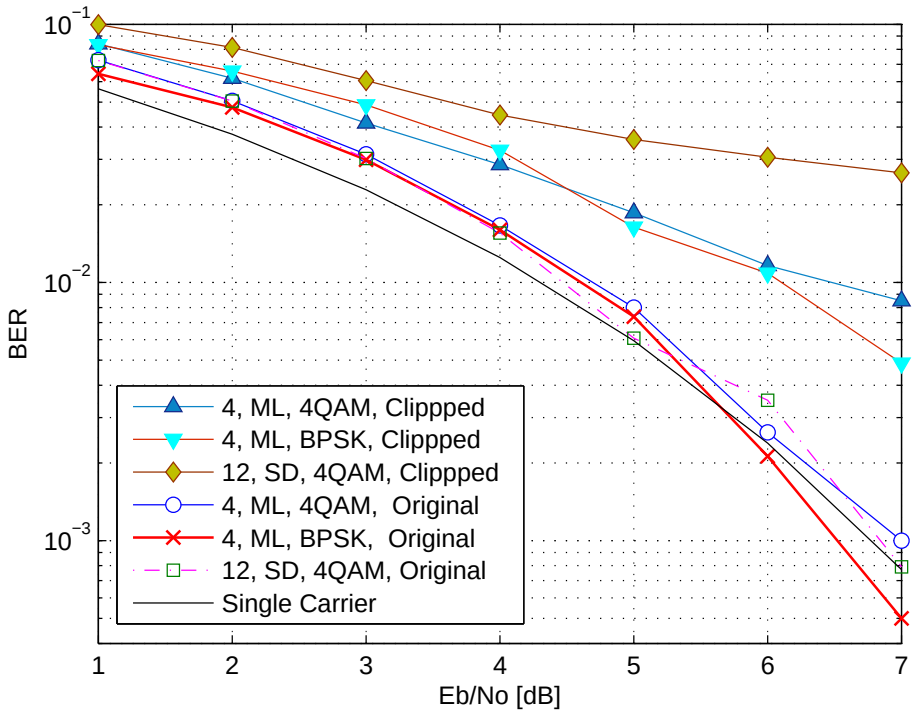

FIGURE 7.12: BER performance of clipped 4 subcarrier SEFDM system modulated with BPSK and 4QAM symbols for $\alpha = 0.8$ and $CR = 4$. ML and SD detection are applied.

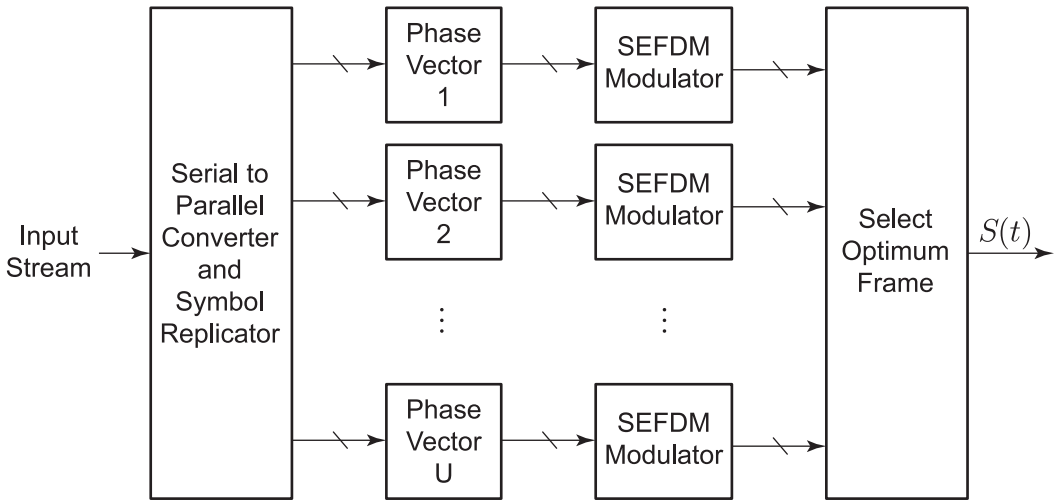

FIGURE 7.13: Block diagram of an SEFDM transmitter employing SLM for PAPR control with U phase vectors.

the number of vectors, however, the computational complexity will also increase proportionally. There is a need to send side information concurrently with transmitted symbols which in turn results in decreasing the throughput.

Fig. 7.13 shows a block diagram of an SEFDM system employing SLM. The system is

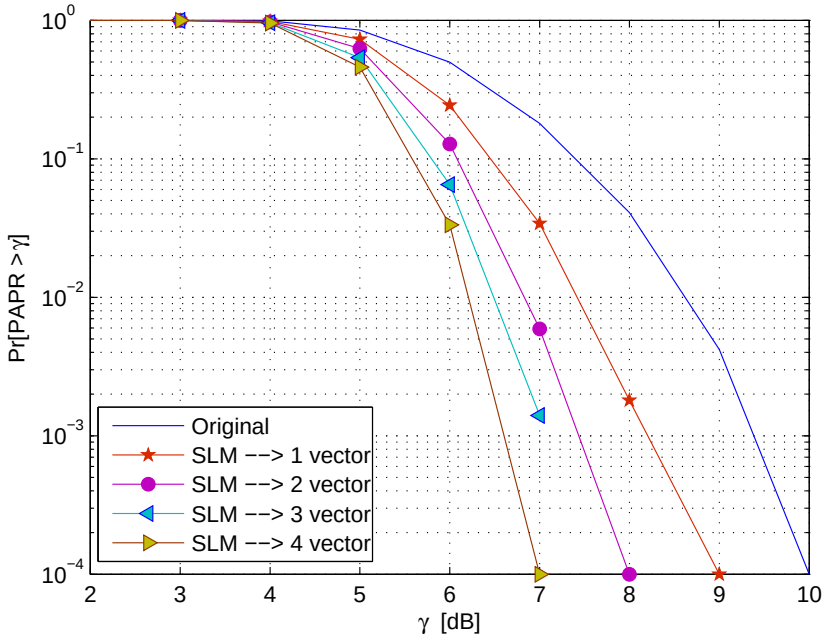

FIGURE 7.14: CCDF of the PAPR of an SEFDM system employing SLM with up to 4 phase vectors for a 32 subcarrier SEFDM system, $\alpha = 0.5$ and 4QAM input symbols.

composed of a bank of SEFDM modulators that generate equivalent SEFDM symbols for the same set of input stream by using different phase vector for each modulator chain. The PAPR of the different SEFDM symbols is evaluated and the symbol that provides the lowest PAPR is forwarded down the channel. It is possible to design the transmitter to use a single SEFDM modulator, however, the generation of the equivalent SEFDM symbols will need to be done sequentially rather than in parallel.

The performance of SLM is investigated by simulations. Random vectors are constructed as described in [154]. Fig. 7.15 and Fig. 7.16 show the plots of the CCDF of an SEFDM system employing SLM for different values of α and different number of subcarriers, respectively. The plots are for systems using SLM with one, two and four phase vectors and show the original signal with no PAPR control. The plots show that substantial PAPR reduction can be achieved. In addition, the efficiency in PAPR reduction increases with the increase in number of vectors.

The spectrum and the BER of SLM based SEFDM are investigated. The spectrum of the resultant signal is depicted in Fig. 7.17 to check for any spectral spreading. Fig. 7.17 shows that the level of out of band emission is different for the different phase vectors.

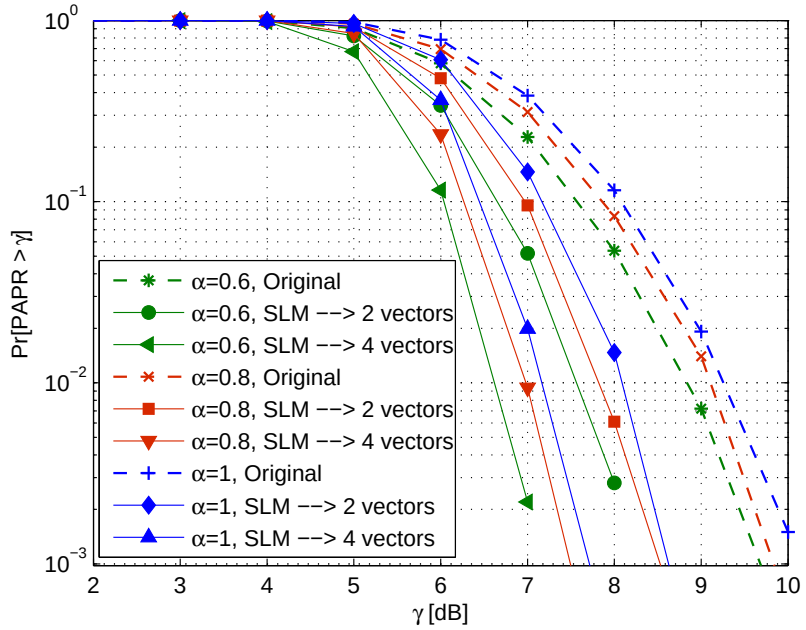

FIGURE 7.15: CCDF of the PAPR of SEFDM systems employing SLM with 4 phase vectors for different values of α, 32 subcarriers and 4QAM input symbols.

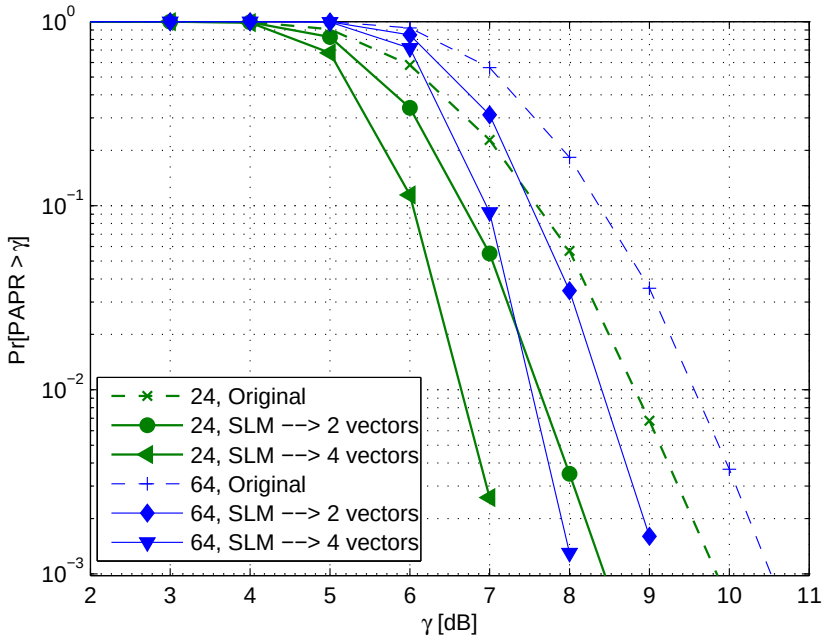

FIGURE 7.16: CCDF of the PAPR of SEFDM systems employing SLM with 4 phase vectors for different numbers of subcarrier for SEFDM system with $\alpha = 0.8$ and 4QAM input symbols.

This observation can be used to control the level of out of band emission using phase vectors.

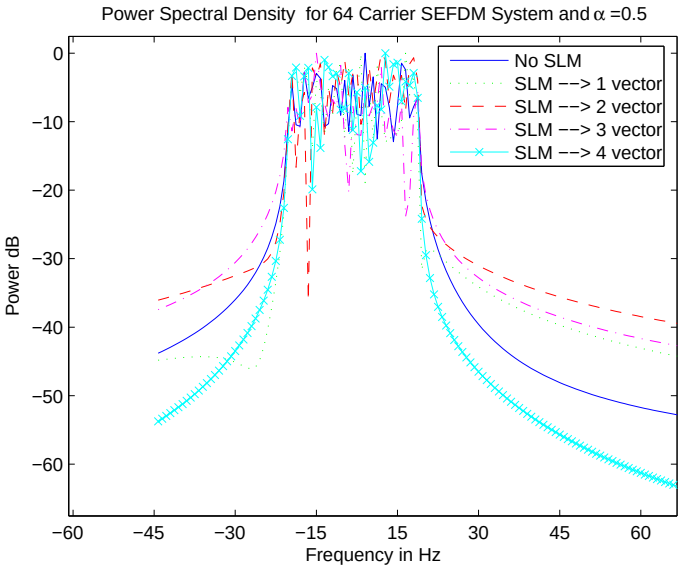

FIGURE 7.17: Spectrum of 64 subcarrier SEFDM symbol using SLM for PAPR control. $\alpha = 0.5$ and input symbols are 4QAM.

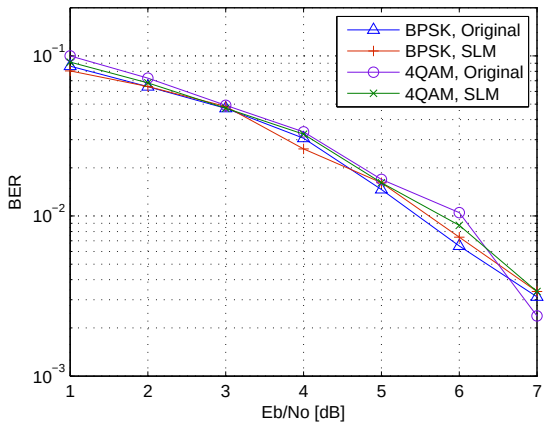

FIGURE 7.18: BER performance of SEFDM system using SLM for 4 subcarrier system with $\alpha = 0.8$ and 4 phase vectors. ML detection is applied.

Finally, the performance of the SLM based SEFDM system is examined in AWGN channel. Fig. 7.18 shows the BER performance of an SEFDM system employing SLM with BPSK and 4QAM symbols. The figure shows no significant effects of SLM on the BER.

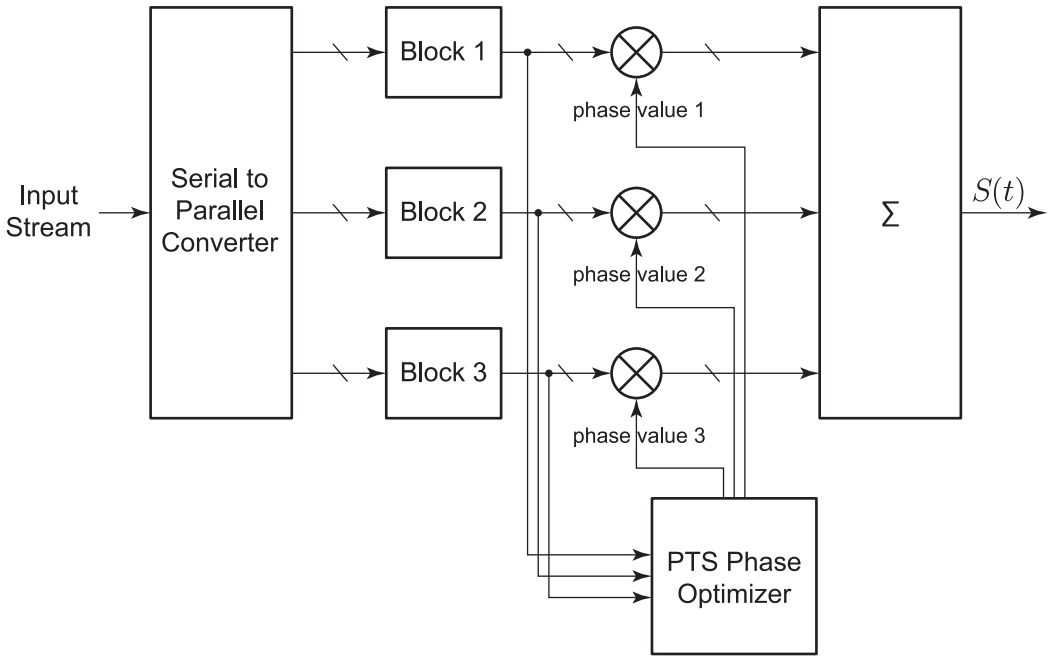

FIGURE 7.19: Block diagram for an SEFDM transmitter employing PTS for PAPR control.

7.4.3 Partial Transmit Sequence (PTS)

PTS is another well known technique for controlling the PAPR of OFDM signal [155]. Again, due to the similarity between the two systems, PTS is imported into SEFDM context. PTS is based on partitioning the OFDM signal into sub-blocks and then applying different phase shifts to each sub-block. The phase shifts are chosen such that the combined output of the sub-blocks is optimized in terms of PAPR [155]. Several procedures for combining the sub-blocks are reported in the literature that trade the reduction in the PAPR with the complexity of searching for the optimum phase shifts [161, 162, 163]. Again, there is a need to inform the receiver of the operation performed at the transmitter to enable the decoding of the received signal by sending side information, thus a resultant reduction in the overall throughput.

Fig. 7.19 shows a block diagram of an SEFDM system employing PTS. The SEFDM signal is divided into three sub-blocks and each sub-block is modified with a separate phase shift. The PAPR reduction is achieved by performing an exhaustive search of the combination of the phase shifts that achieves the lowest PAPR. The complexity of the search for the optimum combination of phase alterations is the main limitation of the PTS method. For instance, for a system that is divided to 3 sub-blocks and assuming

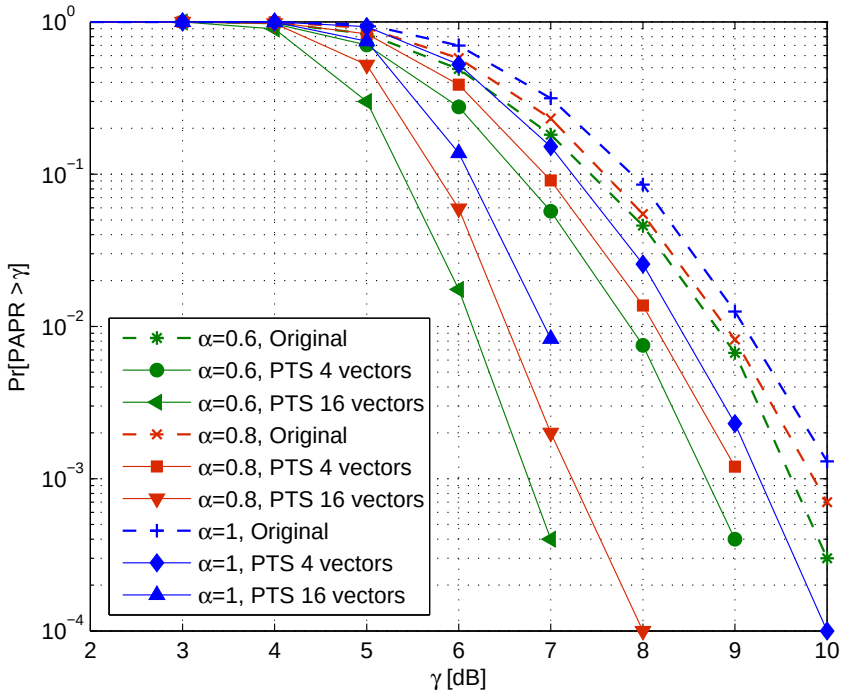

FIGURE 7.20: CCDF of the PAPR of SEFDM systems employing PTS using 4 , 16 vectors for different values of α for 32 subcarrier SEFDM system with 4QAM input symbols.

that only two phase changes are available, there is a need to choose the optimum SEFDM symbol (i.e. the one with minimum PAPR) from a set of 2^3 possibilities.

The efficiency of PTS in reducing the PAPR of SEFDM system is examined by simulations. Fig. 7.20 and Fig. 7.21 displays the CCDF of the PAPR of an SEFDM system employing PTS for different values of α and N. It can be seen from the figure that PTS showed higher efficiency in PAPR reduction when using 4 phase vectors leading to a search of 2^4 combinations for each SEFDM symbol.

The spectrum and BER performance of the PTS based SEFDM system are examined. The spectrum of the PTS based system is provided in Fig. 7.22 showing that the spectrum of the SEFDM system is maintained. The spectrum of the PTS manipulated signal showed some decrease in the out of band emission for the case of 16 phase vectors. This indicates that the concepts of PTS may be examined for the reduction of out of band emission. Finally, the BER of an SEFDM system using PTS is depicted in Fig. 7.23. The figure show slight BER reduction for BPSK input symbols case.

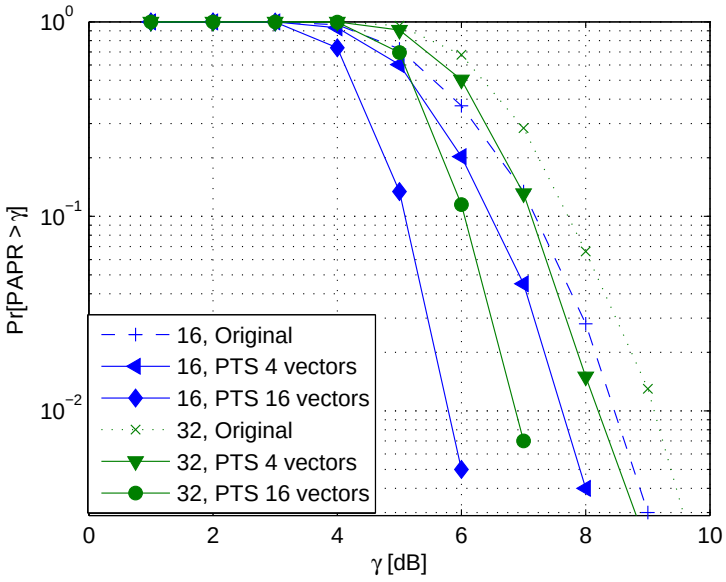

FIGURE 7.21: CCDF of PAPR of SEFDM system employing PTS using 4 , 16 vectors for different numbers of subcarriers for SEFDM system with $\alpha = 0.8$ and 4QAM input symbols.

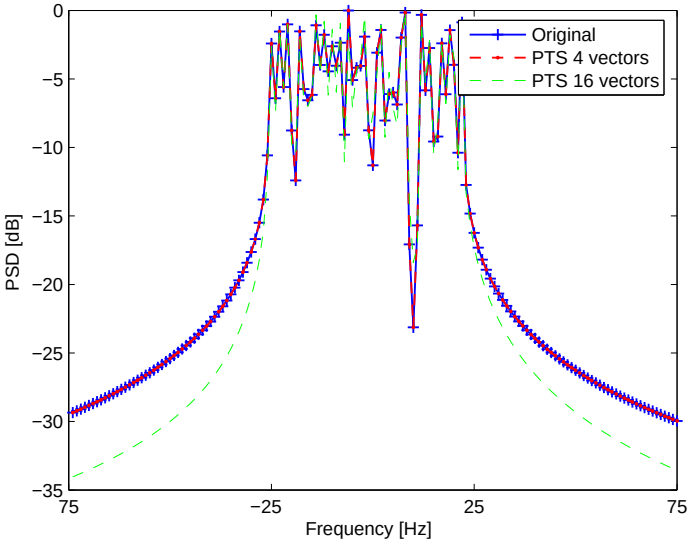

FIGURE 7.22: Spectrum of a 64 subcarrier SEFDM system using PTS for PAPR control. $\alpha = 0.75$ and input symbols are 4QAM.

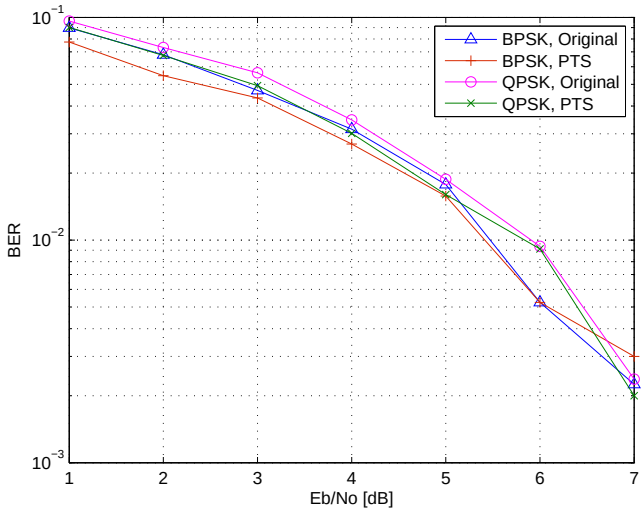

FIGURE 7.23: BER performance of an SEFDM system using PTS for 4 subcarrier system with $\alpha = 0.8$ and 16 phase vectors.

7.5 SLiding Window (SLW) PAPR Reduction Technique

The PAPR reduction techniques explored in section 7.4 are specifically designed for OFDM systems, therefore may not be optimum for the SEFDM signal design. In this section a new technique to reduce the PAPR in SEFDM system is proposed. The technique makes use of the properties of the SEFDM signal to achieve PAPR reduction. The performance of the proposed technique is investigated by simulations in terms of its efficiency in PAPR reduction and its effects on the performance of the system. As simulations uses discrete samples of the system it was necessary to abide by the rule of the minimum number of samples needed to capture all the peaks in the signal. Oversampling by a factor of 4 is used in all reported simulations.

7.5.1 Sliding the SEFDM Signal

Consider the SEFDM symbol with index $l = 0$ from equation (2.3) which can be denoted as

$$x(t) = \frac{1}{\sqrt{T}} \sum_{n=0}^{N-1} s_n \exp(j2\pi n\alpha t/T). \tag{7.12}$$

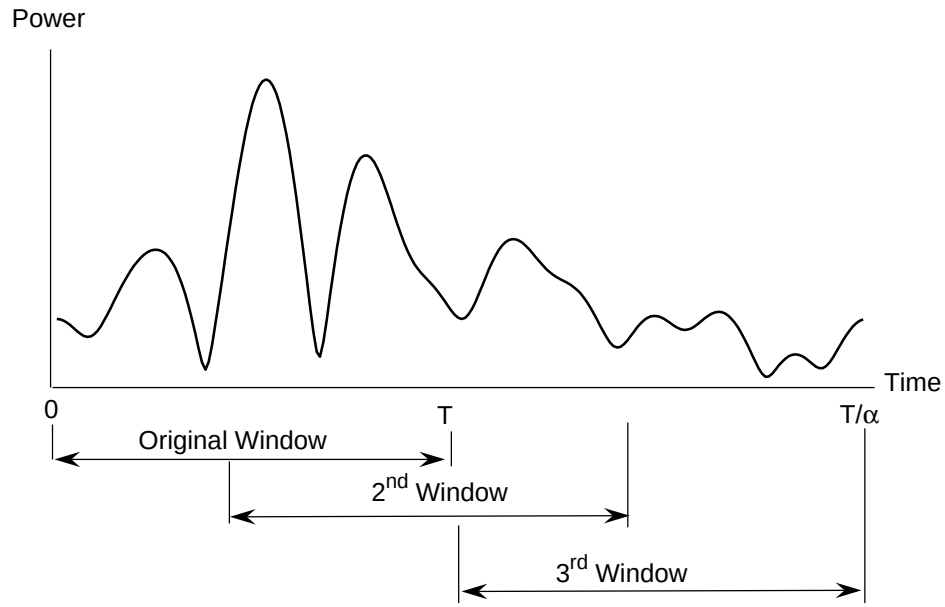

FIGURE 7.24: An SEFDM symbol in time duration of $[0 - T/\alpha]$. The concept of the different time windows

The SEFDM symbol is transmitted in the time interval $[0 - T]$, however, the expression on the RHS of (7.12) has a period equal to T/α. To maintain the characteristic relationship between Δf and T for SEFDM system, it is necessary to restrict the transmission duration to T seconds. However, there is no restriction on the exact instant to start transmission. This observation is utilized here to search for a time window in the interval $[0 - T/\alpha]$ during which the signal has the minimum PAPR as illustrated in Fig. 7.24. The different time windows should all be of duration of T seconds. It can be seen from Fig. 7.24 that each window has a different peak value and expectedly a different PAPR. The window that captures the signal at its minimum PAPR can be transmitted down the channel and consequently the overall PAPR of the system will be reduced. Effectively, this is as if a sliding time window is applied on the signal from which the term SLiding Window, or shortly (SLW), is coined for this PAPR reduction technique. The Sliding window is effectively a translation in time, resulting in no modification of the signal.

The efficiency of SLW in reducing the PAPR stems from the fact that by expressing

a signal using equivalent representations, the probability of having PAPR value larger than a threshold decreases in similar manner as in SLM and PTS [154]. Assuming that the probability of the PAPR of a signal exceeding a value γ is given by $[P_r(PAPR > \gamma)]$, then the probability of the lowest PAPR obtained from k different representation of the signal exceeding γ denoted $[P_r(PAPR_{lowest} > \gamma)]$ is given by

$$[P_r(PAPR_{lowest} > \gamma)] = [P_r(PAPR > \gamma)]^k , \tag{7.13}$$

which is always less than $P_r(PAPR > \gamma)$.

7.5.2 The IDFT Implementation of SLW

The SLW PAPR reduction technique can be integrated with the IDFT design for generating SEFDM signal proposed in chapter 4. From chapter 4, the SEFDM signal is expressed as

$$X[k] = \frac{1}{\sqrt{\alpha}} \mathcal{F}_k^{-1,M} \left\{ S' \right\} \tag{7.14}$$

for $0 \leq k \leq \rho N - 1$, where $M = \rho N/\alpha$, $\mathcal{F}^{-1,M}\{A\}$ is the M point IDFT of the N long sequence A, ρ is an oversampling factor to ensure that all peaks in the signal are captured and

$$S' = \begin{cases} s_i & 0 \leq i < N \\ 0 & N \leq i < M - 1 \end{cases} \tag{7.15}$$

for $S = [s_0, \cdots s_{N-1}]$ is a vector of input symbols. The IDFT can generate M time samples with the same frequency contents of the SEFDM system, of these samples the ones that correspond to the interval $[0 - T]$ are actually transmitted. This indicates that the sliding can be implemented simply by changing the starting sample index for the different time windows. Then, the PAPR of the different windows are calculated and the one with lowest PAPR is transmitted.

Consider the SEFDM signal at the output of the IDFT in any of the transmitters architectures proposed in [60, 61], the outputs of the IDFT are time samples given by

$$X[k] = \frac{1}{\sqrt{M}} \sum_{n=0}^{M-1} s_n^{'} \exp\left(j2\pi nk\alpha/M\right), \tag{7.16}$$

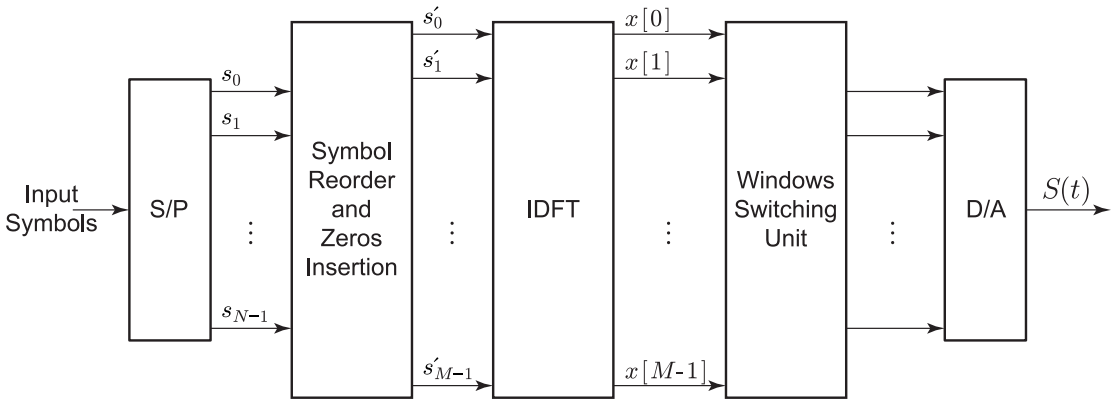

FIGURE 7.25: Block diagram for an SEFDM transmitter employing SLW for PAPR control.

where $k = 0, 1, \cdots, \rho N - 1$. The SEFDM signal is originally generated by selecting the first ρN samples. Now define a time window as

$$W_g = \begin{cases} 1 & , a_g \leq k < a_g + \rho N - 1 \\ 0 & , elsewhere \end{cases}, \tag{7.17}$$

where a_g marks the starting instant of the window and g denotes the window index. The resultant signal will be

$$X[k] = 1/\sqrt{M} \sum_{n=0}^{M-1} W_g \, s_n^{'} \exp(j2\pi nk\alpha/M). \tag{7.18}$$

The effect of applying the window W_g will limit k to values within that window. In other words by substituting by $k = h + a_g$ for $h = 0, 1, \cdots, \rho N - 1$, where h corresponds to time samples only within W_g, equation (7.18) can be rewritten as

$$\begin{aligned} X[h + a_g] &= \tfrac{1}{\sqrt{M}} \sum_{n=0}^{M-1} s_n e^{j2\pi n(h+a_g)\alpha/M}, \\ &= \tfrac{1}{\sqrt{M}} \sum_{n=0}^{M-1} s_n e^{j2\pi n a_g \alpha/M} e^{j2\pi nh\alpha/M}. \end{aligned} \tag{7.19}$$

Equation (7.19) illustrates how the different windows result in different translations in time benefiting from the fact that in the IDFT evaluation the translation in time can be expressed equivalently as a phase shift in the frequency domain.

Fig. 7.25 depicts an implementation of the proposed technique. $s_i^{'}$ is the i^{th} modified symbol that is obtained after the reordering and zero insertion into the original information symbols necessary for SEFDM signal design as shown in equation (7.15). The outputs of the IDFT are fed into a module that calculates the PAPR and as such determines the optimum window in terms of the PAPR and allows the transmission of the time samples within that window to the next stage in the transmitter. The receiver will need to be informed of the time window used at the transmitter to be able to decode the signal. Such information is typically sent as side information which in turn reduces the overall throughput.

7.5.3 Sliding Mechanism: Fixed Sliding vs Dynamic Sliding

The way the sliding windows are designed will dictate the performance of the system. Sliding can be performed by locating the peak of the signal and then slide the window to the location that results in the exclusion of the peak. Such sliding will be performed on a symbol by symbol basis, therefore, termed dynamic sliding. Furthermore, the dynamic sliding can be repeated to ensure that the slider sweeps all of the available time samples space and captures the window with the minimum PAPR. Dynamic sliding can be performed in few steps, however, the amount of the side information needed at the receiver is expected to be high. Unless there is an efficient method to transmit the side information, it may not be practical to perform dynamic sliding.

Another way is to design fixed time windows that are known to both the transmitter and receiver. The PAPR of all the windows is checked for every SEFDM symbol and the one with the minimum PAPR is chosen. Such a sliding mechanism fixes the amount of the side information as the needed side information will be $log_2 w$ bits for w time windows.

7.5.4 Performance Evaluation

The performance of SLW is evaluated by numerical simulations in terms of efficiency in PAPR reduction and effects on spectrum and BER. Simulated signals were heavily oversampled to ensure that all peaks are captured.

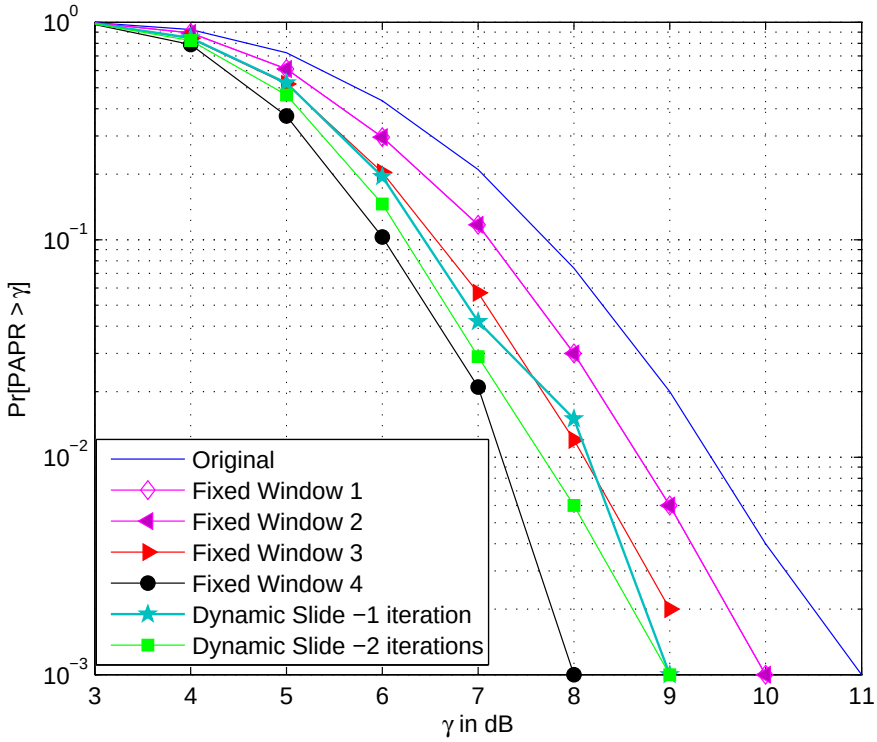

FIGURE 7.26: CCDF of the PAPR of an SEFDM system employing SLW for dynamic sliding and 4 windows in fixed sliding. The system has 12 subcarrier with $\alpha = 0.5$ and 4QAM input symbols.

Fig. 7.26 shows the CCDF for a system employing SLW. The system depicted employs dynamic sliding with one and two iterations, and fixed sliding with 4 windows. It can be clearly seen that substantial PAPR reduction (up to 3 dB) is obtained with 4 time windows, whereas dynamic sliding achieved competitive results (< 1 dB) with just two iterations. However, the side information is required to communicate the dynamic sliding performed can be high (enough information to locate the peak samples locations), whereas only two bits are needed to send the used window index in this example of fixed sliding.

The performance of SLW in PAPR reduction is evaluated for different values of α in Fig. 7.27. The figures confirm that SLW provides PAPR reduction as described. The level of PAPR reduction varies with the level of bandwidth compression. As α increases the SEFDM symbol duration increases with respect to the signal period, hence the overlapping between windows increases and the potential of PAPR reduction decreases consequently.

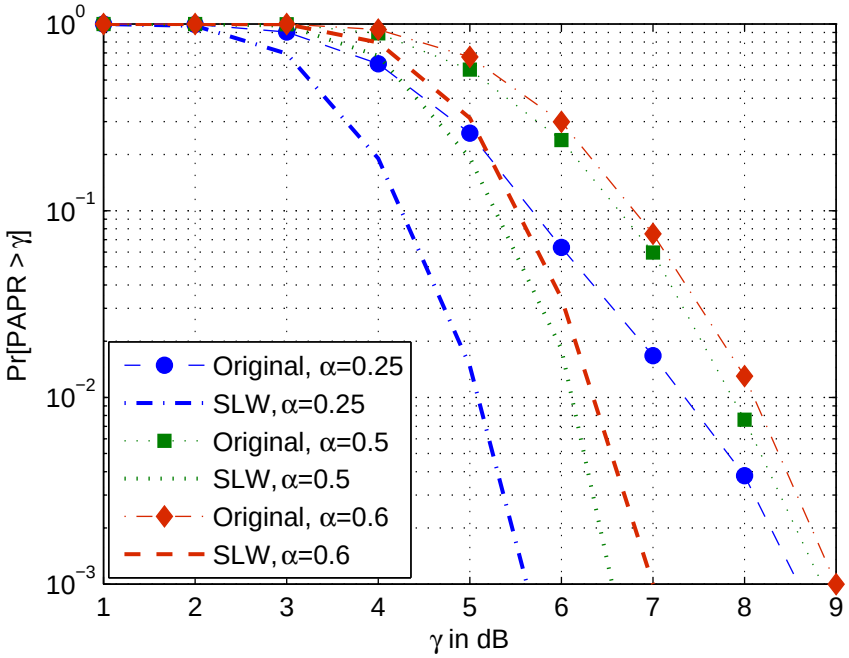

FIGURE 7.27: CCDF of PAPR of 16 subcarrier SEFDM employing SLW (with 4 windows) for different α values.

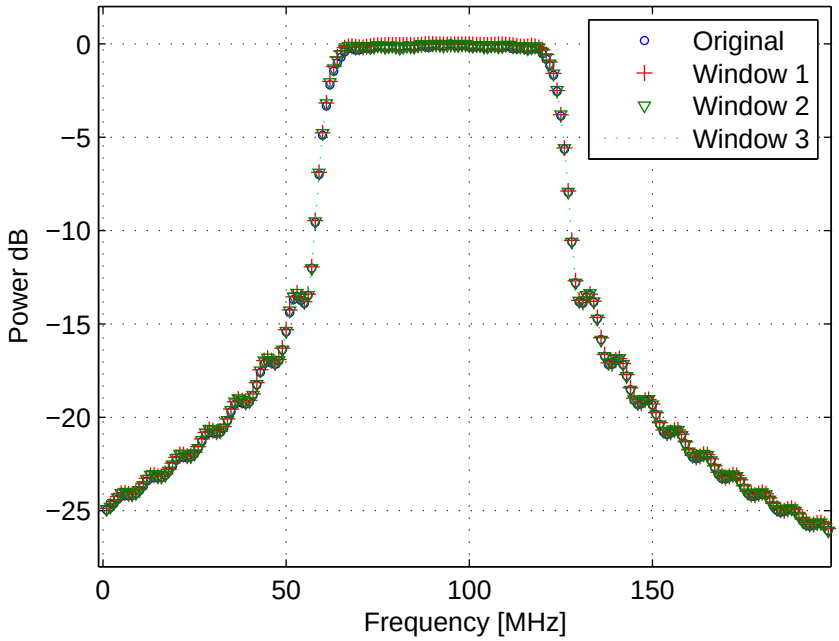

FIGURE 7.28: Spectrum of 16 subcarrier SEFDM system, $\alpha = 0.5$ and 4QAM input symbols using SLW for PAPR control.

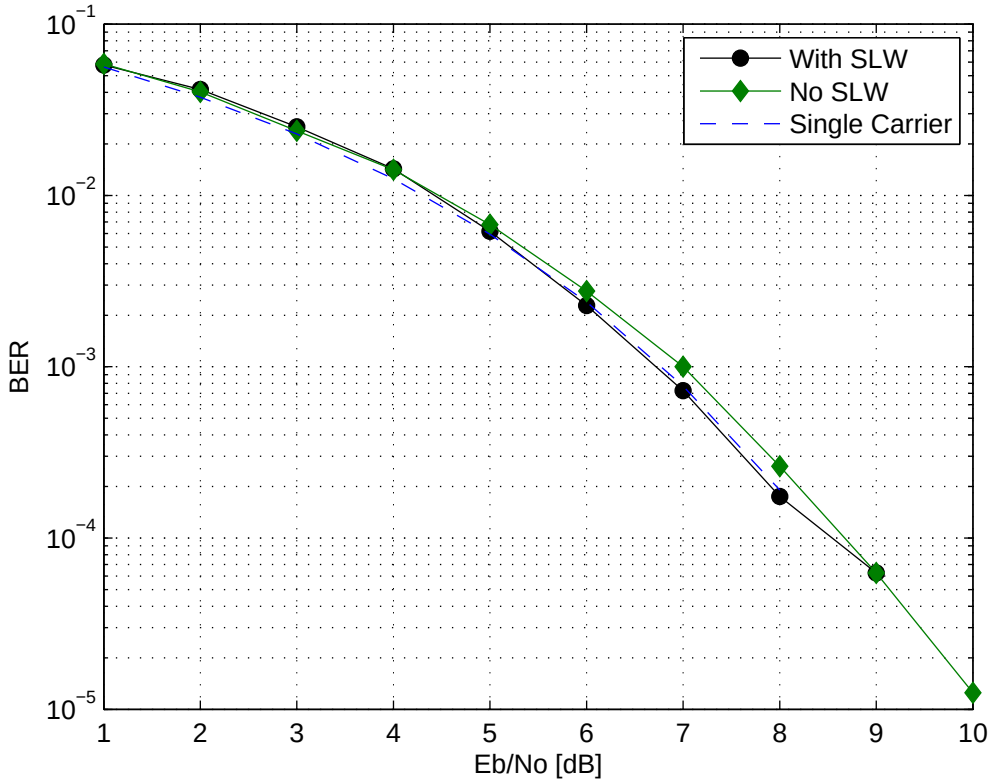

FIGURE 7.29: BER performance of SEFDM system using SLW for 4 subcarrier system with $\alpha = 0.8$ and 4QAM input symbols.

The spectrum of the signal and the BER performance after applying SLW were examined numerically. Fig. 7.28 displays the spectrum of the original SEFDM signal and three other proposed slided signals. As expected, all the windows maintained the same 3 dB bandwidth, whilst the BER performance remains unaffected by the sliding as displayed in Fig. 7.29 using conventional SEFDM receiver [21].

Fig. 7.30 depicts SLW, PTS and SLM PAPR reduction for a 16 carrier SEFDM system for $\alpha = 0.5$ for the same side information requirement. The figure shows that SLW outperforms PTS with 4 phase vectors by about 1 dB at 10^{-2}, whereas SLM showed almost the same PAPR reduction probability as SLW. However, SLW has the advantage of ease of implementation since it is easily integrated with the SEFDM IDFT based transmitter. SLW mainly relies on the IDFT based transmitter architecture and does not require any multiplication or addition operations at the transmitter. Moreover, there is no need to duplicate the IDFT module in the system as it is the case with SLM and PTS. In addition, there is almost no added complexity in the reception side

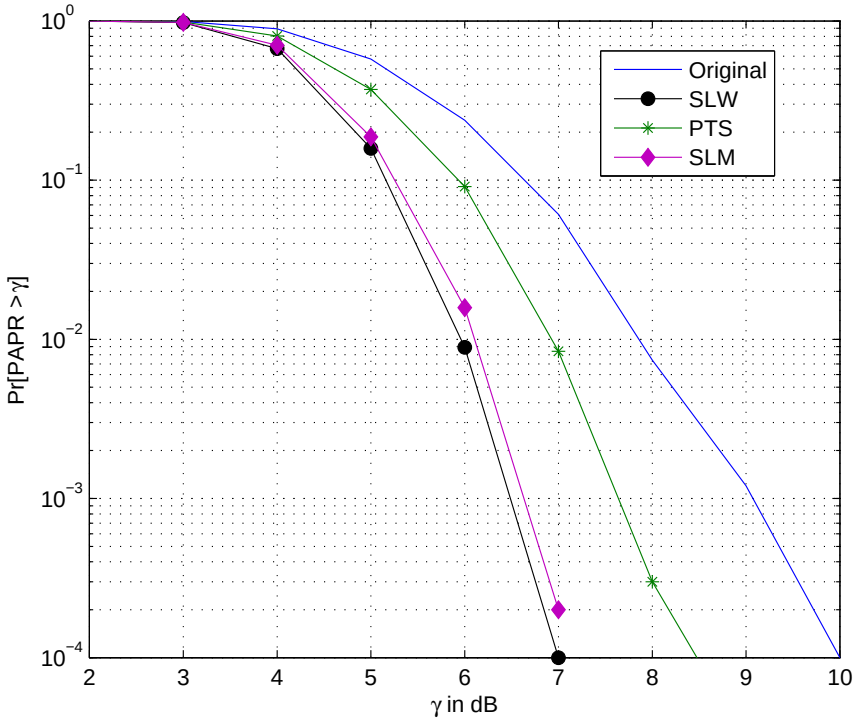

FIGURE 7.30: CCDF of PAPR of a 12 subcarrier SEFDM system with $\alpha = 0.5$ using SLW, PTS and SLM techniques for the same side information requirement for the PAPR reduction

for a system using SLW. The receiver will only need to slide the recovering functions, conjugate subcarriers or IMGS bases for MF or correlation demodulation, respectively, in time to maintain synchronization with the transmitter.

7.6 Conclusions

This chapter addressed the issue of Peak to Average Power Ratio (PAPR) in SEFDM system. Mathematical derivations of the instantaneous power of the SEFDM system together with simulations have confirmed that the SEFDM signal will exhibit random power variations during transmission time. The statistics of the PAPR of the signal exceeding certain level were examined by simulations that generate the CCDF of the PAPR. It is found that an SEFDM signal has a lower probability to exceed a PAPR value than an equivalent OFDM signal, nevertheless, the SEFDM signal exhibited significant occurrences of PAPR exceeding high values.

Methods imported from OFDM system were applied to SEFDM system. In particular, clipping, selective mapping (SLM) and partial transmit sequences (PTS) were examined for use in SEFDM system. Studying the effects of clipping on the signal provided information about how the system may be affected when no PAPR control technique is used. The results obtained shows that the clipped SEFDM signal suffers from increased out of band emission. In addition, the BER performance showed deterioration even for small system size and ML detection. With increasing the number of subcarriers and using SD, the BER performance showed further degradations. This result confirms that the uncontrolled PAPR will pose detrimental effects on the system performance, if the PAPR exceeded the dynamic range of the transmitter circuitry.

In the pursuit of PAPR reduction in SEFDM, it was necessary to evaluate the effects of reduction techniques on the performance of the system. Performance measures used here are the CCDF to evaluate the efficiency of PAPR reduction, the BER and power spectral density. Obtained results suggest that using any of the three techniques (clipping, SLM and PTS) provide PAPR reduction with varying efficiencies and performance penalties. Clipping achieves the required PAPR reduction but introduces out of band interference and BER degradations while SLM and PTS provide less PAPR reduction with no impact on spectrum or BER performance, yet it requires sending side information along the data.

A new method specially tailored for SEFDM system was designed and evaluated. The method makes use of the simple digital implementations of SEFDM transmitters offering substantial PAPR reduction of about $2-3$ dB. Most of the techniques proposed in the OFDM literature provide about 2 dB reduction. In addition, the proposed method does not require any BER or spectrum compromises. The method is termed SLiding Window (SLW) PAPR reduction technique as the PAPR reduction is realized by sliding a time window over an extended symbol duration, comparing the achieved PAPR reduction and eventually transmitting the window with the lowest PAPR. The SLW follows a similar philosophy as SLM and PTS. In the three techniques the signal is expressed in different ways and the one with the lowest PAPR is transmitted. However, in SLW no multiplication or addition operations are applied on the signal, as the time dimension is exploited to choose the optimum time to capture the SEFDM signal. In SLM and PTS the reduction is achieved by changing the phase of the individual carriers randomly where in SLW it is achieved by changing the phase of the combined signal. Moreover,

there is no need to duplicate the IDFT module in the system as is the case with SLM and PTS. The signal is basically the same signal but sampled at a later or earlier times. The receiver needs not change the mechanisms of detection, but will need to slide any recovering functions in time to maintain synchronization with the transmitter.

To conclude, the work in this chapter shows that the SEFDM signal can exhibit high PAPR. If the dynamic range of transmitter circuitry is not matched to the signal PAPR requirements and the PAPR is not controlled, the system will experience performance degradations in the form of spectral spreading and BER performance deterioration. On the other hands, several techniques can be used for the control of the PAPR with the SLW being the most prominent candidate for its high efficiency in PAPR control and the lower complexity of realization. Nevertheless, SLW requires sending side information and the benefit of avoiding the effects of the uncontrolled PAPR needs to be weighed against the reduction in throughput required for the PAPR reduction.

Chapter 8

SEFDM in Fading Channels, Performance, Channel Estimation and Equalization

8.1 Introduction

Previous chapters discussed the characteristics of the SEFDM signal, efficient generation and reception techniques. The system has been investigated in AWGN channel in order to identify its intrinsic issues. In practical systems, performance investigations need to address practical channel options, particularly investigations in the wireless channel to assess the potential of improving the utilization of the limited spectrum. The work in [84] has proposed the use of Iterative Modified Gram Schmidt (IMGS) bases for signal demodulation followed by Sphere Decoder (SD) joint channel equalizer and symbol detector. The system was tested in two fixed channel scenarios where channel estimation was performed using pilot SEFDM symbols. Three issues arise from this work. First, the proposed system uses IMGS bases for the demodulation, therefore will require orthonormalization process and a bank of correlators customized for system structure. Second, the results presented in [84] have indicated that the SD algorithm is capable of achieving performance close to OFDM for bandwidth savings of 20%. However, as discussed in section 6.5, the SD suffers from variable complexity, therefore is not optimized for hardware designs. Third, the work has shown that the accuracy of the proposed channel

estimator suffers with the increase in bandwidth compression level. The work in this chapter addresses the three discussed issues and proposes solutions that overcome their shortcomings.

The structure of the SEFDM transceiver is revisited and the use of the Matched Filter (MF) proposed in chapter 5 is extended to the system in fading channel. The effects of the MF demodulation is verified by deriving and numerically investigating a Maximum Likelihood (ML) joint equalizer and detector and then the associated SD using MF based statistics. Then, an improved method for channel estimation is proposed and its operation verified. The derived technique builds on the findings on the structure of the SEFDM system from chapter 3. This new estimator is termed Partial Channel Estimator (PCE) as it invokes a subset of the system subcarriers that contains the relatively orthogonal carriers. That is PCE activates only the orthogonal or near orthogonal subcarriers within the SEFDM symbol and transmits pre-determined pilots symbols onto these carriers. This way the ill conditioning of the system is avoided as the sent pilot SEFDM symbols contain only orthogonal subcarriers. The performance of the proposed estimator is examined in terms of accuracy of estimation and impact on the error performance. Numerical investigations of the PCE have demonstrated the superiority of the technique over techniques employing fully loaded SEFDM symbols.

Furthermore, equalization of the faded SEFDM signal is considered using linear and sphere-wise equalization techniques. In particular, performance of linear equalizers Zero Forcing (ZF) and Minimum Mean Square Error (MMSE) is briefly investigated. Moreover, the use of the Truncated Singular Value Decomposition (TSVD) for signal equalization and detection is proposed. The TSVD facilitates substantial error performance improvement over ZF and MMSE. Finally, the use of the Fixed Complexity Sphere Decoder (FSD) and the combined FSD-TSVD for jointly equalizing and detecting the SEFDM signal is proposed. Numerical results demonstrate superior performance when compared to linear techniques.

Overall, the work in this chapter is considered an introduction to the examination of the SEFDM in fading channels. Further studies in different channel conditions can be useful to determine the most suited systems to adopt the SEFDM criteria.

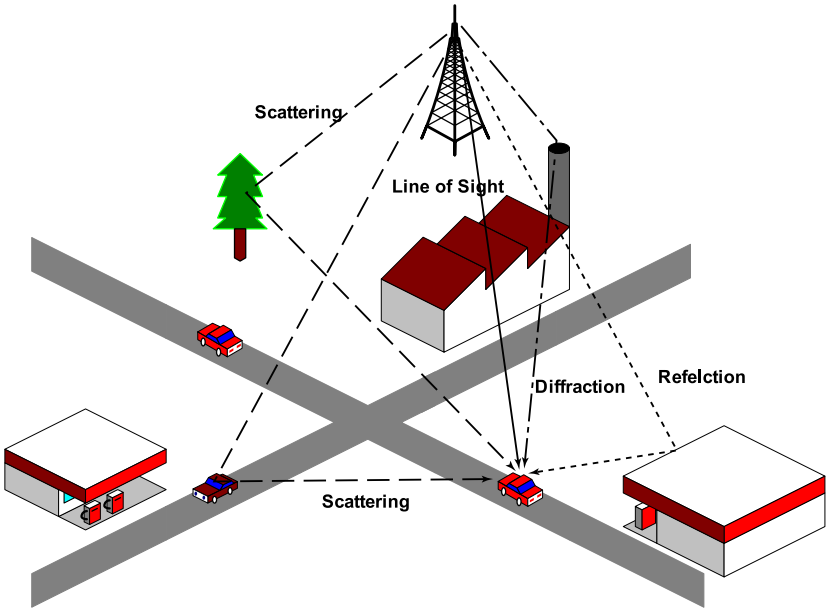

FIGURE 8.1: Multipath propagation environment.

8.2 The Wireless Channel: Preliminaries

The wireless channel represents the main resource for the wireless communications as well as the main source of their limitation. To start with the spectrum is a resource that needs to be used and divided with the interest of operators and users. On the other hand, spectrum access is a resource that constitutes a main initial cost for the wireless communications service providers which is eventually covered in the tariffs imposed on users end. Spectral efficiency is therefore an issue that affects the users, service providers and regulating bodies.

The nature of wireless signal propagation subjects the signal to many forms of impairments, thus constrains the performance of wireless systems and their spectral needs. Sources of impairments in the wireless channel include: in band interference from other signals in the same channel; out of band interference from signals in adjacent channels; noise from different sources; and multipath fading. Multipath fading occurs due to the fact that the transmitted electromagnetic signal may follow different routes (and methods) before arriving at the receiver such as reflection, diffraction and scattering as illustrated in Fig. 8.1.

In a multipath propagation environment, the different signal versions received experience different amplitude and phase changes. At the receiver, the signals add up vectorially

and depending on the phase of the different waves the superposition could be constructive or destructive resulting in changes of the signal over time, frequency and distance [168, 169]. Furthermore, the wireless channel state can vary with time, thus different symbols and parts of symbols may take different durations to arrive at reception side leading to intersymbol interference (ISI). In addition, due to the relative motion of the communicating parties and/or the scatterers in the surrounding environment, the received signal phase will have some changes over time which represents a frequency shift known as the Doppler shift. This frequency shift is directly proportional to the velocity and direction of motion with respect to the direction of arrival of the received multipath signal and may cause what is known as frequency spreading. Overall, a signal propagating through multipath environment may suffer from random changes in its amplitude and phase, random frequency shifts and can be dispersed in time.

In general, the multipath channel is identified by a set of parameters that describe the frequency and time dispersive nature of the channel. Delay spread and coherence bandwidth describe the time dispersive nature of the channel whereas the Doppler frequency and the coherence time describe the frequency dispersive nature of the channel.

Delay spread describes the broadening of the transmitted symbol in time due to the supperposition of the copies arriving via different propagation paths where the coherence bandwidth describes the range of frequencies over which the channel response is considered flat. When the signal bandwidth is less than the channel coherence bandwidth, the different frequency components of the signal experience flat fading. On the other hand, if the signal bandwidth is greater than the channel bandwidth the signal will encounter frequency selective fading as the frequency components outside the coherence bandwidth will be treated in a different way compared to the component within the coherence bandwidth [168, 1].

Due to the Doppler effect the spectrum of the transmitted signal may be broadened as Doppler spread. Doppler spread is defined as the range of frequencies over which the Doppler spectrum is nonzero [1]. In addition, the channel may exhibit different Doppler shifts over time, where the time duration over which the channel response is invariant is denoted as the coherence time. Based on the channel coherence time and the signal transmission time two fading types are classified: fast and slow. Fast fading, also termed time selective fading, happens when the symbol period is greater than the coherence time

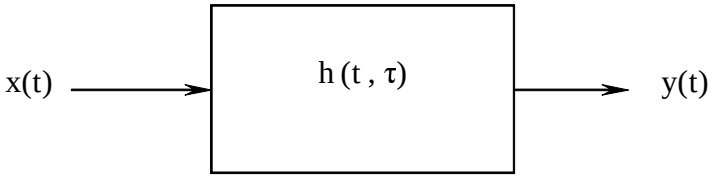

FIGURE 8.2: Wireless channel model.

of the channel while slow fading occurs when the symbol period is much smaller than the coherence time of the channel.

As discussed above the fading is categorized based on the two characterizing features of multipath channel which is time variant and dispersant. The delay spread leads to time dispersion and frequency selective fading. The Doppler spread leads to frequency dispersion and time selective fading. The type and extent of fade experienced by a signal depends on signal parameters such as bandwidth and symbol period and channel parameters such as delay spread, coherence bandwidth and coherence time.

8.2.1 Modelling the Multipath Channel

Modelling the multipath channel is vital for understanding the wireless channel and to design appropriate mitigation techniques. However, due to the varying nature of the wireless propagation, channel models are typically based on statistics from measurements for a specific system or spectrum allocation [170]. The multipath structure of the channel is determined by channel sounding techniques such as direct pulse measurements, spread spectrum slicing correlator measurements, and swept frequency measurements.

To accommodate the time and frequency dispersive nature of the channel, the mobile radio channel is modelled as a linear filter with a time varying Channel Impulse Response (CIR) $h\left(t,\tau\right)$ [1], which is a function of t to represent the time variations of the channel, and τ to represent the channel multipath delay, thus the input/output relationship of the channel depicted in Fig. 8.2 is defined as

$$y\left(t\right)=h\left(t,\tau\right)\otimes x\left(t\right), \tag{8.1}$$

where $\otimes$denotes the convolution operation.

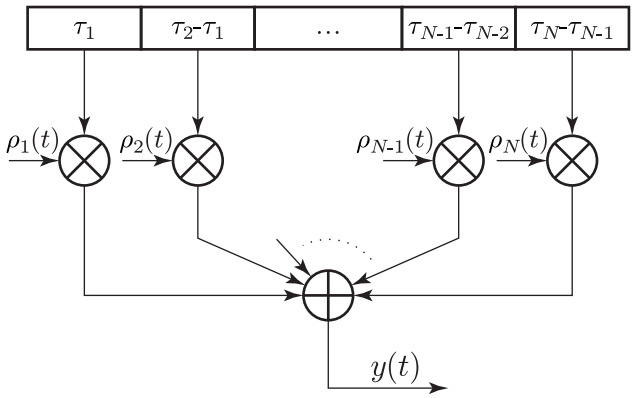

FIGURE 8.3: Tapped delay line (TDL) channel model.

Simulations models of the wireless channel can be deterministic or stochastic [171]. Deterministic models assume knowledge of the structure of the channel and that the channel remains the same for the specified duration of channel use. On the other hand, stochastic models treat some aspects of the channel as random processes. For narrowband signals the channel is usually modelled with statistical Rayleigh, Rician and Nakagami fading with one path as the signal duration being sufficiently longer than the delay of the channel [1]. For wideband signals, channel models follow the Wide-Sense Stationary Uncorrelated Scattering (WSSUS) assumption [172] and are modelled as Tapped Delay Lines (TDL) [173, 174, 175, 64], depicted in Fig. 8.3. The general TDL model has the low pass impulse response as

$$h(\tau, t) = \sum_{n=1}^{N(t)} \rho_n(\tau_n(t), t)\, \delta(\tau - \tau_n(t)), \tag{8.2}$$

where $N(t)$ denotes the time-varying number of multipath components, $\rho_n(\tau_n(t), t)$ are the low pass time-varying complex channel coefficients and $\tau_n(t)$ are the time varying delays. The parameters of the TDL model can be fixed or random, and are time invariant or time varying to reflect different channel conditions.

The power of the tap gains is drawn from the Power Delay Profile (PDP) whereas the Probability Density Function (PDF) of each gain is defined by the Doppler spectrum to reflect the frequency dispersive nature of the channel. The PDP $P(\tau)$, also known as the multipath intensity profile, represents the average received power as a function of the delays. Commonly assumed forms for $P(\tau)$ are uniform and exponential [176]. The Doppler spectrum B_d indicates how fast the channel characteristics are changing. In

simulations, the channel path gains are filtered to reflect the required Doppler spectrum noting that the different paths may experience different Doppler conditions. A widely used model for Doppler filtering is the Jakes' model [169].

To create a snapshot of the channel, typically a random number of paths is generated. Then, different path delays are drawn from the distribution of delays. Following that, random processes corresponding to the number of paths are generated. Each process is filtered to reflect the associated Doppler Spectrum. Finally, the power of the random processes is adjusted according to the PDP values corresponding to the delays. The created snapshot of the channel is valid for as long as a fixed number of multipath components and their associated delays can be assumed. A practical limitation of the TDL model is that the delays are variable and can take values that are fractions of the sampling duration, therefore, may require a huge amount of oversampling. This issue is solved by the adopting a uniformly spaced TDL model [173]. The uniformly spaced TDL model generates an equivalent TDL model with a new number of taps and equal delays with tap gains that are adjusted so that the resultant model is equivalent to the discrete multipath channel with non-uniformly spaced delays.

8.3 Design and Assessment Methodology

The SEFDM system in fading channel is constructed from the same main system blocks as described in previous chapters. The SEFDM signal may be generated following any of the proposed IDFT based structures in chapter 4. The signal propagates through a fading channel and then suffers AWGN at reception side. The receiver is constructed of the two main components investigated in chapter 5: the first stage collects the statistics and the second performs equalization and detection.

The study of the SEFDM signal in fading channel started with mathematically modelling the SEFDM system with fading channel effects. Following that, it is proposed to perform the demodulation with the conjugate carriers which will be denoted as Matched Filter (MF), although the matching here refers to the signal generator operation and does not include matching to the channel. The MF notation is kept to maintain the similarity of the system design with the one proposed in chapter 5 and to distinguish this work from the system presented in [84] that uses IMGS bases at the demodulation stage.

The proposal of the use of the MF based system is motivated by the desire to maintain the complexity reduction facilitated by the MF based demodulation as discussed in chapter 5. Following, the optimal joint equalizer and detector for the MF based system is derived and verified against previous proposal by numerical simulations. In addition, the design of improved estimator and equalizers is pursued based on the findings about the system properties and the investigated detection techniques in chapters 3 and 6, respectively. The performance of the proposed techniques is investigated via detailed numerical simulations.

Investigations of the performance in wireless channels require the use of simulation models and the identification of relevant channel conditions and parameters. The type and extent of fade experienced by a signal depends on signal parameters such as bandwidth and symbol period and channel parameters such as delay spread, coherence bandwidth and coherence time. The simulations considered the SEFDM under three main channel scenarios: static, quasi static channel and time varying. For the static channel two channels are imported from the work in [84] for SEFDM system and [177] for OFDM and termed Channel 1 and Channel 2, respectively. Both channels are static with different number of paths. Testing under these two channels is undertaken mainly to facilitate a comparison with the work in [84] for SEFDM system. Nevertheless, the fact that these channels are fixed is utilized to demonstrate the potential and challenges of the SEFDM signal in fading channels. Particularly, the fixed channels facilitate the exploration of the effect of having systems with different number of subcarriers. Channel 1 particularly, is an optimistic scenario, however, it serves the purpose of demonstration of the correctness of the model and gives insight into the performance trends of the SEFDM system with the introduction of channel effects. Channel 2 is a more hostile channel with more paths and longer delays than Channel 1.

The second channel scenario is a quasi static channel designed and termed Channel 3. The channel is considered quasi static as it does not significantly change within an SEFDM symbol transmission, and it is time variant over the duration of the transmission of few symbols. Channel 3 is composed of random number of paths and random paths delays set within an upper bound of 8 paths and a third of transmission time, respectively. For Channel 3 the power of the path gains is drawn from the multipath intensity profile

TABLE 8.1: COST207 reference models.

Area Type	**PDP**	**Range**
Rural Area (RA)	$\frac{9.2}{1-e^{-6.44}}e^{-9.2\tau}$	$0<\tau<0.7$
Typical Urban (TU)	$\frac{1}{1-e^{-7}}e^{-\tau}$	$0<\tau<7$
Bad urban (BU)	$\frac{2}{3(1-e^{-5})}e^{-\tau}$ $\frac{1}{3(1-e^{-5})}e^{5-\tau/\mu s}$	$0<\tau<5$ $5<\tau<10$
Hilly	$\frac{1}{(1-e^{-7})/3.5+0.1(1-e^{-5})}e^{-3.5\tau}$ $\frac{0.1}{(1-e^{-7})/3.5+0.1(1-e^{-5})}e^{15-\tau}$	$0<\tau<2$ $15<\tau<20$

TABLE 8.2: Simulation parameters for Channels 1, 2 and 3. T_s is the sampling period.

Channel	Parameters	Description	Impulse Response
Channel 1 [84]	Fixed		$h(t)=0.8767\delta(t)-0.2279\delta(t-3T_s)$
Channel 2 [84, 177]	Fixed		$h(t)=0.8767\delta(t)-0.2279\delta(t-3T_s)$ $+0.1315\delta(t-7T_s)$ $-0.4032e^{i\pi/2}\delta(t-10T_s)$
Channel 3: Quasi static channel [this work]			
	No of paths	random	1-8
	PDP	exponential	$\frac{9.2}{1-e^{-6.44}}e^{-9.2\tau/1ms}$
	Delay	random	$0<\tau<\frac{T}{5}$

of the COST 207 [1]reference model for rural area (RA), provided in Table. 8.1. The purpose of Channel 3 is to examine performance changes with some degree of uncertainty facilitated by the random aspects of the proposed channel. In addition, Channel 3 provides similar channel conditions for different number of subcarriers which is not supported by Channel 1 and 2.

Table. 8.2 lists the parameters of each channel and Fig. 8.4 depicts the impulse and frequency response of Channel 1 and 2 and a time snapshot of Channel 3 . Fig. 8.5 depicts the time varying nature of Channel 3 where the channel is recorded for the time taken to transmit 60 SEFDM symbols. The figure shows the slow fading property of the channel.

Furthermore, Channel 4 is designed to model a fast time varying channel and is used in section 8.5 only. Channel 4 is designed to have a single path Rayleigh channel to focus on the effects of the time varying nature [37]. The channel exhibits two Doppler

[1]COST207 is a work group established by CEPT. COST207 specified suitable channel models for typical propagation environments classified into four categories: areas with rural character (RA=rural area), Typical urban for cities (TU=typical urban), densely built urban areas with bad propagation conditions (BU=bad urban), and hilly terrains (HT, hilly terrain). Based on the WSSUS assumption, COST207 developed specifications for the delay power spectral density and the Doppler power spectral density for the four categories mentioned before[169].

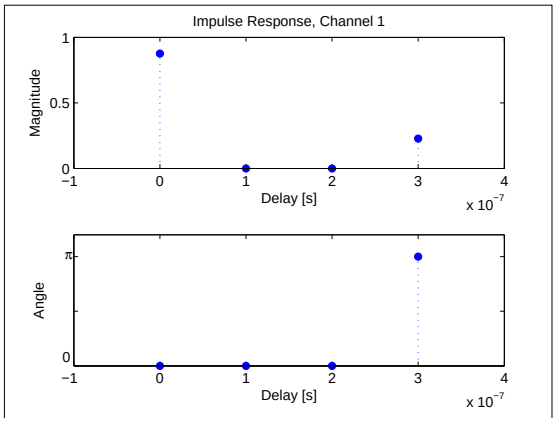

(A) IR, Channel 1.

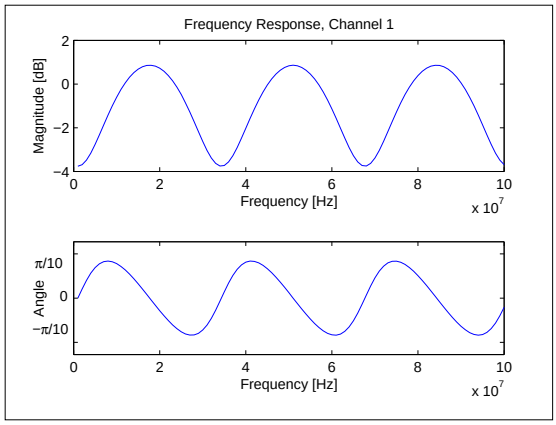

(B) FR, Channel 1.

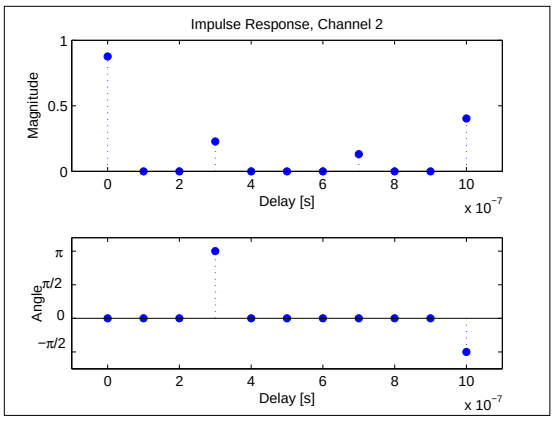

(C) IR, Channel 2.

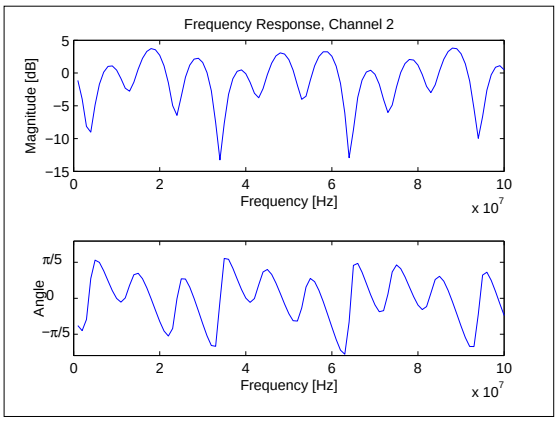

(D) FR, Channel 2.

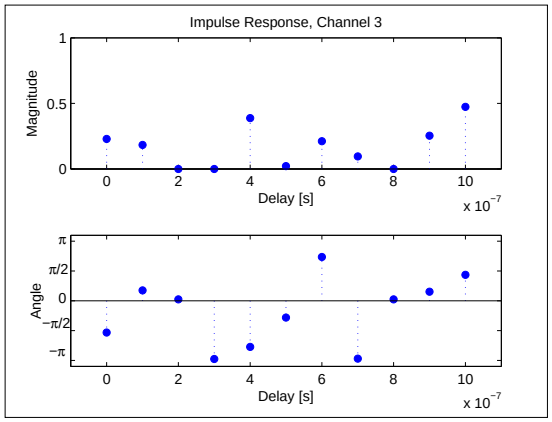

(E) IR, Channel 3.

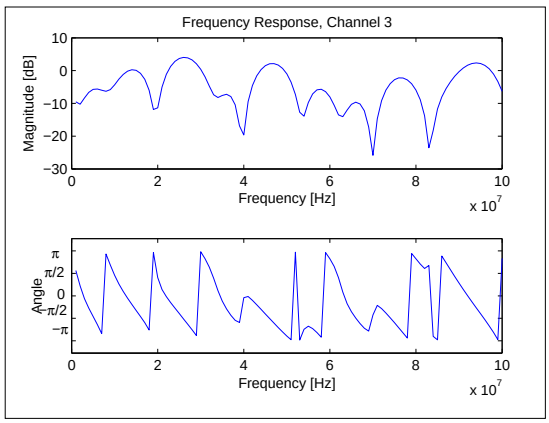

(F) FR, Channel 3.

FIGURE 8.4: The impulse and frequency response (IR) and (FR), respectively, of Channels 1 and 2 and a time snapshot of Channel 3.

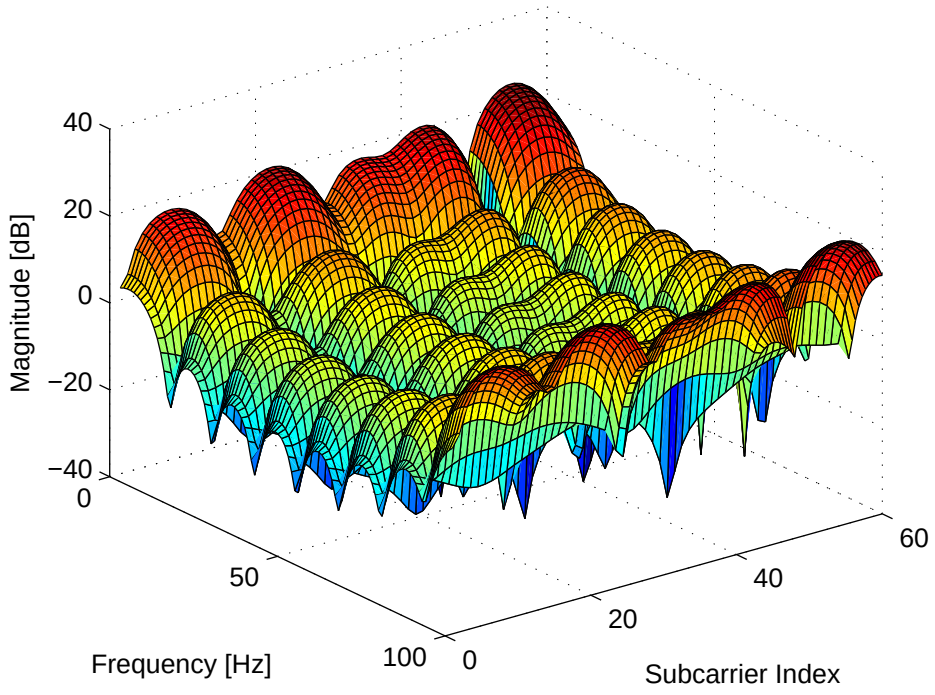

FIGURE 8.5: The time variance of Channel 3.

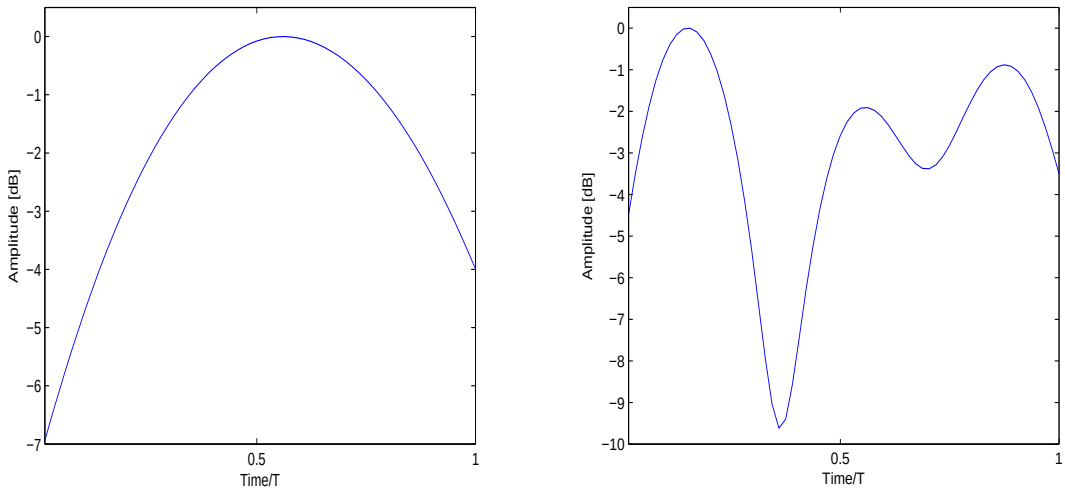

(A) $T_c = 0.75T$. (B) $T_c = 0.3T$.

FIGURE 8.6: A time snapshot of the impulse response of Channel 4.

TABLE 8.3: Signal and channel simulation parameters.

Parameters	Notation	Values
Input symbols data rate	R_b	1 Mbps
Number of subcarriers	N	Different values
SEFDM symbol duration	$T = N/R_b$	
SEFDM signal bandwidth	$BW \simeq \frac{\alpha N - \alpha + 2}{T}$	
Sampling frequency ($\geq$ Nyquist rate)	$F_s = 2R_b$	2 MHz
Channel coherence time	$T_c = (0.3, 0.75)\, T$	
Doppler Frequency	$f_d = 0.423/T_c$[1]	

frequencies and serves to test for the effects of frequency dispersion on the SEFDM signal. Parameters for the Doppler effect are based on a coherence time that is a fraction of the total transmission time. This ensures that the channel does change within one SEFDM symbol transmission.

It is worth noting that the described channels are designed to reflect the performance in fading channels in general, thus do not particularly describe any existing system. However, some parameters are drawn from existing models to keep the channels realistic. The reason behind this is not to associate the SEFDM system proposal to a particular existing application and/or system specification but to explore the general boundaries of the system.

To asses the performance of the SEFDM signal in fading channels, numerical investigations are carried under the described channels. The SEFDM signal parameters for the simulations are displayed in Table. 8.3. Finally, in this work the performance in the case of perfect Channel State Information (CSI) and optimal equalization and detection is investigated to provide a benchmark for the other investigated cases. The perfect CSI case represents the best case scenario, though may not be obtainable, it can provide an upper bound on performance. Optimal equalization and detection may not be realizable but can be used to derive the ultimate upper bound on system performance. In addition, where appropriate, performance is compared against OFDM system performance and theoretical error performance curves.

8.4 Modelling the SEFDM System in Discrete Multipath Fading Channel

Considering an SEFDM signal $x(t)$ passing through a discrete multipath fading channel, the output signal of this channel is described as

$$y(t) = \sum_{1}^{\nu} \rho_n(t)\, x(t - \tau_n) + w(t), \tag{8.3}$$

where $\rho_n(t)$, τ_n represents respectively the attenuation and propagation delay associated with the n^{th} multipath component and $w(t)$ defines an AWGN noise term. The k^{th} received sample can be described from the channel response and the transmitted samples of the signal as

$$Y[k] = \sum_{1}^{\nu} h_{n,k} X[n] + W, \tag{8.4}$$

where h represents the discrete CIR and ν is the delay of the channel in terms of number of samples. Assuming that the interblock interference is cancelled either with employing guard bands or cyclic prefix, the system can then be expressed in matrix form as

$$Y = \mathbf{H}\mathbf{\Phi}S + W, \tag{8.5}$$

The matrix $\mathbf{H}$ contains the CSI and its structure varies according to the type of fading encountered. When the fading process remains constant for the duration of sending at least one SEFDM symbol, the channel matrix $\mathbf{H}$ in this case is fixed for that duration and is Toeplitz and lower triangular, thus the first column of $\mathbf{H}$ gives all the required information to construct the matrix as

$$\mathbf{H} = \begin{bmatrix} h_1 & 0 & \cdots & 0 \\ h_2 & h_1 & & \\ \vdots & & & \vdots \\ h_{Q-1} & h_{Q-2} & \ddots & 0 \\ h_{Q,1} & h_{Q,2} & \cdots & h_1 \end{bmatrix}. \tag{8.6}$$

Such channels as represented by equation (8.6) can be found in systems with fixed channel conditions and in systems experiencing slow fading where for one symbol transmission and/or multiple bursts the channel remains static.

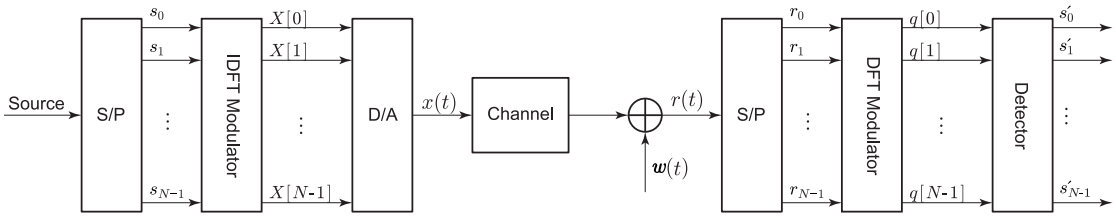

FIGURE 8.7: The SEFDM transceiver in fading channel, $q[i] = R[i]$.

For time varying channels the variations in the channel response can lead to subsequent symbols facing different channel states and that the different time samples of the same symbol encountering variable states of the channel. The channel matrix, displayed in equation (8.7), is for this case lower triangular and not Toeplitz as is the case for static and slow fading channels.

$$\mathbf{H} = \begin{bmatrix} h_{1,1} & 0 & \cdots & 0 \\ h_{2,1} & h_{2,2} & & \\ \vdots & & & \vdots \\ h_{Q-1,1} & h_{Q-2,1} & \ddots & 0 \\ h_{Q,1} & h_{Q,2} & \cdots & h_{Q,Q} \end{bmatrix}. \tag{8.7}$$

8.5 Optimal Joint Channel Equalization and Symbol Detection

The characteristic of the channel will vary based on the environment where the communication is taking place and consequently the effects on the signal vary. Regardless of the type of channel, equalization of the channel effects is applied to maintain reliable communication. Equalization of the channel can be performed first then the receiver structure follows any of the discussed detectors in AWGN channel. However, to improve efficiency the equalization can be combined with the detection stage in what is known as joint channel equalization and symbol detection. The work in [84] investigated the IMGS based system in fading channel and proposed the SD algorithm for the joint equalization and detection. In this work, the MF based system as proposed in chapter 5 is considered and its optimal joint equalizer-detector is investigated.

Fig. 8.7 depicts a block diagram of an SEFDM transceiver in fading channel. The transmitter is based on the IDFT design proposed in chapter 4. The receiver obtains

statistics of the signal by the DFT block as proposed in chapter 5 and then applies joint equalization and detection methods to estimate the transmitted symbols. In this case the demodulated signal is expressed as

$$R = \mathbf{\Phi}^{*}\mathbf{H}\mathbf{\Phi}S + W_{\mathbf{\Phi}^{*}}. \tag{8.8}$$

The problem is formulated to estimate the transmitted symbols based on the collected statistics R. Following similar analysis as in section 5.4.2, the Maximum Likelihood (ML) detection of the system is expressed as

$$\hat{S}_{ML} = \min_{s \in Q^N} \left\| \mathbf{\Phi}^{*^{-1}} \left(R - \mathbf{\Phi}^{*}\mathbf{H}\mathbf{\Phi}S_m \right) \right\|^2. \tag{8.9}$$

Equation (8.9) shows that the ML equalizer-detector requires knowledge of the CSI represented by the matrix $\mathbf{H}$. Typically, the CSI is obtained by estimation either based on the transmission of known symbols or totally blind estimation.

The performance of the ML equalizer-detector is investigated by numerical simulations conducted in Channels 1, 2 and 4. The ML equalizer-detector is realized by performing an exhaustive search of all transmitted symbols combinations assuming perfect CSI at reception end. The combination of the perfect CSI and optimal equalization and detection is investigated to provide a benchmark for other cases. Later on in the chapter, investigations under realistic CSI are conducted and benchmarked against the perfect CSI case. Simulations are constrained to systems with 4 subcarriers due to the complexity of the detector. Fig. 8.8 depicts the performance of the described ML equalizer-detector in Channel 1 and 2. The figures show that with the reduction in the value of α, degradation is observed with more severity for the case of 4QAM input symbols. Interestingly, the figures indicate that for $\alpha > 0.6$, performance in Channel 2 is better than in Channel 1. However, this observation is valid for this case of number of subcarriers as will be shown in subsequent work.

The SEFDM signal is also tested in the time varying Channel 4. Fig. 8.9 depicts the BER performance for $\alpha = 0.8, 1$ in Channel 4 for coherence time $T_c = [0.3, 0.75]\,T$ with BPSK and 4QAM input symbols. Fig. 8.9a and 8.9b show that for $\alpha = 0.8$, the systems performed close to OFDM with improvement in the performance observed with the increase in the time variability of the channel. This may be attributed to that

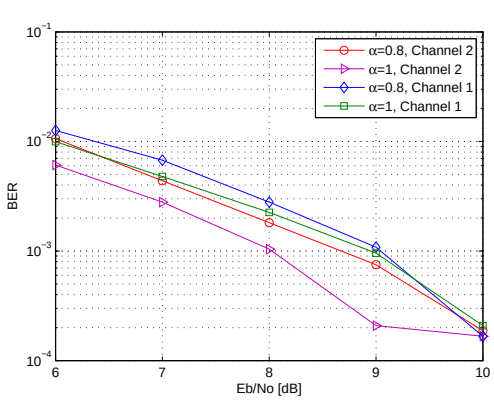

(A) 4QAM

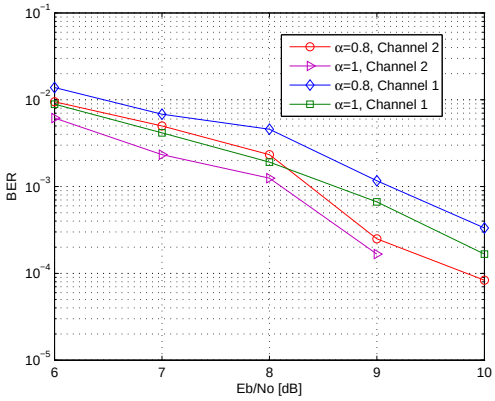

(B) BPSK

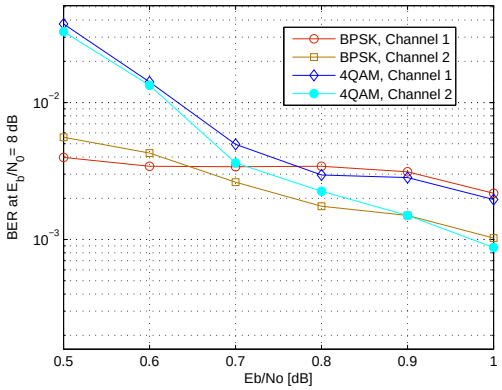

(C) $\alpha = 0.5 - 1$.

FIGURE 8.8: BER performance of the ML equalizer-detector in Channel 1 and 2, for a system with 4 subcarriers.

with fast fading the probability to encounter good channel state within the transmission time of one symbol increases. In addition, Fig. 8.9c show that for $\alpha \geq 0.8$, the system with BPSK input symbols exhibited better BER than OFDM. Nevertheless, the system assumes perfect CSI, therefore, the observed performance may not hold if perturbed CSI is used.

8.5.1 Sphere Decoder (SD)

The ML detector is overly complex, therefore, joint channel equalization and signal detection using Sphere Decoder (SD) algorithm is pursued in a similar manner to the proposal in [84] for IMGS based system. The main difference between this work and the work in [84] is the replacement of the IMGS stage with the DFT demodulator. This

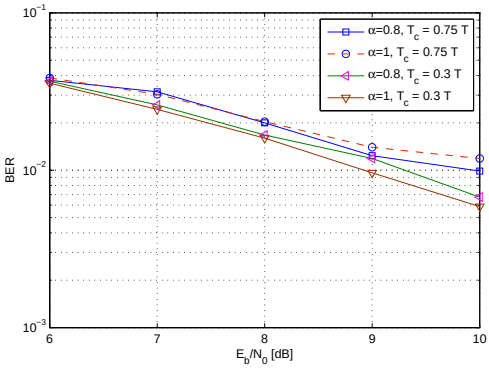

(A) BPSK

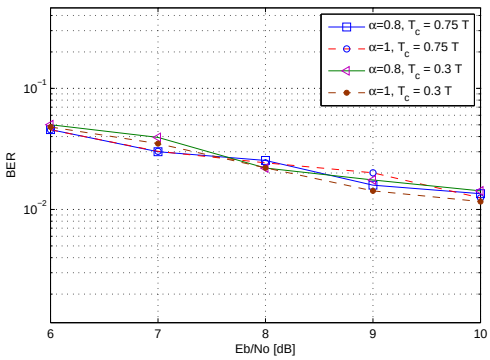

(B) 4QAM

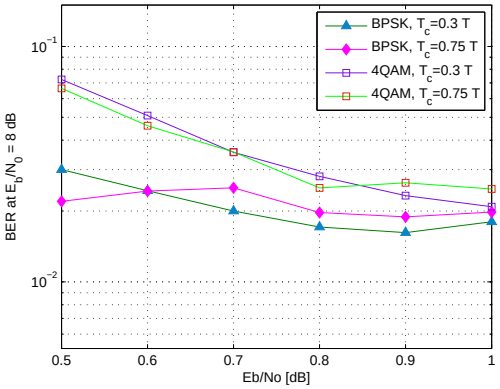

(C) $\alpha = 0.5 - 1$.

FIGURE 8.9: BER performance of the ML equalizer-detector in Channel 4 for a system with 4 subcarriers.

leads to different cost function of the ML estimate shown in equation (8.9), where the ML estimates are modified through the multiplication with the inverse of the Hermitian conjugate of the carriers matrix $\mathbf{\Phi}$.

As the SD algorithm constrains the search for the solution within the predefined radius g, thus, the SD solution is expressed as

$$\hat{S}_{SD} = \min_{s \in Q^N, \, \|R - \mathbf{C}S\|^2 \leq g} \left\| \mathbf{\Phi}^{*^{-1}} \left(R - \mathbf{\Phi}^* \mathbf{H} \mathbf{\Phi} S \right) \right\|^2. \tag{8.10}$$

The algorithm then follows similar steps as detailed in section 5.5 for the SEFDM system in AWGN channel.

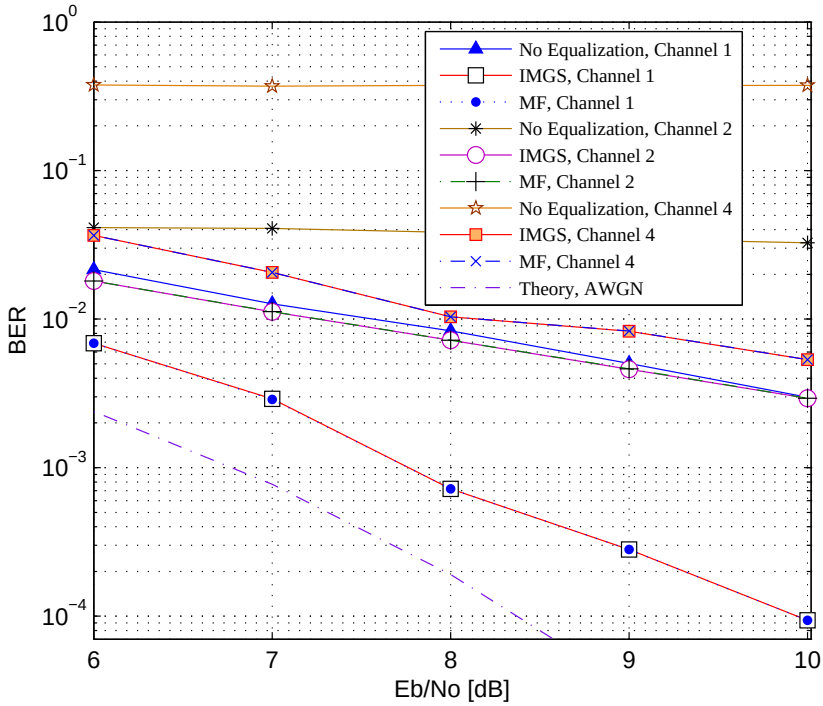

FIGURE 8.10: SD joint equalizer and detector for SEFDM signal in Channel 1, 2 and 4 for 16 subcarrier system, $\alpha = 0.8$ and 4QAM input symbols.

The proposed SD joint channel equalizer and symbol detector was simulated assuming perfect CSI for SEFDM system carrying 4QAM symbols. Fig. 8.10 depicts the BER of the SD equalizer-detector tested in Channels 1, 2 and 4. The figure shows that the MF based system achieves the same error performance as the IMGS system in the different channels, therefore enabling the benefit of the complexity reduction associated with the MF based system. The figure shows that the performance of the SEFDM system deteriorates with the deterioration in the channel conditions reflected by the three simulated channels which is confirmed in Fig. 8.11 for system for $0.7 \leq \alpha \leq 1$. Furthermore, Fig. 8.11 shows that the SD equalizer-detector can maintain the same performance as OFDM for bandwidth savings of 20% for Channel 1 and 30% for Channels 2 and 4. This suggests that the fading channel effect can be dominant over intrinsic system limitations arising from being ill conditioned. The results for the ML and SD joint equalizer-detector in the time varying Channel 4 show that if perfect CSI is available the performance will depend on the encountered level of fading. The same performance is observed for OFDM when the designed ML and SD equalizer-detector is used.

Previous analysis assumes perfect CSI, whereas in practice equalization depends on

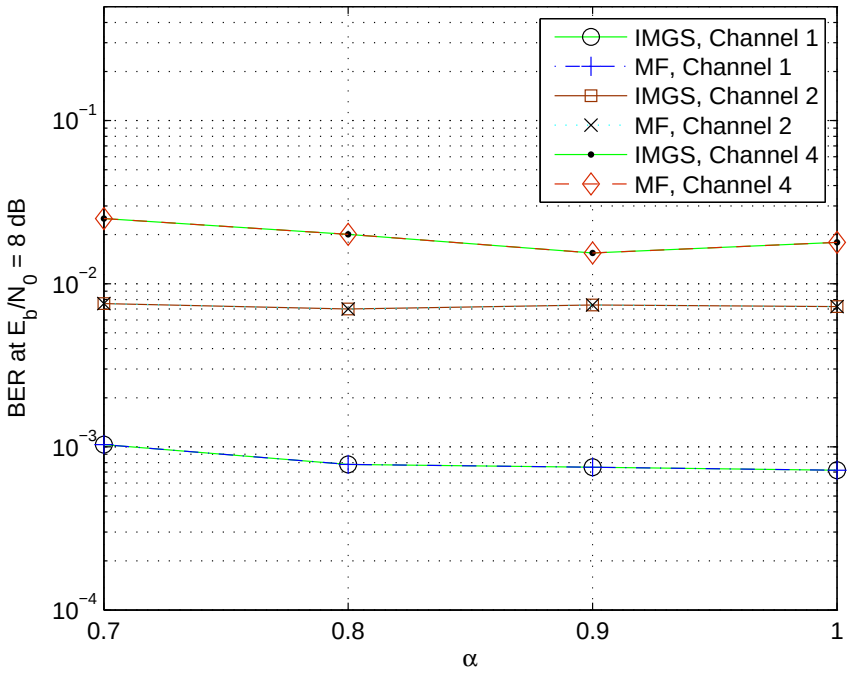

FIGURE 8.11: SD joint equalizer and detector for SEFDM signal in Channel 1, 2 and 4 for 12 subcarrier system and 4QAM input symbols.

estimation of the channel state, hence, in the next section, an improved channel estimator for the SEFDM system is proposed. The SD equalizer-detector is much simpler than the ML, however, exhibits variable complexity as explained in chapters 5 and 6. Therefore, in section 8.7 reduced complexity joint channel equalizer and symbol detectors are proposed and evaluated.

8.6 Channel Estimation

A signal passing through multipath channel can be severely distorted. The signal arrives dispersed in time and frequency according to the type of channel encountered. Therefore, equalization is applied to compensate for the detrimental effects of the channel. However, equalization, in general, requires knowledge of the channel state. Such knowledge is typically acquired by performing channel estimation in either time domain or frequency domain or both. In the study in section 8.5, perfect knowledge of the CSI is assumed in order to avoid any effects on the performance of ML or SD joint equalizer-detector due to disturbances in the CSI. Nevertheless, in practical conditions the assumption of

perfect CSI is difficult to achieve. This section deals with the channel estimation issue and presents a new estimator that provides better estimation accuracy.

In general, channel estimation is a topic extensively researched for OFDM systems leading to proposals of many estimation techniques in time and/or frequency [178, 179, 180, 181]. A typical approach for estimating the time domain response of the channel is by dedicating a burst of transmitted symbols to convey a pre-determined training (or pilot) sequence. The receiver works out the channel response based on the received signal and the knowledge of the pilots used. On the other hand, for estimating the frequency response of the channel, pilot symbols are sent at predefined frequencies to determine the channel response at such frequencies and the complete frequency response is derived by interpolation which could be simple linear interpolation or low pass filtering [43]. The minimum number of pilot frequencies is decided by the Nyquist sampling theorem, though in the case of simple linear interpolation oversampling is needed. Whether using pilot tones or a training sequence, the receiver needs to apply algorithms to extract channel response from the received signal. Techniques discussed in the literature include Least Squares (LS), Minimum Mean Square Error (MMSE) and ML each offering different estimation accuracy and complexity [182]. Furthermore, the estimation of the fading channel is dependent on the conditions of the channel. In the case of the quasi static channels, the estimation needs to be frequent enough to capture the significant time changes in the channel. In fast fading conditions, the channel estimation is commonly applied in conjunction with channel tracking algorithms that aims to capture the changes in the channel [183, 184, 185]. Nevertheless, estimation based on reserving whole transmission burst or parts within certainly reduces the overall throughput of the system, consumes power and requires computational effort. Therefore, blind and semi-blind estimation techniques without or with limited known transmitted bursts, respectively, have been proposed for OFDM using expectation maximization algorithm, ML and iterative techniques in [186, 187, 188, 189].

The orthogonal structure of the subcarriers in OFDM system has simplified the process of channel estimation [190]. In particular, the perfect conditioning of the OFDM system results in the time domain estimation to be affected only by the type of channel encountered. In addition, the orthogonal subcarriers in the OFDM system allows for the frequency domain estimation to use a subset of subcarriers to carry the pilots and

the rest carry information symbols, thus, reducing the lost throughput for estimation. Unfortunately, these features are missed in the SEFDM case due to the lack of orthogonality, thus motivating a research for efficient and reliable estimators for the channel in this case. The work in [84] suggested the use of pilot symbols for channel estimation. Performance investigations for two cases of static channels have shown that performance of the estimator deteriorates with the reduction in the value of α, an effect that is linked to the ill conditioning of the SEFDM system. Therefore, the next subsection presents a newly designed estimation algorithm for the SEFDM signal that relies on the mathematical foundation of the SEFDM system presented in chapter 3 to address the ill conditioning of the SEFDM system.

8.6.1 The Partial Channel Estimator (PCE)

The work in [84] discussed the possibility of estimating the channel by transmitting randomly generated pilot SEFDM symbols. The CIR is then estimated using ZF with the knowledge of the transmitted pilots. As discussed in chapter 3, the ill conditioning of the SEFDM system can substantially corrupt the performance of techniques such as ZF, as the system becomes sensitive to small perturbations (i.e. noise). Therefore, in this section, a new channel estimation technique is presented to overcome the discussed difficulty. The technique simply relies on invoking the mutually orthogonal subcarriers within the SEFDM pilot symbol, to construct a robust scheme against the noise in the system. The new estimation technique is termed the Partial Channel Estimator (PCE) to reflect the pilots structure. The main concept of the PCE relies on the property of the SEFDM subcarriers derived in Theorem 3.1, where it is proved that there are subsets within the SEFDM subcarriers that are mutually orthogonal. Based on this feature, the design of pilot symbols for channel estimation is optimized to avoid the effects of the ill conditioning of the system that arises with the increase in the number of subcarriers and/or bandwidth compression levels.

Let P be the $N \times 1$ pilot symbol vector, the PCE is characterized by the definition of the pilot vector as

$$P(i) = \begin{cases} p_i & , i \in \mathcal{I} \\ 0 & , \text{ otherwise} \end{cases}, \tag{8.11}$$

where p_i denotes the value of the i^{th} pilot symbol which is typically drawn from the same constellation cardinality of the input information symbols and $\mathcal{I}$ denotes the indices of the orthogonal subcarriers in the chosen subset as explained in Theorem 3.1 and appendix A. The pilots are then modulated on top of the subcarriers and transmitted down the fading channel. The number of orthogonal sets and orthogonal subcarriers is dependent on the value of α and the number of subcarriers as explained in Theorem 3.1 and appendix A. As the value of α gets closer to 1, the correlation between the subcarriers decreases and the system approaches orthogonality as demonstrated in section 3.3. Therefore, the design of the pilots for the PCE can use more subcarriers and still achieve better performance. That is near orthogonal subcarriers sets can be used in place of the orthogonal one in order to improve estimation resolution. Another advantage of the PCE is the reduction of the required power due to the reduction in the number of transmitted symbols and the associated subcarriers.

Based on the received pilot symbols, channel estimation can be carried out in the time or frequency domain. Frequency domain estimation generates estimates of the sampled frequency response, therefore require interpolation. In addition, if only orthogonal subcarriers are activated in the pilot symbols, a cyclic prefix can be inserted at the start of each PCE symbol and estimation can follow conventional OFDM techniques [179, 181], however, the estimation part of the receiver will be totally separate from the main signal reception part. In this work, estimation is carried in the time domain where the CIR is extracted from the SEFDM pilot symbol based on solving a LS problem. The advantage of this design is that the PCE symbol can include more subcarriers by activating the near orthogonal subcarriers and that the estimation is carried through the main signal reception part with only loading the appropriate parameters based on the knowledge of the pilots.

Fig. 8.12 illustrates the PCE in contrast to the Full Channel Estimator (FCE) where a whole SEFDM symbol is dedicated to carry pilots. The hollow circle corresponds to the nulled frequency tones, where reducing the number of transmitted subcarriers leads to reducing the ICI. At reception, the incoming signal contaminated with AWGN, denoted by W, is expressed as

$$R = \mathbf{H}\mathbf{\Phi}P + W, \tag{8.12}$$

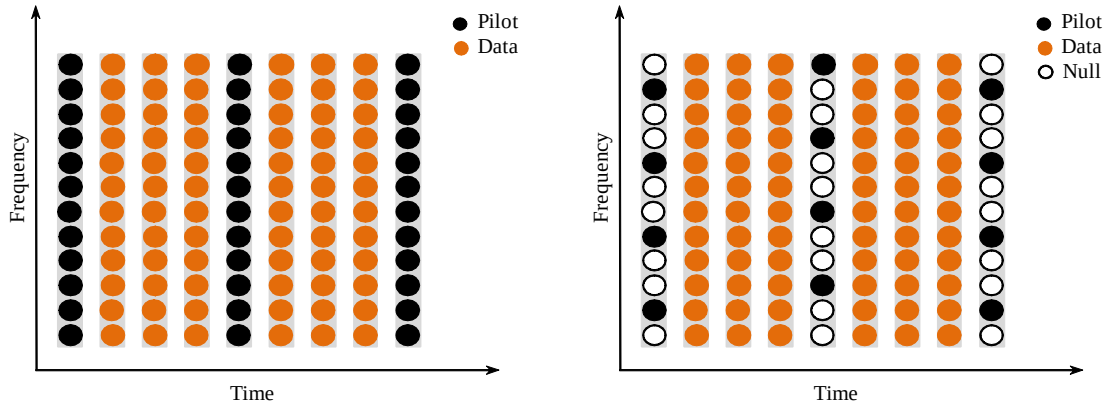

(A) FCE (B) PCE

FIGURE 8.12: Illustration of SEFDM FCE and PCE.

where the structure of the matrix $\mathbf{H}$ is defined in equations (8.6) and (8.7). For this work a quasi static channel, where the channel does not change within an SEFDM symbol transmission period is assumed. In this case, the linear regression model in equation (8.12) can be rearranged as

$$R = \mathbf{P}h + W, \tag{8.13}$$

where the vector h is a $\nu \times 1$ as ν represents the delay in terms of number of samples, and the matrix $\mathbf{P}$ is a $Q \times \nu$ lower triangular Toeplitz matrix whose first column is equal to the vector $X = \mathbf{\Phi}S$ and first row defined as $[X[0], 0, \cdots, 0]$. The estimate of the channel $\hat{h}$ is obtained from the LS solution as

$$\hat{h} = \min \|R - \mathbf{P}h\|^2, \tag{8.14}$$

which has the solution

$$\hat{h} = \mathbf{P}^* (\mathbf{P}\mathbf{P}^*)^{-1} R, \tag{8.15}$$

$$= h + \mathbf{P}^* (\mathbf{P}\mathbf{P}^*)^{-1} W. \tag{8.16}$$

To highlight the properties of the $Q \times \nu$ matrix $\mathbf{P}$, it is expressed as

$$\mathbf{P} = \begin{bmatrix} x_0 & 0 & & & 0 \\ x_1 & x_0 & 0 & & 0 \\ x_2 & x_1 & x_0 & 0 & 0 \\ & & & & 0 \\ x_{\nu-1} & x_{\nu-2} & & & x_0 \\ & & & & \\ x_{Q-1} & & & & x_{Q-\nu-1} \end{bmatrix}. \tag{8.17}$$

The matrix $\mathbf{P}$ is then detailed in terms of the constituent matrix $\mathbf{\Phi}$ and input symbol vector S as

$$\mathbf{P} = \begin{bmatrix} \mathbf{\Phi_1} & 0 & & & 0 \\ \mathbf{\Phi_2} & \Phi_1 & 0 & & 0 \\ \Phi_3 & \Phi_2 & \Phi_1 & 0 & 0 \\ & & & & 0 \\ \Phi_\nu & \Phi_\nu & & & \Phi_1 \\ & & & & \\ \Phi_Q & & & & \Phi_{Q-\nu} \end{bmatrix} \begin{bmatrix} S & 0 & \cdots & 0 \\ & S & 0 & 0 \\ \vdots & & \ddots & \\ 0 & 0 & \cdots & S \end{bmatrix}, \tag{8.18}$$

where $\mathbf{\Phi}_i$ denotes the i^{th} row of the carriers matrix $\mathbf{\Phi}$. Equation (8.18) is expressed equivalently as

$$\mathbf{P} = \tilde{\mathbf{\Phi}}\mathbf{S}, \tag{8.19}$$

where $\mathbf{S}$ is the $\nu \times \nu$ block diagonal matrix whose main diagonal elements are equal to the vector S and $\tilde{\Phi}$ is a block matrix constructed from block matrices in equation (8.20)

$$\begin{bmatrix} \boldsymbol{\Phi} & \begin{matrix} 0 \\ \\ \\ \boldsymbol{\Phi}_{1:Q-1} \end{matrix} & \begin{matrix} 0 \\ 0 \\ \\ \boldsymbol{\Phi}_{1:Q-2} \end{matrix} & \begin{matrix} \cdots \\ \ddots \\ \cdots \\ \end{matrix} & \begin{matrix} 0 \\ 0 \\ \vdots \\ 0 \\ \boldsymbol{\Phi}_{1:Q-\nu} \end{matrix} \end{bmatrix} \tag{8.20}$$

where $\boldsymbol{\Phi}_{1:i}$ denotes the matrix constructed from the rows 1 to $Q-i$ of $\boldsymbol{\Phi}$. The structure of the $\mathbf{P}$ matrix is closely related to the matrix $\boldsymbol{\Phi}$ which is shown to be become ill conditioned with the increase in the number of subcarriers and/or bandwidth compression level, consequently the solution that is based on inverting such matrices will suffer from noise amplification. The solution in equation 8.16 is the same as the ZF solution for the full loaded estimator, however, the structure of the pilot symbols ensures that the underlying elements of the matrix $\mathbf{P}$ are constructed from an orthogonal subset of the subcarriers and hence eliminates the effect of the ill conditioning found in the full loaded system. Even when near orthogonal subcarriers are used, the conditioning of the PCE system will be better than FCE due to the reduction of the correlation between the subcarriers. Another important design consideration is the power of the pilots. The FCE technique can increase the PAPR greatly if the combination of symbols sent corresponds to a high PAPR. This is because the FCE employs all the subcarriers and the chosen pilot symbols combination may exhibit high PAPR. On the other hand, in principle the PAPR of PCE pilot SEFDM symbols is lower than an FCE system using the same pilots values, due to the fewer subcarriers in the former.

Fig. 8.13 depicts an SEFDM system with Channel Estimator block. As discussed earlier, the PCE estimation can utilize the main system structure, whilst, frequency domain estimation will need a stand alone estimator branch.

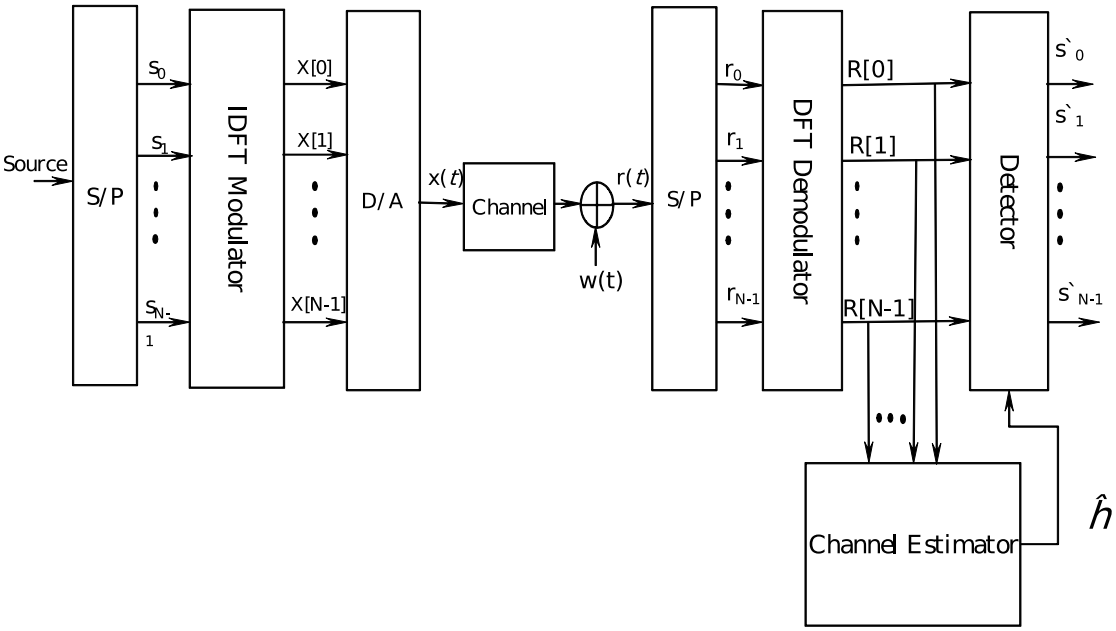

FIGURE 8.13: Block diagram of SEFDM channel estimator.

8.6.2 Channel Estimation Numerical Results

In the literature, the examining of the performance of channel estimator is evaluated through different parameters. The design of the pilots can be optimized to achieve a targeted performance measure such as the Mean Square Error (MSE) in channel estimation, the BER, the channel capacity and the Doppler mitigation [178, 180, 191]. In this work, the performance of the PCE is investigated by numerical simulations under the three channel conditions described in Table. 8.2. The performance is evaluated using two measures: first the MSE is evaluated to highlight the comparison between the proposed concept and FCE method. Secondly, the effects of the improved estimator on the BER performance and complexity are evaluated.

The MSE, used to evaluate the accuracy of the proposed estimator, is calculated as

$$\text{MSE} = E\left\{\left[h-\hat{h}\right]\left[h-\hat{h}\right]^{'}\right\}. \tag{8.21}$$

The MSE of PCE and FCE obtained channel estimates is recorded under three pilot power designs and the three channels listed in Table. 8.2. The performance is investigated with respect to the level of bandwidth compression or α and the number of subcarriers. Fig. 8.14a depicts the MSE of the error in channel estimation for the PCE and FCE techniques for a system using pilots based on random values. That is randomly

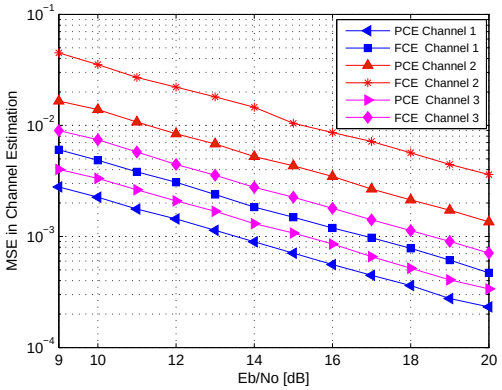

(A) Number of subcarriers 16, $\alpha = 0.5$.

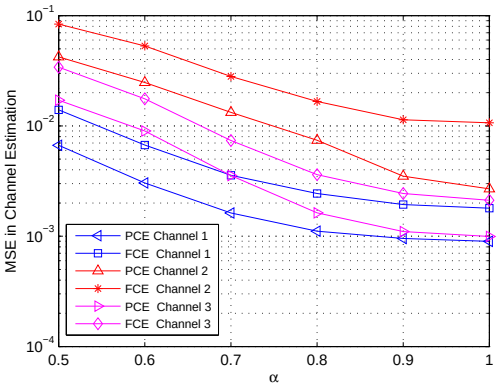

(B) Number of subcarriers 16 and $E_b/N_0 =$ 11dB.

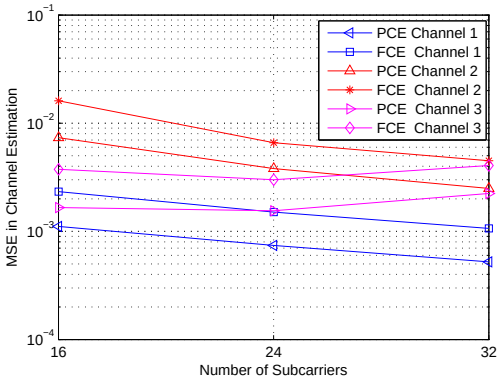

(C) $\alpha = 0.8$ and $E_b/N_0 = 11$dB.

FIGURE 8.14: MSE of PCE and FCE with respect to E_b/N_0, α and number of subcarriers, with 4QAM pilot symbols. Random pilots are used for both techniques.

generated 4QAM symbols are used in the pilot SEFDM symbols. The use of random pilots for both techniques eliminates any power based bias. The figure demonstrates the superiority of the PCE technique. The MSE in channel estimation for PCE is lower than the FCE case and the difference grows with worsening channel conditions as seen in how the MSE difference is higher for Channel 2 results. Fig. 8.14b depicts the MSE in channel estimation for the three channels for different values of α. The figure highlights an increase in the MSE with respect to the reduction in α, however, the PCE maintained lower MSE values. The main reason is related to the conditioning of the SEFDM system previously discussed in chapter 3. With the reduction in α, the SEFDM system becomes more ill conditioned, therefore the sensitivity of the estimates to the noise increases. The PCE reduces the effects of the ill conditioning as, only a subset of the subcarriers is excited and thus the subcarriers can be close to be orthogonal, yet will

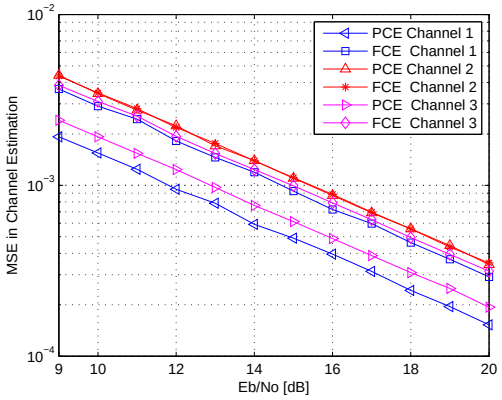

(A) Number of subcarriers 16, $\alpha = 0.5$.

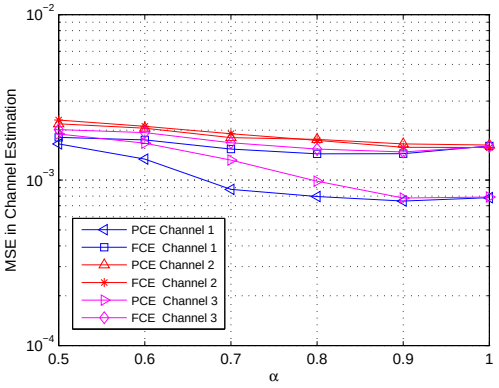

(B) Number of subcarriers 16 and $E_b/N_0 =$ 11dB.

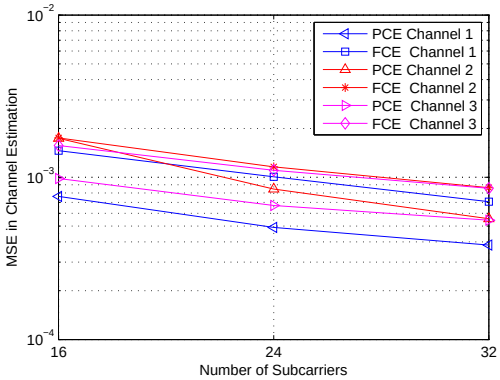

(C) $\alpha = 0.8$ and $E_b/N_0 = 11$dB.

FIGURE 8.15: MSE of PCE and FCE with respect to E_b/N_0, α and number of subcarriers, with 4QAM pilot symbols. Equal symbols as pilots for both estimators.

also experience degradation but with less impact as FCE.

Then a fixed equal pilots are tested for both PCE and FCE systems. This arrangement introduces a high peak (the highest possible peak) in the case of the FCE system. Although it demonstrated substantial estimation improvement, this choice is not recommended as it will increase the high PAPR occurrences in the system and if a PAPR control scheme is employed the FCE estimator looses its advantage in contrast to the PCE estimator. The PCE maintained the estimation advantage for Channel 1 and 3 which improved further with the increase in the number of subcarriers. This observed performance suggests that the estimator accuracy is affected by the condition of the channel. Specially, that the increase in the number of subcarriers is effectively improving the channel condition for the case of Channel 1 as it has fixed delay and the more

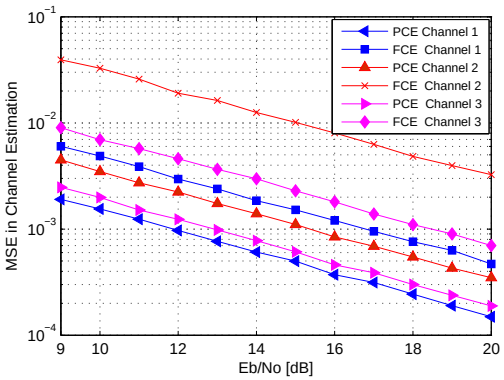

(A) Number of subcarriers 16, $\alpha = 0.5$.

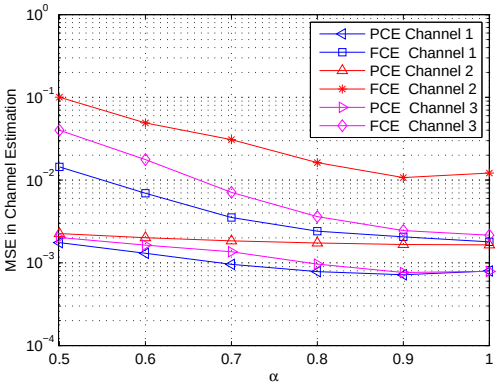

(B) Number of subcarriers 16 and $E_b/N_0 = 11$dB.

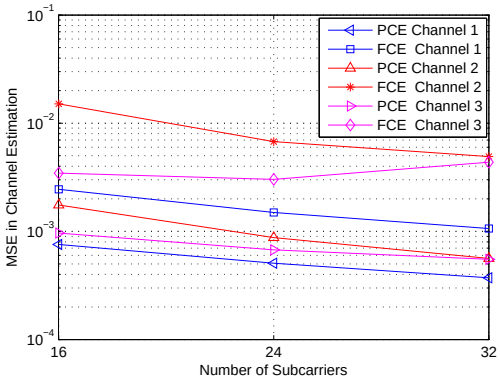

(C) $\alpha = 0.8$ and $E_b/N_0 = 11$dB.

FIGURE 8.16: MSE of PCE and FCE with respect to E_b/N_0, α and number of subcarriers, with 4QAM pilot symbols. Random symbols for FCE and equal symbols for PCE are used.

the subcarriers the longer is the transmission time which reduces the effects of delay of the static channel.

The third scenario is a combination of the two previous scenarios. The PCE enjoy less PAPR probability due to the use of fewer subcarriers, therefore, can enjoy the benefit of using the equal pilots combination. On the other hand, the FCE uses random pilots as in the original proposal in [84] and also to ensure no impact on the PAPR of the system. Fig. 8.16 depicts the performance in this case. This choice of pilot symbols widens the difference in the MSE for PCE and FCE and substantial improvement is observed for PCE system.

Furthermore, the effect of the estimation accuracy on the error performance of the system is addressed. To assess this, the proposed PCE estimator is tested for the equalization

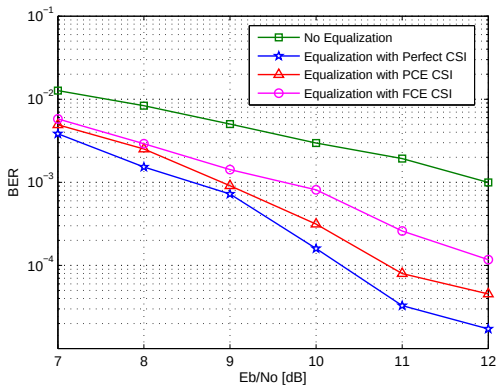

(A) BER

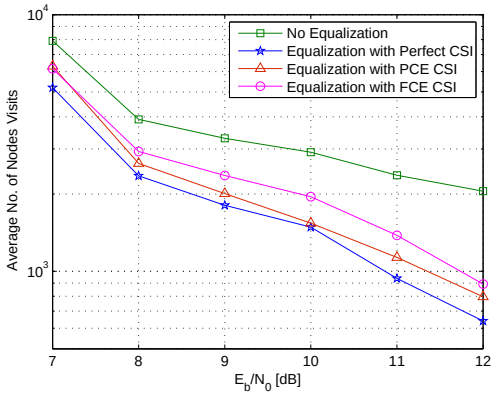

(B) Average number of nodes visits.

FIGURE 8.17: BER and complexity performance of PCE based equalization and detection for 16 subcarrier system, $\alpha = 0.8$, 4QAM symbols in Channel 1.

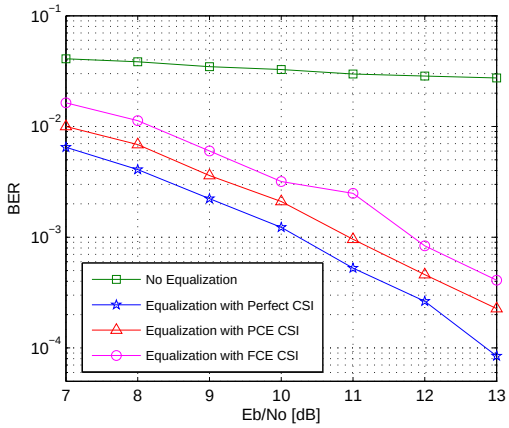

(A) BER

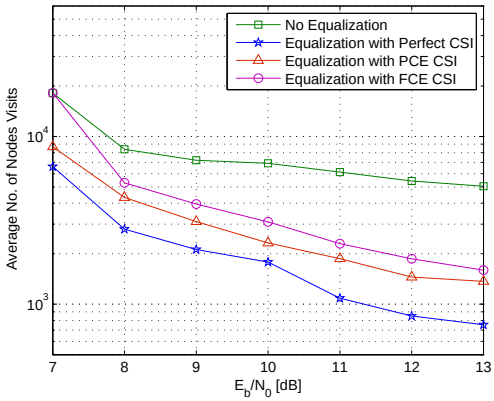

(B) Average number of nodes visits.

FIGURE 8.18: BER and complexity performance of PCE based equalization and detection for 16 subcarrier system, $\alpha = 0.8$, 4QAM symbols in Channel 2.

of simulated SEFDM system. Joint channel equalization and detection using SD is performed as discussed in section 8.5.1. Fig. 8.17 and Fig. 8.18 depict the BER of a system equalized with channel estimates obtained via PCE in fading Channel 1 and 2 as in Table. 8.2 and the required complexity in terms of average number of node visits. For comparisons, the figure shows the performance of the system for the case of no equalization, equalization with FCE estimated channel and perfect equalization where full CSI is available. The plots clearly demonstrate the BER advantage of the newly suggested PCE for channel estimation over FCE. Signals equalized with PCE obtained channel estimates show 1dB power advantage for BER of 10^{-3} and reduction of average number of nodes visits corresponding to 1 dB power boost.

8.7 Reduced Complexity Joint Channel Equalization and Symbol Detection

As already mentioned, the work in [84] has suggested an SD based joint equalizer-detector. In addition, the work in section 8.5 extended the use of the SD to the MF based system. Numerical results in [84] and in section 8.5 indicates good BER performance. Nevertheless, the complexity of the SD algorithm is variable as discussed in section 6.5, thus poses a challenging implementation task. Therefore, in this section, reduced complexity joint channel equalizers and symbol detectors are explored.

Join channel equalization and symbol detection using ZF, MMSE is proposed. In addition, equalization based on the TSVD is proposed to cater for channel effects in a similar manner as proposed for SEFDM signal detection in chapter 8. The main advantage of these linear equalizers is the low and fixed complexity, however, their performance is affected by the conditioning of the channel and for SEFDM system case is impaired by the conditioning of the system itself. The investigations of the linear equalizer-detectors are mainly pursued to form the comparison grounds for the use of iterative decoders.

Following that, the use of the FSD to equalize and detect jointly the SEFDM signal is proposed and evaluated. The FSD algorithm provides a fixed complexity alternative to the SD and is thus well suited for hardware implementation. The FSD algorithm facilitates substantial error performance improvement over linear detectors. To further improve the FSD performance, the combined FSD-TSVD equalizer-detector is proposed. The error performance is investigated by means of simulations in fixed static or quasi static channels as described in section 8.3.

8.7.1 Zero Forcing (ZF) and Minimum Mean Square Error (MMSE)

The ZF equalizer aims to eliminate the effect of the channel by applying an equalizer response that is the reciprocal of the CIR. This is basically a process to de-convolve the signal from the channel. That is for a received faded signal R described by equation (8.8), the ZF equalizer is defined as

$$R_{ZF} = \mathbf{H}^* \left(\mathbf{H}\mathbf{H}^*\right)^{-1} R, \tag{8.22}$$

where $\mathbf{H}^* \left(\mathbf{H}\mathbf{H}^*\right)^{-1}$ is the Moore - Penrose pseudoinverse of $\mathbf{H}$. The equalized signal R_{ZF} can then be used in conjunction with any of the detectors discussed in chapters 5 and 6.

The ZF can be applied as a joint channel equalizer and symbol detector and the estimated transmitted symbols at the output of the equalizer-detector will be described by

$$\hat{S}_{ZF} = \left\lfloor \mathbf{\Phi}^*\mathbf{H}^*\mathbf{\Phi} \left(\mathbf{\Phi}^*\mathbf{H}\mathbf{C}^*\mathbf{H}^*\mathbf{\Phi}\right)^{-1} R \right\rceil . \tag{8.23}$$

Nevertheless, the received signal arrives corrupted by AWGN, therefore, the use of the ZF equalizer-detector can lead to noise enhancement. ZF equalization is useful for interference limited systems or regions of operation, whereas, applying ZF to noise limited systems leads to noise enhancement and thus poor error performance.

To compensate for the noise enhancement in ZF equalization, the MMSE equalizer includes a noise related term. The MMSE equalizer is expressed as

$$R_{MMSE} = \mathbf{H}^* \left(\mathbf{H}\mathbf{H}^* + \frac{1}{\sigma_w^2}\mathbf{I}\right)^{-1} R, \tag{8.24}$$

where σ_w^2 is the noise variance and $\mathbf{I}$ is the identity matrix. In a similar manner to ZF, the MMSE equalized signal can be combined with the previously discussed detectors in chapters 5 and 6 to estimate the originally transmitted symbols. The MMSE can be used to construct a joint channel equalizer and symbol detector as

$$\hat{S}_{MMSE} = \left\lfloor \mathbf{\Phi}^*\mathbf{H}^*\mathbf{\Phi} \left(\mathbf{\Phi}^*\mathbf{H}\mathbf{C}^*\mathbf{H}^*\mathbf{\Phi} + \frac{1}{\sigma_w^2}\mathbf{I}\right)^{-1} R \right\rceil . \tag{8.25}$$

8.7.2 The TSVD

To overcome the limitations caused by the conditioning of the channel and the SEFDM system, equalization based on the TSVD is proposed. The TSVD equalizer uses a TSVD based pseudoinverse of the channel and is expressed as

$$R_{TSVD} = \mathbf{H}_\zeta R, \tag{8.26}$$

where $\mathbf{H}_{\zeta}$ is TSVD based pseudoinverse of $\mathbf{H}$ derived as

$$\mathbf{H}_{\xi} = \mathbf{V}\mathbf{\Sigma}_{\xi}^{-\mathbf{1}}\mathbf{U}^{*}, \tag{8.27}$$

where $\mathbf{U}$, $\mathbf{V}$ and $\mathbf{\Sigma}_{\xi}^{-\mathbf{1}}$ are obtained from the SVD of $\mathbf{H}$ as

$$\mathbf{H} = \mathbf{U}\mathbf{\Sigma}\mathbf{V}^{*}, \tag{8.28}$$

where $\mathbf{U}$ and $\mathbf{V}$ unitary matrices whose columns are the eigenvectors of $\mathbf{H}\mathbf{H}^{*}$ and $\mathbf{H}^{*}\mathbf{H}$ respectively and $\mathbf{\Sigma}$ =diag $(\sigma_1, \sigma_2, \cdots, \sigma_N)$, for σ_i is the i^{th} singular value of $\mathbf{H}$.$\mathbf{\Sigma}_{\xi}^{-\mathbf{1}}$ = diag $(1/\sigma_1, 1/\sigma_2, \cdots, 1/\sigma_{\xi}, 0, \cdots, 0)$ and ξ is the truncation index.

Furthermore, a joint TSVD based channel equalizer and symbol detector may be derived. The TSVD equalizer-detector is defined as

$$\hat{S}_{ZF} = \lfloor \mathbf{\Upsilon}_{\mathbf{H}} R \rceil , \tag{8.29}$$

where $\mathbf{\Upsilon}_{\mathbf{H\Phi}}^{\zeta}$ is TSVD pseudoinverse of the combined channel-subcarriers matrix Υ = $\mathbf{\Phi}^{*}\mathbf{H}\Phi$.

$$\Upsilon_{\mathbf{H}\Phi}^{\zeta} = \mathbf{V}_{\mathbf{H\Phi}}\mathbf{\Sigma}_{\mathbf{H\Phi}_{\xi}}^{-\mathbf{1}}\mathbf{U}_{\mathbf{H\Phi}}^{*}. \tag{8.30}$$

The TSVD joint channel equalizer and symbol detector applies TSVD principles to the matrix $\mathbf{\Phi}^{*}\mathbf{H\Phi}$ that describes the system generator matrix and the channel response.

8.7.3 Numerical Results for Linear Equalizers

The performance of the ZF, MMSE and TSVD joint equalizer-detectors is examined by numerical simulations. Fig. 8.19, 8.20 and 8.21 depicts the performance of ZF, MMSE and TSVD joint equalizer-detector in Channels 1, 2 and 3, respectively for different values of α and number of subcarriers for BPSK and 4QAM input symbols. The recorded BER curves show that, in general, the performance deteriorates with the increase in the number of subcarriers and the level of bandwidth compression. In addition, the figures show that the TSVD equalizer-detector facilitates a superior BER performance to that of the ZF and the MMSE.

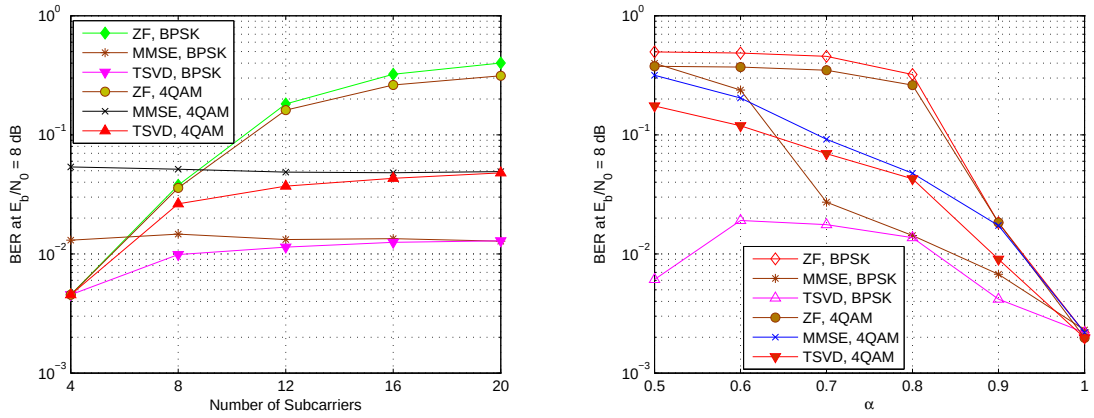

(A) $\alpha = 0.8$. (B) 16 subcarrier system.

FIGURE 8.19: BER performance of SEFDM for different number of subcarriers and α values in Channel 1.

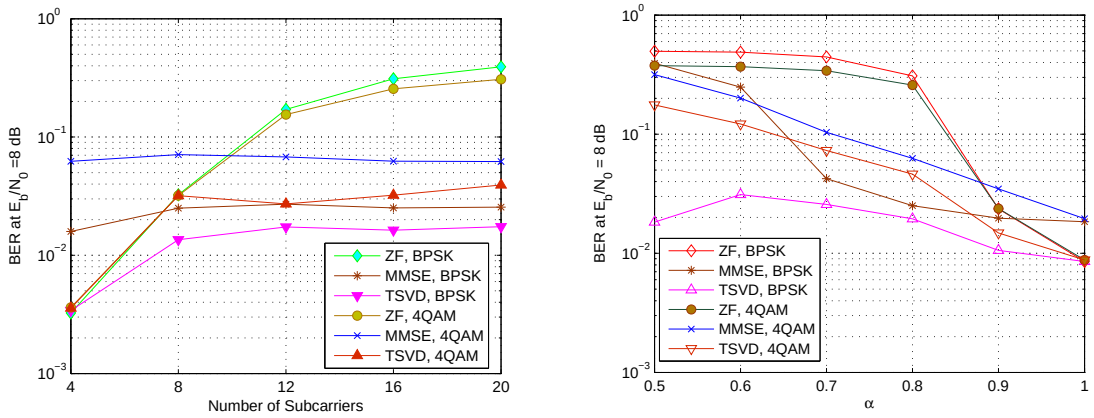

(A) $\alpha = 0.8$. (B) 16 subcarrier system.

FIGURE 8.20: BER performance of SEFDM for different number of subcarriers and α values in Channel 2.

Furthermore, examining the performance in the three channels in the figures shows that the BER performance degrades with the deterioration in the channel conditions, nevertheless, the advantage of the TSVD over the ZF and MMSE increases. In particular, Fig. 8.21b, depicting the performance in Channel 3, shows that for BPSK input symbols the TSVD equalizer-detector supports BER performance close to that of an OFDM system (case $\alpha = 1$), but for 4QAM input symbols the TSVD equalizer-detector exhibits performance that is dependent on α value.

Fig. 8.22 depicts the performance of the TSVD joint equalizer-detector in Channels 1, 2 and 3 for the cases of no CSI, PCE CSI, FCE CSI and perfect CSI. The figure shows

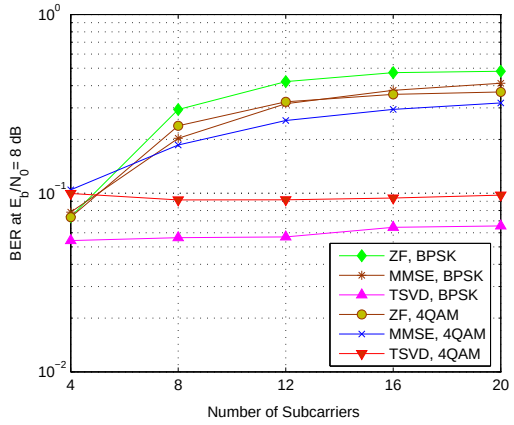

(A) $\alpha = 0.8$.

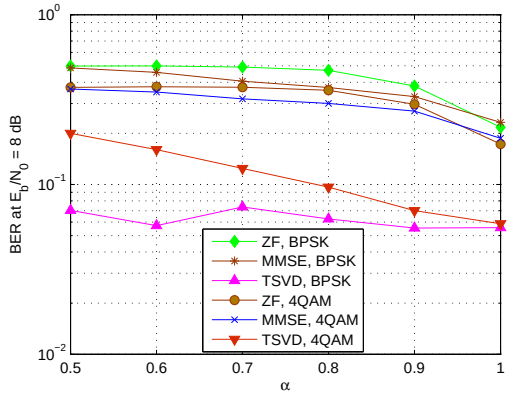

(B) 16 subcarriers system.

FIGURE 8.21: BER performance of SEFDM for different number of subcarriers and α values in Channel 3.

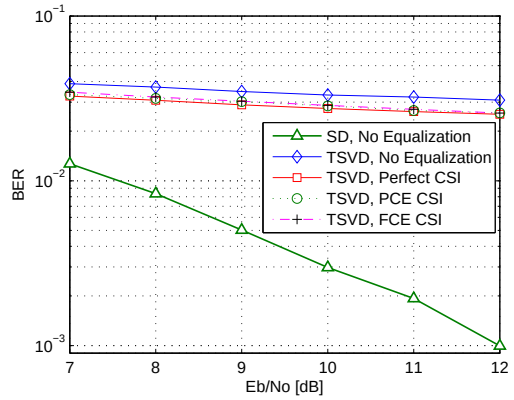

(A) Channel 1.

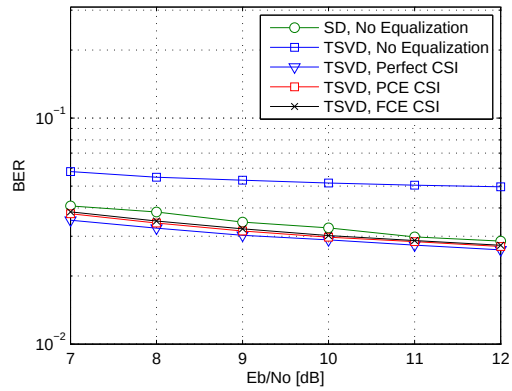

(B) Channel 2.

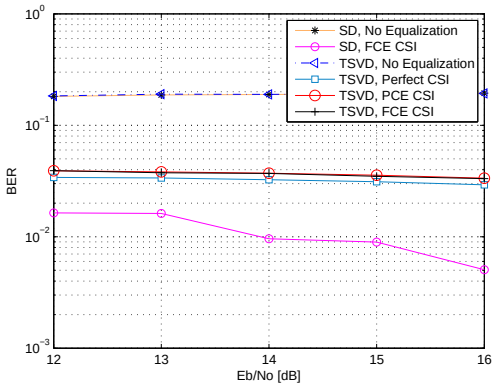

(C) Channel 3, 12 subcarrier.

FIGURE 8.22: BER performance of SEFDM system with 16 subcarrier, $\alpha = 0.8$ with 4QAM input symbol for no equalization, FCE, PCE and perfect equalization in Channels 1, 2 and 3. Performance of SD is plotted for comparisons.

that the BER performance with estimated CSI using PCE or FCE is close to the case of perfect CSI. In addition, Fig. 8.22a and Fig. 8.22b show that the BER performance in Channel 1 and 2 of the TSVD with perfect CSI is worse than SD with no CSI while for Channel 3 Fig. 8.22c shows that the performance of the TSVD with any CSI is better than SD with no CSI but worth than SD with FCE CSI. This indicates that significant performance degradation is associated with the TSVD joint equalizer-detector even if perfect CSI is available which in turn indicate further degradations if ZF or MMSE is used.

8.7.4 The FSD

Linear equalizers are of low complexity, however, are limited in terms of equalization efficiency. On the other hand ML equalization requires exponential complexity but results in better BER performance. SD reduces the complexity requirement, yet has variable decoding time. Therefore, in this section, it is proposed to use the FSD to jointly equalize and detect the SEFDM signal in fading channel. The FSD equalizer-detector restricts the SD search to solve equation (8.10) to examine w points at search level and follows the same steps detailed in section 6.5.1 to estimate the originally transmitted symbols starting from the ML problem in equation (8.9).

To assess the performance of the FSD equalizer-detector, numerical simulations are conducted for different system parameters and Channels 1, 2 and 3 described in section 8.3. In all cases the maximum tree width is restricted to 64 nodes.

Fig. 8.23 presents the BER of the FSD equalizer-detector under Channel 1 conditions and for the cases of no CSI, FCE and PCE estimated CSI and perfect CSI at the receiver. The figure shows slight BER degradation when compared to the BER of the SD equalizer-detector. Furthermore, the plots maintain the BER advantage of the PCE over the FCE for the FSD equalizer-detector.

Fig. 8.24 displays the BER for FSD equalizer-detector under Channel 2 conditions. When compared to the performance in Channel 1 in Fig. 8.23, degradations of the BER performance due to the worsening channel conditions is observed under the different CSI options. Nevertheless, the gap between the SD obtained solution is reduced and the FSD algorithm provided near optimal performance.

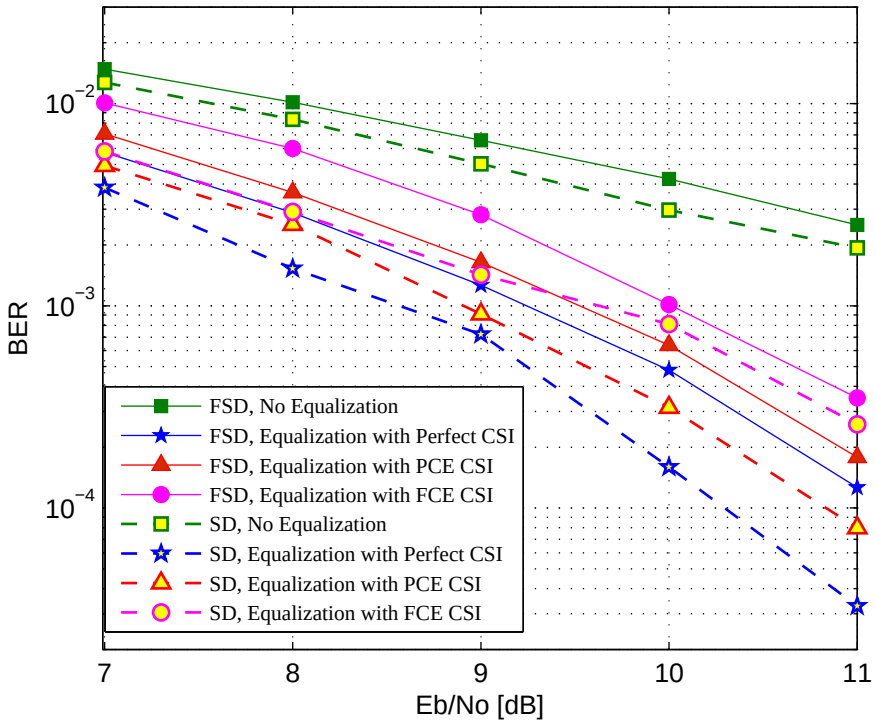

FIGURE 8.23: BER performance of FSD for a 16 subcarrier SEFDM system for $\alpha = 0.8$ and 4QAM input symbols in Channel 1.

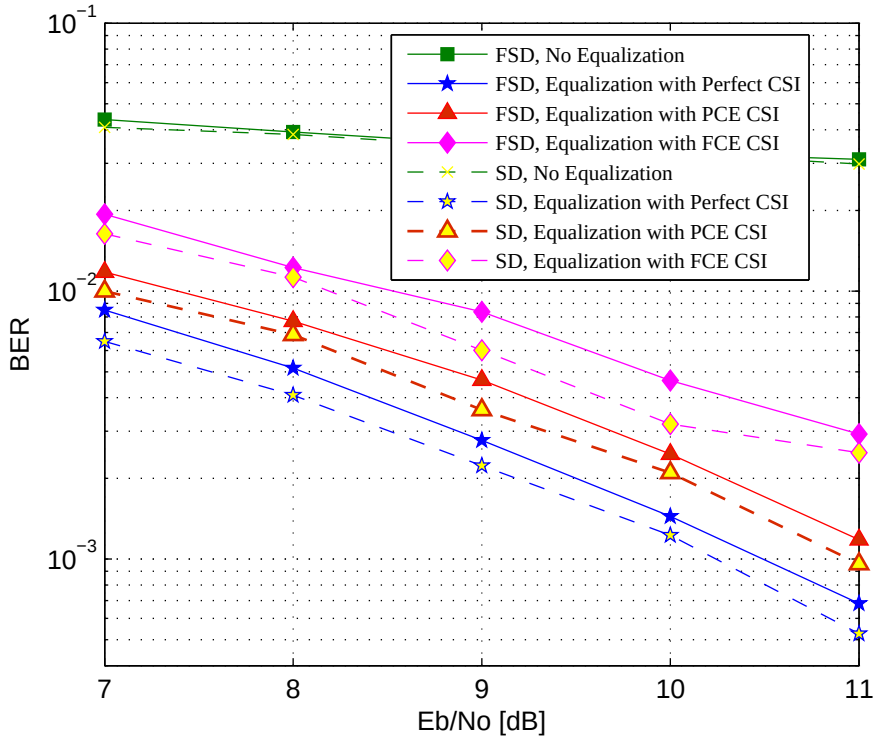

FIGURE 8.24: BER performance of FSD for a 16 subcarrier SEFDM system for $\alpha = 0.8$ and 4QAM input symbols in Channel 2.

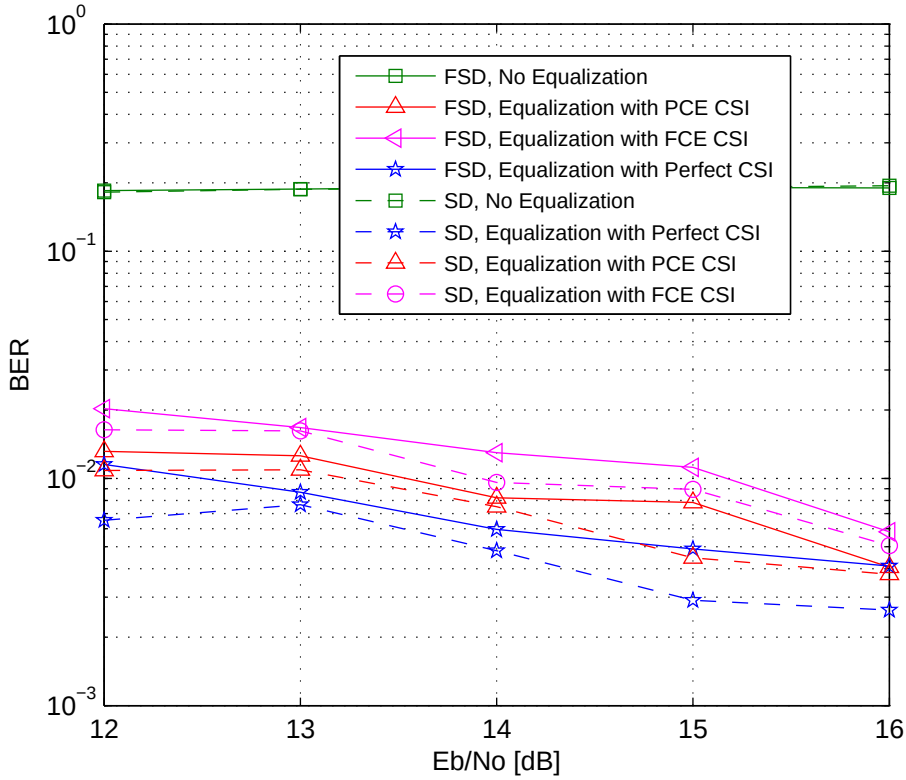

FIGURE 8.25: BER performance of FSD for a 16 subcarrier SEFDM system for $\alpha = 0.8$ and 4QAM input symbols in Channel 3.

Fig. 8.25 depicts the BER performance of the FSD equalizer-detector under Channel 3 conditions. The BER performance for the different CSI options is within close vicinity to that of the SD equalizer detector.

Fig. 8.26a and Fig. 8.26b depict the BER performance in Channel 2 with respect to the number of subcarriers, and different bandwidth compression ratios, respectively. The figures show that the BER performance degrades with the increase in the number of subcarriers and the reduction in the bandwidth compression ratio.

8.7.5 The FSD-TSVD

To further improve the performance of the FSD joint equalizer-detector, it is proposed to combine it with the TSVD as proposed previously for the system in AWGN channel in chapter 6. The FSD-TSVD joint equalizer-detector starts with obtaining a TSVD estimate, followed by an FSD search. However, the FSD is modified in a similar manner as described in section 6.6.1 for SEFDM in AWGN channel.

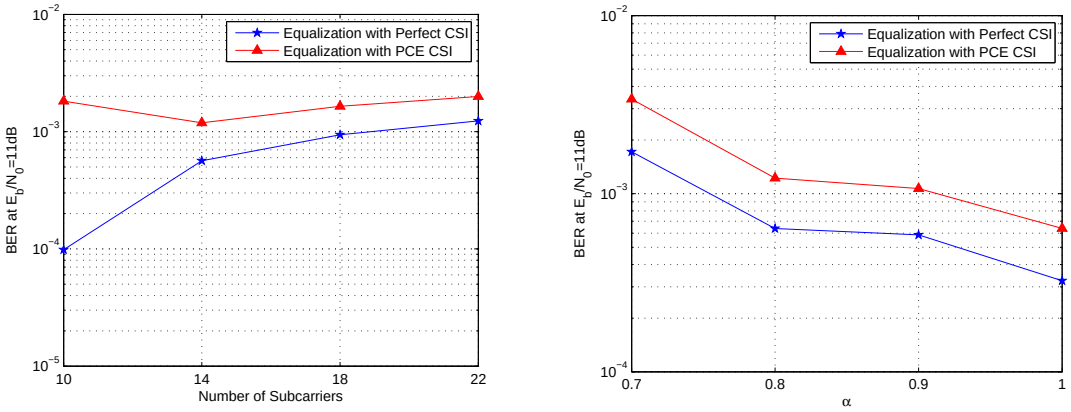

(A) $\alpha = 0.8$. (B) 16 subcarrier system.

FIGURE 8.26: BER performance of SEFDM system in Channel 2 for a system with 4QAM input symbols

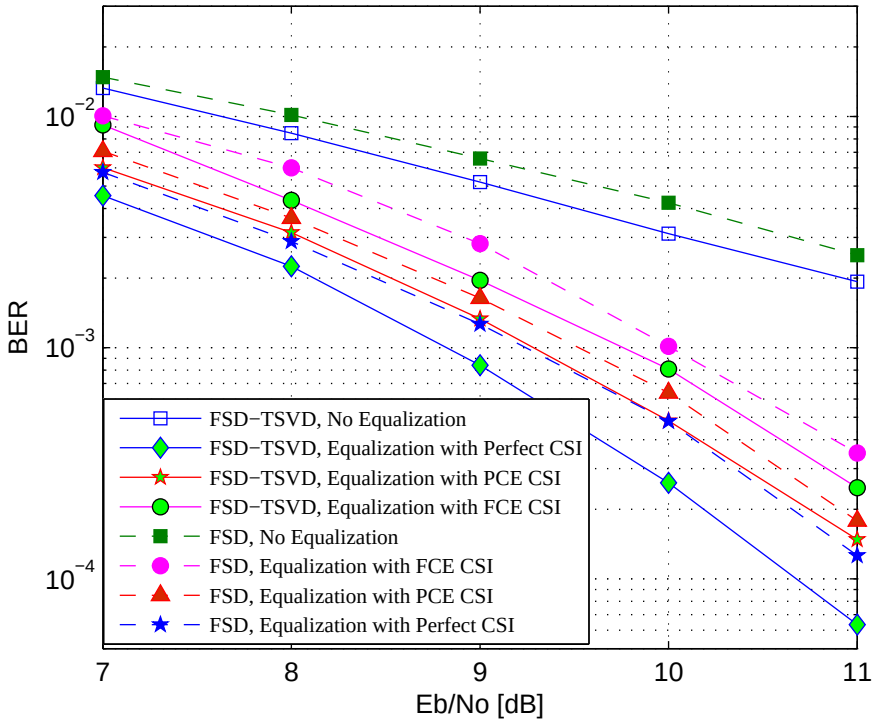

FIGURE 8.27: BER performance of the FSD-TSVD vs that of the FSD for a 16 subcarrier SEFDM system for $\alpha = 0.8$ and 4QAM input symbols in Channel 1.

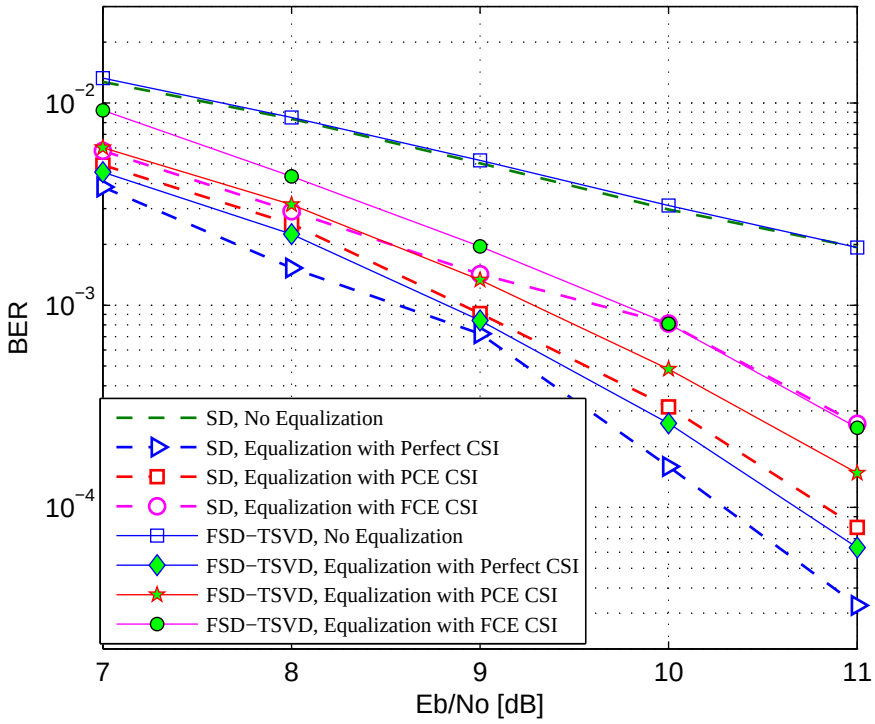

FIGURE 8.28: BER performance of the FSD-TSVD vs that of the SD for a 16 subcarrier SEFDM system for $\alpha = 0.8$ and 4QAM input symbols in Channel 1.

The performance of the FSD-TSVD joint equalizer-detector is investigated by numerical simulations in Channels 1 and 2. In all cases the maximum tree width is restricted to 64 nodes. Fig. 8.27 depicts the BER of the FSD-TSVD equalizer-detector in Channel 1. The figure shows the BER advantage of the FSD-TSVD equalizer-detector over the FSD. To highlight this advantage further, Fig. 8.28 shows the BER performance of the FSD-TSVD alongside that of the SD. The figure shows that the FSD-TSVD performs closer to the SD for Channel 1. This improvement is of greater impact in Channel 2, as shown in Fig. 8.29 that the FSD-TSVD equalizer-detector performs almost the same as the SD.

Fig. 8.30 depicts the BER performance for $N = 24, 32$ and $\alpha = 0.7 - 1$ in Channels 1 and 2. The figure shows degradation in the performance with the increase in the bandwidth compression level with less steepness in the case of Channel 2. In addition, Fig. 8.31 depicts the BER for different pairs of α and N values. The figure further confirms the degradation associated with the increase in the number of subcarriers and/or the bandwidth compression level. Nevertheless, the figure shows performance with good

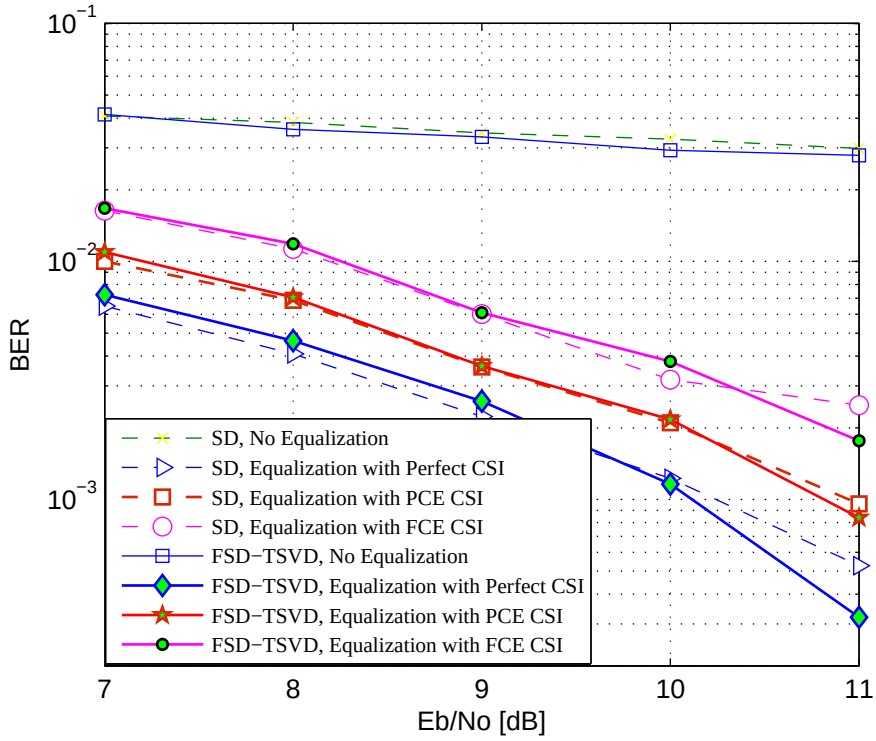

FIGURE 8.29: BER performance of the FSD-TSVD vs that of the SD for a 16 subcarrier SEFDM system for $\alpha = 0.8$ and 4QAM input symbols in Channel 2.

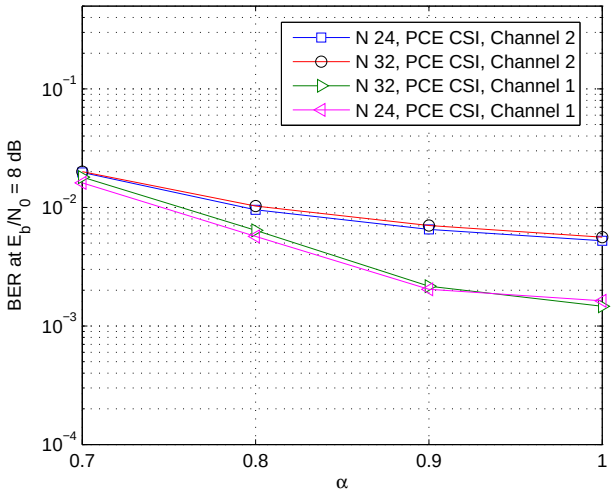

FIGURE 8.30: Performance of FSD-TSVD in Channel 1 and 2 for different numbers of subcarriers and α values for systems with 4QAM input symbols.

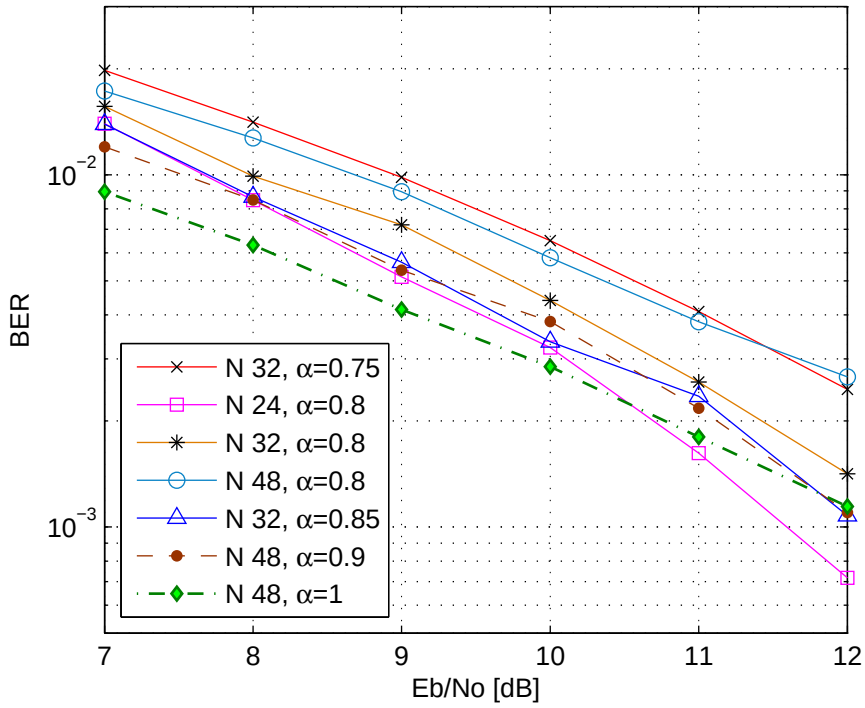

FIGURE 8.31: Performance of FSD-TSVD in Channel 2 for different numbers of sub-carriers and α values for systems with 4QAM input symbols.

vicinity to that of OFDM, noting that the FSD-TSVD complexity can be increased to reduce the gap further. The numerical results indicate the advantage of combining the TSVD principles with the FSD in improving the error performance. In cases, where lower BER can be tolerated, this advantage can be translated to reduction in the complexity of the FSD algorithm (i.e. reducing tree width).

8.8 Discussion and Conclusions

This chapter dealt with the SEFDM system in fading channels. The work covered modelling the SEFDM system in fading channel, performance investigations and system design improvements particular to channel estimation and equalization.

First the developed MF based demodulation proposed for the system in AWGN channel was extended to the system in fading channels. The suitability of this proposal was verified for operation in fading channels by the investigations of an optimal joint channel equalizer and symbol detector based on ML criteria. The proposal of the MF

based demodulation facilitates substantial complexity reduction over original system proposal where orthonormal bases are generated and used for signal demodulation. The derivation and numerical investigations of the ML joint equalizer-detector confirmed no performance penalty associated with the MF demodulator. In addition, the SD algorithm was derived for the case of the MF demodulation. Numerical simulations of the SD joint equalizer-detector in conjunction with MF based demodulator in static, quasi static and time varying channels confirmed an identical error performance as that of the system demodulation with orthonormal bases.

Then, the issue of channel estimation in the case of SEFDM system was addressed. A new channel estimation for SEFDM system was proposed and evaluated. The estimator relied on the characteristic of that a portion of SEFDM subcarrier can be mutually orthogonal. This was utilized in designing a pilot based channel estimation strategy that can overcome the ill conditioning that arises in the SEFDM system with the increase in the number of subcarriers and/or the bandwidth compression level. Different pilot arrangements were discussed with a focus on their impact on the estimation accuracy and the practical limitation in terms of the PAPR of the signal. Numerical results have demonstrated that the developed Partial Channel Estimator (PCE) can achieve superior performance to estimation techniques relying on full estimation. Results further suggested that the accuracy of the estimation is affected by the severity of the fading process. Investigations of the error performance highlighted the impact of the estimation accuracy. The results showed two dimensional improvement as the proposed PCE technique facilitated error performance improvement and complexity reduction.

The chapter then focused on compensating the fading effects by investigating new equalizers for SEFDM system with their performance investigated by numerical simulations adopting typical channel models and parameters. ZF and MMSE equalization were examined for SEFDM system. Numerical results have confirmed that the performance of the ZF and MMSE is poor as expected.

In addition, equalization based on the TSVD was proposed. The TSVD equalizer showed enhanced error performance when compared to ZF and MMSE, yet still poor except for low bandwidth compression levels. Therefore, it is concluded that the TSVD gives the best performance among the three linear equalizers, however, such performance is restricted in terms of the supported bandwidth compression level and modulation level.

Then, joint equalization and detection based on the FSD was considered. The FSD equalizer improved the error performance at low and fixed complexity. Furthermore, the combined FSD-TSVD joint equalizer-detector is proposed and evaluated. The FSD-TSVD joint equalizer-detector showed performance improvement specially when combined with PCE estimation.

Overall, the SEFDM system demonstrated performance comparable to that of OFDM for bandwidth savings of 20% . The SD joint equalizer-detector provided best performance at the cost of the variable complexity where the FSD-TSVD joint equalizer-detector performed close to the SD, specially with worsening channel conditions in terms of longer delays, at a fraction of the SD complexity.

Indeed, further investigations are deemed useful for a wider range of channel scenarios. Investigations of the interblock interference and the applicability of cyclic prefix and guard bands can be useful. Having covered channel estimation and equalization, the work in this chapter, demonstrates the potential of the SEFDM system for operation in realistic channel environments and highlights a road map towards further investigations in wireless channels.

Chapter 9

Precoded SEFDM System

9.1 Introduction

The appealing bandwidth savings offered by the SEFDM system proposal is plagued by the increased complexity due to the loss of orthogonality. All versions of spectrally efficient multicarrier systems proposed so far employ complex detection algorithms to extract the transmitted symbols out of the ICI. In this chapter, precoding the SEFDM signal is proposed. Precoding techniques are proposed in the literature for different purposes such as achieving channel capacity, targeted BER and transmit power in MIMO systems [119], optimize signal design in the presence of interference in MC-CDMA [192] and PAPR control in multicarrier systems [193, 165]. The common denominator in precoding techniques is that the signal is manipulated prior transmission using transforms that bring out desired attributes while adhering to system constraints such as total input power. The proposed precoding strategy for SEFDM system facilitates simpler detection for the same bandwidth savings as an equivalent uncoded SEFDM system. The strategy is based on localizing the effects of the lost orthogonality in a portion of the transmitted symbols. The receiver is in two parts where the detection of the "strong"[1] channels uses scalar division and slicing operation and the rest of the symbols are detected using complex detectors such as the Maximum Likelihood (ML) or Sphere Decoder (SD). Receivers that employ hybrid systems have been investigated before for SEFDM detection to reduce complexity as discussed in chapters 2 and 6 for AWGN channel and chapter

[1] In this chapter the words strong and weak are used to describe the channels with low and high signal to interference ratio, respectively.

8 for fading channels. The proposed system herein relies on precoding to localize the effect of the lost orthogonality in a subset of the transmitted symbols. The dimension of the complex part of the receiver is pre-determined and is smaller than the original system. In addition, the coding adds immunity to the symbols against the noise. Simple architecture of the precoded SEFDM system based on IDFT/DFT blocks for transmission and reception is proposed. The performance is investigated by extensive numerical investigations in AWGN and fading channels.

9.2 The Precoded SEFDM Transmitter

The SEFDM transmitter modulates a block of N complex symbols denoted by S onto the non-orthogonal carriers. In the precoded SEFDM system this block is first coded based on the knowledge of the correlation coefficients matrix $\mathbf{C}$ derived in equation (3.11) before the SEFDM modulation. As $\mathbf{C}$ is Hermitian, it can be diagonalized using eigenvalue decomposition as

$$\mathbf{C} = \mathbf{U}\mathbf{\Lambda}\mathbf{U}^{*}, \tag{9.1}$$

where $[\cdot]^{*}$ is the Hermitian transpose, $\mathbf{U}$ is a unitary matrix (i.e. $\mathbf{U}^{*}\mathbf{U} = \mathbf{I}$) and $\mathbf{\Lambda}$ is a diagonal matrix that contains the eigenvalues of $\mathbf{C}$. Chapter 3 investigated the properties of the $\mathbf{C}$ matrix. Particularly, it is shown that $(1-\alpha)\,N$ of the eigenvalues of $\mathbf{C}$ are less than 1 as shown in Fig. 3.10.

The precoded SEFDM signal is designed by multiplying the input symbols S by $\mathbf{U}$, prior to the SEFDM modulation, as

$$\widetilde{S} = \mathbf{U}S. \tag{9.2}$$

The coding matrix $\mathbf{U}$ is unitary, therefore the power of symbols is preserved as

$$\left\|\widetilde{S}\right\|^{2} = S^{*}\mathbf{U}^{*}\mathbf{U}S = \|S\|^{2}, \tag{9.3}$$

where $\|\cdot\|$ denotes the Euclidean norm of a vector. The signal at the output of the transmitter will be

$$X = \mathbf{\Phi}\widetilde{S}, \tag{9.4}$$

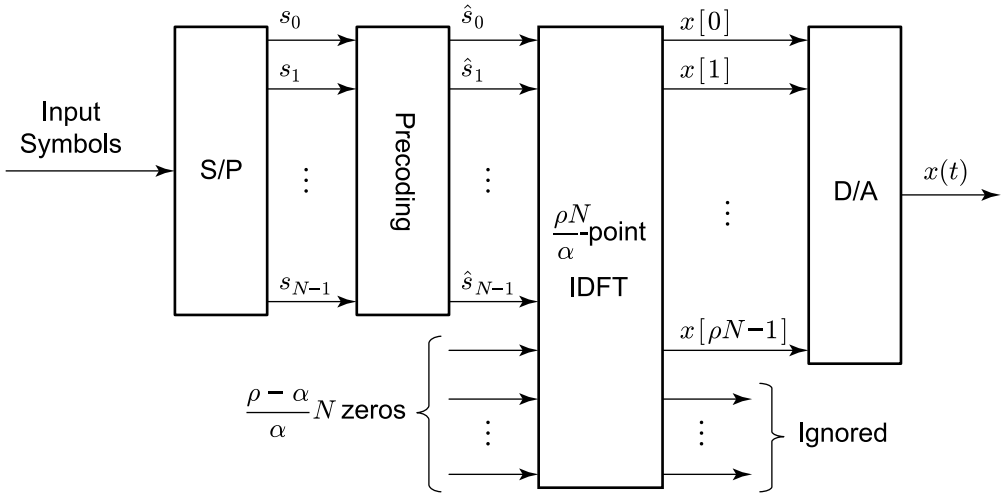

FIGURE 9.1: The Precoded SEFDM transmitter. The incoming symbols are grouped in blocks of N, coded, SEFDM modulated and converted to the continuous time domain.

and can be equivalently expressed as

$$X[k] = \frac{1}{\sqrt{\alpha}} \mathcal{F}_k^{-1,\rho N/\alpha} \left\{ \hat{S} \right\}, \tag{9.5}$$

for Q samples where $0 \leq k < Q-1$, where $\mathcal{F}^{-1,\rho N/\alpha}\{A\}$ is the $\rho N/\alpha$ point IDFT of the N long sequence A and $\rho = Q/N$. The SEFDM modulation of the precoded symbols vector can follow any of the proposed transmitter structures proposed in chapter 4. Fig. 9.1 depicts the IDFT based precoded SEFDM transmitter. The incoming symbols are first coded to adapt to the characteristics of the system. The IDFT block performs the SEFDM modulation and the resultant time samples are converted to continuous time domain by the D/C block.

9.3 The Precoded SEFDM Receiver

Assuming that the SEFDM signal is transmitted over AWGN channel, the received signal $y(t)$ will be

$$y(t) = x(t) + w(t), \tag{9.6}$$

where $w(t)$ denotes the AWGN term. Now consider an SEFDM receiver that starts by projecting the incoming signal onto the conjugates of the original SEFDM carriers. For

Y a vector of the samples of $y(t)$, the collected statistics vector R is obtained as:

$$\begin{aligned} R &= \mathbf{\Phi}^* Y, && (9.7)\\ &= \mathbf{C}\widetilde{S} + W_{\Phi}, && (9.8) \end{aligned}$$

where R is $N \times 1$ vector of collected statistics of the projection of the vector Y onto the conjugates of the SEFDM subcarriers, $\mathbf{C}$ denotes the cross correlation coefficient matrix derived in section 3.3 and W_{Φ} denotes the vector of the noise samples that are projected onto the conjugate of the SEFDM subcarriers given by $\mathbf{\Phi}^*$. Pre-multiplying equation (9.7) by $\mathbf{U}^*$ leads to

$$\begin{aligned} \mathbf{U}^* R &= \mathbf{U}^* \mathbf{C}\widetilde{S} + \mathbf{U} W_{\mathbf{\Phi}} \\ R_{\mathbf{U}^*} &= \mathbf{\Lambda}\mathbf{U}^* \widetilde{S} + W_{\mathbf{U}\mathbf{\Phi}}, && (9.9) \end{aligned}$$

the last line is obtained by substitution from equation (9.1). Note that $\mathbf{U}^*$ is unitary, hence, multiplying with it maintains the same noise power. Substitution of equation (9.2) in equation (9.9) yields

$$R_{\mathbf{U}^*} = \mathbf{\Lambda} S + W_{\mathbf{U}\mathbf{\Phi}}, \tag{9.10}$$

whose elements can be written as

$$\hat{r}_i = \lambda_i s_i + w_i, \tag{9.11}$$

which in turn leads to

$$\hat{s_i} = \lfloor \hat{r}_i / \lambda_i \rceil, \tag{9.12}$$

where $\hat{s_i}$ is the estimate of the i^{th} transmitted symbol. The previous analysis decomposes the SEFDM system into N parallel channels. The estimates of all transmitted symbols are obtained as

$$\hat{S}_P = \left\lfloor R_{\mathbf{U}^*} \Lambda^{-1} \right\rceil. \tag{9.13}$$

Estimation of the symbols requires scalar division followed by slicing operation. In addition, if the input symbols are modulated using phase modulations schemes such as QPSK and 4QAM, a slicing operation applied directly on $R_{\mathbf{U}^*}$ is sufficient to estimate

transmitter symbols as Corollary 3.2 shows that all the eigenvalues of the $\mathbf{C}$ matrix are positive and real. Furthermore, the estimation of individual symbols becomes directly linked to the eigenvalue of the $\mathbf{C}$ matrix. The quality of the estimates $\hat{s}$ depends on the eigenvalues of $\mathbf{C}$. If these eigenvalues diminish the effect from the noise in the system will greatly obstruct the successful estimation of the transmitted symbols. This suggests that all the channels that correspond to the relatively large eigenvalues will exhibit better BER performance compared to the channels with small eigenvalues. This can be seen by including the eigenvalues effects in the theoretical QPSK BER formula

$$P_e\left(i\right) = 0.5 * erfc\left(\sqrt{\lambda_i \frac{E_b}{N_0}}\right), \tag{9.14}$$

where $P_e\left(i\right)$ refers to the probability of error of the i^{th} channel defined in equation 3.2 and $erfc\left(\cdot\right)$ is the complementary error function. The modified BER formula considers the change in the signal to noise ratio for the decomposed channels that is created by the multiplication with the eigenvalues. From the eigenvalues of the $\mathbf{C}$ matrix it is noted that approximately αN of the transmitted symbols experience almost no power drainage. Nevertheless, the number of the relatively large eigenvalues can be altered by modifying the value of α used to generate the coding matrix $\mathbf{U}$ and is further discussed in section 9.4.

Depending on the value of α used for the precoding, $(1-\alpha)N$ of the estimates obtained from the scaling and slicing operation are discarded and re-estimated based on the accepted αN estimates and a new set of statistics. The fresh set of statistics is obtained by the projection of the received signal onto an orthonormal set of bases. The bases are chosen so as to alleviate the effect of the precoding on the remaining channels. In other words, the goal of the projection is to yield a linear model that boosts the chance to detect correctly the remaining symbols. It is proposed here to generate this set of bases by applying QR decomposition, which is equivalent to using Gram Schmidt orthonormalization process, on a desired system generator matrix. The choice of the system generator matrix will be clarified further with examples in next sections. An orthogonal matrix $\mathbf{Q}$ is obtained from the QR decomposition

$$\mathbf{QR} = \mathfrak{C}, \tag{9.15}$$

where $\mathbf{Q}$ is a unitary matrix, $\mathbf{R}$ is an upper triangular matrix and $\mathfrak{C}$ is the system generator matrix which includes the coding matrix $\mathbf{U}$, thus given as $\mathfrak{C} = \mathbf{\Phi U}$. Thus, the signal statistics denoted as $R_{\mathbf{Q}}$ are obtained as

$$R_{\mathbf{Q}} = \mathbf{Q}^{*} Y^{'}, \tag{9.16}$$

$$= \mathbf{M}S + W, \tag{9.17}$$

where $Y^{'}$ represent a shifted set of time samples of $y(t)$, $\mathbf{M}$ represents the projection of the SEFDM carriers onto the orthonormal set of bases represented by the columns of $\mathbf{Q}$ and W denotes the projected noise term. Now express the vector of estimates of the transmitted symbols in the precoded SEFDM as

$$\hat{S} = \hat{S}_{ML} \cup \hat{S}_{P}, \tag{9.18}$$

where $\hat{S}_{ML}$ is $(1-\alpha)\,N \times 1$ vector obtained by performing ML detection of the complete set of transmitted symbols based on the knowledge of $\hat{S}_{P}$. The ML detection for the remaining symbols is defined as

$$\hat{S} = \min \left\| R_{\mathbf{Q}} - \mathbf{M} \left[S : \hat{S}_{P} \in S \right] \right\|^{2}, \tag{9.19}$$

which reads as the estimates vector $\hat{S}$ that minimizes the norm and contains the estimates $\hat{S}_{P}$. The matrix $\mathbf{M}$ can be partitioned to $\mathbf{M} = \left[\hat{\mathbf{M}} \;\; \mathbf{M}_{P} \right]$, where

$$\hat{\mathbf{M}} = \mathbf{M}\left[1 : N, 1 : (1-\alpha)\,N\right]$$

and

$$\mathbf{M}_{P} = \mathbf{M}\left[1 : N, (1-\alpha)\,N + 1 : N\right]$$

and $\hat{S}$ will be

$$\hat{S} = \min \left\{ \left\| R^{-} - \hat{\mathbf{M}} \hat{S}_{ML} \right\|^{2} \right\}, \tag{9.20}$$

where $R^{-} = R_{\mathbf{M}} - \mathbf{M}_{P} \hat{S}_{P}$. From equation (9.20) it is clear that the dimension of the ML detector will be $G^{(1-\alpha)N}$ instead of G^{N} where G is the constellation cardinality.

Fig. 9.2 shows the architecture of the proposed SEFDM receiver which consists of two reception streams. The first reception stream starts by projecting the incoming signal onto the conjugate subcarriers as in equation (9.7) as it is the case with the MF based demodulator proposed in chapter 6, therefore the projection is realized by the N/α point DFT block according to the equation

$$\begin{aligned} R[k] &= \frac{1}{\sqrt{Q}} \sum_{k=0}^{Q-1} Y[k] \exp\left(\frac{-j2\pi nk\alpha}{Q}\right) \\ &= \mathcal{F}_k^{N/\alpha} \{Y\} \text{ for } 0 \leq k < Q, \end{aligned} \tag{9.21}$$

where $\mathcal{F}^{N/\alpha}\{A\}$ is the N/α point DFT of the N long sequence A. The DFT outputs are then processed as in equation (9.9) to equation (9.12) in the Scalar Division and Slicing Block which produces αN estimates that are taken forward as outputs and $(1-\alpha)N$ estimates that are discarded. That is the symbols that receives apparent power boost are kept and symbols that experience power depletion are discarded and re-estimated via the second reception stream. The second reception path starts by collecting statistics of the incoming signal in the Demodulator 2 block which is proposed to use orthonormal bases in this work. Then, a detection algorithm that considers the αN symbols estimated in the first reception stream to reduce the search space to $(1-\alpha)N$. The detection algorithm for the second path can be ML or SD with reduced search space, where simpler detection arrangements are proposed in the next section.

9.3.1 Layered ZF and Iterative Cancellation (IC)

As discussed in previous section, $(1-\alpha)N$ of the transmitted symbols are estimated based on the knowledge of αN of the symbols. The remaining symbols are described by the equation

$$R^- = \hat{\mathbf{M}}\hat{S}_{ML} + \hat{W}, \tag{9.22}$$

where $\hat{W}$ denotes the noise after subtracting the strong channels. A simple approach to estimate $\hat{S}_{ML}$ is by applying ZF principles as

$$\hat{S}_{ML} = \left\lfloor \hat{\mathbf{M}}^{-1} R^- \right\rceil. \tag{9.23}$$

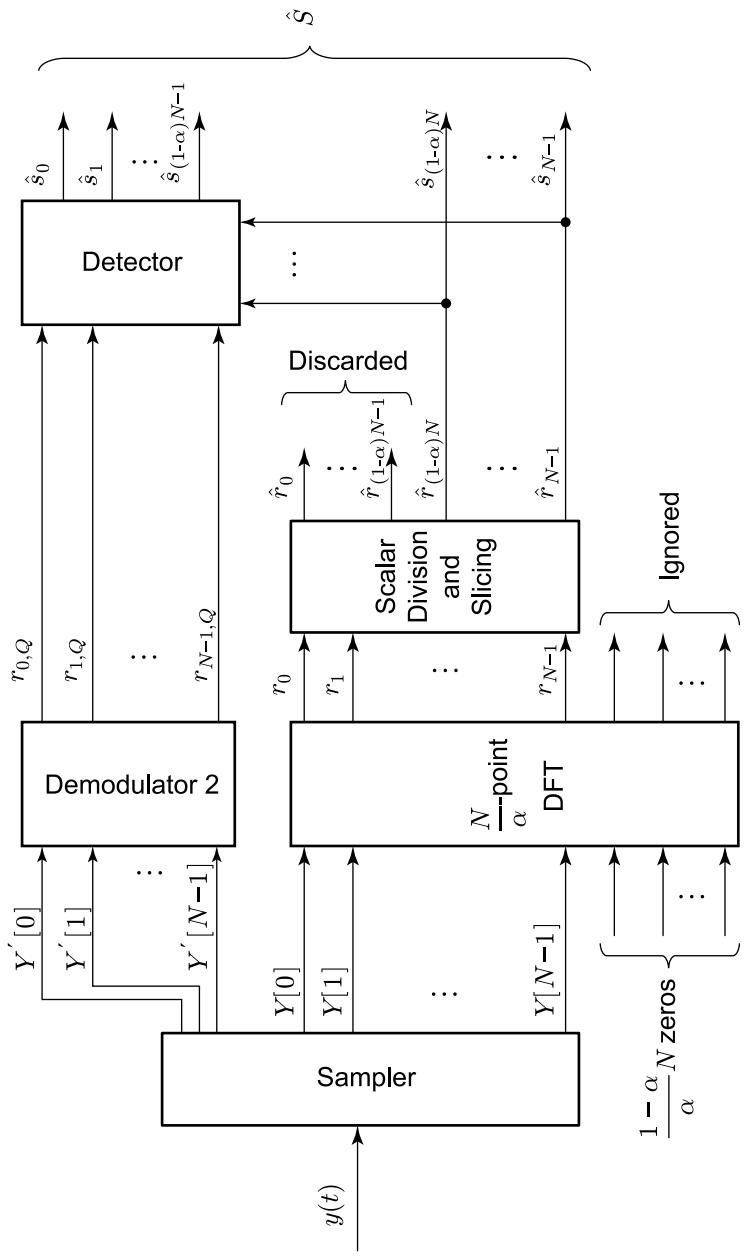

FIGURE 9.2: The SEFDM receiver. Incoming signal is projected, demodulated and decoded. The discarded symbols are then re-estimated using the detector block which can employ ML or SD or any other algorithm that accounts for the ICI in the system.

This is termed here Layered ZF as the symbols are detected in two steps; first the precoded channels and then the remaining channels are estimated based on the knowledge obtained from the first stage.

Furthermore, the triangular structure of the $\hat{\mathbf{M}}$, suggests that the estimation of the symbols in $\hat{S}_{ML}$ can be realized iteratively in a similar approach as Iterative Cancellation suggested in [57]. At the i^{th} level the corresponding symbol is found as

$$\hat{S}_{i,ML} = \left\lfloor R_i^- - \frac{1}{\hat{m}_{i,i},} \left[\hat{m}_{i,i+1}, \cdots, \hat{m}_{i,(1-\alpha)N}\right] \left\lfloor \begin{array}{c} \hat{S}_{i+1,ML} \\ \vdots \\ (1-\alpha)\, N_{i,ML} \end{array} \right\rceil \right\rceil . \tag{9.24}$$

The performance of the Layered ZF and IC detectors is investigated by means of numerical simulations in section 9.5 alongside ML detection.

9.4 The Code Design and Precoding Effect

The precoding proposed here falls in the category of unitary transformations. Basically, it is a transformation that maps the underlying system to itself while preserving its inner product. Nevertheless, in order to optimize the design of the precoded system, an investigation of the effect of coding on the re-arranged system can be useful. The precoding facilitates high performance for the relatively "strong" channels, thus the main concern here is to improve the detectability of the "weak" channels. At this end, the conditioning of the system describing the "weak" channels becomes crucial for its performance. In particular, the effects of the precoding on the singularvalues/eigenvalues structure of the system as the re-distribution of the energy may alter these values. The condition number may be the same but for different values of the minimum and maximum eigenvalues. Looking at the precoded demodulation only, it is clear that it results in performance degradation for the "weak" channels, therefore, it becomes necessary to design the codes so as to facilitate good performance for these channels through the second detection path.

One way to improve the detectability of the "weak" channels is by applying a unitary transform that results in a better re-structuring of the system. A key insight to design

differentiated coding spaces rely on the observation that an SEFDM system with any α value, contains the samples of any other systems with lower α value provided that the systems have the same number of subcarriers and symbol duration. Theorem 9.1 provides the proof to this insight.

Theorem 9.1. *The time domain signal of an SEFDM symbol with symbol duration of T and bandwidth compression α_1 contains the time domain signal (compressed in time) of an SEFDM symbol with same number of subcarriers, symbol duration and bandwidth compression α_2 and carrying the same input symbols, if $\alpha_1 > \alpha_2$.*

Proof. Express one SEFDM symbol for both systems as $x_{\alpha_1}(t)$ and $x_{\alpha_2}(t)$ as

$$x_{\alpha_1}(t) = \frac{1}{\sqrt{T}} \sum_{n=0}^{N-1} s_n e^{(j2\pi n \alpha_1 t/T)}, \tag{9.25}$$

and

$$x_{\alpha_2}(t) = \frac{1}{\sqrt{T}} \sum_{n=0}^{N-1} s_n e^{(j2\pi n \alpha_2 t/T)}. \tag{9.26}$$

Equation (9.26) can be written as

$$x_{\alpha_2}(t) = \frac{1}{\sqrt{T}} \sum_{n=0}^{N-1} s_n e^{(j2\pi n \alpha_1 (\alpha_2/\alpha_1) t/T)}, \tag{9.27}$$

which leads to

$$x_{\alpha_2}(t) = x_{\alpha_1}\left(\frac{\alpha_2}{\alpha_1} t\right). \tag{9.28}$$

For $\alpha_1 > \alpha_2$, $x_{\alpha_2}(t)$ is completely contained within $x_{\alpha_1}(t)$. □

This insight shows that the choice of the samples set for any SEFDM system can be designed to reflect a different system with smaller bandwidth. This insight relies on the duality of the time and frequency spaces and is directly linked to the signal generation principles in SEFDM proposed in chapter 4 where the signal covers portions of the unit circle of complex z-plane. Fig. 9.3 depicts the time domain signals of two SEFDM systems to highlight the insight proved in Theorem 9.1. The figure plots the time samples versus their respective indices within one SEFDM symbol transmission time for systems with $\alpha = 1$ and $\alpha = 0.5$. For the case of $\alpha = 1$, 20 time samples are shown whereas the case of $\alpha = 0.5$ shows 10 samples. Both systems are sampled uniformly in the interval

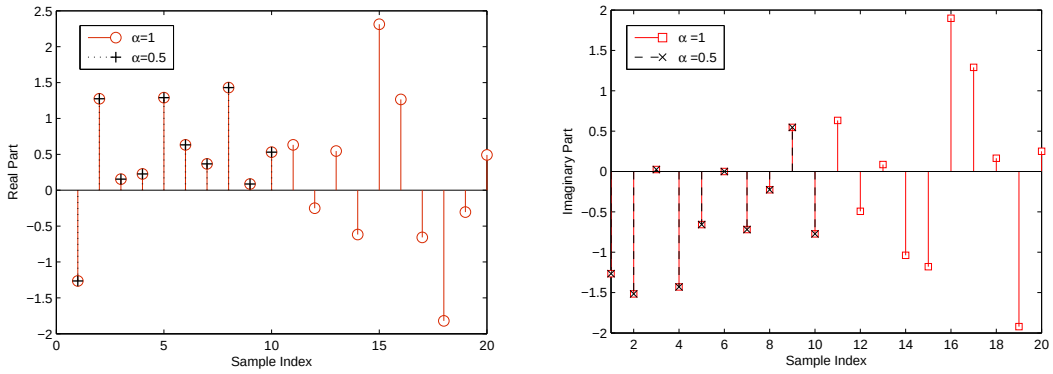

(A) Real Part of Samples (B) Imaginary Part of Samples

FIGURE 9.3: Real and imaginary parts for time samples for system with $\alpha = 1$ and 0.5, showing 20 and 10 samples per one SEFDM symbol respectively.

$[0 - T]$. The downgrade in the sampling rate is consistent with the reduction in the bandwidth in the case of $\alpha = 0.5$. The figure demonstrates that the real and imaginary parts of the time samples have the same values but occur at different instants of time.

The outcome of the discussed insight is that the precoding system need not be restricted to the exact value of α in the system. That is the precoding can be performed using a different α value where the receiver needs to invoke the time signal (or samples) corresponding to the coding α_c in order to achieve the coding advantage revealed in equation (9.12). Thus, the generalized coding matrix $\mathbf{U}$ is defined from

$$\mathbf{C}_{code} = \mathbf{U}\mathbf{\Lambda}_{code}\mathbf{U}^*, \tag{9.29}$$

where $\mathbf{C}_{code}$ is the correlation matrix of the subsystem corresponding to α_c where $\alpha_c \leq \alpha$.

Examining the plots of the eigenvalues and singularvalues of the SEFDM system under different coding arrangements, indicate that it is useful to use different coding space to improve the error performance. Figs. 9.4 to 9.6 depict the eigenvalues and singular-values to highlight the effects of the different precoding schemes. Fig. 9.4 depicts the eigenvalues of an 8 subcarrier system with $\alpha = 0.85$ under three different coding spaces corresponding to equivalent systems with $\alpha = 0.85, 0.7$ and 0.5. In this figure and sub-sequent figures the values are connected with dashed faded lines to aid the visibility of the points. The figure shows that coding with $\alpha = 0.5$ results in fewer strong channels, yet with highest peak values, whereas coding with the same system $\alpha = 0.85$ resulted

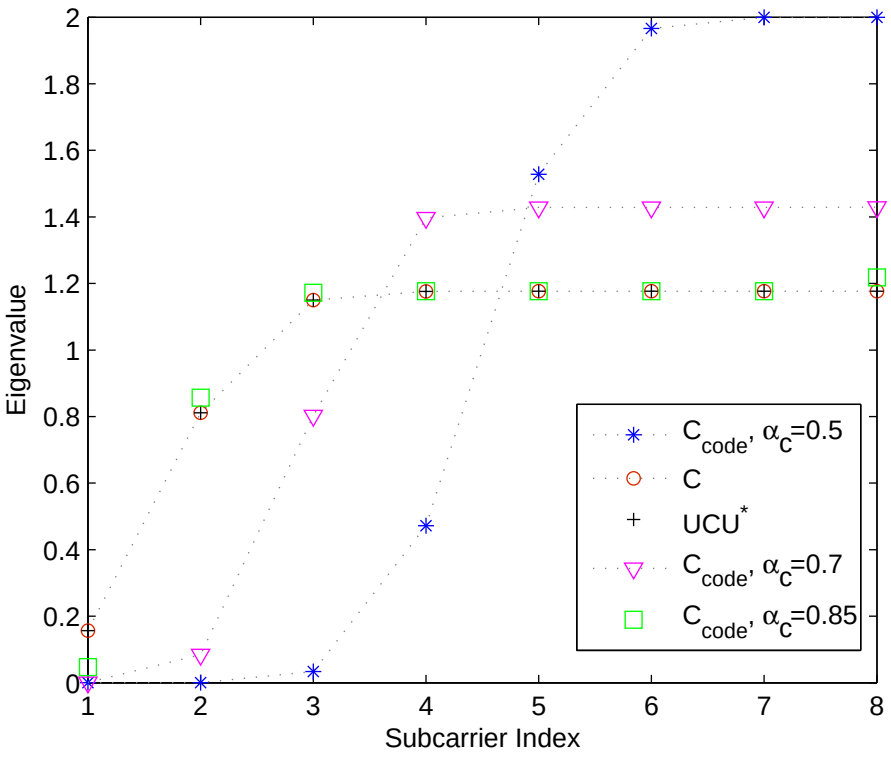

FIGURE 9.4: The eigenvalues of the precoded system for 8 subcarrier system with $\alpha = 0.85$. Three coding schemes are displayed corresponding to $\alpha_c = 0.85, 0.7$ and 0.5. The legend shows the matrix whose eigenvalues are plotted and the corresponding α_c.

in more moderately strong channels with the lowest peak values. The small eigenvalues correspond to the "weak" channels that are detected through the other reception path as explained in previous section. Fig. 9.5 depicts the diagonal elements of the matrix $\mathbf{M}$. These elements represent the singularvalues of the decomposed matrix. The figure shows that coding with the same α maintains the same distribution of the singularvalues, therefore, the detection of the "weak" channels will suffer. However, coding with a different code space ($\alpha_c = 0.7, 0.5$) resulted in a pattern of the singular values of the "weak" channels similar to the system without coding. Coding with $\alpha = 0.5$ resulted in maximum singular values higher than the corresponding one in the original system.

To further highlight the different codes effects, Fig. 9.7 presents a map of the Euclidean distance between all possible combinations of BPSK input symbols for 4 subcarrier system with $\alpha = 0.8$. Basically, the Euclidean distance between the SEFDM symbols is the dominant factor in the performance of the ML detector and consequently an upper bound for other detectors. Examining the map of the original and coded systems in Fig.

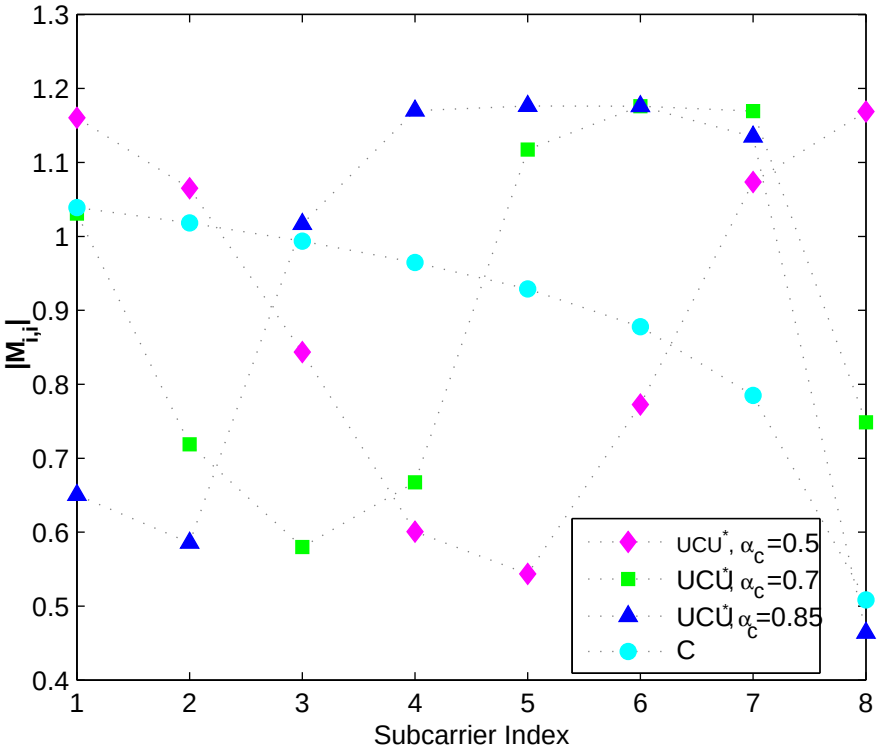

FIGURE 9.5: The singularvalues of the $\mathbf{M}$ matrix for 8 subcarrier system with $\alpha = 0.85$. Three coding schemes are displayed corresponding to $\alpha_c = 0.85, 0.7$ and 0.5. The legend shows the matrix whose singularvalues are plotted and the corresponding α_c.

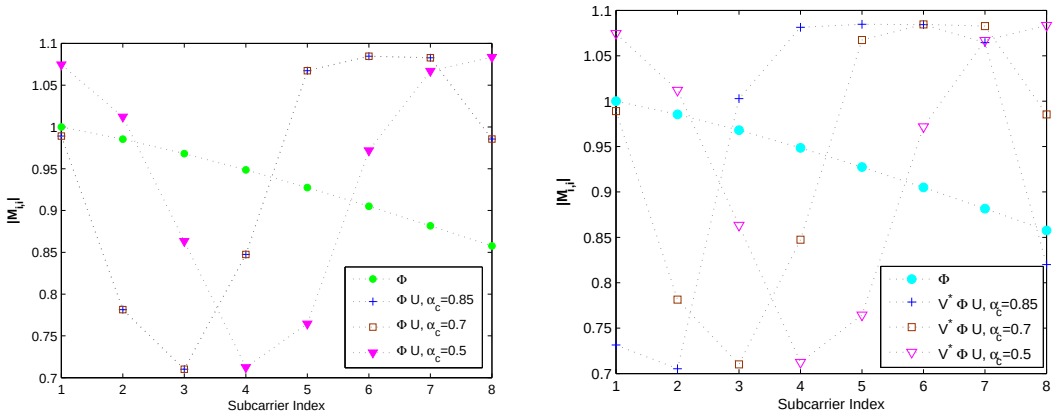

FIGURE 9.6: Different unitary transform effects. Plots show the singularvalues of the $\mathbf{M}$ matrix for 8 subcarrier system with $\alpha = 0.85$. Three coding schemes are displayed corresponding to $\alpha_c = 0.85, 0.7$ and 0.5. The legend shows the matrix whose singularvalues are plotted and the corresponding α_c, where $\mathbf{V}$ is defined from the SVD of $\mathbf{\Phi U}$.

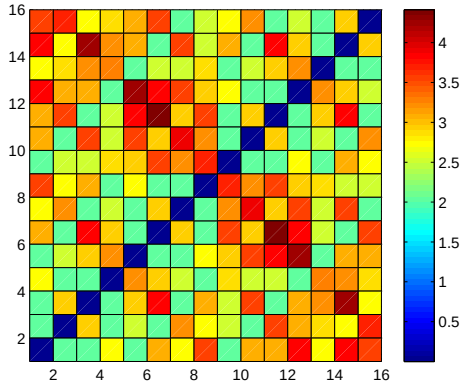

(A) Original.

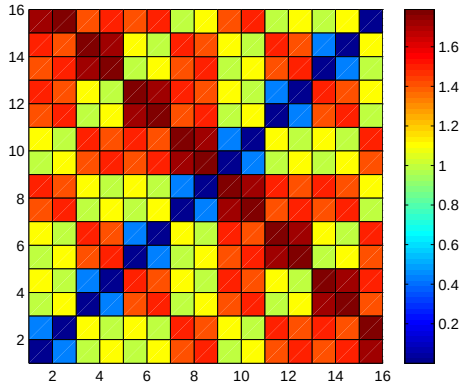

(B) Precoded with $\alpha_c = 0.8$.

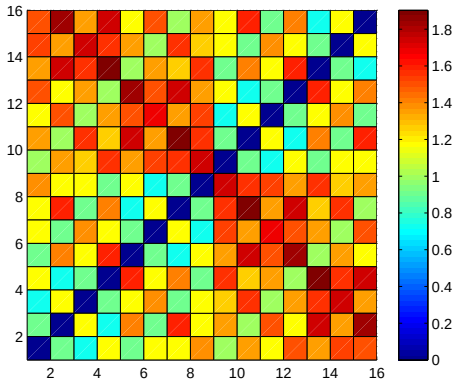

(C) Precoded with $\alpha_c = 0.5$.

FIGURE 9.7: Euclidean distance between the 4^2 possible SEFDM symbols for 4 subcarrier system, $\alpha = 0.8$ carrying BPSK input symbols.

9.7a and 9.7b respectively, shows that the precoding results in increasing the distance between some candidate SEFDM symbols and reduces the distance for neighbouring symbols. Examining Fig. 9.7c shows that precoding with a different code space results in a milder effect in terms of the increment or reduction of the distance between the candidate solutions, thus indicates better immunity against noise.

Furthermore, the spectrum of the precoded signal is examined. Theoretically, multiplication by a unitary matrix should not change the power spectral density of the signal. Numerical verifications show that the spectrum of original SEFDM signal and the coded one are very close, as shown in Fig.9.8. Nevertheless, it is noted that the peaks in the precoded spectrum are less than the original one.

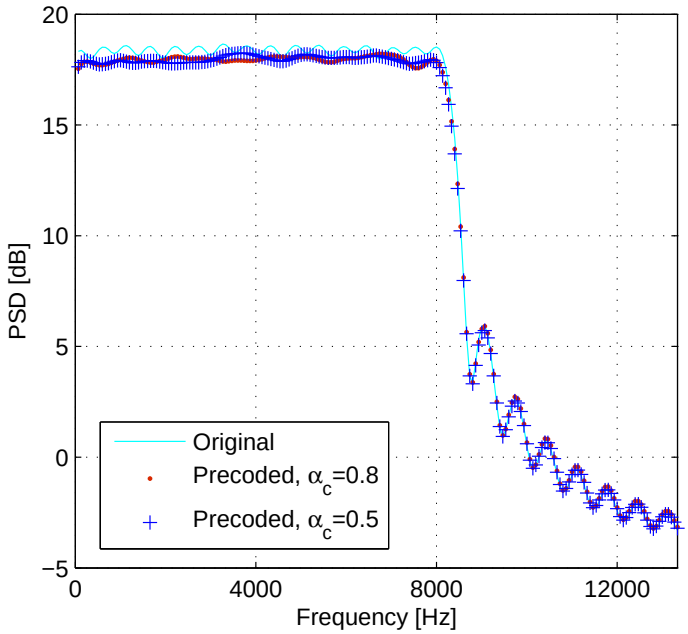

FIGURE 9.8: Spectrum of 16 subcarrier original SEFDM and precoded SEFDM system for $\alpha = 0.8$ with coding spaces corresponding to $\alpha = 0.8$ and 0.5.

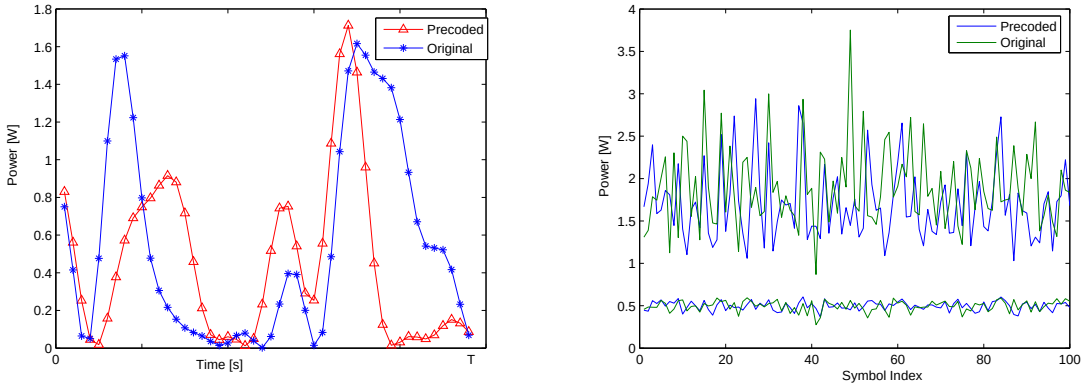

(A) Instantaneous power per SEFDM symbol.

(B) Peak and average power per SEFDM signal.

FIGURE 9.9: Instantaneous power for SEFDM signal with and without the coding.

Finally the power of the modulated symbol in the case of coding is examined and compared to the original system. Fig. 9.9a shows the instantaneous power for an SEFDM symbols before and after the coding. The plot shows that the distribution of the power within transmission time for the coded symbol is different. In addition, Fig. 9.9b shows the peak and average power for 100 SEFDM symbols. It can be seen that in most cases the peak power of the coded signal is less than the original. This observation is further confirmed by examining the CCDF of the PAPR exceeding a threshold level γ depicted

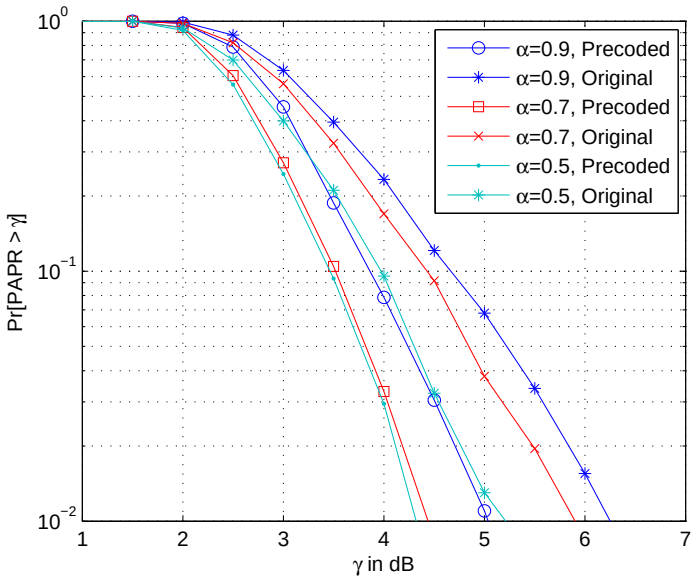

FIGURE 9.10: PAPR of SEFDM system with and without precoding for 10 subcarrier system with 4QAM input symbols.

in Fig. 9.10 for the coded and original signal. The figure shows that the precoded SEFDM exhibit lower PAPR than the original one.

9.5 Performance Investigations

Performance of the precoded SEFDM system was tested by extensive numerical simulations for systems carrying 4QAM modulated symbols for different values of α and numbers of subcarriers. The simulations aimed to verify the expected BER reduction.

Fig. 9.11 shows the BER performance of the individual channels for different values of α, obtained by performing direct slicing for the complete set of carriers based on equation (9.13) and calculating the BER per channel based on statistics on the symbols estimated at that channel index. Fig. 9.11 shows that a number of the individual channels can experience BER that is lower than OFDM case. The number of the "strong" channels and their BER performance is proportional to α. That is with the increase in α, the BER rate per channel gets closer to an average value for the case of $\alpha = 1$, which is OFDM case, while the number of channels with lower BER decreases. The estimates corresponding to the "strong" channels exhibited lower BER due to the apparent power boost they receive from the discarded channels. Then the estimates corresponding to

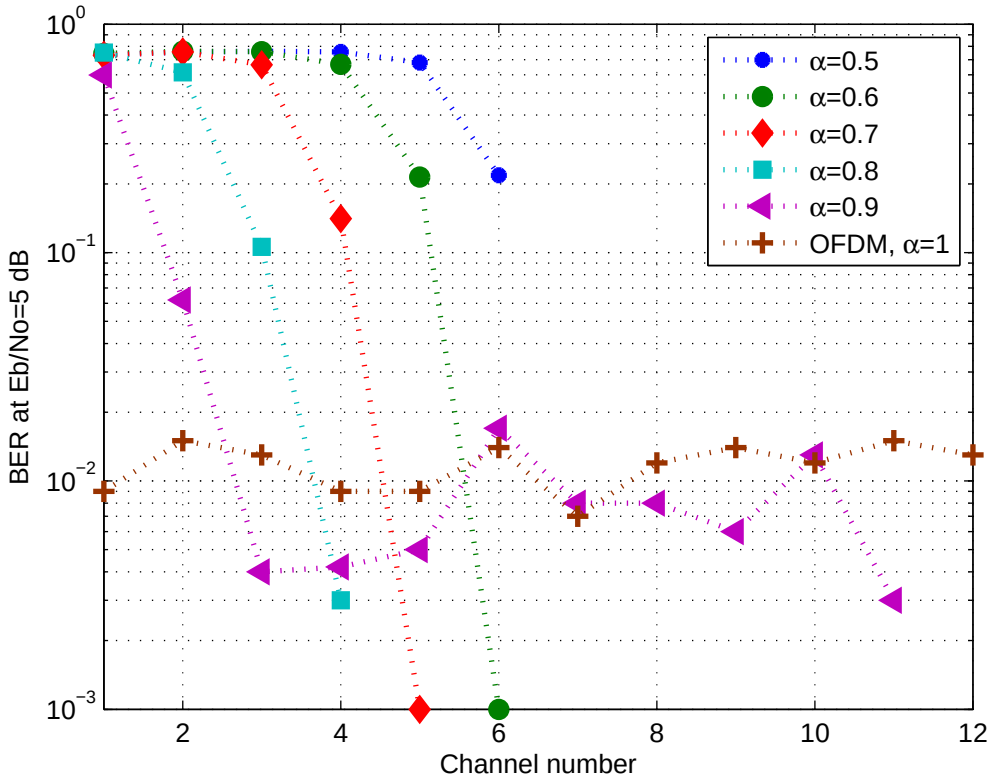

FIGURE 9.11: BER performance of individual channels of a precoded SEFDM signal carrying 4QAM symbols for $\alpha = 0.5 - 1$. Detection is based on scalar division and slicing.

the "weak" channels are discarded and re-estimated by applying detection algorithm on a fresh samples set from the incoming signal with the aid of the retained estimates corresponding to the "strong" channels. Fig. 9.12shows the BER for the simulated individual channels with respect to E_b/N_0 and the corresponding BER performance curves based on equation (9.14). It is worth emphasizing that the energy per bit is calculated based on the input symbols prior to the coding and the SEFDM modulation. The modification of the theoretical BER formula is to reflect the signal to noise ratio changes that appears after demodulation in the decomposed channels in the form of multiplication with the eigenvalues of the $\mathbf{C}$ matrix. Again, the results in Fig. 9.12 confirmed that the BER performance of the individual channels is different as depicted in Fig.9.12. Symbols corresponding to channels with the relatively high eigenvalues exhibited low BER compared to the symbols corresponding to the "weak" channels as is expected from the BER formula in equation (9.14) which is depicted in Fig. 9.12. .

Fig. 9.13 depicts the BER performance with respect to α. The figure shows that SEFDM

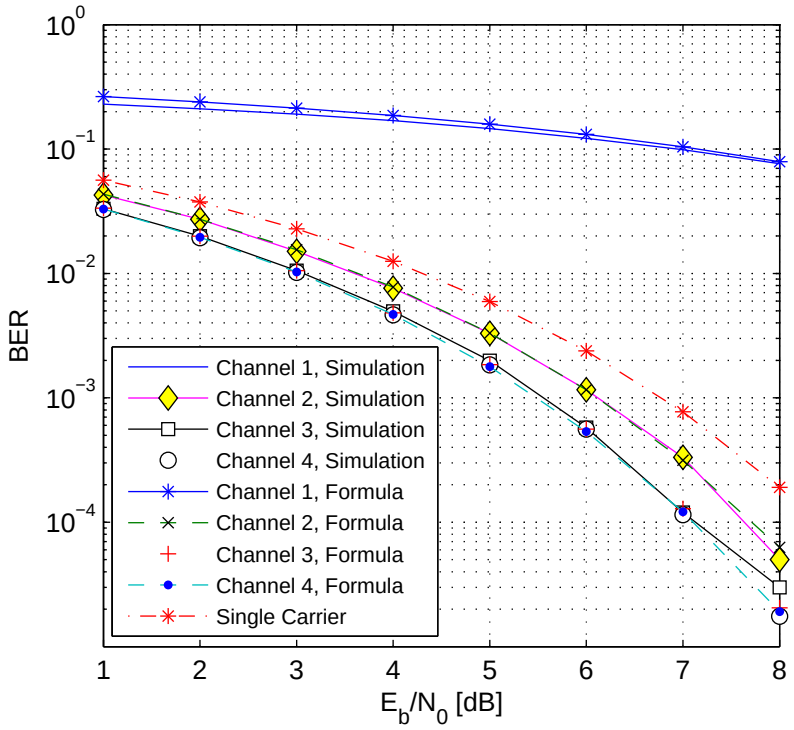

FIGURE 9.12: BER per individual channel from simulation and formula.

systems with $\alpha \geq 0.8$ and $4, 8$ subcarriers can outperform ML detected uncoded system in terms of the BER, thus demonstrating the advantage of the coding. However, this advantage requires an increase in the receiver complexity over OFDM yet less than original SEFDM requirement. For the SEFDM system with 4 subcarriers, BER performance, superior to ML detected SEFDM and OFDM, can be achieved by simply utilizing a shifted samples set as shown in Fig. 9.13a. Using different code space results in extending the improved BER performance to bandwidth savings of 30% as shown in Fig. 9.13b. Meanwhile, Fig. 9.13c shows that this coding approach (i.e. shifted samples) is not sufficient when the number of subcarriers is increased to 8. In this case, precoding with a different coding space resulted in performance better than uncoded SD detect SEFDM system with the same number of subcarriers as shown in Fig. 9.13d. In addition, the figures depict the performance of the layered ZF and IC detectors. In particular, the IC detector shows performance that approaches ML detection for the case of 4 subcarriers specially when using different coding space. With the increase of the number of subcarriers the performance of the IC shows degradation specially when different coding space is used. The figures show that for $\alpha \geq 0.9$ the layered ZF and IC achieve the same ML performance. Furthermore, Fig. 9.14 depicts the error performance for $4, 8, 12$ and

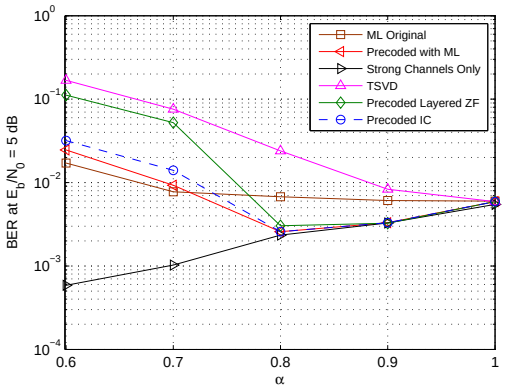

(A) 4 subcarrier system with shifted samples set.

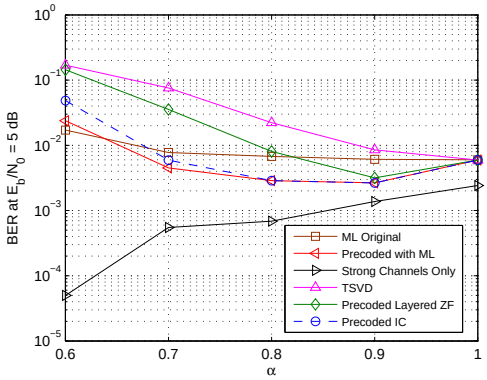

(B) 4 subcarrier system with shifted samples set and coding space of $\alpha_c = \alpha - 0.2$.

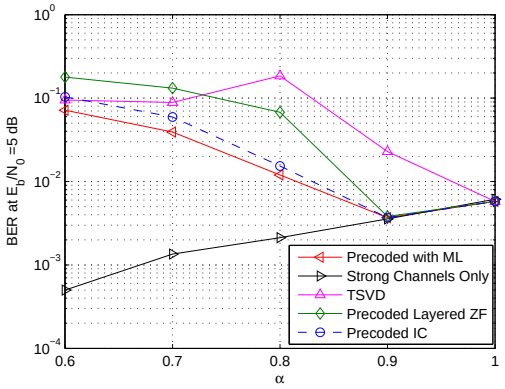

(C) 8 subcarrier system with shifted samples set.

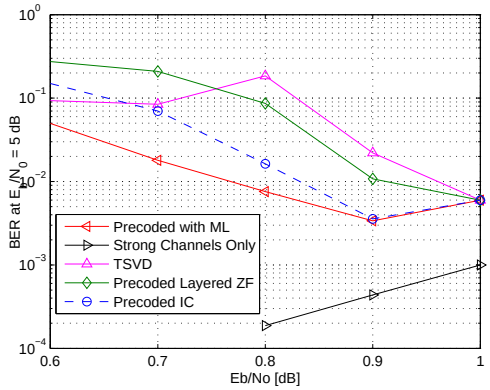

(D) 8 subcarrier system with shifted samples set and coding space of $\alpha_c = \alpha - 0.3$.

FIGURE 9.13: BER of precoded SEFDM for 4 and 8 subcarriers for $\alpha = \{0.6 - 0.9\}$, $\alpha = 1$ gives performance of uncoded OFDM system.

16 subcarriers. The figure indicates performance degradation with the increase in the number of subcarriers

Fig. 9.15 depicts the performance of the precoded system with respect to E_b/N_0. The figure shows that for system with few subcarriers it is possible to achieve performance that is better than OFDM for substantial bandwidth savings. With the increase in the number of subcarriers and to maintain the improved error performance it is needed to reduce bandwidth savings, however it is considered a development as it supported close to ML performance to systems with number of subcarriers that are challenging to implement or simulate.

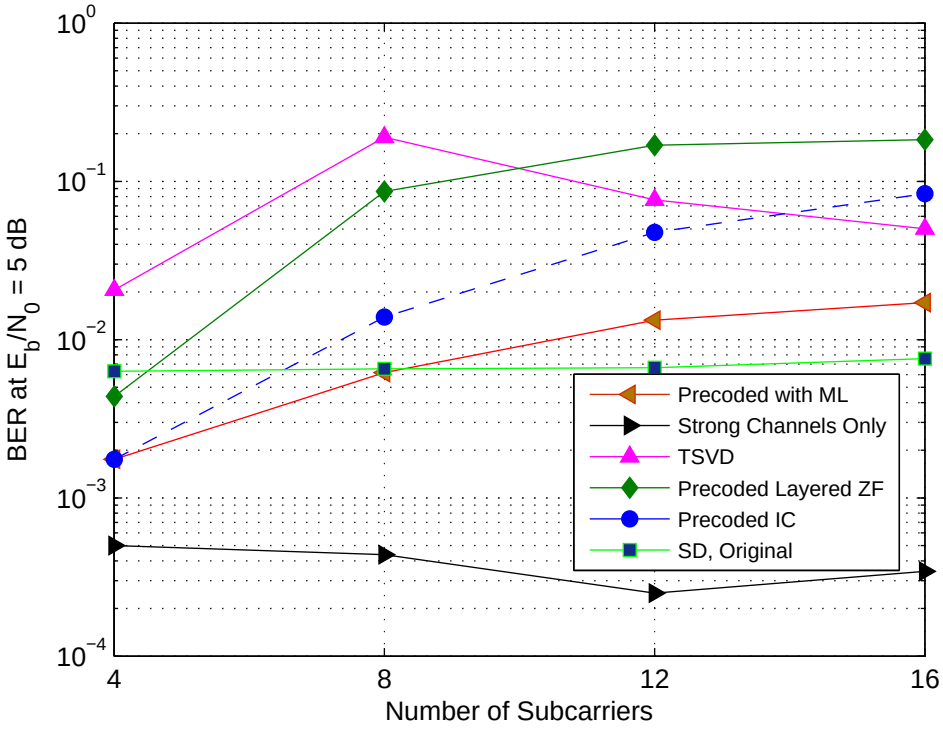

FIGURE 9.14: N=4 shifted samples set and coding space $\alpha_c = \alpha - 0.3$.

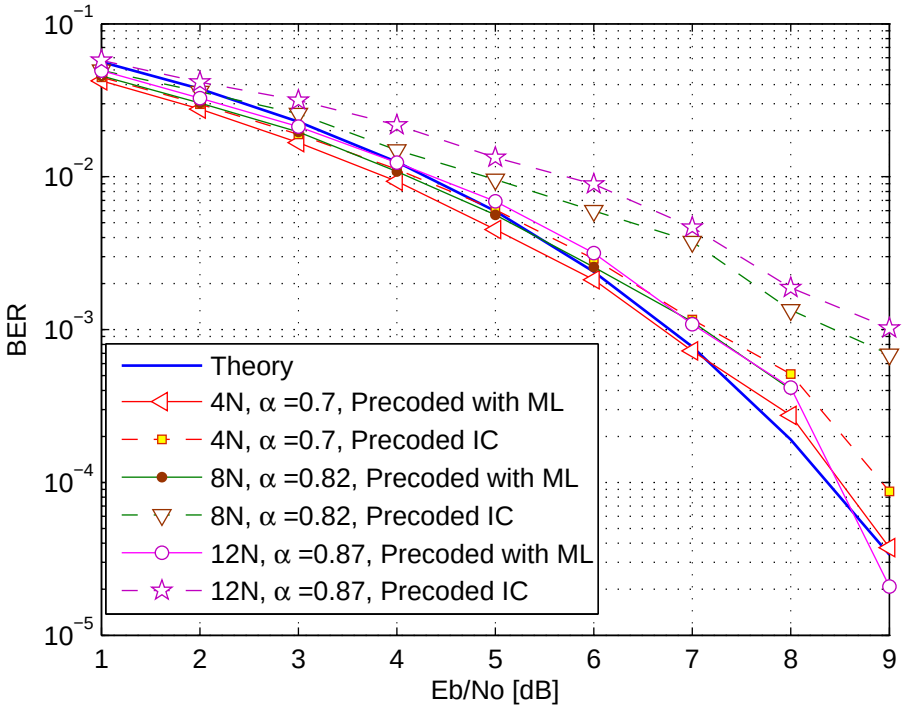

FIGURE 9.15: N=4 shifted samples set and coding space $\alpha_c = \alpha - 0.2$.

9.6 Complex Sphere Decoder (CSD)

The exhaustive ML detection poses a limitation on the achievable system size, despite the improvement facilitated by the coding. Therefore, Sphere Decoder (SD) is proposed to reduce complexity requirements. To suit the structure of the precoded SEFDM, the Complex Sphere Decoder (CSD) is proposed to maintain the order of the symbols estimated via the division and slicing operations whereas the real SD will require mixing already decoded symbols with the ones to be decoded.

The complex sphere decoder (CSD) follows the same rule for SD in that it solves the ML problem by examining the points that satisfy a radius constraint. The main advantage of CSD is that there is no need for the real decomposition. Complex symbols denoted as $s = s_{Re} + js_{Im}$ are decoded directly starting with QPSK and then by expressing higher level symbols as combinations of scaled and rotated QPSK symbols [83, 194, 195, 36].

Starting from equation (9.20), the detection of the symbols $\hat{S}_{ML}$ is pursued using CSD assuming 4QAM input symbols. The 4QAM input symbols can be expressed as

$$s_i = re^{j\theta_i}, \theta_i \in \left\{\frac{\pi}{4}, \frac{3\pi}{4}, \frac{5\pi}{4}, \frac{7\pi}{4}\right\}. \tag{9.30}$$

The candidate points lie on the circle of a radius $r = \sqrt{2}$, thus the input symbols vector S is equivalently expressed by its phase value as $\Theta = [\theta_1, \cdots, \theta_N]$. Based on equation (9.20), the CSD algorithm solves the following equation

$$\min \left\| \hat{\mathbf{M}} \left(\hat{r}e^{j\hat{\Theta}} - re^{j\Theta} \right) \right\|^2 \leq g, \tag{9.31}$$

where $\hat{r}e^{j\hat{\Theta}}$ is the representation of $R^-/\hat{\mathbf{M}}$ in polar coordinates and g is the sphere radius. Noting that $\hat{\mathbf{M}}$ is an upper triangular matrix, the Cholesky decomposition of the RSD is eliminated and the CSD search starts from the η^{th} level, where $\eta = (1-\alpha)N$, by solving the inequality

$$\left\| \hat{r}_\eta e^{j\hat{\theta}_\eta} - re^{j\theta_\eta} \right\|^2 \leq \frac{g}{\hat{m}^2_{\eta,\eta}}, \tag{9.32}$$

$$\hat{r}^2_\eta + r^2 - 2\hat{r}_\eta r \cos\left(\hat{\theta}_\eta - \theta_\eta\right) \leq \frac{g}{\hat{m}^2_{\eta,\eta}}. \tag{9.33}$$

or equivalently

$$\cos\left(\hat{\theta}_\eta - \theta_\eta\right) \geq \frac{1}{2\hat{r}_\eta r}\left[\hat{r}_\eta^2 + r^2 - \frac{g}{\hat{m}_{\eta,\eta}^2}\right] = \kappa. \tag{9.34}$$

The value of κ, decides the existence of points within the search sphere [83]. If $\kappa > 1$, there are no points within the search sphere and for $\kappa < -1$, the search sphere contains all constellation points. For $-1 < \kappa < 1$, the range of candidate points is given by

$$\left(\hat{\theta}_\eta - \arccos(\kappa)\right) \leq \theta_\eta \leq \left(\hat{\theta}_\eta + \arccos(\kappa)\right). \tag{9.35}$$

The bounds can be transformed to integer search by subtracting $\pi/4$ and multiplying by $4/2\pi$ as

$$\left\lceil \frac{2\pi}{4}\hat{\theta}_\eta - \arccos(\kappa) - \frac{\pi}{4} \right\rceil \leq \vartheta_\eta \leq \left\lfloor \frac{2\pi}{4}\hat{\theta}_\eta + \arccos(\kappa) - \frac{\pi}{4} \right\rfloor, \tag{9.36}$$

where $\vartheta_\eta \in [1, 2, 3, 4]$, $\vartheta_\eta = \frac{2\pi}{4}\theta_\eta + \frac{\pi}{4}$. This is designed for 4QAM constellation but can be extended to other modulation levels that can expressed as combinations of 4QAM. The search continues in the same manner as the RSD explained in section 5.5 where at each level the candidate points are selected and the radius is updated accordingly.

9.7 CSD Results

Numerical simulations of precoded systems where the "weak" channels are estimated using the CSD algorithm are conducted. Fig. 9.16 shows the performance with respect to E_b/N_0. The figure shows that near optimum performance can be achieved for systems with low bandwidth savings. In addition, the precoded system shows improved performance for regions with low E_b/N_0.

Fig. 9.17 shows the BER for different values of α. The figure shows that performance better than OFDM can be achieved for systems supporting bandwidth reduction by 10% or less. Furthermore, the figure shows that the advantage of the use of the CSD becomes clearer with the reduction in α whereas Layered ZF and IC provided the same performance for bandwidth savings of 5% or less.

Fig. 9.17 shows the BER with respect to the number of subcarriers. The figure shows that the performance degrades with the increase in the number of subcarriers as expected

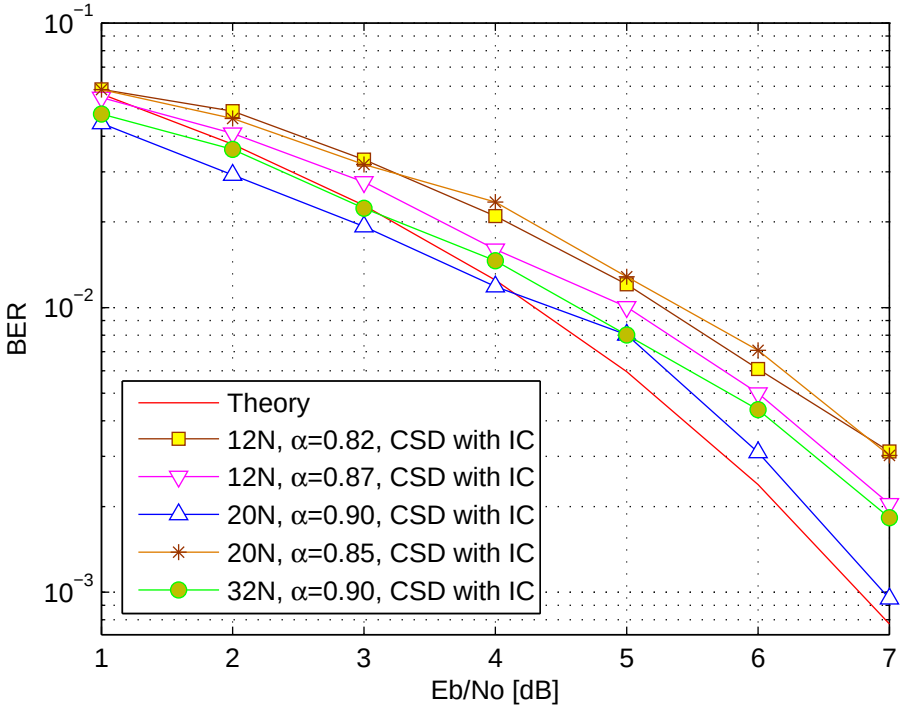

FIGURE 9.16: BER performance of CSD detected precoded SEFDM systems with 4QAM input symbols, different numbers of subcarriers and α values and $\alpha_c = \alpha - 0.3$.

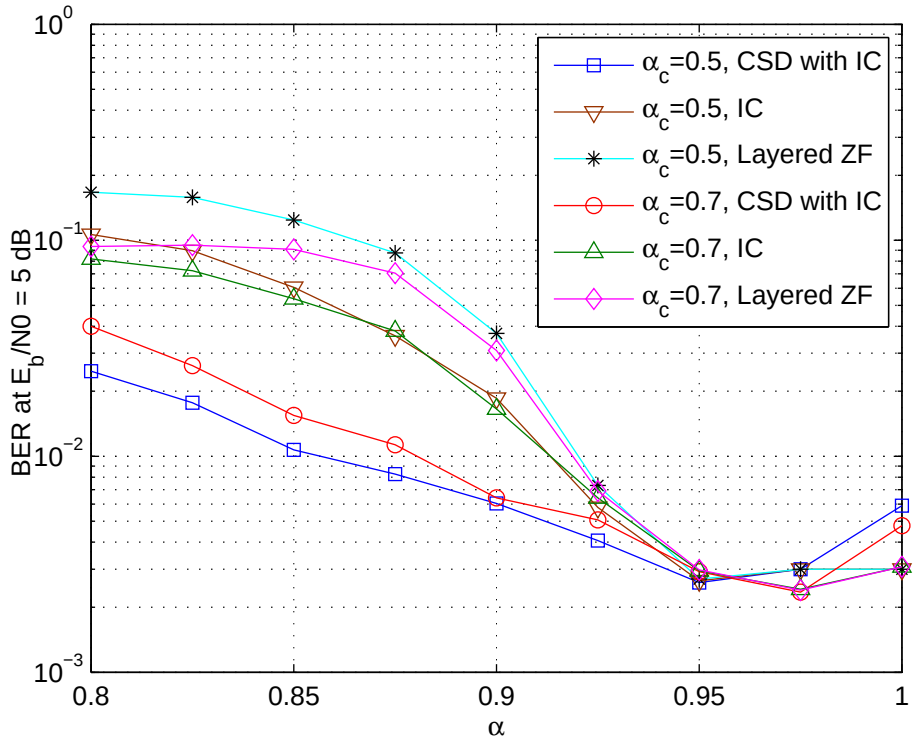

FIGURE 9.17: BER performance of a 20 subcarrier precoded SEFDM system with 4QAM input symbols.

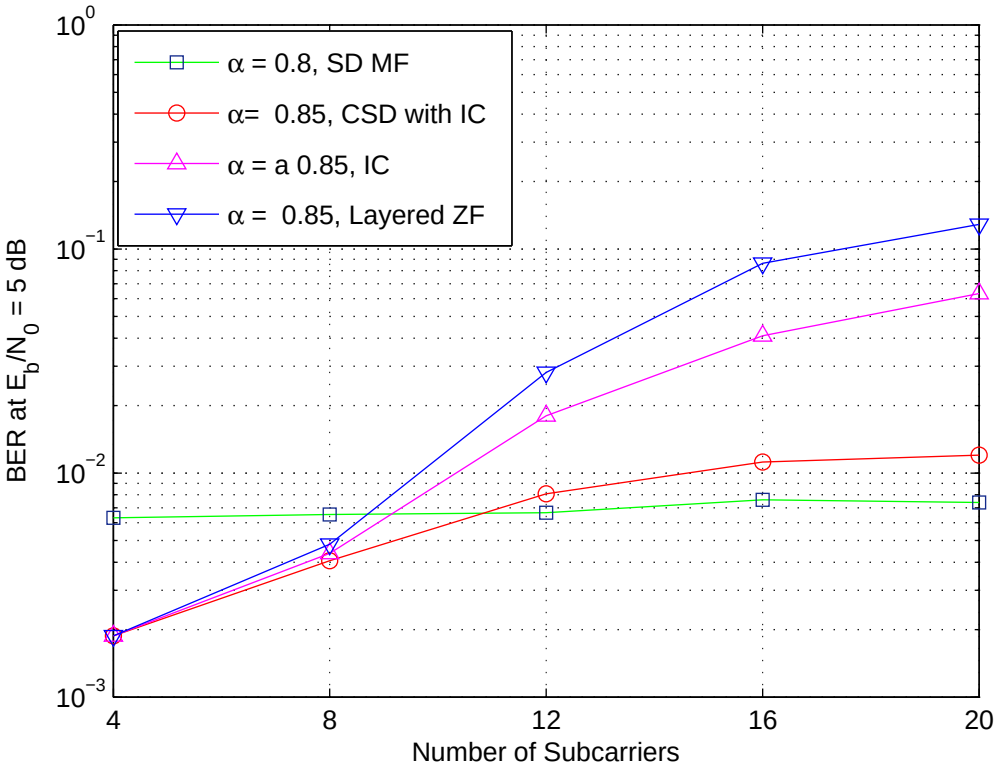

FIGURE 9.18: BER performance of precoded SEFDM system with 4QAM input symbols and $\alpha_c = 0.5$.

and discussed in chapter 3. In addition, the figure shows that the advantage of the use of the CSD over Layered ZF and IC is increased with the increase in the number of subcarriers.

9.8 Precoding in Fading Channel

The precoding concepts can be extended to fading channels. In this case, the code is designed with considerations of the channel, therefore, channel state information (CSI) at transmission side is needed. Such information is typically obtained in the form of feedback from receiver. In systems with symmetric channels, a transceiver may use the CSI obtained in the receiver part. In this case the coding is performed based on the relationship

$$\mathbf{U}\boldsymbol{\Lambda}\mathbf{U}^{*} = \boldsymbol{\Phi}^{*}\tilde{\mathbf{H}}^{*}\tilde{\mathbf{H}}\boldsymbol{\Phi}, \tag{9.37}$$

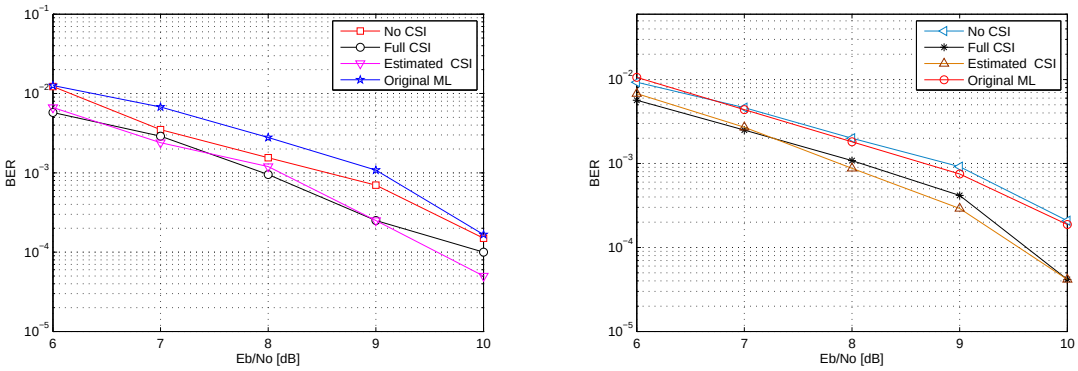

(A) Channel 1. (B) Channel 2.

FIGURE 9.19: BER for precoded system in fading channel for $\alpha = 0.8$, $N = 4$ in Channel 1 and Channel 2. Precoding uses $\alpha_c = 0.5$.

where the matrix $\tilde{\mathbf{H}}$ represent the CSI, thus it can be the exact channel matrix, an estimate of the channel matrix or an identity matrix in case of no CSI or AWGN channel. The receiver will have the same structure as the system in AWGN, where $\alpha_c N$ of the symbols are estimated using division and slicing operations and $(1 - \alpha_c) N$ are estimated using joint channel equalizer and symbol detector based on ML or SD as derived for the uncoded system in sections 8.5 and 8.5.1.

9.8.1 Numerical Results

As a proof of concept numerical simulations for precoding in fading channel are presented using ML joint equalizer-detector for the discarded $(1 - \alpha_c) N$ symbols. The simulations include precoding with perfect CSI, estimated CSI and no CSI at transmitter end. At the reception side, perfect CSI is assumed in order to exclude any effects that may arise due to equalization with some CSI inaccuracies. Fig. 9.19 shows the BER of a precoded system detected with ML in Channel 1 and Channel 2 described in section 8.3, with the parameters listed in Table. 8.2. Plots for both channels show that ignoring channel effects in the precoding leads to performance degradations, whereas, using estimated CSI led to performance close to the full CSI at transmitter case. Moreover, both figures demonstrated the coding advantage by showing that the precoded system with full or estimated CSI exhibited BER advantage equivalent to 1 dB power boost when compared to uncoded system. Furthermore, performance in Channel 1 show that precoding with no CSI resulted in performance better than uncoded system where performance in Channel

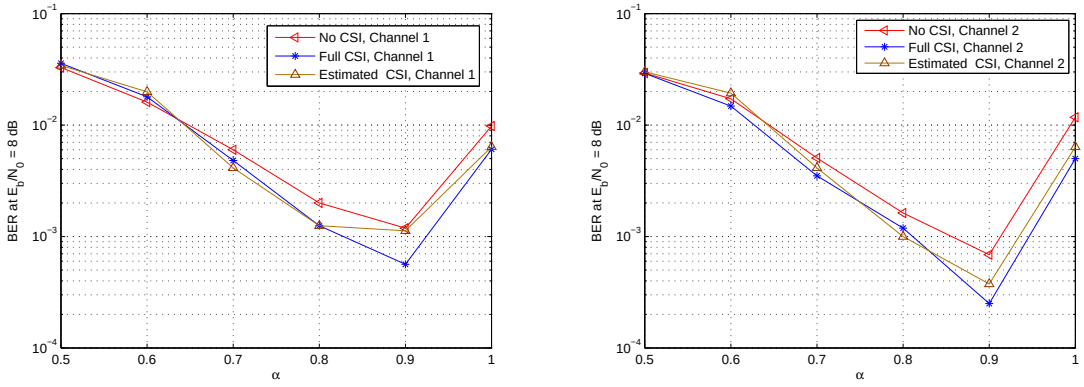

(A) Channel 1. (B) Channel 2.

FIGURE 9.20: BER for precoded system in fading channel for $N = 8$ subcarriers in fading channel. Precoding uses $\alpha_c = 0.5$.

2 indicate that precoding with no CSI is the same as the uncoded system, which indicates that the coding advantage in case of no CSI may be dependent on the channel conditions.

Fig. 9.20 depicts the performance for different values of α. The plots show the precoding advantage in terms of improved BER performance over that of OFDM for bandwidth savings up to 30%.

9.9 Conclusions

In this chapter a new precoding technique based on the knowledge of the intercarrier interference is proposed for the SEFDM system. The coding adapts the SEFDM signal to enable access to individual carriers by transforming the SEFDM modulation to parallel independent channels. Depending on the value of α it is shown that the coding results in that some of the channels experience amplification while some experience power depletion. Detection of the symbols corresponding to the relatively "strong" channels was achieved in the form of scalar division and/or slicing operations. Whilst, the rest of symbols were estimated using a sophisticated detector such as Maximum Likelihood (ML) or Sphere Decoder (SD) where the use of the Complex Sphere Decoder (CSD) is proposed to support systems with more subcarriers and lower complexity. One main advantage of the precoding is that the complexity of the detector is reduced due to the reduction

of the size of the problem. An implementation of the system using the IDFT/DFT operation was proposed which can be specially useful when considering systems that are based on OFDM technology as the two systems employ many similar building blocks.

BER simulations confirmed performance superior to other detection strategies for SEFDM system and similar and in some cases superior to OFDM. For bandwidth savings of 10% or less, the precoded system showed improved BER performance over OFDM with minimal increase in complexity. The numerical results showed that this advantage can be achieved for systems with relatively large numbers of subcarriers ≥ 20. For systems with few subcarriers (˜4), it is shown that the precoded system can deliver improved BER performance over OFDM for substantial bandwidth savings ($\sim 30\%$) . This enhancement is facilitated by the coding which effectively redistributes the power of the symbols such that some of the symbols suffer less from the AWGN and then these symbols are used to estimate the highly attenuated symbols.

The concepts of precoding were extended to fading channel conditions. Numerical investigations of ML joint equalization and detection for the "weak" channels were conducted. Results demonstrated the advantage of precoding in fading channels. Nevertheless, the ML joint equalizer-detector restricted the dimension of the problem. Future work may consider using CSD to test the concepts for larger systems.

Last, the precoding strategy proposed here also allows for the trade off between complexity and BER performance by altering the coding space which in turn decides the size of the two reception streams.

Chapter 10

Conclusions

This thesis investigated the Spectrally Efficient FDM system (SEFDM) which proposes enhanced spectrum utilization relative to Orthogonal Frequency Division Multiplexing (OFDM) system. Spectral efficiency is increased by relaxing the orthogonality condition while maintaining the same transmission rate per individual channel, hence, for the same bandwidth allocation SEFDM offers higher throughput than OFDM. SEFDM, as a concept, is relatively new with some disconnected historical pointers, therefore, many issues remain open and untackled. In general, the loss of orthogonality brings along many design and implementation challenges. Previous work indicated that the SEFDM signal exhibited some characteristics that needed further modelling. The generation of the signal remained complicated while the reception followed complex algorithms that can be challenging to realize in hardware. All these issues required attention in order to assess and then realize the potential of the SEFDM system. To address these points, the work in this thesis was conducted in two main parts; firstly the concept of non-orthogonal communications with its transmitter and the receiver design were addressed in order to first establish the needed foundation and then to propose realistic alternatives to the transmission and reception problem. To achieve that, mathematical modelling, system design and assessment were carried under the assumption of AWGN channel. The second part, addressed practical limitations in terms of the Peak to Average Power Ratio (PAPR) and how to control it, the performance of the SEFDM system in fading channels with a focus on equalization and channel estimation and finally the precoding of the SEFDM signal.

As a starting point, the SEFDM signal was mathematically modelled and studied. The work started by building a discrete model of the system. Based on this model, the Intercarrier Interference (ICI) created by the loss of orthogonality was derived with closed form formulas. The structure and behaviour of the ICI terms were identified and used in the development of the receiver in subsequent work. Following that, the mathematical model of the received SEFDM signal was constructed and was shown to rely on the same parameters irrespective of the use of correlation receiver or matched filtering. The characteristic of the SEFDM received signal was proved to be dependent on the ICI matrix, as such the properties of the system can be examined by investigating this matrix. Investigations of the ICI matrix proved that although the system will not be singular, it can appear singular due to the finite resolution of computation machines. In addition, the conditioning of the SEFDM system was investigated through investigating the conditioning of the ICI matrix. The conditioning of the system was proved to deteriorate significantly with the increase in the number of subcarriers and/or the bandwidth compression level.

Secondly, the generation of the SEFDM system was addressed. Based on the discrete SEFDM signal model, an efficient framework for the realization of such signal using the standard Inverse Discrete Fourier Transform (IDFT) was proposed. The framework resulted in the design of three transmitter structures that relied on standard IDFT operations, where each can be efficiently implemented with the IFFT algorithm. The proposed transmitters substantially reduces the complexity of SEFDM signal generation. The complexity of the SEFDM generation approaches that of OFDM and the transmitter structures employ building blocks similar to OFDM. Furthermore, the designed algorithm can facilitate the IDFT design for any Frequency Division Multiplexed (FDM) signal with arbitrary subcarrier spacing such as the MASK OFDM system. Hardware realizations of the transmitters based on the proposed designs have already been developed and tested at UCL.

The work progressed to focus on the reception side and the demodulator which is the first of the two components of the receiver was addressed. The use of demodulation based on Matched Filtering (MF) was proposed. The MF based demodulator uses the same subcarrier structure and as such was designed following the principles developed for the transmission end, using standard Discrete Fourier Transform (DFT) operations.

The introduction of the MF based demodulation led to the elimination of the orthonormalization step and the standardization of the correlation stage which requires a custom designed bank of multipliers and adders which are now achieved with the DFT with a similar complexity as that of the transmitter. That is, the significance of the DFT demodulator is not only the reduction of complexity but also the standard operation, thus the system becomes well suited for implementation. The optimal solution for the MF demodulated signal in AWGN channel was derived. This solution aims to minimize the probability of error and was designed to include the effect of the colouring of the noise which occurs due to the non-orthogonal frames used at the demodulation stage (i.e. the non-orthogonal subcarriers). The optimal solution follows Maximum Likelihood (ML) criteria. Numerical investigations of the derived solution using an exhaustive search algorithm demonstrated that the same error performance of an SEFDM system with orthonormal bases is achieved. This proved that the MF demodulator achieves substantial complexity reduction at no premium at performance. To further reduce the complexity of the detection, the Sphere Decoder (SD) algorithm was proposed to solve the derived optimal solution. Numerical investigations again demonstrated the same error performance and complexity requirement for the SD detector as for an SEFDM system with orthonormal bases. The outcome of this work is that the complexity that used to be associated with the demodulation stage of SEFDM receiver, in the form of orthonormalization operations and the system specific bank of correlators, is eliminated with no effects on performance. This stage now uses standard DFT operations where three arrangements with different sizes and numbers of DFT blocks were proposed to offer flexibility. At this point, all additional complexity associated with the SEFDM system when compared to the OFDM system is localized at the detection end.

The issue of the detection was addressed by proposing low complexity detectors with improved performance. In particular, the design of improved linear detectors was achieved. Design of the Truncated Singular Value Decomposition (TSVD) based detector led to improved error performance at the same complexity as for ZF detection. The use of TSVD for SEFDM detection was motivated by the findings of the mathematical study of the system. As the SEFDM system is classified as an ill conditioned system, the proposal of TSVD came to address this issue and alleviate the effects of the ill conditioning on the generated estimates. The TSVD detector was shown to provide substantially

improved performance over ZF and MMSE as expected and to support large number of subcarriers without further performance deterioration.

Furthermore, another linear detection algorithm was designed and termed Selective Equalization (SelE). The introduction of the SelE detector was motivated by the fact that the ICI in the system is in inverse proportion to the distance between the subcarriers in frequency. Therefore, the SelE detector is designed to account for selected ICI contributions that exceed a pre-determined level. Numerical investigations of the SelE detector have shown improved performance over ZF and MMSE for BPSK and 4QAM symbols and over TSVD for BPSK symbols. The SelE is simpler than the TSVD as it does not require the SVD operation and relies on inversion of the matrix containing the selected ICI contributions where all proposed detection techniques, save the ML, require matrix inversion. However, when the inverse of a matrix is realized with an SVD operation, the TSVD and SelE require the same complexity.

Despite the substantial BER performance improvement over ZF and MMSE, the TSVD and SelE linear detectors do not provide the same quality of communications as ML and SD. On the other hand, the use of SD is plagued by the variable complexity that renders the implementation task to be overly demanding in terms of size and computational resource utilization, therefore, the use of the Fixed Sphere Decoder (FSD) was proposed. Numerical investigations have shown that the FSD provided improved sub-optimal performance over linear detectors with fixed complexity and allowed a trade off between performance and complexity. In addition, it was proposed to combine the FSD with the TSVD detector to bridge the performance gap. The FSD-TSVD detector achieved near optimum performance for bandwidth savings of 25% and imposed an acceptable 2.5 dB power penalty for savings of 35% at BER of 10^{-3} with fixed and substantially reduced complexity.

The outcome of the first part of the thesis is in the proposal of different options for an end to end SEFDM system in AWGN channel. The proposed system requires minimal complexity increment at transmission end compared to OFDM. Demodulation is of similar complexity to the transmitter where all the effort is localized at the detection stage. Reduced complexity alternatives that facilitate a trade off between error performance and complexity were proposed and shown to provide near optimum performance with low and fixed complexity.

The second part of the thesis commenced with investigations of the PAPR of the SEFDM system. It was found that in the SEFDM system the PAPR decreases with the bandwidth compression factor α. Clipping was investigated to provide an insight into the performance of SEFDM system without controlling the PAPR. Clipping increased the out of band emission, while the in band distortion caused by clipping led to a significant increase in the BER where the SD detector exhibited 4 dB power penalty at a BER as high as 2%. Therefore, the control of the PAPR was addressed by applying Selective Mapping (SLM) and Partial Transmit Sequence (PTS). Both systems were found to achieve PAPR reduction. Moreover, a new technique termed SLiding Window (SLW) PAPR control technique was designed for PAPR control in SEFDM system. The technique was based on the fact that the SEFDM signal is periodic with a period greater than the actual symbol period. Hence, the transmitted symbol can be chosen by applying a sliding time window of the SEFDM symbol duration over the total signal period. A transmitter design incorporating the SLW was proposed. Performance simulations confirmed that SLW achieves PAPR reduction up to 4 dB compared to 2-3 dB in the literature.

The SEFDM signal in fading channel was then studied. As a starting point, the proposal of matched filtering for SEFDM demodulation was extended to the case of fading channel and the corresponding optimal solution was derived. The MF was matched to the SEFDM generator system without including the channel. The derived optimal joint channel equalizer and symbol detector in this case was based on ML criteria. Then, the use of SD for joint channel equalization and symbol detection is extended to the MF demodulation case. Numerical investigations confirmed that the MF based demodulation joint equalizer-detector in the form of ML and SD achieved the same error performance as systems with orthonormalization. This way the complexity reduction achieved in the case of the system in AWGN was extended to the fading channel case. Furthermore, the channel estimation in the SEFDM system was considered. The findings about the conditioning and the ICI in the system from the mathematical framework were utilized to design an enhanced channel estimator, termed Partial Channel Estimator (PCE). The PCE achieved more accurate estimates and thus facilitated improved error performance and complexity reduction. Furthermore, joint channel equalization and symbol detection with linear detectors was studied in detail. Particularly, ZF, MMSE and TSVD were investigated with TSVD achieving best performance of the three yet still sub-optimal.

Then, the FSD joint equalizer-detector was investigated to benefit from the fixed complexity and later combined with the TSVD. Numerical results have shown that the FSD provided improved BER performance over linear joint equalizer-detectors, whereas the FSD-TSVD resulted in near optimum performance when combined with the use of PCE for channel estimation. The conducted investigations indicated that there is good potential for the SEFDM signal in wireless communications. The signal maintained the same error performance trends as in AWGN in terms of performance degradation with the increase in bandwidth compression levels. Nevertheless, the deviation from the OFDM case was less than in AWGN channel, indicating that the adverse effects of the loss of orthogonality may not be dominant in the presence of fading conditions.

Finally, manipulations of the SEFDM signal prior to transmission was attempted to boost error performance and reduce complexity. Precoding of the SEFDM signal was proposed. The codes were designed so that on the reception side the effects of the loss of orthogonality were localized in a subset of the transmitted subchannels that require complex detection in the form ML or Complex Sphere Decoder (CSD) with the rest of the symbols detected with simple linear detector. In addition, precoding in the case of fading channel was addressed. Numerical investigations have shown that the use of precoding improves the performance for specific values of bandwidth compression levels. Two important improvements of this arrangement are error performance boost for some of the channels and the reduction of the complexity of the overall system.

To summarize, the appealing SEFDM concept is challenged by the loss of orthogonality that complicates the required transmitter and receiver tasks and degrades performance. The work presented in this thesis tackled both complexity and performance issues. The combined outcome is in different end to end system options that address both complexity reduction and performance enhancement. Regarding the complexity, the transmitter and demodulator designs presented in this work substantially reduced the complexity to a point close to OFDM. The heavy complexity demand is localized at the detector end with four detection alternatives requiring lower complexity being proposed and evaluated. Regarding performance, the work maintained the same performance while achieving transmitter and demodulator complexity reduction. The proposed linear detectors achieved improved performance and the proposal of the FSD-TSVD achieved near optimum performance while satisfying complexity reduction goal. The design and

evaluation of the PAPR control techniques, channel estimators and equalizers, and precoded system demonstrated the potential of SEFDM in practical settings.

10.1 Ongoing Related Work

The research reported in this thesis has led to the development of related work that is in progress at UCL in the form of two Engineering Doctorate (EngD) projects and two MSc projects. As an interim step towards realizing the proposed techniques in hardware, models of the system are being built using Advanced Design System (ADS). Designs of the single block IDFT based transmitter are achieved and are being used to study the performance of the system. In addition, models of the DFT based demodulator are being finalized and are used in conjunction with ZF and direct slicing. Precoded systems were also modelled with ADS [196]. The aim of these models is to provide platforms for further performance investigations that incorporate the typical restrictions in hardware design.

In addition, hardware implementation of the transmitter and receiver is underway. FPGA based transmitters using the multiple IDFT blocks have been built and tested [132]. The FPGA system reported was structured to allow for different modulation formats, bandwidth compression and number of subcarriers and allowed reconfigurability through the use of a modified Ethernet stack [133]. The work is progressing towards the implementation of the transmitter as an Application Specific Integrated Circuit (ASIC) [131, 129]. In addition, the hardware design of the DFT based MF demodulator was addressed in conjunction with ZF and TSVD based detectors [136].

10.2 Future Work

The SEFDM system still remains an open research topic and many issues need further investigation. In addition, the work in this thesis has opened new research directions which show potential improvements and advances, therefore, the author wish to propose the following points for future work:

- **Hardware prototyping and testing of an end to end system.** The proposed techniques at transmission and reception ends place the system on a path for an end to end implementation. Yet, the implementation is faced with challenges. One challenge for the transmitter design is the choice of system parameters that matches available hardware requirements. It is recommended to study the effects of approximations of the parameters of the SEFDM signal. Another work around the components choice issue is to perform backward designs where the number of subcarriers is adjusted to achieve a given bandwidth utilization for a given set of component. This is also applicable to the demodulator and solving this issue will automatically answer the demodulation problem. In addition, it will be useful to implement the single IDFT transmitter as it requires less complexity than that of the design using multiple IDFTs. Furthermore, implementations of SLW can be pursued based on the single IDFT transmitter designs. For the detection implementation, the FSD and FSD-TSVD are the best candidates. Implementations of the FSD for MIMO systems have been reported [148, 145], however, designs for SEFDM need to consider the relatively large number of subcarriers. It is also considered useful to implement the SelE sub-optimal detector for three reasons: it requires low complexity, provides better BER and is more suited to the limited precision of hardware than ZF. Finally, implementations of ML and SD detectors for small sized systems, (~ 8 subcarriers and BPSK), may be considered which will not require huge complexity specially benefiting from the developments in MIMO system [137].

- **Channel estimation.** The PCE concept is flexible and can be extended to design a completely orthogonal structure within the SEFDM system bandwidth with any resolution. That is, to design a new subcarriers set for the estimator block where the number of subcarriers is chosen to satisfy orthogonality principles. In this case, the estimator block will be based on OFDM principles. If OFDM based PCE estimator is used, the system can use comb type estimation where pilots are interleaved with information symbols. All findings for OFDM estimation will automatically apply to this concept [178, 179, 180, 181]. For instance, with the addition of a cyclic prefix to the pilot symbol, the demodulation of the pilots can follow OFDM principles. The drawback is that the system will not be using the

same frequency contents of SEFDM for which the estimation is used, therefore, may require interpolation.

- **Precoding of the SEFDM signal covering:**
  - Investigations of alternative code designs that invest in the observed changes of the Euclidean distance maps in Fig. 9.7. One possible direction to investigate is the use of differential modulation and differential encoding and/or to impose constraints on the transmitted symbols so that the close symbols constellation occurs only under controlled conditions. In addition, the fact that the close Euclidean distances are restricted to few symbols around the desired one, suggests that a confined ML search can achieve the same performance as a complete one. This suggests that investigations of the use of pruned ML [90] or SD [91] search can lead to further complexity reduction.
  - Extension of the objectives of precoding of the SEFDM to include further performance improvements in terms of system capacity, better resilience to interference and fading channels. Precoding concepts are used in many communications systems to achieve different objectives, such as to maximize MIMO channel capacity [119] and optimize signal design in the presence of interference in MC-CDMA [192]. It is considered useful to design the codes for SEFDM system that incorporate a multitude of objectives.
  - Investigations of SEFDM precoding for OFDM system. To study the potential and challenges of applying SEFDM precoding concepts on OFDM and assess the impact on the performance of the precoded OFDM in AWGN and fading channels. Theorem 9.1 showed that the OFDM signal contains all possible SEFDM coding spaces, therefore, precoding of the OFDM signal can then be pursued using coding spaces corresponding to any fractional spacing value. Nevertheless, the implication of the coding on the detectability of the OFDM signal needs to be addressed. Such study should identify any potential for BER improvement and assess the required complexity.

- **Investigate the effects of synchronization and timing errors on the performance of the SEFDM signal.** In OFDM systems, synchronization errors destroy the orthogonality between the subcarriers, therefore can severely degrade

the successful symbol detection [43]. Nevertheless, the effects of the synchronization and timing errors in SEFDM are not expected to pose the same challenge as for OFDM. The system will have ICI in all cases; the difference is that the ICI is not predefined. The work in SelE suggests that it can be advantageous to account for truncated ICI contributions, however, SelE gives sub-optimal performance and the impact of these offsets needs to be assessed for the optimal detection. It is considered necessary to study the effects of such errors on the performance of the system. Such study may also cover the effect of generation of the SEFDM signal with approximate IFFT operations which can be treated as deterministic frequency shifts, thus can be incorporated in the detector design.

- Investigate the potential of applying SEFDM concepts and developed techniques to other communication systems. In particular to apply the designed TSVD and FSD-TSVD algorithm on other detection problems that suffer from ill conditioning. In particular, MIMO systems suffer from ill conditioned channels [149], therefore there is a potential to investigate the TSVD performance in such channels. In addition, recalling that the use of the FSD was initially suggested for MIMO systems [144], it can be useful to investigate the performance of the FSD-TSVD algorithm for the cases where the MIMO channel is ill conditioned.

- From the work presented in this thesis, the author would like to generalize the concepts of non-orthogonal multicarrier system. Orthogonality is a state and is defined in time and frequency. This dual requirement leads to the existence of non-orthogonal systems within orthogonal one. For instance, depending on the sampling of an OFDM system, an SEFDM system with specific number of subcarriers and α can be identified (i.e. taking N samples from the first half of OFDM samples leads to an N subcarrier SEFDM system with $\alpha = 0.5$). The significance of this argument relies in the fact that non-orthogonal samples carry some form of diversity. This diversity can be invoked when part of the transmission is corrupted or merely for added guarantee of performance. The importance of this concept relies on specifying methods to identify the inherent diversity within orthogonal and non-orthogonal systems and hence exploit this knowledge to improve performance.

- Many other ideas including: SEFDM with pulseshaping where different pulses are explored and their respective performance is assessed, export the concepts of

SEFDM to access techniques and propose SEFDMA and investigate the potential of combining SEFDM with diversity techniques to alleviate the performance degradation observed in SEFDM system.

Overall, this thesis has provided new methods and techniques for realizable non-orthogonal and spectrally efficient multicarrier system. It is hoped that the research in this thesis will pave the way to realistic use of such systems in practical settings.

Appendix A

Illustration of Theorem 3.1

Theorem 3.1 shows that there can be orthogonal subcarriers within the SEFDM subcarriers. In this section, this theorem is illustrated by examples. For $\alpha = b/c$ and $b \leq c$, Table. A.1 presents the possible orthogonal subsets of the subcarriers. The table indicates that for a given number of subcarriers, increasing the value of α leads to the existence of more subsets of orthogonal subcarriers but with fewer subcarriers in each subset. In general, for a system with N subcarriers and $\alpha = 1/c$, a subset of k orthogonal subcarriers can be defined by the indices

$$(a_0, a_0 + c, a_0 + 2c, \ \cdots \ , a_0 + c\,(k-1))\,. \tag{A.1}$$

<table>
<tr><th>b
c</th><th>1</th><th>2</th><th>3</th><th>4</th></tr>
<tr><td rowspan="4">1</td><td rowspan="4">All</td><td rowspan="4">(1, 3, 5, 7, 9, 11, 13, 15)
(2, 4, 6, 8, 10, 12, 14, 16)</td><td rowspan="4">(1, 4, 7, 10, 13, 16)
(2, 5, 8, 11, 14)
(3, 6, 9, 12, 15)</td><td>(1, 5, 9, 13)</td></tr>
<tr><td>(2, 6, 10, 14)</td></tr>
<tr><td>(3, 7, 11, 15)</td></tr>
<tr><td>(4, 8, 12, 16)</td></tr>
<tr><td rowspan="4">2</td><td rowspan="4">All</td><td rowspan="4">(1, 4, 7, 10, 13, 16)
(2, 5, 8, 11, 14)
(3, 6, 9, 12, 15)</td><td>(1, 5, 9, 13)</td></tr>
<tr><td>(2, 6, 10, 14)</td></tr>
<tr><td>(3, 7, 11, 15)</td></tr>
<tr><td>(4, 8, 12, 16)</td></tr>
<tr><td rowspan="4">3</td><td rowspan="4">All</td><td>(1, 5, 9, 13)</td></tr>
<tr><td>(2, 6, 10, 14)</td></tr>
<tr><td>(3, 7, 11, 15)</td></tr>
<tr><td>(4, 8, 12, 16)</td></tr>
<tr><td>4</td><td>All</td></tr>
</table>

TABLE A.1: Orthogonal subsets within SEFDM system for $\alpha = b/c$, $b \leq c$ and N subcarriers where $N = 16$. The numbers denote the subcarrier index starting from 1.

By definition the highest possible index is N, hence

$$a_0 + c\,(k-1) \leq N, \tag{A.2}$$

which leads to

$$k \leq \frac{N - a_0}{c} - 1. \tag{A.3}$$

Equation A.3 shows that there are three cases that lead to the reduction of the number of the orthogonal subcarriers within a subset: the first two affect all the subsets in the system and occur with the reduction of the value of α for a given N and a_0 or the number of subcarriers, N, for a given c and $a_0$values. The third case may affect some of the subsets and occur with the increase in value of a_0, that the number of the orthogonal subcarriers for a subset depends on the index of its first subcarrier. The equation also shows that the number of orthogonal subsets equals c.

Appendix B

Derivations of Lemma 3.1

In these lines all the steps followed to simplify the angular term of the determinant in Lemma 3.1 are provided, starting from the expression of the angular term in equation 3.47:

$$\begin{aligned}
\angle\{\det(\Phi)\} &= \prod_{0\le i<k\le N-1} -j\, e^{\frac{j\pi\alpha(k+i)}{N}} \\
&= (-j)^{N\left(\frac{N-1}{2}\right)} \prod_{k>1}^{N-1} e^{\frac{j\pi\alpha k}{N}} \prod_{\substack{i\ge 0}}^{k-1} e^{\frac{j\pi\alpha i}{N}} \\
&= (-j)^{N\left(\frac{N-1}{2}\right)} \prod_{k>1}^{N-1} e^{\frac{j\pi\alpha k}{N}} e^{\frac{j\pi\alpha\sum_0^{k-1} i}{N}} \\
&= (-j)^{N\left(\frac{N-1}{2}\right)} \prod_{k>1}^{N-1} e^{\frac{j\pi\alpha k}{N}} e^{\frac{j\pi\alpha k\left(\frac{k-1}{2}\right)}{N}} \\
&= (-j)^{N\left(\frac{N-1}{2}\right)} \prod_{k>1}^{N-1} e^{\frac{j\pi\alpha k(k+1)}{2N}} \\
&= (-j)^{N\left(\frac{N-1}{2}\right)} e^{\frac{j\pi\alpha\sum_1^{N-1} k(k+1)}{2N}}. \qquad \text{(B.1)}
\end{aligned}$$

The exponent term $\sum_1^{N-1} k\,(k+1)$ is simplified as

$$\begin{aligned}\sum_{1}^{N-1} k^2 + k &= \sum_{1}^{N-1} k^2 + \sum_{1}^{N-1} k \\ &= \left\{ \frac{(N-1)^3}{3} + \frac{(N-1)^2}{2} + \frac{(N-1)}{6} \right\} + \frac{N\,(N-1)}{2} \\ &= \frac{\left(N^2-1\right) N}{3}. \end{aligned} \tag{B.2}$$

Thus, the angular term becomes

$$\angle \{\det(\Phi)\} = (-j)^{N\left(\frac{N-1}{2}\right)} e^{\frac{j\pi\alpha\left(N^2-1\right)}{6}}. \tag{B.3}$$

List of References

[1] T. S. Rappaport, *Wireless Communications Principles and Practice*. Prentice Hall, PTR, 1996.

[2] T. Keller and L. Hanzo, "Adaptive multicarrier modulation: A convenient framework for time-frequency processing in wireless communications," *Proceedings of the IEEE*, vol. 88, no. 5, pp. 611–640, May 2000.

[3] H. Schulze and C. Luders, *Theory and Applications of OFDM and CDMA*. John Wiley & Sons Ltd, 2005.

[4] R. R. Mosier and R. G. Clabaugh, "Kineplex, a bandwidth efficient binary transmission system," *AIEE Transactions (Part I: Communications and Electronics)*, vol. 76, pp. 723–728, Jan 1958.

[5] R. W. Chang, "Synthesis of band-limited orthogonal signals for multichannel data transmission," *Bell Systems Technical Journal*, vol. 45, pp. 1775–1796, December 1966.

[6] B. Saltzberg, "Performance of an Efficient Parallel Data Transmission System," *IEEE Transactions on Communication Technology*, vol. 15, no. 6, pp. 805–811, 1967.

[7] R. Chang and R. Gibby, "A theoretical study of performance of an orthogonal multiplexing data transmission scheme," *IEEE Transactions on Communication Technology*, vol. 16, no. 4, pp. 529–540, Aug. 1968.

[8] US3488445A. US Patent, Orthogonal frequency division multiplex data transmission system, January 1970. Filed in November 1966 by R. W. Chang.

[9] J. Salz and S. B. Weinstein, "Fourier transform communications," *Bell Telephone Laboratories*, 1969.

[10] S. Weinstein and P. Ebert, "Data transmission by frequency-division multiplexing using the discrete fourier transform," *IEEE Transactions on Communication Technology*, vol. 19, no. 5, pp. 628–634, 1971.

[11] J. A. C. Bingham, "Multicarrier modulation for data transmission: an idea whose time has come," *IEEE Communications Magazine*, vol. 28, no. 5, pp. 5–14, 1990.

[12] E. Dahlman, S. Parkvall, J. Skold, and P. Beming, *3G Evolution: HSPA and LTE for Mobile Broadband*, 2nd ed. Elsevier Ltd., 2008.

[13] D. Astely, E. Dahlman, A. Furuskar, Y. Jading, M. Lindstrom, and S. Parkvall, "LTE: the evolution of mobile broadband," *IEEE Communications Magazine*, vol. 47, no. 4, pp. 44–51, 2009.

[14] H. Holma and A. Toskala, Eds., *LTE for UMTS: OFDMA and SC-FDMA Based Radio Access*. John Wiley & Sons Ltd, 2009.

[15] S. Ramseler, M. Arzberger, and A. Hauser, "MV and LV powerline communications: new proposed IEC standards," in *Proc. IEEE Transmission and Distribution Conf*, vol. 1, 1999, pp. 235–239.

[16] P. Achaichia, M. Le Bot, and P. Siohan, "OFDM/OQAM: A Solution to Efficiently Increase the Capacity of Future PLC Networks," *IEEE Transactions on Power Delivery*, vol. 26, no. 4, pp. 2443–2455, 2011.

[17] H. Sanjoh, E. Yamada, and Y. Yoshikuni, "Optical orthogonal frequency division multiplexing using frequency/time domain filtering for high spectral efficiency up to 1 bit/s/Hz," in *Proc. Optical Fiber Communication Conf. and Exhibit OFC 2002*, 2002, pp. 401–402.

[18] W. Shieh and C. Athaudage, "Coherent optical orthogonal frequency division multiplexing," *Electronics Letters*, vol. 42, no. 10, pp. 587–589, 2006.

[19] M. R. D. Rodrigues and I. Darwazeh, "Fast OFDM: a proposal for doubling the data rate of OFDM schemes," in *Proceedings of the International Conference on Telecommunications*, vol. 3, June 2002, pp. 484–487.

[20] F. Xiong, "M-ary amplitude shift keying OFDM system," *IEEE Transactions on Communications*, vol. 51, no. 10, pp. 1638–1642, Oct. 2003.

[21] M. R. D. Rodrigues and I. Darwazeh, "A spectrally efficient frequency division multiplexing based communications system," in *Proceedings of the 8th International OFDM Workshop, Hamburg*, 2003. [Online]. Available: http://eprints.ucl.ac.uk/70597/

[22] M. Hamamura and S. Tachikawa, "Bandwidth efficiency improvement for multi-carrier systems," in *Proc. 15th IEEE International Symposium on Personal, Indoor and Mobile Radio Communications PIMRC 2004*, vol. 1, Sep. 5–8, 2004, pp. 48–52.

[23] W. Jian, Y. Xun, Z. Xi-lin, and D. Li, "The prefix design and performance analysis of DFT-based overlapped frequency division multiplexing (ovFDM-DFT) system," in *Proc. 3rd International Workshop on Signal Design and Its Applications in Communications IWSDA 2007*, Sep. 23–27, 2007, pp. 361–364.

[24] F. Rusek and J. B. Anderson, "The two dimensional Mazo limit," in *International Symposium of Information Theory, ISIT '05.*, vol. 57, 2005, pp. 970–974.

[25] ——, "Multistream faster than Nyquist signaling," *IEEE Transactions on Communications*, vol. 57, pp. 1329–1340, 2009.

[26] S. Yamamoto, K. Yonenaga, A. Sahara, F. Inuzuka, and A. Takada, "Achievement of subchannel frequency spacing less than symbol rate and improvement of dispersion tolerance in optical OFDM transmission," *IEEE/OSA Journal of Lightwave Technology*, vol. 28, no. 1, pp. 157–163, 2010.

[27] A. Chorti and I. Kanaras, "Masked M-QAM OFDM: A simple approach for enhancing the security of OFDM systems," in *Proc. IEEE 20th Int Personal, Indoor and Mobile Radio Communications Symp*, 2009, pp. 1682–1686.

[28] A. Chorti, "Masked-OFDM: A physical layer encryption for future OFDM applications," in *Proc. IEEE GLOBECOM Workshops (GC Wkshps)*, 2010, pp. 1254–1258.

[29] J. Salz, "Optimum mean-square decision feedback equalization," *Bell Systems Technical Journal*, vol. 52, no. 8, pp. 1341–1373, 1973.

[30] J. E. Mazo, "Faster than Nyquist signalling," *Bell Systems Technical Journal*, vol. 54, pp. 429–458, Oct 1975. [Online]. Available: http://www.alcatel-lucent.com/bstj/vol54-1975/articles/bstj54-8-1451.pdf

[31] J. E. Mazo and H. J. Landau, "On the minimum distance problem for faster-than-Nyquist signaling," *IEEE Transactions on Information Theory*, vol. 34, no. 6, pp. 1420–1427, 1988.

[32] D. Hajela, "On computing the minimum distance for faster than Nyquist signaling," *IEEE Transactions on Information Theory*, vol. 36, no. 2, pp. 289–295, 1990.

[33] ——, "On faster than Nyquist signaling: Computing the minimum distance," *Journal of Approximation Theory*, vol. 63, no. 1, pp. 108–120, Oct. 1990. [Online]. Available: http://www.sciencedirect.com/science/article/pii/002190459090118A

[34] ——, "On faster than Nyquist signaling: further estimations on the minimum distance," *SIAM Journal on Applied Mathematics*, vol. 52, no. 3, pp. 900–907, 1992. [Online]. Available: http://link.aip.org/link/?SMM/52/900/1

[35] I. Kanaras, A. Chorti, M. Rodrigues, and I. Darwazeh, "An optimum detection for a spectrally efficient non orthogonal FDM system," in *Proceedings of the 13th International OFDM Workshop, Hamburg*, August 2008.

[36] ——, "Spectrally efficient FDM signals: Bandwidth gain at the expense of receiver complexity," in *IEEE International Conference On Communications*, 2009, pp. 1–6.

[37] T. K. L. Hanzo, W.T. Webb, *Single and Multi-Carrier Quadrature Amplitude Modulation: Principles and Applications for Personal Communications, WLANS and Broadcasting*. John Wiley and IEEE press, 2000.

[38] J. Cimini, L. J., "Analysis and simulation of a digital mobile channel using orthogonal frequency division multiplexing," *IEEE Transactions on Communications*, vol. 33, no. 7, pp. 665–675, 1985.

[39] W. Zou and Y. Wu, "COFDM: An overview," *IEEE Transactions on Broadcasting*, vol. 41, no. 1, pp. 1–8, 1995.

[40] G. Raleigh and J. Cioffi, "Spatio-temporal coding for wireless communication," *IEEE Transactions on Communications*, vol. 46, no. 3, pp. 357–366, 1998.

[41] M. Russell and G. Stuber, "Interchannel interference analysis of OFDM in a mobile environment," in *Proc. IEEE 45th Vehicular Technology Conference*, vol. 2, 1995, pp. 820–824 vol.2.

[42] H.-C. Wu, "Analysis and characterization of intercarrier and interblock interferences for wireless mobile OFDM systems," *IEEE Transactions on Broadcasting*, vol. 52, no. 2, pp. 203–210, 2006.

[43] L. Hanzo and T. Keller, *OFDM and MC-CDMA: A Primer*. John Wiley & Sons Ltd, IEEE Press, 2006.

[44] E. Feig, F. Mintzer, and A. Nadas, "Digital implementation of frequency division multiplexing on peak-limited channels," in *Proc. Int Acoustics, Speech, and Signal Processing ICASSP-89. Conf*, 1989, pp. 1364–1367.

[45] S. Merchan, A. Armada, and J. Garcia, "OFDM performance in amplifier nonlinearity," *IEEE Transactions on Broadcasting*, vol. 44, no. 1, pp. 106–114, 1998.

[46] R. HAAS and J. C. BELFIORE, "A time-frequency well-localized pulse for multiple carrier transmission," *Wireless Personal Communications*, pp. 1–18, 1997.

[47] W. Kozek and A. Molisch, "Nonorthogonal pulseshapes for multicarrier communications in doubly dispersive channels," *IEEE Journal on Selected Areas in Communications*, vol. 16, no. 8, pp. 1579–1589, 1998.

[48] M. Vetterli and J. Kovacevic, *Wavelets and Subband Coding*. Prentice Hall, 1995.

[49] H. G. Feichtinger and K. Grochenig, *Non-orthogonal wavelet and Gabor expansions, and group representations, chapter in "wavelets and their applications"*. Jones and Bartlett, 1992.

[50] P. Schniter, "A new approach to multicarrier pulse design for doubly dispersive channels," in *In Proc. Allerton Conf. Commun., Control, and Computing*, 2003, pp. 1012–1021.

[51] ——, "On the design of non-(bi)orthogonal pulse-shaped FDM for doubly-dispersive channels," in *Proc. IEEE Int. Conf. Acoustics, Speech, and Signal Processing (ICASSP '04)*, vol. 3, 2004.

[52] T. Strohmer and S. Beaver, "Optimal OFDM system design through optimal sphere coverings," *2001 IEEE International Conference on Acoustics, Speech, and Signal Processing, 2001. Proceedings. (ICASSP '01)*, vol. 4, pp. 2373–2376 vol.4, 2001.

[53] ——, "Optimal OFDM design for time-frequency dispersive channels," *IEEE Transactions on Communications*, vol. 51, no. 7, pp. 1111–1122, July 2003.

[54] A. Kliks, H. Bogucka, I. Stupia, and V. Lottici, "A pragmatic bit and power allocation algorithm for NOFDM signalling," in *Proc. IEEE Wireless Communications and Networking Conf. WCNC 2009*, 2009, pp. 1–6.

[55] D. Schafhuber, G. Matz, and F. Hlawatsch, "Pulse-shaping OFDM/BFDM systems for time-varying channels: ISI/ICI analysis, optimal pulse design, and efficient implementation," in *Proc. 13th IEEE Int Personal, Indoor and Mobile Radio Communications Symp*, vol. 3, 2002, pp. 1012–1016.

[56] I. Trigui, M. Siala, S. Affes, A. Stephenne, and H. Boujemaa, "Optimum pulse shaping for OFDM/BFDM systems operating in time varying multi-path channels," in *Proc. IEEE Global Telecommunications Conf. GLOBECOM '07*, 2007, pp. 3817–3821.

[57] I. Kanaras, "Spectrally efficient multicarrier communication systems: signal detection, mathematical modelling and optimisation," Ph.D. dissertation, University College London, June 2010.

[58] D. H. Bailey and P. N. Swarztrauber, "The Fractional Fourier Transform and applications," *SIAM Review*, vol. 33, pp. 389–404, Sept 1991.

[59] L. Bluestein, "A linear filtering approach to the computation of discrete Fourier transform," *IEEE Transactions on Audio and Electroacoustics*, vol. 18, no. 4, pp. 451–455, 1970.

[60] S. I. A. Ahmed and I. Darwazeh, "IDFT based transmitters for spectrally efficient FDM system," in *London Communication Symposium*, Sep 2009.

[61] S. Isam and I. Darwazeh, "Simple DSP-IDFT techniques for generating spectrally efficient FDM signals," in *IEEE, IET International Symposium on Communication Systems, Networks and Digital Signal Processing*, Jul 2010, pp. 20 – 24.

[62] ——, "On the digital design of non-orthogonal spectrally efficient frequency division multiplexed (FDM) signals," in *4th International Symposium on Broadband Communications (ISBC'10)*, Jul 2010.

[63] ——, "IDFT-DFT techniques for generating and receiving spectrally efficient FDM signals," *American Journal for Engineering and Applied Sciences*, 2010 (submitted).

[64] J. G. Proakis and M. Salehi, *Digital Communications*. McGraw-Hill, 2008.

[65] I. Kanaras, A. Chorti, M. Rodrigues, and I. Darwazeh, "Analysis of sub-optimum detection techniques for bandwidth efficient multi-carrier communication systems," in *Proceedings of Cranfield Multi-Strand Conference*, April 2008.

[66] G. H. Golub and C. F. V. Loan., *Matrix Computations*, 3rd ed. The John Hopkins University Press, 1996.

[67] J. L. Miro Rozloznik Luc Giraud and J. van den Eshof, "Rounding error analysis of the classical Gram Schmidt process," CERFACS, Tech. Rep., 2004.

[68] J. W. D. B. Noble, *Applied Linear Algebra*, 2nd ed. Prentice Hall, 1977.

[69] A. Bjorck and C. Paige, "Loss and recapture of orthogonality in the modified Gram-Schmidt algorithm," *SIAM Journal on Matrix Analysis and Applications*, vol. 13, pp. 176–190, Jan 1992.

[70] H. Ge, "Iterative Gram-Schmidt orthonormalization for efficient parameter estimation," in *Proc. IEEE International Conference on Acoustics, Speech and Signal Processing*, vol. 4, May 12–15, 1998, pp. 2477–2480.

[71] D. F. Scofield, "A note on Lowdin orthogonalization and the square root of a positive self-adjoint matrix," *International Journal of Quantum Chemistry*, vol. 7, pp. 561–568, 1972.

[72] I. Mayer, "On Lowdin's method of symmetric orthogonalization," *International Journal of Quantum Chemistry*, vol. 90, pp. 63–65, 2002.

[73] J. A. E. J. G. Aiken and J. A. Goldstein, "On Lowdin orthogonalization," *International Journal of Quantum Chemistry*, 1980.

[74] I. Kanaras, A. Chorti, M. Rodrigues, and I. Darwazeh, "A new quasi-optimal detection algorithm for a non orthogonal Spectrally Efficient FDM," in *Proc. 9th Int. Symp. Communications and Information Technology ISCIT 2009*, 2009, pp. 460–465.

[75] A. Goldsmith, *Wireless Communications*. Cambridge University Press, 2005.

[76] A. S. Martin Grotschel, Laszlo Lovasz, *Geometric Algorithms and Combinatorial Optimization*, 2nd ed. Springer-Verlag, 1993.

[77] B. Hassibi and H. Vikalo, "On the sphere-decoding algorithm I. Expected complexity," *IEEE Transactions on Signal Processing*, vol. 53, no. 8, pp. 2806–2818, 2005.

[78] U. Fincke and M. Pohst, "Improved methods for calculating vectors of short length in a lattice, including a complexity analysis," *Mathematics of Computation*, vol. 44, no. 170, pp. 463–471, 1985. [Online]. Available: http://dx.doi.org/10.2307/2007966

[79] H. Jafarkhani, *Space-Time Coding, Theory and Practice*. Cam, 2005.

[80] R. A. Horn and C. R. Johnson, *Matrix Analysis*. Cambridge University Press, 1985.

[81] C. P. Schnorr and M. Euchner, "Lattice basis reduction: improved practical algorithms and solving subset sum problems." in *Math. Programming*, 1993, pp. 181–191.

[82] E. Agrell, T. Eriksson, A. Vardy, and K. Zeger, "Closest point search in lattices," *IEEE Transactions on Information Theory*, vol. 48, no. 8, pp. 2201–2214, 2002.

[83] B. M. Hochwald and S. ten Brink, "Achieving near-capacity on a multiple-antenna channel," *IEEE Transactions on Communications*, vol. 51, no. 3, pp. 389–399, 2003.

[84] A. Chorti, I. Kanaras, M. Rodrigues, and I. Darwazeh, "Joint channel equalization and detection of spectrally efficient FDM signals," in *IEEE 21th Personal, Indoor and Mobile Radio Communications Symposium 2010, IEEE PIMRC'10,*, Sep 2010.

[85] I. Kanaras, A. Chorti, M. Rodrigues, and I. Darwazeh, "Investigation of a semidefinite programming detection for a spectrally efficient FDM system," in *Proc. IEEE 20th Int Personal, Indoor and Mobile Radio Communications Symp*, 2009, pp. 2827–2832.

[86] Z.-Q. Luo and W. Yu, "An introduction to convex optimization for communications and signal processing," *IEEE Journal on Selected Areas in Communications*, vol. 24, no. 8, pp. 1426–1438, 2006.

[87] J. Jalden and B. Ottersten, "The diversity order of the semidefinite relaxation detector," *IEEE Transactions on Information Theory*, vol. 54, no. 4, pp. 1406–1422, 2008.

[88] W.-K. Ma, P.-C. Ching, and Z. Ding, "Semidefinite relaxation based multiuser detection for M-ary PSK multiuser systems," *IEEE Transactions on Signal Processing*, vol. 52, no. 10, pp. 2862–2872, 2004.

[89] M. Kisialiou and Z.-Q. Luo, "Performance analysis of quasi-maximum-likelihood detector based on semi-definite programming," in *Proc. IEEE Int. Conf. Acoustics, Speech, and Signal Processing (ICASSP '05)*, vol. 3, 2005.

[90] I. Kanaras, A. Chorti, M. Rodrigues, and I. Darwazeh, "A combined MMSE-ML detection for Spectrally Efficient non Orthogonal FDM signal," in *Proceedings of IEEE Broadnet conference*, September 2008.

[91] ——, "A fast constrained sphere decoder for ill conditioned communication systems," *IEEE Communications Letters*, vol. 14, no. 11, pp. 999–1001, 2010.

[92] C. Hansen, *Rank Deficient and Discrete Ill Posed Problems.* SIAM, 1998.

[93] T. Cui and C. Tellambura, "An efficient generalized sphere decoder for rank-deficient MIMO systems," *IEEE Communications Letters*, vol. 9, no. 5, pp. 423–425, 2005.

[94] D. Karampatsis, M. R. D. Rodrigues, and I. Darwazeh, "Performance comparison of OFDM and FOFDM communication systems in typical GSM multipath environments," in *Proceedings of the London Communications Symposium*, Sept 2003, pp. 117–120.

[95] D. Karampatsis, "Modelling and performance assessment of OFDM and Fast-OFDM wireless communication systems," Ph.D. dissertation, University College London, August2004.

[96] K. Li, "Implementation and evaluation of Fast OFDM systems with complex modulation schemes," Master's thesis, University College Lodon, 2006.

[97] ——, "Fast orthogonal frequency division multiplexing (Fast-OFDM) for wireless communications," Ph.D. dissertation, University College London, 2008.

[98] J. Zhao and A. D. Ellis, "A novel optical fast OFDM with reduced channel spacing equal to half of the symbol rate per carrier," in *Proc. Conf Optical Fiber Communication (OFC), collocated National Fiber Optic Engineers Conf. (OFC/NFOEC)*, 2010, pp. 1–3.

[99] S. K. Ibrahim, J. Zhao, D. Rafique, J. A. O'Dowd, and A. D. Ellis, "Demonstration of world-first experimental optical Fast OFDM system at 7.174Gbit/s and 14.348Gbit/s," in *Proc. 36th European Conf Optical Communication (ECOC) and Exhibition*, 2010, pp. 1–3.

[100] S. Takahashi, M. Hamamura, and S. Tachikawa, "A demodulation complexity reduction method using M-algorithm for high compaction multi-carrier modulation systems," in *Proc. 1st International Symposium on Wireless Communication Systems*, 2004, pp. 418–422.

[101] Y. Hou and M. Hamamura, "Bandwidth efficiency of PC-OFDM systems with high compaction multi-carrier modulation," in *Proc. International Conference on Wireless Communications, Networking and Mobile Computing*, vol. 1, Sep. 23–26, 2005, pp. 197–200.

[102] W. Hao, S. Jie, and L. Dao-ben, "Application of Gabor transform in a novel time frequency division multiplex system," in *Proc. 4th IEEE Int. Conf. Circuits and Systems for Communications ICCSC 2008*, 2008, pp. 220–224.

[103] W. H. S. Jie and L. Dao-ben, "A time frequency division multiplex system and fast detection approach base on Gabor transform," in *Proc. Global Mobile Congress 2009*, 2009, pp. 1–6.

[104] H. JIANG and D.-b. LI, "Overlapped frequency-time division multiplexing," *The Journal of China Universities of Posts and Telecommunications*, vol. 16, no. 2, pp. 8–13, Apr. 2009. [Online]. Available: http://www.sciencedirect.com/science/article/pii/S1005888508601934

[105] X. JIN and D.-b. LI, "Decoding OvTDM with sphere-decoding algorithm," *The Journal of China Universities of Posts and Telecommunications*, vol. 15, no. 4, pp. 35–39, Dec. 2008. [Online]. Available: http://www.sciencedirect.com/science/article/pii/S1005888508603994

[106] P. Sun, X. Yang, and D. Li, "Lattice reduction aided MMSE-SIC detection for non-orthogonal frequency division multiplexing signals," in *Proc. Third Int. Conf. Communications and Networking in China ChinaCom 2008*, 2008, pp. 527–532.

[107] Y. MO, X. YANG, and D.-b. LI, "Semidefinite programming detection for OvHDM signal," *The Journal of China Universities of Posts and Telecommunications*, vol. 15, no. 3, pp. 8–12, 18, Sep. 2008. [Online]. Available: http://www.sciencedirect.com/science/article/pii/S1005888508600990

[108] F. Rusek and J. B. Anderson, "Successive interference cancellation in multistream faster-than-Nyquist signaling," in *International Conference on Wireless Communications and Mobile Computing*, 2006, pp. 1021–1026.

[109] F. Rusek and J. Anderson, "Improving OFDM: multistream faster than Nyquist signaling," in *6th Int. ITG Conf. Source and Channel Coding*, Apr 2006.

[110] A. Prlja, J. B. Anderson, and F. Rusek, "Receivers for faster-than-Nyquist signaling with and without turbo equalization," in *Proc. IEEE Int. Symp. Information Theory ISIT 2008*, 2008, pp. 464–468.

[111] D. Dasalukunte, F. Rusek, and V. Owall, "An iterative decoder for multicarrier faster-than-Nyquist signaling systems," in *Proc. IEEE Int Communications (ICC) Conf*, 2010, pp. 1–5.

[112] D. Dasalukunte, F. Rusek, J. B. Anderson, and V. Owall, "Transmitter architecture for faster-than-Nyquist signaling systems," in *Proc. IEEE Int. Symp. Circuits and Systems ISCAS 2009*, 2009, pp. 1028–1031.

[113] D. Dasalukunte, F. Rusek, V. Owall, K. Ananthanarayanan, and M. Kandasamy, "Hardware implementation of mapper for faster-than-Nyquist signaling transmitter," in *Proc. NORCHIP*, 2009, pp. 1–5.

[114] D. Dasalukunte, F. Rusek, and V. Owall, "Multicarrier faster-than-Nyquist transceivers: hardware architecture and performance analysis," *IEEE Transactions on Circuits and Systems I: Regular Papers*, vol. 58, no. 4, pp. 827–838, 2011.

[115] D. O. North, "An Analysis of the factors which determine signal/noise discrimination in pulsed-carrier systems," *Proceedings of the IEEE*, vol. 51, no. 7, pp. 1016–1027, 1963.

[116] A. Córdova, W. . Gautschi, and S. Ruscheweyh, "Vandermonde matrices on the circle: Spectral properties and conditioning," *Numerische Mathematik*, vol. Volume 57, Number 1, pp. 577–591, December, 1990.

[117] P. J. S. G. Ferreira, "Superresolution, the recovery of missing samples, and Vandermonde matrices on the unit circle," in *Proceeding of the 1999 Workshop on Sampling Theory and Applications*, August 1999.

[118] L. Berman and A. Feuer, "On perfect conditioning of Vandermonde matrices on the unit circle," *Electronic Journal of Linear Algebra*, vol. 16, pp. 157–161, July 2007.

[119] I. E. Telatar, "Capacity of multi-antenna Gaussian channels," *European Transactions on Telecommunications*, vol. 10, pp. 585–595, 1999.

[120] P. Ferreira, "The eigenvalues of matrices that occur in certain interpolation problems," *IEEE Transactions on Signal Processing*, vol. 45, no. 8, pp. 2115–2120, 1997.

[121] V. Namias, "The fractional order Fourier Transform and its application to quantum mechanics," *IMA Journal of Applied Mathematics*, vol. 25, no. 3, pp. 241–265, Mar. 1980. [Online]. Available: http://imamat.oxfordjournals.org/content/25/3/241.abstract

[122] N. Ahmed, T. Natarajan, and K. R. Rao, "Discrete Cosine Transform," *IEEE Transactions on Computers*, no. 1, pp. 90–93, 1974.

[123] B. Lee, "A new algorithm to compute the discrete cosine Transform," *IEEE Transactions on Acoustics, Speech, and Signal Processing*, vol. 32, no. 6, pp. 1243–1245, 1984.

[124] A. Macedo and E. Sousa, "Coded OFDM for broadband indoor wireless systems," in *Proc. 'Towards the Knowledge Millennium' Communications ICC 97 Montreal 1997 IEEE International Conference on*, vol. 2, 1997, pp. 934–938 vol.2.

[125] A. V. Oppenheim and R. W. Schafer, *Discrete-time signal processing.* Prentice Hall, 1989.

[126] T. Nagell, *Residue Classes and Residue Systems.* New York: Wiley, 1951.

[127] K. M. Aamir, M. A. Maud, and A. Loan, "On Cooley-Tukey FFT method for zero padded signals," in *Proc. IEEE Symp. Emerging Technologies*, 2005, pp. 41–45.

[128] H. V. Sorensen and C. S. Burrus, "Efficient computation of the DFT with only a subset of input or output points," *IEEE Transactions on Signal Processing*, vol. 41, no. 3, pp. 1184–1200, 1993.

[129] P. N. Whatmough, M. Perret, S. Isam, and I. Darwazeh, "VLSI architecture for a reconfigurable spectrally efficient FDM baseband transmitter," *IEEE Journal on Circuits and Systems*, 2011.

[130] h. Aeroflex PXI RF modular instruments. [Online]. Available: http://www.aeroflex.com/ats/products/category/PXI.html

[131] P. N. Whatmough, M. Perret, S. Isam, and I. Darwazeh, "VLSI architecture for a reconfigurable spectrally efficient FDM baseband transmitter," in *IEEE International Symposium on Circuits and Systems (IEEE ISCAS'11)*, 2011.

[132] M. R. Perrett and I. Darwazeh, "Flexible hardware architecture of SEFDM transmitters with real-time non-orthogonal adjustment," in *IEEE 18th International Conference on Telecommunications (IEEE ICT'11)*, 2011.

[133] ——, "A simple ETHERNET stack implementation in VHDL to enable FPGA logic reconfigurability," in *International Conference on Reconfigurable Computing and FPGAs*, 2011.

[134] I. Kanaras, A. Chorti, M. Rodrigues, and I. Darwazeh, "An overview of optimal and sub-optimal detection techniques for a non orthogonal spectrally efficient FDM," in *London Communication Symposium*, Sep 2009.

[135] A. Papoulis and S. U. Pillai, *Probability, Random Variables and Stohastic Processes*, 4th ed. McGraw-Hill, 2002.

[136] R. C. Grammenos, S. Isam, and I. Darwazeh, "FPGA design of a truncated SVD based receiver for the detection of SEFDM signals," in *22nd Personal, Indoor and Mobile Radio Communications Symposium 2011, IEEE PIMRC'11,*, 2011.

[137] A. Burg, "VLSI circuits for MIMO communication systems," Ph.D. dissertation, Swiss Federal Institute of Technology Zurich, 2006.

[138] P. C. Hansen, "The truncated SVD as a method for regularization," *BIT Numerical Mathematics*, vol. 27, pp. 534–553, Dec 1987.

[139] ——, "Truncated singular value decomposition solutions to discrete ill-posed problems with ill-determined numerical rank," *SIAM Journal on Scientific and Statistical Computing*, vol. 11, pp. 503–518, May 1990.

[140] ——, "The discrete picard condition for discrete ill- posed problems," *BIT*, vol. 30, pp. 658–672, 1990.

[141] K. Jbilou, L. Reichel, and H. Sadok, "Vector extrapolation enhanced TSVD for linear discrete ill-posed problems," *Numerical Algorithms*, vol. 51, pp. 195–208, 2009.

[142] L. G. Barbero and J. S. Thompson, "A fixed-complexity MIMO detector based on the complex sphere decoder," in *Proc. IEEE 7th Workshop Signal Processing Advances in Wireless Communications SPAWC '06*, 2006, pp. 1–5.

[143] ——, "Fixing the complexity of the sphere decoder for MIMO detection," *IEEE Transactions on Wireless Communications*, vol. 7, no. 6, pp. 2131–2142, 2008.

[144] ——, "Extending a fixed-complexity sphere decoder to obtain likelihood information for turbo-MIMO systems," *IEEE Transactions on Vehicular Technology*, vol. 57, no. 5, pp. 2804–2814, 2008.

[145] M. S. Khairy, M. M. Abdallah, and S. E.-D. Habib, "Efficient FPGA implementation of MIMO decoder for Mobile WiMAX system," in *Proc. IEEE Int. Conf. Communications ICC '09*, 2009, pp. 1–5.

[146] T. F. Chan and Hansen, "Computing truncated SVD least squares solutions by rank revealing QR-factorizations„" CAM Report 86-01, Dept. of Mathematics, U.C.L.A, Tech. Rep., 1986.

[147] M. Rahmati, M. S. Sadri, and M. A. Naeini, "FPGA based singular value decomposition for image processing applications," in *Proc. Int. Conf. Application-Specific Systems, Architectures and Processors ASAP 2008*, 2008, pp. 185–190.

[148] L. G. Barbero and J. S. Thompson, "FPGA design considerations in the implementation of a fixed-throughput sphere decoder for MIMO systems," in *Proc. Int. Conf. Field Programmable Logic and Applications FPL '06*, 2006, pp. 1–6.

[149] R. Radzokota, E. Golovins, and N. Ventura, "Linear detector performance in ill-conditioned MIMO OFDM channel," in *Proc. Int. Conf. Ultra Modern Telecommunications & Workshops ICUMT '09*, 2009, pp. 1–7.

[150] S. Isam, I. Kanaras, and I. Darwazeh, "A Truncated SVD Approach for Fixed Complexity Spectrally Efficient FDM Receivers," in *IEEE Wireless Communications & Networking Conference (IEEE WCNC'11)*, 2011.

[151] S. Isam and I. Darwazeh, "Design and Performance Assessment of Fixed Complexity Spectrally Efficient FDM Receivers," in *IEEE 73rd Vehicular Technology Conference (IEEE VTC'11)*, 2011.

[152] Y. Wu and W. Y. ZOU, "Performance simulation of COFDM for TV broadcast application," *SMPTE*, May 1995.

[153] J. Tellado, *Multicarrier Modulation with Low PAPR: Applications to DSL and Wireless*. Kluwer Academic Press, 2000.

[154] R. Bäuml, R. F. H. Fischer, and J. B. Huber, "Reducing the peak-to-average power ratio of multicarrier modulation by selected mapping," *Electronics Letters*, vol. 32, pp. 2056–2057, 1996.

[155] S. H. Muller and J. B. Huber, "OFDM with reduced peak-to-average power ratio by optimum combination of partial transmit sequences," vol. 33, no. 5, 1997, pp. 368–369.

[156] T. May and H. Rohling, "Reducing the peak-to-average power ratio in OFDM radio transmission systems," in *Proc. 48th IEEE Vehicular Technology Conference VTC 98*, vol. 3, 1998, pp. 2474–2478 vol.3.

[157] J. Tellado and J. M. Cioffi, "Efficient algorithms for reducing PAR in multicarrier systems," in *Proc. IEEE International Symposium on Information Theory*, Aug. 16–21, 1998, p. 191.

[158] S.-W. Kim, J.-K. Chung, and H.-G. Ryu, "PAPR reduction of the OFDM signal by the SLM-based WHT and DSI method," in *Proc. TENCON 2006. 2006 IEEE Region 10 Conference*, Nov. 14–17, 2006, pp. 1–4.

[159] X. Yang, J. Wang, and D. Li, "Selected mapping in correlatively coded OFDM," in *Proc. Second International Conference on Communications and Networking in China CHINACOM '07*, Aug. 22–24, 2007, pp. 1121–1125.

[160] S. Y. Le Goff, S. S. Al-Samahi, B. K. Khoo, C. C. Tsimenidis, and B. S. Sharif, "Selected mapping without side information for PAPR reduction in OFDM," *IEEE Transactions on Wireless Communications*, vol. 8, no. 7, pp. 3320–3325, Jul. 2009.

[161] L. Yang, R. Chen, K. Soo, and Y. Siu, "An efficient sphere decoding approach for PTS assisted PAPR reduction of OFDM signals," *AEU - International Journal of Electronics and Communications*, vol. 61, pp. 684–688, 2007.

[162] J. Cimini, L.J. and N. Sollenberger, "Peak-to-average power ratio reduction of an OFDM signal using partial transmit sequences," *IEEE Communications Letters*, vol. 4, no. 3, pp. 86–88, 2000.

[163] P. Boonsrimuang and T. Paungma, "Proposal of improved PTS method for OFDM signal in the multi-path fading channel," in *Proc. 5th International Conference on*

Electrical Engineering/Electronics, Computer, Telecommunications and Information Technology ECTI-CON 2008, vol. 1, May 14–17, 2008, pp. 401–404.

[164] K. G. Paterson and V. Tarokh, "On the existence and construction of good codes with low peak-to-average power ratios," *IEEE Transactions on Information Theory*, vol. 46, no. 6, pp. 1974–1987, Sep. 2000.

[165] S. Slimane, "Reducing the peak-to-average power ratio of OFDM signals through precoding," *IEEE Transactions on Vehicular Technology*, vol. 56, no. 2, pp. 686–695, 2007.

[166] D. Guel and J. Palicot, "Analysis and comparison of clipping techniques for OFDM Peak-to-Average Power Ratio reduction," in *Proc. 16th International Conference on Digital Signal Processing*, Jul. 5–7, 2009, pp. 1–6.

[167] D. Wulich, N. Dinur, and A. Glinowiecki, "Level clipped high-order OFDM," *IEEE Transactions on Communications*, vol. 48, no. 6, pp. 928–930, Jun. 2000.

[168] J. D. Parsons, *The Mobile Radio Propagation Channel*, 2nd ed. John Wiley & Sons Ltd, 2000.

[169] M. Patzold, *Mobile Fading Channels*. John Wiley & Sons Ltd, 2002.

[170] A. Aguiar and J. Gross, "Wireless channel models," Technical University Berlin, TKN Technical Report TKN-03-007, April, 2003.

[171] A. F. Molisch, *Wireless Communications*. Wiley, IEEE, 2011.

[172] P. Bello, "Characterization of randomly time-variant linear channels," *Communications Systems, IEEE Transactions on*, vol. 11, no. 4, pp. 360 –393, december 1963.

[173] M. C. Jeruchim, P. Balaban, and K. S. Shanmugan, *Simulation of Communications Systems*. Kluwer Academic/Plenum Publishers, 2000.

[174] W. H. Tranter, K. S. Shanmugan, and T. S. Rappaport, *Communication systems simulation with wireless applications*. Prentice Hall, 2003.

[175] C. B. Rorabaugh, *Simulating Wireless Communication Systems*. Prentice Hall, 2004.

[176] E. J. P. M. G. Linnartz. Wireless communication. Web resource. [Online]. Available: www.WirelessCommunication.NL

[177] X. Wang, P. Ho, and Y. Wu, "Robust channel estimation and ISI cancellation for OFDM systems with suppressed features," *IEEE Journal on Selected Areas in Communications*, vol. 23, no. 5, pp. 963–972, 2005.

[178] M. Morelli and U. Mengali, "A comparison of pilot-aided channel estimation methods for OFDM systems," *IEEE Transactions on Signal Processing*, vol. 49, no. 12, pp. 3065–3073, 2001.

[179] L. Harjula, A. Mammela, and Z. Li, "Comparison of channel frequency and impulse response estimation for space-time coded OFDM systems," in *Proc. VTC 2002-Fall Vehicular Technology Conf. 2002 IEEE 56th*, vol. 4, 2002, pp. 2081–2085.

[180] L. Tong, B. M. Sadler, and M. Dong, "Pilot-assisted wireless transmissions: general model, design criteria, and signal processing," *IEEE Signal Processing Magazine*, vol. 21, no. 6, pp. 12–25, 2004.

[181] S. Werner, M. Enescu, and V. Koivunen, "Combined frequency and time domain channel estimation in mobile MIMO-OFDM systems," in *Proc. IEEE International Conference on Acoustics, Speech and Signal Processing ICASSP 2006*, vol. 4, 2006, pp. IV–IV.

[182] J.-J. van de Beek, O. Edfors, M. Sandell, S. K. Wilson, and P. O. Borjesson, "On channel estimation in OFDM systems," in *Proc. IEEE 45th Vehicular Technology Conf*, vol. 2, 1995, pp. 815–819.

[183] Y. Li, J. Cimini, L. J., and N. R. Sollenberger, "Robust channel estimation for OFDM systems with rapid dispersive fading channels," *IEEE Transactions on Communications*, vol. 46, no. 7, pp. 902–915, 1998.

[184] G. Dona and W. A. Krzymien, "MMSE channel estimation using two-dimensional filtering in rapid time-variant environments," in *Proc. VTC 2005-Spring Vehicular Technology Conf. 2005 IEEE 61st*, vol. 1, 2005, pp. 490–494.

[185] S.-Y. Leong, J. Wu, C. Xiao, and J. C. Olivier, "Fast time-varying dispersive channel estimation and equalization for an 8-PSK cellular system," *IEEE Transactions on Vehicular Technology*, vol. 55, no. 5, pp. 1493–1502, 2006.

[186] K.-H. Chang and C. N. Georghiades, "Iterative joint sequence and channel estimation for fast time-varying intersymbol interference channels," in *Proc. IEEE Int Communications ICC '95 Seattle, 'Gateway to Globalization' Conf*, vol. 1, 1995, pp. 357–361.

[187] L. Mazet, V. Buzenac-Settineri, M. de Courville, and P. Duhamel, "An EM based semi-blind channel estimation algorithm designed for OFDM systems," in *Proc. Conf Signals, Systems and Computers Record of the Thirty-Sixth Asilomar Conf*, vol. 2, 2002, pp. 1642–1646.

[188] A. Zia, J. P. Reilly, and S. Shirani, "Channel identification and tracking using alternating projections," in *Proc. IEEE Workshop Statistical Signal Processing*, 2003, pp. 430–433.

[189] M.-X. Chang and Y. T. Su, "Blind and semiblind detections of OFDM signals in fading channels," *IEEE Transactions on Communications*, vol. 52, no. 5, pp. 744–754, 2004.

[190] V. K. Jones and G. C. Raleigh, "Channel estimation for wireless OFDM systems," in *Proc. Bridge to Global Integration. IEEE Global Telecommunications Conf. GLOBECOM 98*, vol. 2, 1998, pp. 980–985.

[191] R. J. Baxley, J. E. Kleider, and G. T. Zhou, "Pilot design for OFDM with null edge subcarriers," *IEEE Transactions on Wireless Communications*, vol. 8, no. 1, pp. 396–405, 2009.

[192] C. Masouros and E. Alsusa, "A hybrid MC-CDM precoding scheme employing code hopping and partial beamforming," in *Proc. IEEE Int. Conf. Communications ICC '09*, 2009, pp. 1–5.

[193] N. Hathi, I. Darwazeh, and J. O'Reilly, "Peak-to-average power ratio performance comparison of different spreading code allocation strategies for MC-CDMA and MC-DS-CDMA," *Electronics Letters*, vol. 38, no. 20, pp. 1219–1220, 2002.

[194] R. S. Mozos and M. J. F.-G. Garcia, "Efficient complex sphere decoding for MC-CDMA systems," *IEEE Transactions on Wireless Communications*, vol. 5, no. 11, pp. 2992–2996, 2006.

[195] L. Zhang, H. Lei, X. Zhang, and D. Yang, "Efficient complex sphere decoding framework for linear dispersion space-time block codes," in *Proc. IEEE 18th Int. Symp. Personal, Indoor and Mobile Radio Communications PIMRC 2007*, 2007, pp. 1–4.

[196] A. Arrazi, "Modelling and performance assessment of spectrally efficient frequency division multiplexing," Master's thesis, Univesity College London, Sep 2010.